Numerical modeling of large-scale compact pv-csp hybrid plants

Dounia Ziyati

THÈSE

Pour obtenir le grade de

Docteur

Délivré par

l'**UNIVERSITÉ DE PERPIGNAN VIA DOMITIA**

Préparée au sein de l'école doctorale

Énergie et Environnement ED 305

Et de l'unité de recherche

PROMES-CNRS UPR 8521

Spécialité:

Science de l'Ingénieur- Energétique et Génie des Procédés

Présentée par **Dounia ZIYATI**

NUMERICAL MODELING OF LARGE-SCALE COMPACT PV-CSP HYBRID PLANTS

Soutenue le 19 Juillet 2022 devant le jury composé de:

M. Mohamed Amara	Chargé de Recherche	INL-Lyon	Rapporteur
M. Daniel Chemisana	Full Professor	Lleida university	Rapporteur
M. Alain Dollet	Directeur de Recherche	PROMES-CNRS	Directeur de thèse
M. Hamid Kachkachi	Full Professor	UPVD	Examinateur
Mme. Stéphanie Parola	Maître de conférence	IES-Montpellier	Examinatrice
M. Alexis Vossier	Chargé de Recherche	PROMES-CNRS	Directeur de thèse

Contents

List of Figures

List of Tables

Nomenclature

$1S$ One-sun

A Module Area, (m^2)

$ARPA-E$ Advanced Research Projects Agency-Energy

$BESS$ Batteries Energy Storage System

$BIPV$ Building Integrated PV

$BIPVT$ Building Integrated PV Thermal

bPV bifacial PV

$CAES$ Compressed Air Energy Storage

CF Capacity Factor, (%)

$CLFR$ Compact Linear Fresnel Reflector

co number of columns

CPV Concentrated Photovoltaics

CR Central Receiver

CSP Concentrated Solar Power

DA Dense Array

DF Demand Factor

DHI Diffuse Horizontal Irradiation, (W/m^2)

DNI Direct Normal Irradiation, (W/m^2)

DS Dispatch strategy

$DSSCs$ Dye-Sensitized Solar Cells

E Photon energy, (eV)

EBH Direct Horizontal Irradiance

EH Electric Heater

EQE External Quantum Efficiency

f Spectral distribution of light, (W/m^2nm)

f_{lpv} Derating factor, (%)

FES Flywheel Energy Storage

FF Fill Factor, (%)

$FlowB$ Flow Battery

$FOCUS$ Full-Spectrum Optimized Conversion and Utilization of Sunlight

G Global Irradiation, (W/m^2)

$GaAs$ Gallium Arsenide

$GaInP$ Gallium Indium Phosphide

GHG Greenhouse Gas

GHI Global Horizontal Irradiation, (W/m^2)

h Convective heat exchange coefficient, (W/m^{2}K)

$HEATS$ Hybrid Electric And Thermal Solar

HT High-Temperature

HTF Heat Transfer Fluid

HX Heat eXchange

IEA International Energy Agency

InP Indium Phosphide

K Number of time steps

k Offset parameter

l number of blocks

$L-PCM$ Localized-Phase Change Material

$LCOE$ Levelized Cost Of Electricity, (\$/kW h)

$LCOH$ Levelized Costs Of Hydrogen, (\$/kg)

$LCOHe$ Levelized Cost Of Heat, (\$/kWh)

$LCOS$ Levelized Cost Of Storage, (\$/kWh)

LFR Linear Fresnel Reflector

LHS Latent Heat Storage

$LHTES$ Latent Heat Thermal Energy Storage

$Li-ion$ Lithium-ion

$LPSP$ Loss of Power Supply Probability, (%)

LSP Luminescent Solar Power

M Number of modules

m avalanche breakdown exponent

MBE Mean Bias Error, (%)

MED Multi Effect Distillation

MJ multi-junction

mPV monofacial PV

MSM Molecular Storage Material

N Number of heliostats

Nb Number of blocks

$NOCT$ Nominal Operating Cell Temperature

$OPVs$ Organic Photovoltaics

ORC Organic Rankine Cycle

P Power, (W)

p number of load values

$P2H$ Power to Hydrogen

PB Power Block

$PCMs$ Phase Change Materials

PD Parabolic Dishes

PF Performance Factor, (%)

PHS Pumped Hydro Storage

PL Photo-Luminescent

PS Parallel Series

$PSCs$ Perovskite Solar Cells

PTC Parabolic Trough Collectors

PV Photovoltaic

$PVGIS$ Photovoltaic Geographical Information System

Q Cumulative energy, (GW h)

$QDSCs$ Quantum Dot Solar Cells

QRS Quartered Rotational Symmetry

R Reflectivity

$RMSE$ Root Mean Squared Error, (%)

ro number of rows

SBS Spectral Beam Splitting

SDB Solar DataBases

SHS Sensible Heat Storage

Si Silicon

SOC State Of Charge

$SolarPILOT$ Solar Power Tower Integrated Layout and Optimization Tool

SPT Solar Power Tower

SQ Shockley-Queisser

$SSLP$ Spectrally Selective Light Pipe

STC Standard Test Conditions

T Temperature, (°C)

t time

TC Thermochemical

$tCPV$ transmissive Concentrator Photovoltaic

TES Thermal Energy Storage

THS Thermochemical Heat Storage

$TIPV$ Thermionic Photovoltaics

TJ Triple Junction

TPV Thermophotovoltaic

U Heat transfer coefficient, ($W/m^2\,K$)

v Velocity, (m/s)

W unitless load parameter

WHR Wasted Heat Recovery

WSF Wavelength-Selective Filter

x x heliostat coordinate, (m)

y y heliostat coordinate, (m)

z z heliostat coordinate, (m)

Greek

α Absorptivity, (%)

α' Energy gap parameter, (eV/K)

β Temperature coefficient of power, (%/K)

β' Energy gap parameter, (K)

δ time step, (min)

λ Wavelength, (nm)

μ Chemical potential, ($kg\,m^2/s^2$)

ρ Reflectivity, (%)

τ Transmittance

θ Incident Angle, (°)

ε Surface emissivity, (%)

ς tilt angle, (°)

ζ Shockley-Queisser index

η Efficiency, (%)

κ	diode bypass coefficient

Physical Constants

σ	Stefan-Boltzmann constant, 5.67×10^{-8} (W/m^{2}K^4)
c	Speed of light in vacuum, 3×10^8 (m/s)
h	Planck constant, 6.62×10^{-34} (J s)
k_B	Boltzmann constant, 1.38×10^{-23} (J/K)
q	Elementary charge, 1.602×10^{-19} (A s)

Subscripts

act	actual
amb	ambiant
$avai$	available
blo	blocking
$bloc$	block
br	breakdown
$conv$	convection
$def\ dum$	definitely dumped after PV recovery
dif	diffuse
dir	direct
dum	dumped
exp	experimental
fix	fix
g	gap
gr	grid
hel	heliostat
in	incident
inc	inclined surface
$inver$	inverter
$load$	load
$loss$	loss
$meas$	measured
Mir	Mirror
mod	module
mpp	maximum power point
mul	multi
$need$	needed
pos	position
$pred$	predicted
rec	receiver
$recov$	recover
ref	reference
$refl$	reflected
rej	reject
s	surface
sc	short circuit
sh	shading
$simp$	simple
$spil$	spillage
SQ	Shockley-Queisser
t	total
th	thermal
$theo$	theoretical

tra	transmission
un	unable
wind	wind

Acknowledgments

This work was carried out by me, but it is a result of the effort, desire, intention, and support of many people. Therefore, this page is dedicated to all those who have cleared the path to this achievement.

First, I would like to thank Drs. Alain Dollet and Alexis Vossier, my thesis directors, for allowing me to carry out this work under their guidance and providing me with the help, knowledge and support. Thank you for trusting me and opening the doors of the Process Material & Solar Energy Laboratory (PROMES).

A sincere thanks to the jury members: Dr Mohamed Amara, Professors Daniel Chemisana and Hamid Kachkachi and Mrs Stéphanie Parola for accepting to read and assess this work.

To Dr. Rodolphe Vaillon, Anne Kaminski and Professor Hamid Kachkachi, members of the evaluation committee, for their valuable comments and suggestions to make this work go forward in the best possible way.

I am grateful to my family for their love and support. In particular, I thank my mother, Fatima Driouiche, for teaching me throughout my life the importance of always learning and being dedicated to what you do. Thank you for giving me the chance to follow up on my dreams, for being so patient with me and for respecting all my choices. To my sisters, Hanane and Noura, thank you for your kind messages.
To my spiritual father, Dr Miloude Rahmoune, thank you for pushing me forward with your words and support. Thank you for never stopping believing in me. I cannot imagine what would've happened if you weren't there when I most needed you. I love you and respect your dedication to your work.

To my second family, Simone and Max Herbert for always trusting in me and making me take a step out of my comfort zone when I wasn't feeling like doing that.
For sure I wouldn't forget Fergie, the best friend anyone can ask for, thanks for the long walks. I know listening to a human talking in Turkish while trying to enjoy your walk and your treat wouldn't be that great for you, but you made my mornings, afternoon and night every-time you were around. To Coca, my road companion, the one who knows how to cheer me up when I feel down, thank you for standing beside me along the way. Ouma, you were always the one I turned to when I was in doubt. I enjoyed

every trip we had together, you made it easy for me even when you didn't have enough energy to do it, but you kept pushing me forward.

I wouldn't forget the people who encouraged me to pursue a research career, starting with Dr Jean-François Henry, Jaona Randrianalisoa, Rachid Saadani and Professor Ayad Rezak. I will always remember: Ibrahim, Clarisse, Jérémy, and Guillaume great office companions from my time at Reims.

To Lynn Blin and Patrick Sandrat, the best coaches I ever had during the three-minute thesis competition (3MTC), thank you for your generosity with your time and patience, and more importantly, thank you for your trust and unlimited support even after the competition. To Jean Jacques, member of PhD student association for your wise word and encouragements by the end of my thesis, it was incredibly helpful to be heard and understood.

Beyond the advisors, I am grateful for the incredible people I meet during these three years at conferences and other events, Nathan, Sinane, Bahrajiti, Jordi, Mostafa, Guillaume, Jérémy, Paul, Flora, Jesse, Miguel, Mouhammed, Malik, Hanane, Janane, Avilian, Vichy, Zeeshan, Ségolène, Charlène, Mouhamed, and José.
To PROMES stuff either administrative or technical members, Nicolas Boullet, Gilles Flamant, Yann Volut, Driss Stitou, Alain Ferrier, Christelle, Samia, Didier, Jean-Pascale, Olivier, Eric, Stan, and Marianne. To Sylvie, those morning chats every Wednesday were great, yet exchanging great recipes were even great. To Abdelhadi, Youssef and Soufiane, for the amazing discussions we had over meals during the integration week; you made the week much more fun with your presence. To Kofi for naming your daughter after me; it's a great honor that I carry with proud. I hope here days will be full of joy and great moments. To members of the badminton club of Estavar for welcoming me despite my loud voice and unexpected reactions each time I had the flyer.

Without Youssef Berro, Amal Moujahid, Pierre-Henri Défieux, Damien Poincain, the journey would have been much more difficult and less fun. To Youssef for making me enjoy the roads differently, from Perpignan to Narbonne to Banuylus to Montpellier, all with a bike rather than a hike. To Amal for the long conversations and advises. To Damien Poincin for making me watch Camelot and make me see what I have been missing for years. To Pierre-Henri Defieux for the late nights at the office and the interesting conversations. To Brice for your energy and good dances we had from time to time. To Srirate and Alex for being of great company at work and while working-out, especially at Agnés classes with your smiles and encouragement you made it easy for me to follow you up. To José for the great time at Grenada and back at your hometown, I will always cherish the moments we had with your friends and family. To Ségolène for convincing me to try one badminton class, one class that turned to years of fun and loud screams xd; thanks for supporting me even when you couldn't bear my screams anymore. To Romain Mannini, you were of great help even when we didn't know each other that much, you were kind and of great support than you can ever

imagine. For that and more, thank you very much. I am glade for having such a great friend like you in my life.

Having good friends willing to go the next mile with you to support you with your craziness, to find the kind words to encourage you when you feel like giving up. To all of the amazing people I know, Didi, Adam, Brahim, Anas, Moad, Youness, Amine, Othmane, Meryam, Souhail, Clémence, Imade, and Hajar.

I cannot but acknowledge my current colleagues for their warm welcome and support, starting with my manager Geoffrey, for his trust and advice.

Finally, special thanks go to my secret hero, the one and only who was able to handle every mood swing with a big smile and warm hugs, thank you for being so patient along the road with me and for your support. The one who could always put a smile on my face even when I didn't feel like smiling. You were there to pick me up when I was feeling low. You are not much of a talker, yet in your way you were able to help me. So thank you for everything. I hope we will share a long and beautiful journey together.

To all of you, THANK YOU!

Introduction

Today, the energy sector presents the primary source of greenhouse gas emissions (GHG), with nearly three-quarters of the total global emissions [1] (Figure 1). This figure is strongly correlated with the continuous increase in energy demand over the years. Achieving the 2050 net zero emissions pathway [49] (i.e., assure proper coordination between perpetuating economic growth and ensuring environmental protection), will require nothing less than the complete transformation of the world's energy systems by speeding the deployment of clean and efficient energy technologies.

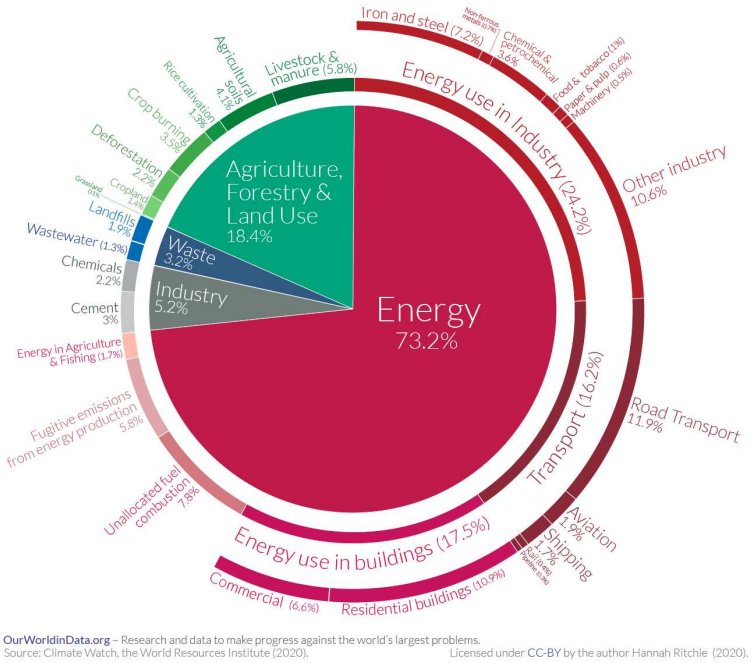

Figure 1: Global greenhouse gas emissions by sector in 2020 [1].

Free, available in some places more than others [50], and easy to harvest with today's well-known technologies, solar energy presents a promising solution to meeting future energy demands in an era of depleting fossil fuel sources [51]. The conversion of solar energy into electricity is usually achieved through either:

- Direct conversion of radiative energy into electricity using photovoltaic systems (PV) [52]. Thanks to continued policy support and cost reductions (see Figure 2), global solar PV generation additions are expected to increase by 49% between 2020 and 2025 according to the International Energy Agency (IEA) [53].

PV modules are cheap, small and can be used in many locations around the world [54]. However, one of the main drawbacks of PV is that it is a very unpredictable source of electricity production, due to the intermittence of the solar resource. This characteristic can penalize grid integration and power supply stability. Battery energy storage systems can improve the dispatchability of PV electricity, but currently, they are too expensive to be implemented on a large scale [55].

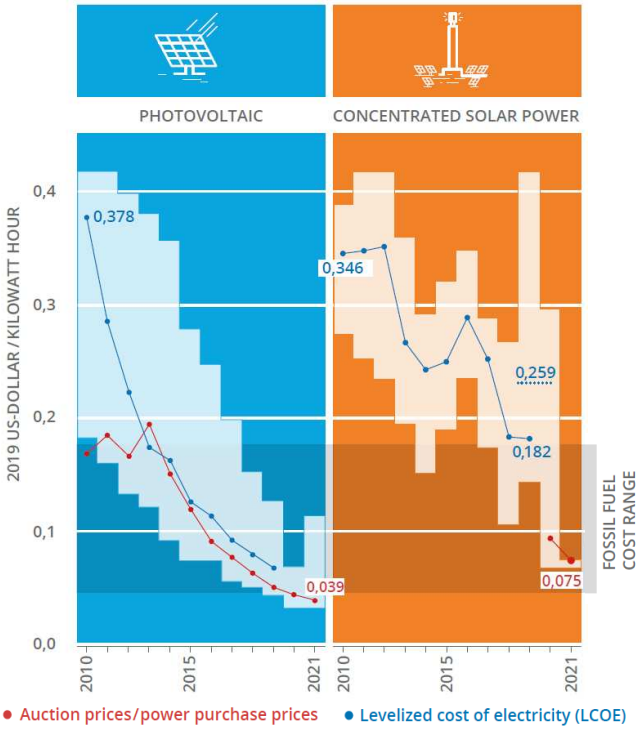

Figure 2: Cost evolution of PV and CSP solar plants between 2010 and 2021. The fossil fuel cost range is highlighted in grey [2].

- Indirect conversion using concentrated solar power plants (CSP) [56]: in this case, solar irradiation is first harvested by a fluid to raise its temperature, then the heated fluid is used to generate steam that drives a turbine-generator set to produce electricity. CSP offers the opportunity to store solar energy as heat using low-cost thermal energy storage systems (TES) [57], for later use at night or during cloudy periods. The TES system not only stabilizes the output of CSP but also makes it flexibly controllable to be able to accommodate intermittent energies such as PV or wind. CSP plants are less deployed with a current installed capacity of about 6 GWe [53] compared to 760 GWe PV, mainly due to the higher levelized cost of electricity (LCOE) (see Figure 2).

Unfortunately, electricity generated directly from the sun generally does not match the demand profile, requiring a site-specific combination of solar technologies with storage systems (e.g. electrochemical, chemical, etc. [58–60]) to ensure that the supply can always meet the electrical demand reliably and cost-effectively [61, 62]. Accordingly, both types of solar technologies are needed for a carbon-free future:
PV for its low-cost electricity and CSP for its ability to store and deliver solar power on demand at any time, day or night. Therefore providing dispatchable electricity via a set of combinations between PV and CSP with TES technologies appears to be an attractive solution.

1 Research background

The idea of combining PV and CSP technologies is not recent: investigation and researches had begun in the late 1970s and early 1980s [63], and significant development have been made since then, to demonstrate proper operation, improve the overall system efficiency, and bring this technology towards commercialization [64].
In this optic, the Advanced Research Projects Agency-Energy (ARPA-E) in the USA provided a funding opportunity in 2013 to launch a program called: Full-Spectrum Optimized Conversion and Utilization of Sunlight (FOCUS) [65, 66], aimed at developing new technologies to convert and store energy through hybrid energy conversion and storage devices. Since this initiation, multiple PV-CSP hybrid approaches have been studied [63], gaining popularity in international markets, for example, Chile [67–71], Morocco [72–75] and South-Africa [76, 77].

The hybridization of PV and CSP systems can be done in two ways: (i) *non-compact* configuration in which the PV and CSP subsystems can be independently planned and integrated by the electric power system [63] and (ii) *compact* configuration such as PV-topping strategy [78] or the spectral beam splitting (SBS) technology [79]. The idea behind the PV-topping system is to recover the heat dissipated by the solar cells operating at high temperatures to produce steam, which is used to generate electricity via the CSP system. On the other hand, the SBS technology is based on the fact that conventional PV cells mainly use visible and near-infrared radiation; thus, the other part of the incident radiation can be separated and used in the thermal receiver of a CSP plant.
Today, *non-compact* PV-CSP systems have entered commercialization phase [64], while *compact* hybrid plants still face several technological challenges [78, 79]. Figure 3 shows the Cerro Dominador *non-compact* PV-CSP hybrid plant with a total capacity of 210 MW, combining a 100 MW PV power plant and the first CSP plant in Latin America with a peak power of 110 MW and 17.5 hours of TES.

Figure 3: Cerro Dominador *non-compact* PV-CSP hybrid plant located in Northern Chile with a peak power of 210 MW [2].

Although several numerical and experimental studies have been conducted to understand the synergies between PV and CSP subsystems in a *compact* configuration, a detailed analysis of the output performance of large-scale *compact* plants is still lacking, which is of utmost importance for a better understanding of the real-time energy distribution within the two subsystems.
Therefore, the main objective of this thesis is to go beyond general descriptions and assumptions to study the annual energy output of two *compact* hybrid systems. To do so, we study the impact of different physical and technical parameters to allow us to identify the best set of operating conditions for each of the two hybrid plants.

To address the above problem, the following principal objectives have been set as follows:

1. Develop a detailed multiphysics model that can predict the energy yield of the two *compact* PV-CSP hybrid plants based on a large-scale CSP plant located in France.

2. Investigate the impact of several relevant parameters on the annual and daily performance of the two *compact* hybrid plants integrating storage system, namely: (i) weather conditions, (ii) two storage dispatch strategies, and (iii) variable demand-supply versus a constant demand.

3. Compare the performance of the two *compact* hybrid plants to three conventional solar technologies to better understand the position of the proposed *compact* plants compared to stand-alone plants.

2 Outline of the thesis

This manuscript is divided into four chapters.

- A detailed literature review is carried out in Chapter 1. This part starts with a description of the main components of solar radiation, along with the operating principles of both PV and CSP technologies, followed by an overview of the main problems encountered in the operation of these two technologies. Then, the light will be shed on solar hybridization as an attractive solution to provide cost-effective and dispatchable solar electricity. This will be followed by a presentation of the main new solar hybridization concepts proposed in the last four years. The objective of these new technologies is to ensure the full utilization of the solar spectrum while enabling the highest conversion efficiencies and maintaining low costs and high dispatch capabilities to the grid.

- In Chapter 2, we develop a comprehensive multiphysics model that provides the annual energy production of two different hybrid technologies, namely the *one-sun* and the *high-temperature* approaches, using the example of a large-scale solar power tower plant (SPT) located in Targassonne, France. With access to the layout of the heliostat field, the characteristics of the thermal receiver, as well as on-site meteorological data, a comparison between the two *compact* hybrid technologies and the stand-alone SPT plant in terms of energy production is performed first by examining the daily and yearly outputs. Then, the impacts of PV cell technology, heat transfer fluid operating temperature and shading effects are discussed.

- In Chapter 3, we assess the behaviour of the two compact hybrid technologies integrating TES using two dispatch strategies. The first aims to prioritize the supply of electrical demand through PV energy when it is available, while the second focuses on minimizing energy curtailments by using electric heating to recover excess PV energy. To go beyond the single case of France, we evaluate the impact of 15 different locations around the world with variable solar radiation levels and climatic conditions. The production performance of the two-hybrid plants is studied, taking into account a constant demand profile over a full year of operation and using high accuracy satellite data. The calculations are performed using the multiphysics model presented in chapter 2.

- In Chapter 4, we perform a critical comparison between the two *compact* hybrid plants and three conventional solar technologies incorporating thermal and electrochemical energy storage systems. In addition to the annual energy production, performance parameters such as the plant capacity factor, the loss of power supply probability and the annual amount of curtailed energy are evaluated. We first evaluated the impact of different weather conditions on the performances of the solar technologies by considering constant and variable load demand profiles over a full year of operation.

Finally, the conclusion addresses each aspect of the presented work as well as the main perspectives. Openings yet to be investigated in future researchers are detailed.

A set of appendices completes the dissertation:

- **Appendix A**, where the main equations used to identify the sun position are given as well as additional parameters concerning the cell technology used and the sizing of the power block of a CSP plant, along with a table summarizing the main results.
- **Appendix B**, consists of two parts; one is for site characteristics and additional details regarding the choice of Solcast as the solar database as well as the validation of the optical model at the selected locations. The other part is devoted to summarizing the obtained results for the remaining sites, as well as additional results to clarify some observations in Chapter 3 and Chapter 4.
- **Appendix C**, despite the high output performance that the *high-temperature* hybrid technology can offer, there are a set of challenges that will slow down the development of this technology compared to the *one-sun* hybrid plant. In this appendix, the focus is on evaluating the impact of non-uniform flux density distribution over the PV-receiver surface when considering different electrical interconnections schemes between the thousands of cells used to efficiently cover the receiver surface on the power output.

Chapter 1

State-of-the-art

Introduction

A continuous energy current from the sun reaches the earth-atmosphere system in the form of electromagnetic radiation, also referred to as solar radiation. Theoretically, this energy is several thousands times higher than the energy demand of the entire world. However, only about half of the solar radiation makes it to the Earth surface [80]; the rest is either absorbed or reflected by clouds, and the atmosphere [3] as shown in Figure 1.1.

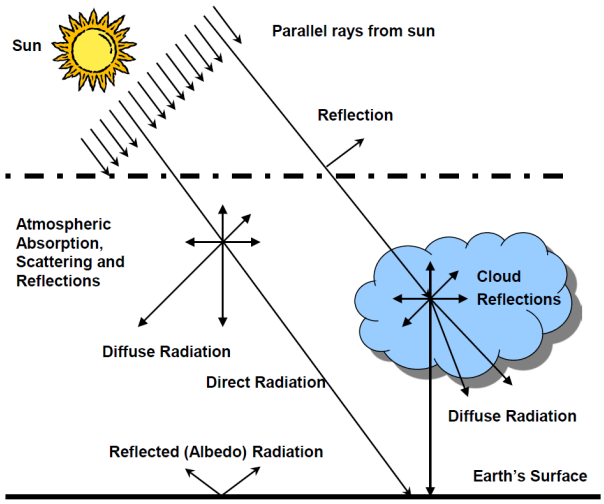

Figure 1.1: Incoming and outgoing solar radiation from the sun, with a representation of the solar radiation components [3].

Accordingly, solar radiation received by a surface is mainly divided into two components: 1) direct normal irradiation (DNI), the radiation received on a surface which is always perpendicular to the photon beam directly coming from the sun, 2) diffused horizontal irradiation (DHI) which refers to the fraction of solar radiation that has encountered a change of direction by scattering molecules and particles in the atmosphere [43]. For tilted surfaces, a third component can be considered known as ground-reflected radiation, i.e. radiation reflected either by the surfaces around the

point of interest or from the ground itself. The global component known as the global horizontal irradiation (GHI) comprises the DNI corrected for the angle of incidence on the surface θ_z and DHI given by Eq. (1.1). Each solar technology uses different components of solar radiation to generate electricity.

$$GHI = DNI \cos(\theta_z) + DHI \tag{1.1}$$

1 Concentrated solar power plants

CSP plants produce electrical power by first converting the sun's DNI component into high-temperature heat. Using an important number of mirrors that follow the sun's course to collect and direct energy into either a line focus (see Figures 1.2(a) and 1.2(c)) or a point focus (see Figures 1.2(b) and 1.2(d)) receiver. The heat is then channelled via a heat transfer fluid (HTF) (e.g. water, thermal oil, molten salt,... [81]), either to directly drive a turbine to produce power or to be stored using the TES unit for later utilization. Four commonly used CSP technologies are shown in Figure 1.2 [48] and Table 1.1 summarizes the major characteristics of these technologies:

(a) PTC [82]

(b) CR [83]

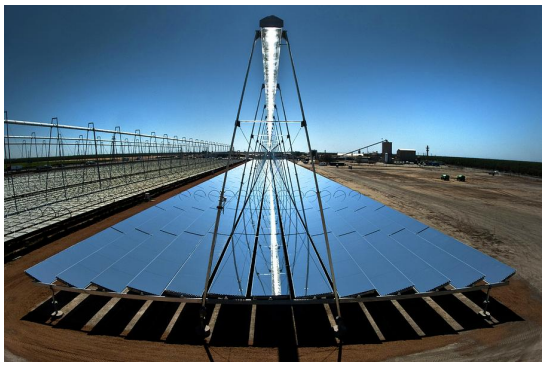

(c) LFR [84]

(d) PD [85]

Figure 1.2: Illustration of the four main CSP technologies: (a) PTC (Noor I Ouarzazate, Morocco 160 MW capacity and 3.5 h TES), (b) SPT (PS10 at Seville, Spain 10 MW), (c) LFR (Rajasthan Sun Technique Energy, 100 MW) and (d) PD (tested at Albuquerque, New Mexico).

- **Parabolic trough collectors** (PTC) account for parallel rows of curved mirrors as shown in Figure 1.2(a). The reflectors focus the sun's rays into absorber tubes covered with a selective coating, allowing tubes to absorb high levels of solar radiation while emitting very little infra-red radiation. All PTC plants currently in commercial operation rely on synthetic oil as the HTF [46]. PTC plants are known for their proven long-term reliability and durability. However, the limiting temperature of the HTF is one of the main design limitations compared to solar power tower technology (see Table 1.1).

- **Solar power towers** (SPT) also known as **central receivers** (CR) use hundreds or thousands of reflectors called heliostats to concentrate the sun's rays on a CR placed atop a fixed tower as shown in Figure 1.2(b). The SPT achieves very high temperatures (see Table 1.1), thereby increasing the efficiency at which heat is converted into electricity and reducing the cost of TES. Yet, SPT plants require high maintenance and equipment's costs.

- **Linear Fresnel reflectors** (LFR) consist of long rows of flat or slightly curved mirrors to reflect the sun's rays onto a downward-facing linear fixed receiver as shown in Figure 1.2(c). The main advantage of LFR systems is that their simple design requires lower investment costs. However, LFR plants are less efficient than PTCs in converting solar energy to electricity. In addition, it is more challenging to incorporate storage capacity into their design.

- **Parabolic dishes** (PD) concentrate the sun's rays at a focal point over the centre of the dish as shown in Figure 1.2(d). PD offer the highest solar-to-electric conversion performance of any CSP system (up to 31.25% [86]). This technology still suffers from a large number of technical complexities as compared to the other CSP technologies as well as concentrating photovoltaics (CPV) plants. One should also point out the lack of large-scale commercial PD plants.

Additionally to the four common CSP plants, the beam down CSP technology offers the possibility of placing the solar receiver on the ground instead of on top of a high tower as done today on commercial CR plants [87, 88] or in the middle with LFR [89]. This technology allows for non-negligible cost reductions due to lower pumping losses, shorter heat-traced piping, and a less costly tower structure. However, relative to CR plants, the optical constraints may result in beam-down designs delivering lower performance.

Today, the majority of installed CSP plants are geographically distributed, in countries with high levels of DNI ($>$ 1800 kWh/m^2/year) (e.g. Spain, Morocco, China, etc.)[50, 90], mainly using PTC and CR technologies [91, 92]. For the PTC technology, this can be justified by the low installation cost and the large experimental feedback compared to the other technologies [93], while the ability of CR plants to reach high operating temperatures ($>$ 1000 °C [94, 95]) translates into higher thermal-to-electric conversion efficiency.

Table 1.1: Comparative table of technical parameters of CSP technologies [46–48].

CSP technology	CR	PTC	PD	LFR
Concentration ratio	600 – 1000	50 – 90	1000 – 3000	35 – 170
HTF operating temperature (°C)	300 – 1200	150 – 400	300 – 1500	150 – 400
Thermal efficiency (%)		30 - 40		
Optical efficiency		Medium	High	Low
Annual solar-to-electric efficiency (%)	20 – 35	15	20 – 35	8 – 10
Annual CF (%)	55 (10h TES)	25 – 28 (no TES) 45 (7h TES)	25 – 28	22 – 24
Grid stability	High with large TES	Medium to high TES or hybr.	Low	Medium
LCOE ($/kWh)	0.2 - 0.29	0.26 - 0.37	—	0.17 - 0.37

What is unique about CSP technology is that when combined with TES, the capacity factor [1] (CF) can be increased from 25% for PTC plants without storage to values up to 45%, with a storage capacity of 7 hours [96]. Conversely, the levelized cost of electricity [2] (LCOE) decreases with increasing TES capacity [98, 99].
As a result, the integration of TES into a CSP plant not only offers significant technical and economical benefits in comparison to a standalone CSP plant, but it also increases the ability of the CSP to provide baseload generation to guarantee a fully dispatchable electrical generation. A detailed description will be given in section 3.

2 Photovoltaic technology

Solar PV is one of the forms of electricity generation that has grown the most in terms of installed capacity [100, 101] and conversion efficiency [102, 103] in recent years. In the following section, a detailed description of the different PV technologies used today to 1) extract the maximum power available for PV panels, 2) reduce the PV panel cost and 3) enhance the PV cell efficiency is given.

2.1 Silicon based PV plants

Silicon (Si) based PV panels guarantee a direct conversion of GHI into electricity, (i.e. PV systems can produce energy during cloudy days, thus can be used practically

[1] The CF is defined as the ratio between the electrical energy output over a year to the electrical energy output calculated assuming the plant is operating continuously at its nominal power.

[2] The LCOE is equal to the sum of all the cost incurring during the lifetime of the project divided by the units of energy produced during its lifetime [97].

in any part of the world, in contrast to CSP plants). Figure 1.3 shows two different configurations 1) fixed-tilt PV plant where the tilt refers to the angle formed between the panel and the horizontal as shown in Figure 1.3(a). A tilt of zero degrees means that the panel is horizontal on the ground, while a tilt of 90 ° means that the panel is perpendicular to the ground, and 2) PV tracking systems that will follow the sun path in the sky on a single (see Figure 1.3(b)) or double axis tracker. PV systems mounted on a tracking system deliver significantly higher electrical power than fixed-tilt systems because they track and face the sun all the time, thus increasing the amount of incoming solar radiation captured [104]. Nevertheless, PV tracking systems require a greater amount of area as compared to fixed PV systems.

(a) (b)

Figure 1.3: (a) A fixed-tilt flat plan PV plant [4], (b) a single-axis tracking plant [5].

2.2 CPV panels

The key principle of concentrated PV (CPV) lies in the use of low cost concentrating mirrors or lenses to focus DNI onto small multi-junction (MJ) cells for high concentration PV plants (concentration varying typically between 300 – 1000 suns [3]). Figure 1.4 shows an exemplary concept of a CPV plant with a close look to a module accounting for many solar cell receivers and housing with electrical connections. Despite all these efforts and research, CPV is still not able to make a significant contribution to the PV market compared to flat PV systems [105], due to the high cost of tracking, optics, and MJ cells (the cost of III-V MJ cells is several hundred times higher than conventional Si cells [106]), but with potentially a competitive LCOE with CSP and flat PV systems in some sunny areas with high DNI resources [54].

[3] 1 sun = 1000 W/m^2 = 1 kW/m^2

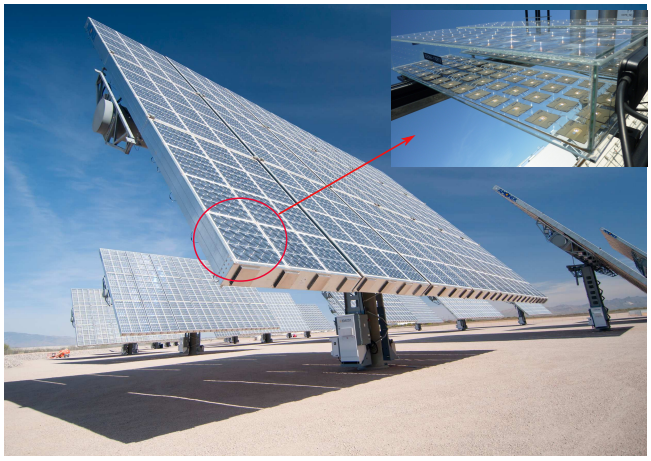

Figure 1.4: A CPV power plant with a close look to a module that consists of many solar cell receivers and housing with electrical connections [6, 7].

2.3 Bi-facial PV systems

The core innovation of bifacial PV (bPV) systems is their ability to capture and utilize light from both sides of the module as shown in Figure 1.5(a). In bPV modules, the same front side light collection process as for monofacial PV (mPV) happens. In addition, light is absorbed from the backside of the module as depicted in Figure 1.5(b).

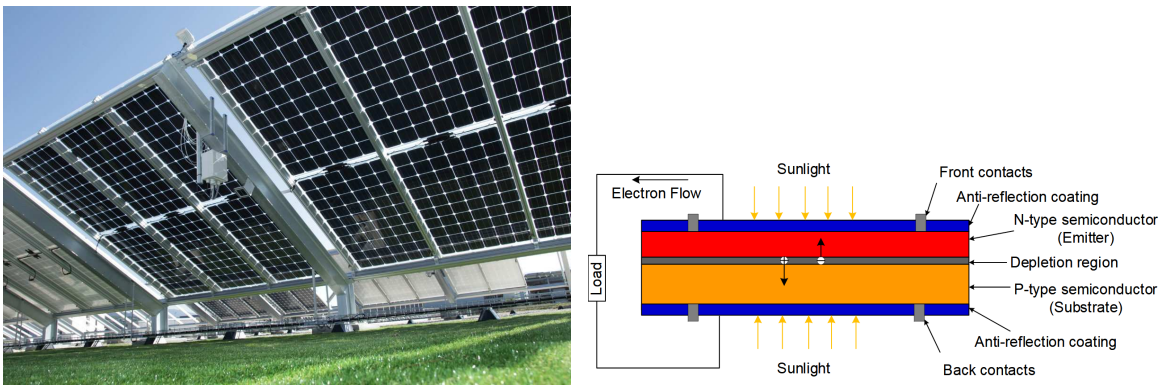

(a) (b)

Figure 1.5: (a) A bifacial PV plant using Si solar cells [8], (b) schematic of a bPV cell technology [9].

The backside light can come from a variety of sources, such as reflection from the ground [4] or a neighbouring row of PV modules. The additional light generates more electrons in the cells, which primarily increases the current of the module. Gu et al. [9] reviewed different configurations proposed over the years. Results showed that bPV modules increase the power output by 5 – 30% in comparison to mPV modules while

[4]Fraction of incident sunlight that the surface reflects. Varies with spectral and angular distribution of light.

presenting lower LCOE. In the same optics, Gu et al. [107] experimentally demonstrated the superiority of bPV over mPV modules under similar ground-measured weather conditions.

2.4 PV with reflector

More recently, the concept of fixing several reflectors near PV panels reflecting sunlight from outside the panel area onto the panel was introduced to enhance the energy output of a conventional PV plant as presented in Figure 1.6. In [108–112] several experiments have been reported to verify the technical and economic interest of this configuration. Results demonstrated a 24% increase of the energy output with reflectors, compared to PV panels without reflectors on an average day. Even though the lifetime of the PV module is reduced from 25 years to 21 years with the integration of mirrors, it generates significantly more electric power which overcomes the lifetime reduction [108].

Figure 1.6: PV with mirrors located on the edges of the module to increase the production [10].

2.5 Solar cell technologies

The aforementioned technologies imply the utilization of Si-based PV cells (except for CPV systems), with increasing efficiencies gradually approaching the theoretical maximum efficiency of a single-junction cell of 33.7% according to the Shockley-Queisser (SQ) detailed balance limit [113]. Figure 1.7 illustrates the progress in the efficiency of solar cells from different semiconductors materials from 2016 to 2020 [114].

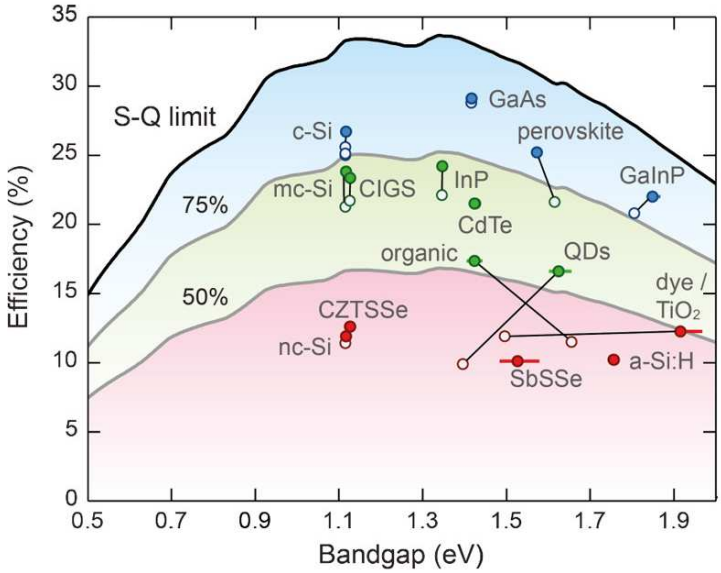

Figure 1.7: Theoretical SQ detailed-balance efficiency limit as a function of material band gap (black line), 75% & 50% of the limit (gray lines). The open symbols show the record efficiencies obtained in April 2016, the filled symbols show the numbers in July 2020 [11, 12].

2.5.1 Silicon cell technology

The primary material used in solar panels today is Si, the second most abundant material on Earth. Two main crystalline structures dominate the Si-PV market:

- **Mono-crystalline**: The single-crystal structure gives the electrons more room to move and creates a better flow of electricity. The best Si cell has an efficiency of 26.7% [115] shown in Figure 1.8, while the best module efficiency is equal to 24.4% by Kaneka company [103] with a lifespan around 25 – 30 years. To approach the theoretical limit of Si [12], series resistance and optical properties must be improved simultaneously to reduce recombination, resistive and optical losses.

- **Polycrystalline**: The high amount of structural defects in a multicrystalline structure gives the electrons less room to move, so it's not as efficient as mono-crystalline Si cells, with average efficiencies between 12 – 18% [115] due to lower purity level and higher defect density as compared to monocrystalline, but the benefit is the price because they're cheaper to produce.

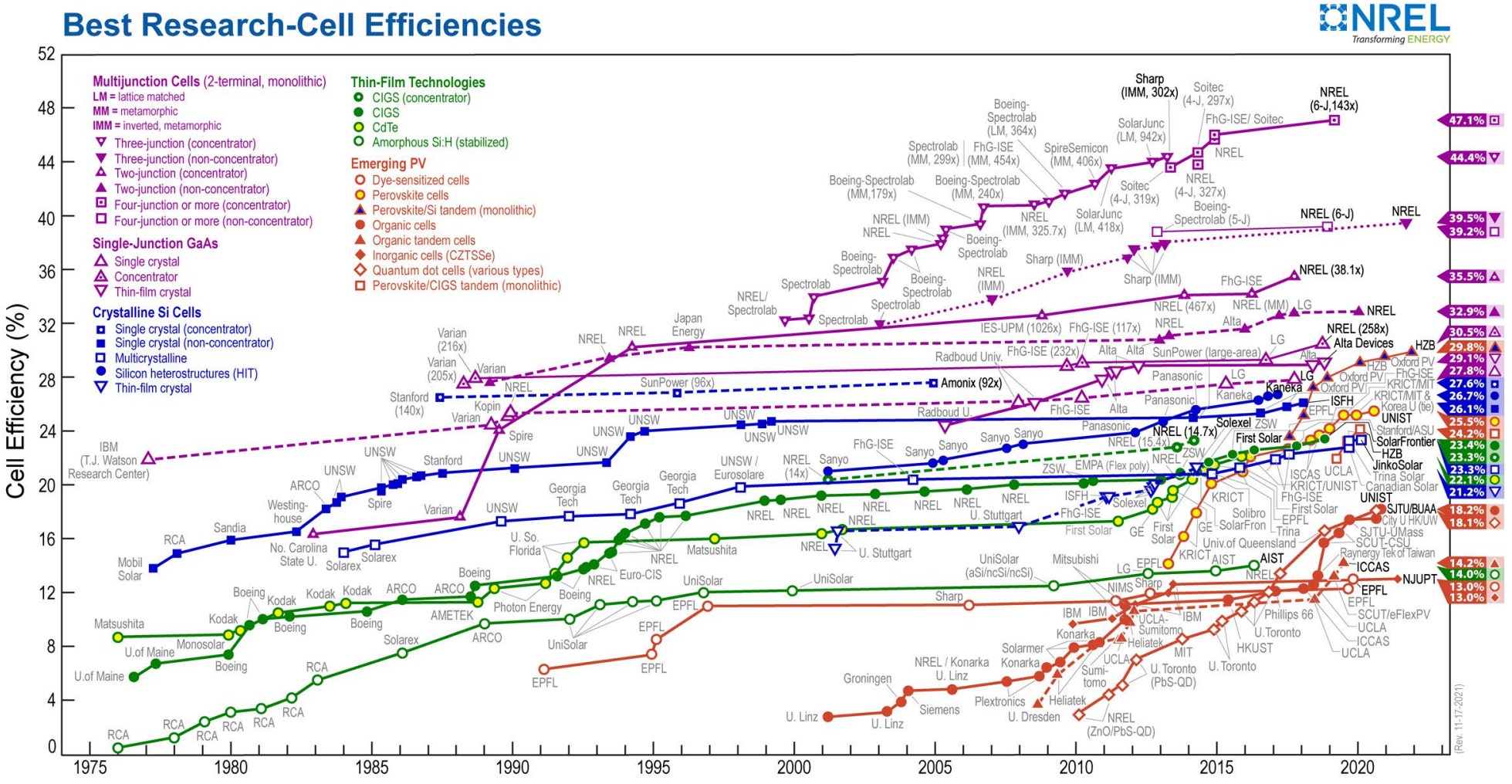

Figure 1.8: Evolution of different cell technologies efficiencies [13].

2.5.2 III-V technology

To date, gallium arsenide (GaAs) holds the record efficiency for single-junction cells with 29.1% achieved by Alta Device thin-film company [115] depicted in Figure 1.9(a). GaAs single-junction has only experienced a small increase in efficiency during the last four years, as shown in Figure 1.7. GaAs cells may operate at much higher temperatures than Si cells with less performance degradation [116, 117]. Their high cost limits their use to CPV and space applications. The toxicity of As is an important concern with GaAs cells. Two other III-V semiconductors have achieved high efficiencies, namely indium phosphide (InP) and gallium indium phosphide (GaInP), with an increase from 22.1% to 24.2% and 20.8% to 22%, respectively between 2016 and 2020 (see Figure 1.7). Developments on InP cells have been minimal in the past decade because of the scarcity and high cost of In, while, the use of GaInP for MJ solar cells has been of great interest lately [118, 119].

2.5.3 Thin-film technology

Thin-film solar cells encompass direct bandgap materials, such as copper indium gallium diselenide (CIGS) (Figure 1.9(b)), cadmium telluride (CdTe) (Figure 1.9(c)) and amorphous-Si (a-Si). The researchers working on thin cells were able to lower fabrication costs and reduce the amount of material which is deposited onto an inexpensive substrate such as glass, polymer, or metal (e.g. 1 µm of thin-film materials is needed to absorb more than 90% of the solar spectrum, compared to 300 µm with indirect bandgap Si wafers). The first two technologies offer higher efficiencies than a-Si, 22.1% and 23.4%, respectively versus 14% for a-Si as shown in Figure 1.8. Thin-film modules are also attracting substantial demand owing to their better heat-transfer properties, simpler integration into building-integrated PV (BIPV) [120] and high conversion efficiencies approaching 19.2% (841 cm^2) for CIGS and 19% (23 573 cm^2) for CdTe [103]. Despite the good performances of CIGS and CdTe solar cells, the scarce reserves of In and Ga could restrict the future development of CIGS along with the scarcity of Te and the scarcity and toxicity of Cd for CdTe.

2.5.4 Emerging technologies

The last generation of PV cell technology accounts for the emerging PV cells which include perovskite solar cells (PSCs) (Figure 1.9(d)), organic photovoltaics (OPVs) (Figure 1.9(e)), dye-sensitized solar cells (DSSCs) (Figure 1.9(f)), and quantum dot solar cells (QDSCs) (Figure 1.9(g)).

① Perovskite solar cells (PSCs)

PSCs are manufactured compounds that share the same crystalline structure as the calcium titanium oxide ($CaTiO_3$) mineral. PSCs can be made through "solution processing", quite similar to process used for the printing of newspapers. Inhere ink-jet printers are used to deposit materials on plastic sheets. Therefore, PSCs are another form of thin-film cells, but with potentially much higher efficiencies (i.e. efficiency

has gone from ∼14% in 2013 to 25.5% in 2021 in single-junction [13]. In comparison to Si efficiency increase since the 1970s, it's an outstanding achievement as depicted in Figure 1.8). Yet, there are challenges around PSCs including, shorter lifespan due to PSCs sensitivity to air and moisture, durability and toxicity since many of the formulations include lead which may present high risks if not handled and recycled correctly. What makes PSCs an enticing Si alternative is that the structure makes them highly effective at converting light photons into usable electricity. In addition, precursor materials are abundant at relatively low costs, making them suitable for mass production [121–123]. Eventually, the record efficiency in the lab needs to be translated into a high module efficiency to be of commercial relevance. To date, the best perovskite module is performing 7% worse than the lab record (18% with 802 cm^2 [103]).

② Organic photovoltaics (OPVs)

OPVs uses the electronic properties of organic material through a light absorption process, initiating a charge transport mechanism within the material. The active layer of OPVs is comprised of donor and acceptor materials for charge separation and transportation, as illustrated in Figure 1.9(e). Organic solar cells can be produced cheaply and in large quantities using high-speed, low-temperature roll-to-roll manufacturing processes and standard printing technologies [124]. Yet, OPVs suffer from stability issues and from relatively low efficiencies (18.2%) [13] compared to commercial Si cells. They are emerging as a niche technology, but their future development is unclear.

③ Dye-sensitized solar cells (DSSCs)

DSSCs convert sunlight via a similar process as for the photosynthesis of plants. Upon illumination of surface, the dye (sensitizer) absorbs a photon, the highest occupied molecular orbital (HOMO) electron is excited and reaches the lowest unoccupied molecular orbital (LUMO). The excited electron is injected from the LUMO to the conduction band of the titanium dioxide (TiO_2) semiconductor. To stabilize the sensitizer, the redox mediator donates its electron to the sensitizer. The electron in the TiO_2 passes through the back contact towards the counter electrode, which allows the redox mediator to regenerate itself [125]. In Figure 1.9(f) the complete cycle of DSSCs is illustrated. Currently, the efficiency of DSSCs (13% as shown in Figure 1.8) is not promising for commercial utilization as compared to other conventional cell technologies, but still, they have some advantages which are motivating researchers to pursue their efforts to develop this technology [17]. The required materials for the overall production of DSSCs are low cost, abundant and biocompatible. One of the key requirements of any solar technology is its stability yet, today's DSSCs cannot withstand bright sunlight without degrading [126].

④ Kesterite Solar Cells

Kesterite solar cells are based on two synthetic compounds copper zinc tin sulphide, (Cu2ZnSnS4) (CZTS) and copper-zinc tin sulfur, and/or selenium ($Cu_2ZnSnSSe_4$) (CZTSSe). The optical and electronic properties of CZTS and CZTSSe are similar to those of CdTe and CIGS. Owing to their low cost, non-toxic, and earth-abundant source materials CZTS and CZTSSe offer an alternative to overcome the scarcity of Te with CdTe and In with CIGS. Currently, the best performing cell has been synthesized by the IBM laboratory, and its efficiency is 12.6% as shown in Figure 1.8 [13]. CZTSSe has a bandgap that is close to that which allows optimal absorption in the SQ limit [12] (see Figure 1.7). Nevertheless, CZTSSe-based photovoltaic cells have not yet reached efficiencies higher than 20%, such as those obtained by CIGS and CdTe [127].

⑤ Quantum dot solar cells (QDSCs)

Finally, QDSCs utilize nanotechnology to manipulate semiconducting materials at extremely small scales (i.e. nanocrystals of elements from the periodic groups II-VI, III-V, or IV-VI) [128]. QDSCs are fabricated by deposition of inks, often using lead sulfide. Because of lead's toxicity, current research seeks a substitute for lead that does not compromise performance. The QDSCs cell's versatility results from the ability of the band gap to be tuned by varying the physical dimensions of the dots. A greater size of a QDSC entails higher absorption peak within the red shifted region due to the shrinking effect of its bandgap. The diameter of QDSCs typically varies from tens to hundreds of nanometers and each size provides distinct electronic and optical properties. Recently scientists at the University of Queensland achieved 18.1% efficiency (see Figure 1.8) [13] in QDSCs.

2.5.5 Multi-junction technology

MJ solar cells involve multiple material layers with different bandgaps, allowing an improved conversion of the broad solar spectrum. In Figure 1.9(i) is depicted the six-junctions MJ cell holding the current efficiency record. This cell is based on III-V semiconductors and has an efficiency of 47.1% under concentrated light (143 suns) [13, 20]. In total there are 140 layers of the six different solar materials and all combined are still less than 1/3 the thickness of a human hair. This value is not so far from the predicted achievable theoretical limit of 62% with 6J cells operating at 300 K and 1000 suns concentration [129]. Approaching 50% efficiency requires an exploration of new materials and device designs [130]. The main constraint of this cell technology is the high cost restraining its utilization for space applications [131] or in solar concentrators.

The fact that PSCs have advanced so far so quickly is very promising. To that end, a significant number of researchers are studying the possibility of combining Si with a thin layer of PSCs film in tandem configurations. In these configurations, Si will absorb the red band of the visible light spectrum, while the PSCs will absorb the blue spectrum [132]. Most recently, Oxford PV has reached a 29.2% efficiency [11]. Table 1.2 summarizes the best solar efficiencies reported in the literature to date using dual junction solar cells. All the tandem cell records are well above that of the record for the individual cells used in each configuration, e.g. 32.8% efficiency is noted for GaInP/GaAs whereas the best cell efficiencies are only 22% and 29.1%, respectively. Additionally, the tandem cell records are below the SQ limiting efficiency reported in Table 1.2, indicating room for improvement in both subcell efficiencies and the tandem geometries.

Table 1.2: Record efficiency of dual junction solar cells under AM1.5 illumination [11].

Tandem materials combination	**Bandgaps** (eV)	η (%)	η_{SQ} (%)
GaInP/GaAs	1.95/1.42	32.8	40.4
PSCs/Si	1.70/1.12	29.2	44.1
PSCs/PSCs	1.82/1.27	24.2	40.9
PSCs/CIGS	1.70/1.13	24.2	43.6
GaAs/Si	1.42/1.12	32.8	—

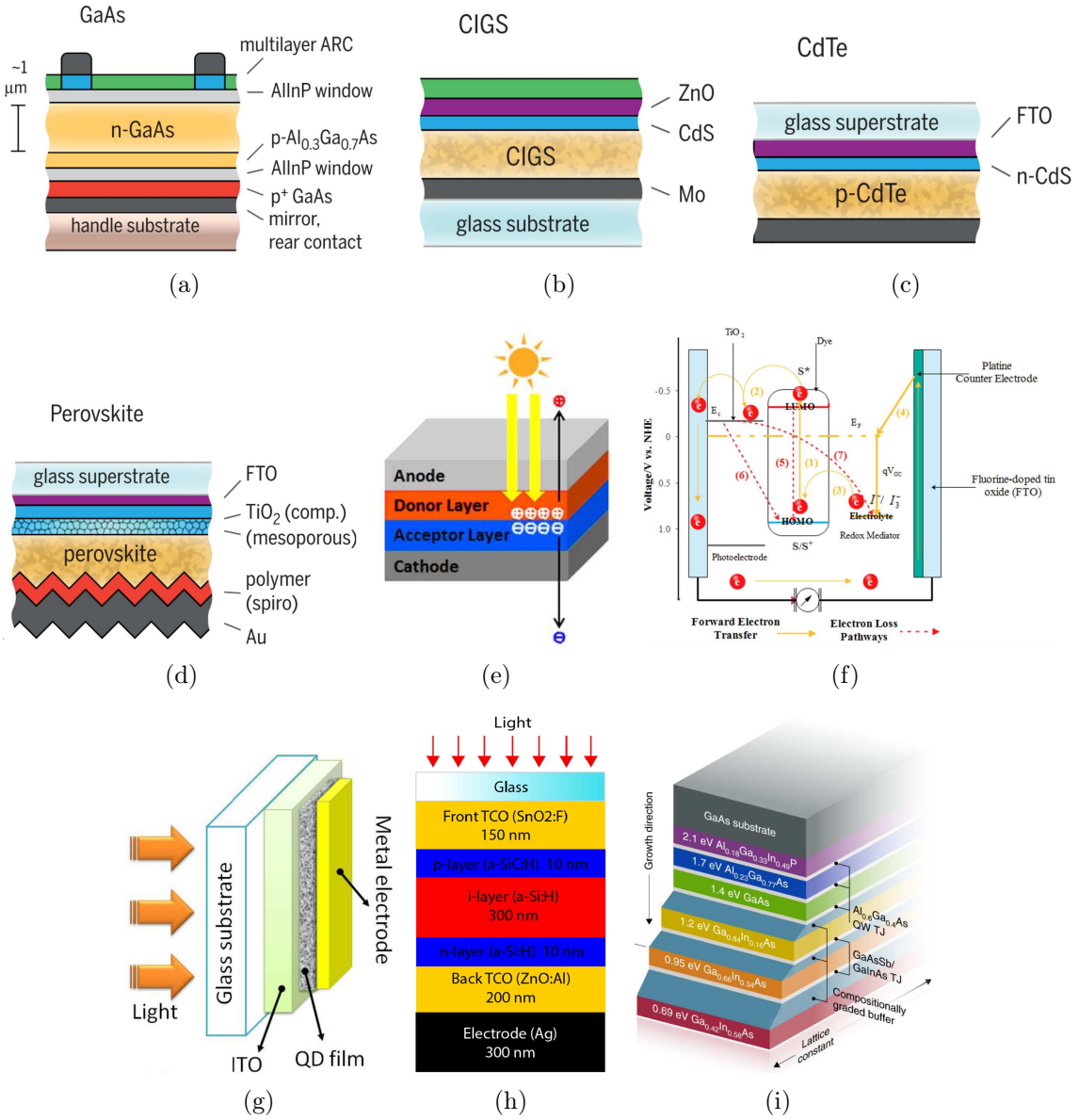

Figure 1.9: Layer and contact geometry for solar cells: (a) GaAs thin film (Alta Devices) [14], (b) CIGS thin film (ZSW stuttgart) [14], (c) CdTe thin film (First Solar) [14], (d) Perovskite thin film (KRICT) [15], (e) Organic cell [16], (f) Structure of DSSC [17], (g) functioning principle of a QDSC [18], (h) a-Si [19], (i) six-junction solar cell with the highest efficiency [20].

2.6 Basic mechanisms of photovoltaic conversion

Solar cells are spectrally selective absorbers made up from semiconductor materials able to convert solar radiation directly to electricity. Figure 1.10 illustrates how a semiconductor material with a given value of bandgap converts photons energy under 1 sun:

- ⇝ Photons with energies lower than the bandgap cannot create free charge carriers, therefore they are not absorbed,
- ⇝ Photons with energies equal to the bandgap can create electron-hole pairs,
- ⇝ High energy photons are inefficiently converted, since a fraction of their initial energy (corresponding to the energy difference between the photon and the bandgap) is wasted as heat in the crystalline network.

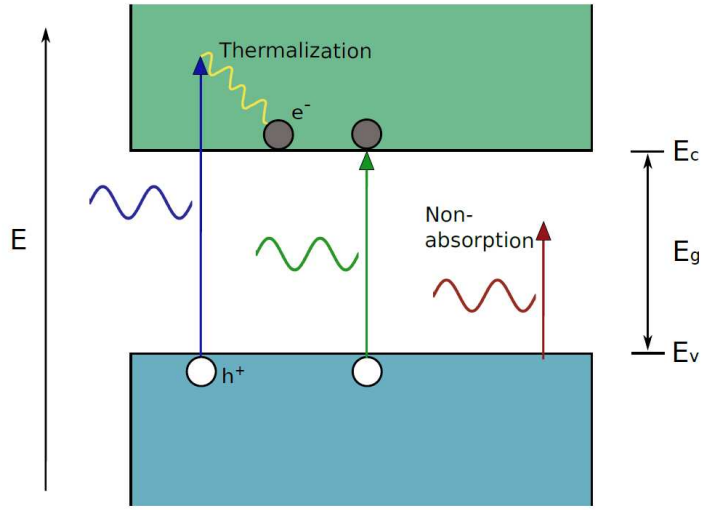

Figure 1.10: Loss mechanisms in a solar cell. e^-, h^+, E_v, E_c and E_g denote electrons, holes, the valence band, conduction band and bandgap energies, respectively [21].

2.7 PV cells electrical characteristics

The behaviour of any solar cell under illumination can be represented as an ideal p-n–junction diode in parallel with a current source in the proximity of the junction as shown in Figure 1.11(a) and described by Eq. (1.2). Therefore, to characterize solar cell performance a series of parameters represented in Figure 1.12 are used. Most important parameters are the: total electric current density J (Eq. (1.2)), short-circuit current density J_{sc} (Eq. (1.3)), dark current density J_D (Eq. (1.4)), open circuit voltage V_{oc} (Eq. (1.8)), maximum generated power P_{mpp} (Eq. (1.9)), fill factor (FF) (1.10) and the power conversion efficiency η (%) (Eq. (1.11)).

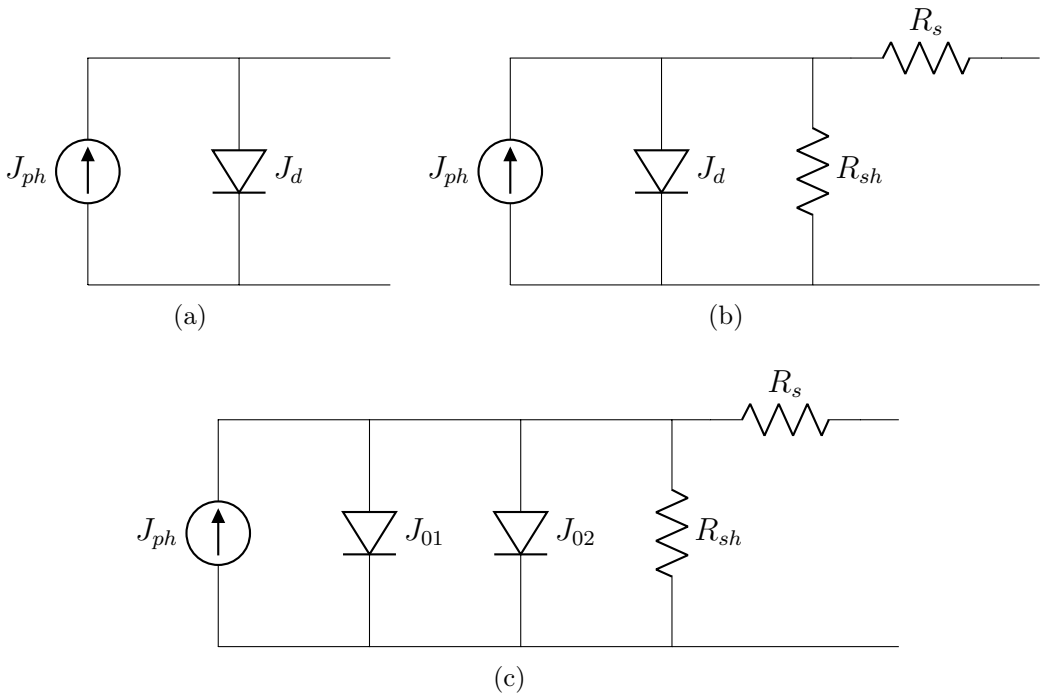

Figure 1.11: Equivalent electric circuit of an: (a) ideal solar cell, (b) a solar cell with parallel to the p-n–junction shunt resistor and in series resistor and (c) a solar cell based on a two-diode model.

The total electric current density in a solar cell is the difference between the short circuit current density J_{ph} and the dark current density J_D:

$$J(V) = J_{ph} - J_D(V) \tag{1.2}$$

where J_{ph} is the photo-generated current density from a solar cell when the voltage across the cell is equal to zero. The J_{ph} is related to the absorbed photon spectrum by measurement of cell's external quantum efficiency (EQE), which is the fraction of the incident photons of energy E to be absorbed and converted to collected charge carriers (i.e. electrical current) described as:

$$J_{ph} = q \int_{E_g}^{\infty} \Phi(E)\, EQE(E)\, dE \tag{1.3}$$

where q, Φ and E_g are the elementary charge, the quantity of energy inside the spectrum distribution of a solar cell and the bandgap, respectively.

The dark current density J_D is voltage-dependent recombination current expressed as:

$$J_D(V) = J_0 \left[\exp\left(\frac{q\,V}{n\,k_B\,T} \right) - 1 \right] \tag{1.4}$$

where, J_0, V, n, k_B and T are dark saturation current density, voltage across the junction, diode ideality factor, Boltzmann constant and temperature, respectively.

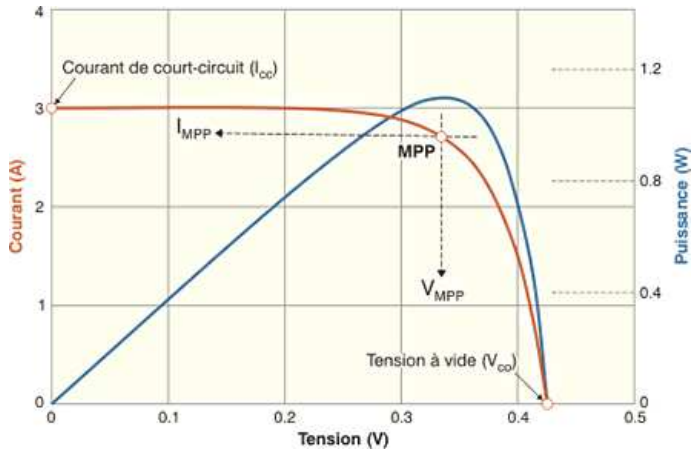

Figure 1.12: General current-voltage (I-V) characteristic curve of a solar cell under illumination with the different cell parameters [22].

Under a number of assumptions detailed in [133], J_0 can be derived easily from the carrier transport equations:

$$J_0 = q\, n_i^2 \left(\frac{D_e}{L_e} \frac{1}{N_A} F_P + \frac{D_h}{L_h} \frac{1}{N_D} F_N \right) \tag{1.5}$$

where F_P and F_N are factors that account for the finite dimensions of the P and N regions respectively. $D_{e,h}$ and $L_{e,h}$ are the diffusion coefficients and the diffusion lengths of the electrons and holes. $N_{A,D}$ are the doping concentration of acceptors and donors and n_i is the intrinsic carrier concentration.

In several works [116, 134], the temperature dependence of $\frac{D_e}{L_e} \frac{1}{N_A} F_P$ (in Eq. (1.5)) is neglected and it is assumed that the temperature dependence of J_0 is driven by that of n_i^2 given by [135]:

$$n_i = 2 \left(\frac{2\,\pi\, k_B\, T}{h^2} \right)^{3/2} \left(m_n^*\, m_p^* \right)^{3/4} \exp\left[-E_g(T)/2\, k_B\, T \right] \tag{1.6}$$

where h is Planck's constant, m_n^* is the effective electron mass, and m_p^* is the effective hole mass. Neglecting eventual temperature dependences of the effective masses, the diode saturation current density can be expressed as [134, 136]:

$$J_0 = C\, T^3 \exp\left[-E_g(T)/k_B\, T \right] \tag{1.7}$$

where C is a constant supposed independent of the temperature.

The open circuit voltage V_{oc}, is the maximum voltage available from a solar cell at zero current flow ($J = 0$). The V_{oc} is defined as:

$$V_{oc} = \frac{n\, k_B\, T}{q} \ln\left[\frac{J_{sc}}{J_0} + 1 \right] \approx \frac{n\, k_B\, T}{q} \ln\left[\frac{J_{sc}}{J_0} \right] \tag{1.8}$$

The maximum power can be extracted by biasing the solar cell at a certain voltage where the JV product would be maximized. The corresponding current density J_{mpp} and voltage V_{mpp} values are not the same as J_{sc} and V_{oc} values and correspondingly lower. Then, the maximum power point (MPP) is defined as:

$$P_{mpp} = V_{mpp} \times J_{mpp} \tag{1.9}$$

Another important parameter is the FF, that defines the sharpness of the JV curve as depicted in Figure 1.13. It is defined as the ratio of the P_{mpp} from a solar cell to the product of the V_{oc} and the J_{sc}.

$$FF = \frac{P_{mpp}}{V_{oc}\, J_{sc}} \tag{1.10}$$

Solar cell efficiency quantifies how much of the collected sunlight the cell is able to convert into electricity. The efficiency of the solar cell η is given as the ratio of the converted electric power to the incoming power from the sun P_{in}:

$$\eta = \frac{P_{mpp}}{P_{in}} = \frac{FF\, V_{oc}\, J_{sc}}{P_{in}} \tag{1.11}$$

Additionally to the above mentioned equivalent circuit of a single-junction solar cell, two equivalent models are commonly used to more precisely describe the behaviour of a real solar cell. The one diode equivalent circuit with series (R_s) and shunt (R_{sh}) resistances represented in Figure 1.11(b), where R_s accounts for resistances that arise from current movement through emitter and base of the solar cell or the resistance of rear and top metal contacts, and R_{sh} accounts for the existence of alternate current pathways through a PV cell. In the presence of both R_s and R_{sh} resistances, the equation of the solar cell is given as [137]:

$$J(V) = J_{ph} - J_0 \left[\exp\left(\frac{q(V + J\,R_s)}{n\,k_B\,T}\right) - 1\right] - \frac{V + J\,R_s}{R_{sh}} \tag{1.12}$$

The two-diode model is a modified form of a single diode circuit that takes into account the effect of recombination within the depletion region by introducing another diode in parallel, as shown in Figure 1.11(c). Its output current density is described by:

$$J(V) = J_{ph} - J_{01}\left[\exp\left(\frac{q(V + J\,R_s)}{n_1\,k_B\,T}\right) - 1\right] - J_{02}\left[\exp\left(\frac{q(V + J\,R_s)}{n_2\,k_B\,T}\right) - 1\right] - \frac{V + J\,R_s}{R_{sh}} \tag{1.13}$$

here n_1 and n_2 are the ideality factors of the two diodes.

In [116] it was indicated that J_{01} and J_{02} increases exponentially with temperature as described by the following proportionalities:

$$\begin{cases} J_{01}(T) \propto T^3 \exp\left[-E_g(T)/k_B\,T\right] & (1.14) \\ J_{02}(T) \propto T^{3/2} \exp\left[-E_g(T)/2\,k_B\,T\right] & (1.15) \end{cases}$$

where n_1 and n_2 are equal to 1 and 2 respectively.

As seen from Figure 1.13 both the R_s and R_{sh} resistances influence FF by modifying the JV curve. At a constant value of the solar irradiance, if the R_s is increased (with the red curve representing an R_s=0), the internal dissipation of energy is enhanced, so the cell becomes less efficient as shown in Figure 1.13(a), and the MPP will slide towards lower voltages and currents. The power loss caused by the presence of a R_{sh} is typically due to manufacturing defects rather than poor solar cell design. Low shunt resistance causes power losses in solar cells by providing an alternate current path for the light-generated current, as shown in Figure 1.13(b). These power loss effects increase with increasing R_s and decreasing R_{sh}.

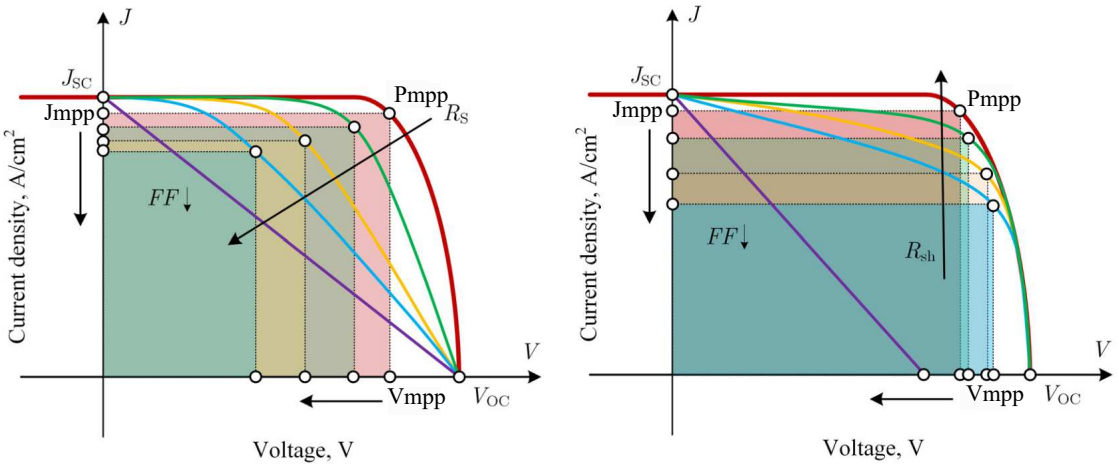

Figure 1.13: Effect of parasitic resistances on the J–V characteristic of a solar cell: (a) series resistance (R_{sh}=Cst.), (b) shunt resistance (R_s=Cst.).

Resistive heating or Joule heating is considered a parasitic effect and is governed by the following equation:

$$P_{loss} = R_s\,J^2 \tag{1.16}$$

As the temperature and concentration influence multiple parameters in different ways, the effect of these ambient conditions on the J-V curve isn't immediately clear.

2.7.1 Impact of temperature

Increasing temperature reduces the bandgap of a semiconductor, thereby affecting most of the semiconductor material parameters, resulting in a decrease in V_{oc} with a slight increase in the J_{sc}. Meanwhile, the diode saturation current density increases proportionally to the cube of the temperature as expressed in Eqs. (1.14) and (1.15). These two phenomena affect the various cell electrical parameters in different ways, as detailed hereafter.

The variation of the short-circuit current density with temperature was found to be basically independent of concentration, and can be written as [138]:

$$\frac{dJ_{sc}}{dT} = -q\,\Phi(E_g)\,\frac{dE_g}{dT} \tag{1.17}$$

This expression is a function of the solar cell material (its bandgap, and bandgap temperature sensitivity) and the spectrum of the irradiation.

Using the single-diode model (Figure 1.11(b)) with Eq. 1.7 as an expression for the diode saturation current density, the temperature coefficient of the saturation current density can be expressed as:

$$\frac{1}{J_0}\frac{dJ_0}{dT} = \frac{3}{T} - \frac{1}{k_B\,T}\left[\frac{dE_g}{dT} - \frac{E_g}{T}\right] \tag{1.18}$$

By differentiating Eqs. (1.8), the temperature dependence of the V_{oc}, we obtain:

$$\frac{dV_{oc}}{dT} = \frac{1}{T}\left[V_{oc} - \frac{n\,E_g}{q} - \frac{3\,n\,k_B\,T}{q}\right] + \frac{n\,k_B\,T}{q}\left[\frac{1}{J_{sc}}\frac{dJ_{sc}}{dT} + \frac{1}{k_B\,T}\frac{dE_g}{dT}\right] \tag{1.19}$$

Green [139] explained how complicated it is to derive generic expressions for the temperature coefficient of the FF, since it depends on a large number of cell parameters. In the case where R_s, R_{sh} and n do not vary strongly with temperature, the following formula is reasonably accurate when using Si solar cells:

$$\frac{1}{FF}\frac{dFF}{dT} = (1 - 1.02\,FF_0)\left[\frac{1}{V_{oc}}\frac{dV_{oc}}{dT} - \frac{1}{T}\right] \tag{1.20}$$

where FF_0 is the ideal FF of a solar cell given as a function of ν_{oc} the normalized voltage equal to $(q\,V_{oc}/n\,k_B\,T)$ [134, 138]:

$$FF_0 = \frac{\nu_{oc} - \ln(\nu_{oc} + 0.72)}{\nu_{oc} + 1} \tag{1.21}$$

Ultimately, $\frac{1}{\eta}\frac{d\eta}{dT}$ is the sum of the corresponding contribution of the relative temperature coefficients of J_{sc}, V_{oc} and FF, the magnitudes of which vary differently with

E_g. The variation in efficiency with temperature can be expressed as [140]:

$$\frac{1}{\eta}\frac{d\eta}{dT} = \frac{1}{V_{oc}}\frac{dV_{oc}}{dT} + \frac{1}{J_{sc}}\frac{dJ_{sc}}{dT} + \frac{1}{FF}\frac{dFF}{dT} \tag{1.22}$$

2.7.2 Impact of concentration

The short-circuit current density J_{sc} of a solar cell depends linearly on the light intensity, such that a device operating under 10 suns would have 10 times the J_{sc} as the same device under 1 sun operation (Eq. (1.23)). Moreover, from the logarithmic dependence of V_{oc} on the concentration ratio X as given by Eq. (1.24).

$$J_{sc}(X) = X\, J_{sc}(1\ sun) \tag{1.23}$$

$$V_{oc}(X) = V_{oc}(1\ sun) + \frac{n\,k_B\,T}{q}\,\ln(X) \tag{1.24}$$

The conversion efficiency of ideal solar cells, increases logarithmically with X, following the V_{oc} trend, and can be expressed by the following expression:

$$\eta = \frac{V_{oc}(X)\,J_{sc}(X)\,FF(X)}{P_{in}(X)} \tag{1.25}$$

Braun et al. [138] investigated the temperature coefficients of concentrator solar cell performance parameters. Using Eq. 1.24 in the derivation of the temperature coefficient of the V_{oc} it can be expressed as:

$$\frac{dV_{oc}(T,X)}{dT} = \frac{V_{oc}(1\ sun)}{T} + \frac{n\,k_B}{q}\ln X + \frac{n\,k_B\,T}{q}\left[\frac{1}{J_{sc}}\frac{dJ_{sc}}{dT} - \frac{1}{J_0}\frac{dJ_0}{dT}\right] \tag{1.26}$$

Using Eq. (1.21) and by replacing the normalized voltage expression with the variation of the V_{oc} with concentration (Eq. (1.24)). The temperature dependence of FF with concentration can be given as [138]:

$$\frac{dFF}{dT} \approx \frac{\ln\left(V_{oc,\ 1sun}(T)\,\frac{q}{n\,k_B\,T} + \ln(X) + 1\right)\left(\frac{dV_{oc,\ 1sun}}{dT}\frac{q}{n\,k_B\,T} - V_{oc,\ 1sun}(T)\,\frac{q}{n\,k_B\,T^2}\right)}{\left(V_{oc,\ 1sun}(T)\,\frac{q}{n\,k_B\,T} + \ln(X) + 1\right)^2} \tag{1.27}$$

3 Energy storage technologies

The intermittency of solar energy can cause unbearable dispatching pressure on the grid during PV power generation processes. Figure 1.14 illustrates an example of the mismatch between the demand for electricity and PV solar generation output. It can be noticed that most solar electricity is produced during the day when the sun is out. As a result, the surplus of solar electricity produced during this time of day is curtailed. However, the highest demand for electricity usually takes place in the morning and the evening. Therefore moving forward PV power systems need to be able to respond to changes in loads by meeting three basic conditions: (1) stability i.e. maintaining power quality and fast response to misalignments (i.e. mismatch between supply and demand), (2) flexibility in matching supply with demand, and (3) adequacy of a power system to cope with load at all times. These conditions pose fundamental challenges regarding the widespread integration of solar energy. One way to meet these challenges is to use energy storage systems (ESS). ESS providing necessary dispatchability for the grid or energy supply is crucial to ensure high and consistent power quality. Each storage application has a very particular requirement in terms of temperature level, storage duration, footprint and system integration [141–143]. In the following section, we discuss and compare the characteristics of the main existing ESS technologies: *thermal*, *electrochemical*, *mechanical*, and *chemical* energy storage. In principle a few other possibilities exist, but they are still quite far from real application.

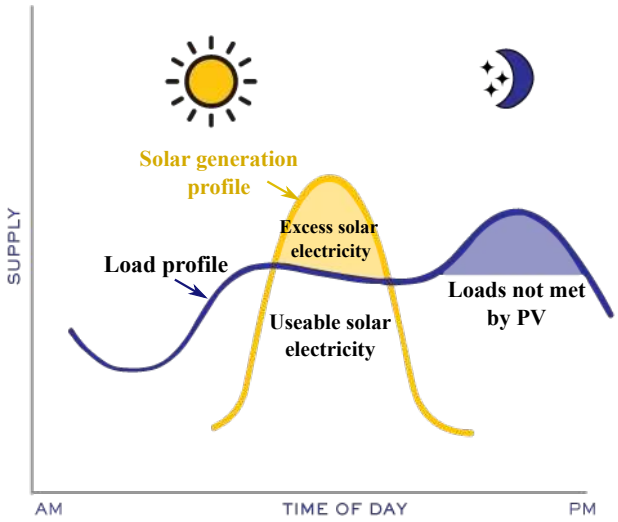

Figure 1.14: Energy production of a PV system during one day. A large amount of solar electricity generated during the day is not being utilized (yellow part of the graph) and at the same time when electricity is needed the most - solar energy is not able to cover the load demand (blue part of the graph).

3.1 Thermal energy storage

Thermal energy storage (TES) is a technology that captures thermal energy by heating a storage medium. The stored energy can be used at a later time for power generation. To effectively conserve heat, three components are typically required: a storage medium with good thermo-physical characteristics, an efficient heat transfer mechanism, and a suitable containment system [60, 144, 145]. The main mechanisms for TES technologies include sensible, latent and thermochemical heat storage detailed hereafter.

3.1.1 Sensible heat storage

Sensible heat storage (SHS) consists of temperature changes in solids (e.g., sand, concrete, or rocks) or liquids (e.g., water, oil, molten salts) media in the forms of charging and discharging processes [146] as shown in Figure 1.15(a). When the temperature increases, energy is absorbed, and when the temperature drops, power is released. SHS has two main advantages: it is cheap in most cases and without the risks associated with the use of toxic materials.

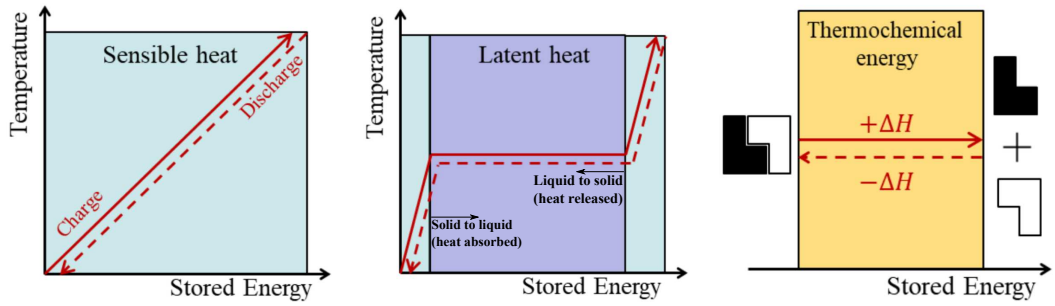

(a) (b) (c)

Figure 1.15: Main mechanisms for TES using: (a) sensible heat storage, (b) latent heat storage, and (c) thermochemical heat storage [23].

Today, the most commonly used TES systems in commercialized CSP plants are based on molten solar salts as an *indirect* or *direct* implementation [64, 147–149]. Nevertheless, systems using latent heat, thermochemical, and other SHS materials are under development. Commonly used molten salts are typically made up of mixture of 60% sodium nitrate ($NaNO_3$) and 40% potassium nitrate (KNO_3) or Hitec mixture (7% $NaNO_3$, 53% KNO_3 and 40% of $NaNO_2$) [150, 151]. A two-tank *direct* molten salt system uses molten salt to collect solar energy and to store it (in a *indirect* configuration two different HTFs are used, one to collect heat from the solar field and another to store heat for later use). Two tanks store the molten salt, a hot tank for the high-temperature molten salt and a cold tank holding low-temperature salt, as illustrated in Figure 1.16(a). Salt from the cold tank (290 °C) is heated by the collected solar thermal energy and pumped into the hot tank to store the heat (565 °C). The high-temperature salt is pumped into the heat exchanger to transfer the heat and then produce steam to generate electricity. The cooled salt is gathered in the cold tank. Nitrate salts

freeze around 200 °C and decompose at 600 °C [152]. These characteristics critically limit the technology to be used at medium-temperature conditions. Molten chloride salt mixtures such as $MgCl_2$/NaCl/KCl with similar thermo-physical properties as the commercial nitrate salt mixtures are being investigated as they operate at higher temperatures (>800 °C), with lower costs [151]. However, the most significant challenge for molten salt TES is the strong corrosivity to the construction materials. Current research aims to study novel HTFs to overcome this limitation. Particles as a mean for TES provide cheap energy storage solution due to (1) their inexpensive price, (2) the ease for storage and (3) their ability to tolerate high temperatures (up to 1000 °C) without any destructive impact as molten salts nor freezing or temperature degradation [24, 153, 154]. The cold particles are conveyed from a cold storage tank up to the receiver, which is impinged by concentrated solar radiation to increase its temperature as depicted in Figure 1.16(b). Hot particles are then sent to a hot storage tank where thermal energy is stored. The hot particles discharge to a heat exchanger via a fluidized bed system [155] to drive the power cycle. Despite the promising futures particle-based technology may offer, today most of the applications are limited to lab-and pilot-scale realizations.

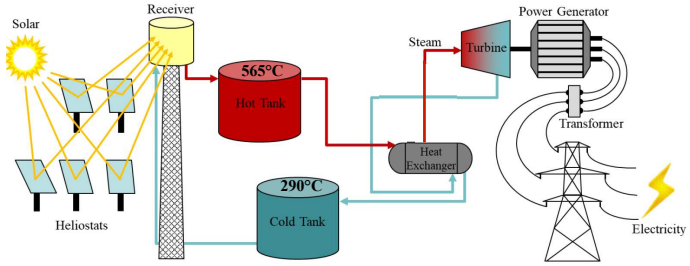

(a)

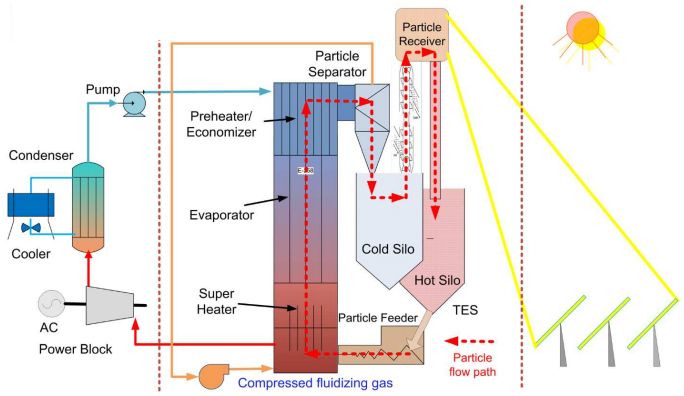

(b)

Figure 1.16: A Schematic of a CR CSP plant with: (a) a *direct* two-tank molten salt TES system [23], and (b) a solid particle system with TES and fluidized bed [24].

In addition to the two-tank system, the one tank thermocline system has been proposed to significantly reduce the system cost [156]. A *dual-medium* thermocline system uses a solid storage medium and a HTF inside a single tank, as shown in

Figure 1.17. Through void spaces between the pebbles, a HTF (liquid or gas) flows. This HTF serves to introduce and extract heat energy during the heat storage and recovery processes. The hot HTF accumulates at the top, and the cold HTF stays at the bottom due to the buoyancy force effect [157]. During the charging process, the hot fluid is injected through the upper part of the tank and flows in the downward direction to exit the storage system at a lower temperature (Figure 1.17). Hence it transfers heat to the solid for storing thermal energy. In the discharging period, the cold HTF moves in the opposite direction to retrieve the stored heat energy from the solid and then exits via the TES top at a higher temperature. Accordingly, recovered energy will be fed to the power block to generate electricity in the CSP plant. With a great saving on storage and containment materials, the cost of thermocline molten salt-based TES can be 45% lower than the two-tank system. Ultimately, levelized cost of storage (LCOS) is about 48% lower than a two-tank TES system [156].

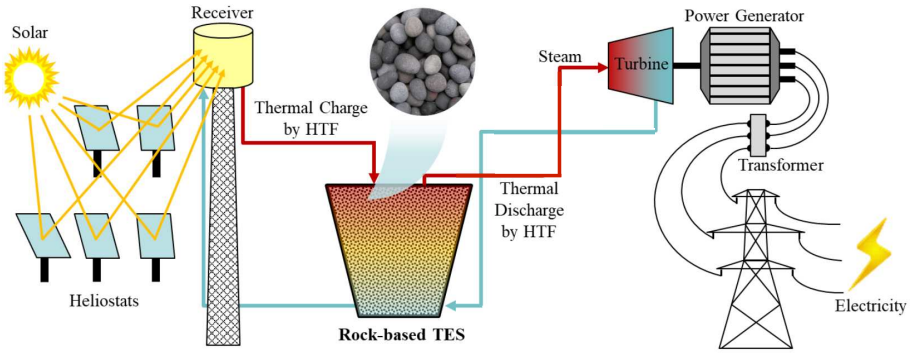

Figure 1.17: A Schematic of a CR CSP plant with a one-tank *dual media* thermocline rock-based TES system [23].

The next generation of TES systems is moving towards high-temperature technologies with attractive cost efficiencies. To this end, Jinge et al. proposed a novel high-temperature sulfur-based thermal battery configuration (SulfurTES) [158, 159] by using elemental sulfur as the storage medium. For this TES system, sulfur is stored using vertically-oriented tubes enveloped in a shell-and-tube heat exchanger system, as shown in Figure 1.18.

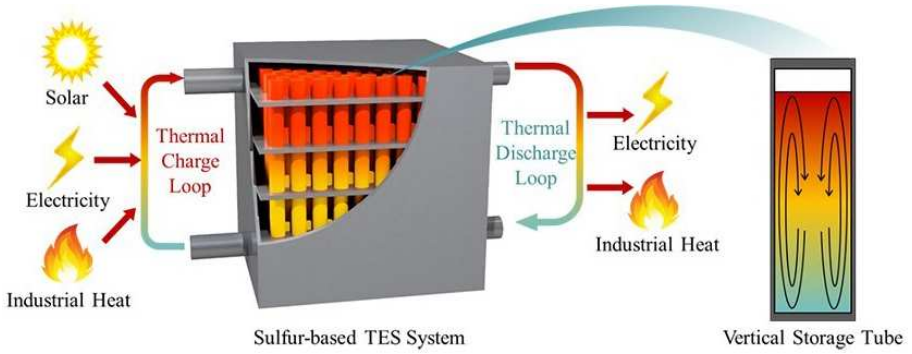

Figure 1.18: Schematic of the SulfurTES thermal battery system [23].

With low cost for the storage and containment materials, high thermal stability and

high heat transfer rate at the liquid stage, SulfurTES shows great potentials to be a competitive technology for future commercial TES plants. Schwaiger et al. [160, 161] studied a configuration using active fluidized bed technology and sand as a heat storage medium known as the sandTES fluidization technique. Sand is a cheap and environmentally friendly storage material that can be used at temperatures well beyond 600 °C. In the sandTES, the air is entering through the distributor floor, thus enabling the fluidization of the storage powder passing in serpentines to travel through the heat exchanger. The technology is cost and energy efficient for small industrial storage. With sandTES, load flexibility and plant dynamics can be improved.

3.1.2 Latent heat storage

Latent heat storage (LHS) is based on the use of phase-change materials (PCMs) [162, 163]. Initially, PCMs act like SHS materials (i.e. temperature increases linearly) then, heat is absorbed or released at a constant temperature with a change in physical state, mainly solid-liquid as shown in Figure 1.15(b). Elarem et al. [164] reviewed different properties of PCMs. PCMs are classified into either organic, inorganic or eutectic materials. PCMs have a range of melting and solidification temperatures, storage density, and thermal conductivity which are considered the base criteria for their selection. Additionally, a proper selection of a PCM is affected by the desirable physical, chemical, and thermodynamic properties and the required applications.

3.1.3 Thermochemical heat storage

Thermochemical heat storage (THS) consists of storing heat through reversible reactions. With heat supply, the bicoulor bloc depicted in Figure 1.15(c) can be dissociated into two components (black) and (white), which can be any phase and stored separately. The original bloc can be formed with a heat release when the black and white blocs are put together. In comparison to the SHS and LHS, the emerging THS technologies have much higher energy densities and much less heat loss at high temperatures [144]. Yet, most products from the thermochemical reactions are gases that can be corrosive and cause a higher containment and system cost [165].

3.2 Electrochemical storage

Electrochemical ESSs are the oldest energy storing technologies where a reversible chemical reaction in the active material through the electrolyte is used for charging/discharging electricity. The most widely used utility-scale batteries energy storage systems (BESS) are lead-acid, lithium-ion, sodium-sulfur, nickel-cadmium, and flow batteries. Lithium-ion (Li-ion) batteries dominate the energy storage market. In Li-ion batteries, the electrode combo is usually a lithium cobalt oxide cathode and a graphite anode. The electrolyte enables the electrical charges to flow between the electrodes, as illustrated in Figure 1.19(a). Despite the declining price Li-ion batteries have encountered since 1991 (97% decline [166]), they remain less competitive than

TES systems, as shown in Table 1.3, and issues remain due to toxic chemical material disposal or recycling of dumped batteries.

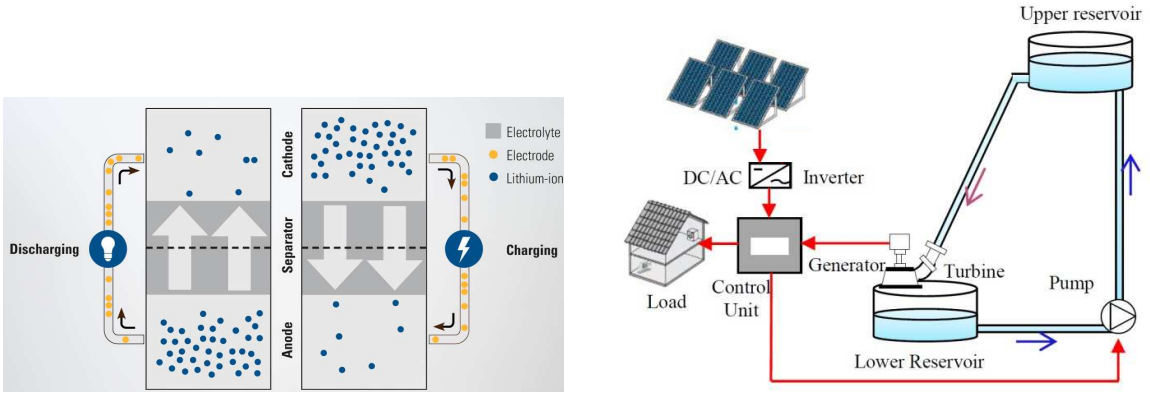

(a) (b)

Figure 1.19: (a) The operating principle of Li-ion batteries during charging and discharging cycles [25]. (b) Schematic of a standalone hybrid PV-PHS system [26].

Other type of batteries called flow batteries separate the charge outside a cell, they are also referred to as external storage batteries. They have two advantages: they can store more energy and for longer periods, but the problem is they are still relatively expensive [143]. Unlike Li-ion batteries, liquid metal batteries are made of a liquid calcium-alloy anode, a molten salt electrolyte and solid particles of antimony cathode. This composition enables the use of low-cost materials and a low number of steps in the cell assembly process [167–169]. Batteries are usually characterized by how much energy and how much power they can provide. In general, technologies do better on one measure than the other. For example, with pumped hydropower, abundant storage is cheap, but fast delivery is expensive whereas for grid-scale storage, both capabilities are crucial. The liquid metal battery can potentially do both. It can store a large amount of energy and deliver that energy quickly, for example, to meet demand instantly when a cloud passes in front of the sun. It should have a long lifetime, unlike the Li-ion battery, and not degrade when completely discharged, unlike the lead-acid battery [142]. Although it seems to be more expensive than pumped hydropower today (see Table 1.3), this kind of battery has no limits on its use.

3.3 Mechanical energy storage

Mechanical energy storage technologies use moving parts to convert electrical energy into mechanical energy. Pumped hydro storage (PHS) is the most commonly used technology throughout the world [170]. PHS stores electricity in the form of hydraulic potential energy. PHS can be used perfectly with renewable energy systems (PV and wind) to increase system dispatchability. For example, when PV power generation is higher than energy demand, the surplus of energy is used to pump water from a low reservoir to a high reservoir, storing energy in the form of gravitational potential

energy as illustrated in Figure 1.19(b). When power needs to be dispatched, water flows back downhill through turbines, releasing the stored energy. The PHS system is quite robust, with distinguished features of simplicity and reliability. Yet, PHS has some drawbacks such as the need for large volumes of water which may present a challenge for locations with water scarcity problems. Flywheel energy storage (FES), also known as kinetic energy storage, is another form of mechanical ESS. The flywheel speeds up as it stores energy by bringing a mass into rotation around an axis and slows down when discharging to deliver the accumulated energy. The fast response characteristics of FES makes them suitable in applications involving solar and wind resource for grid frequency balancing [171]. However, FES systems are still not considered a mature technology because they are expensive compared to other ESSs [143]. The third type of mechanical ESS is compressed air energy storage (CAES) systems. In CAES the air is compressed and stored in a large underground reservoir called cavern. Upon energy demand, pressurized air is released to a turbine to generate electricity. Although CAES systems are mature technologies, they are still subject of studies that aim to identify how their current efficiencies (42 – 55%) can be improved [141].

3.4 Chemical storage

Chemical ESSs are important long-term ESSs in the form of chemical bonds of molecular compounds. It is further classified as hydrogen storage and biofuels [172]. A fuel cell is a device that generates electricity through an electrochemical reaction. In a fuel cell, electrical energy is utilized to decompose water into oxygen and hydrogen. These gases can be stored and again combined to release the stored energy. Fuel cells do not need to be periodically recharged like batteries but instead, continue to deliver electricity as long as a fuel source is provided. Power to hydrogen (P2H) provides a promising solution to the geographic mismatch between sources of renewable energy and the market due to its technological maturity and flexibility. A key barrier to the large-scale deployment of P2H is its low overall energy efficiency and high-cost [173]. The solar hydrogen approach is under the early stage of development. Brey et al. discussed how the use of hydrogen as a storage system will play an important role in the decarbonization plan by 2030 in Spain [174]. By using electrolysis to convert the surplus electrical power into hydrogen, 7.27 TWh of the surplus renewable energy can be reused, and 2.54 million tons of CO_2eq can be avoided every year. Due to the limited reserves of fossil fuels and their significant impact on the environment, there is a need to develop sustainable fuels. Today, biological processes are being used in both the storage and production of energy. The production of biomass originates from plants and animal waste. The two most common types of biofuels in use today are ethanol and biodiesel [175]. There are various ways of making biofuels, but they generally use chemical reactions, fermentation, and heat to break down the starches, sugars, and other molecules in plants. The resulting products are then refined to produce a fuel that cars or other vehicles can use. Achieving technologies to produce fuels from biomass feedstocks sustainably and cost-effectively at a very large scale remains a challenge.

Table 1.3: General characteristics of different ESSs.

ESS		**Volumtric Energy density** (Wh/L)	**Lifetime** (years)	**Levelized Cost of Storage** (LCOS) ($/kWh)	**Typical Response time**	**Refs.**
Mechanical	PHS	0.5 – 1.5	30 – 60	5 – 100	3 – 10 min	[141]
	FES	20 – 80	15 – 20	1000 – 5000	ms	[141]
	CAES	3 – 12	20 – 40	400 – 1000	10 min	[176]
Electrochemical	Li-ion	80 – 150	14 – 16	194 – 242	ms	[177]
	FlowB	16 –60	5 – 20	150 – 1000	ms	[177, 178] [143]
	Lead-acid	50 – 80	5 – 15	200 – 400	min – h	[178]
Thermal	SHS	0.02 – 0.03	5 – 15	0.1 – 10		[145]
	LHS	0.05 – 1	10 – 20	10 – 50		[145]
	TCES	0.5 – 1	20+	8 – 100		[145, 179]
Chemical	Hydrogen	500 – 3000	5 – 20	1 – 15	s	[143, 180]

In the aforementioned section, we highlighted how ESSs will help improving the dispatchability of renewable resources and how continuous efforts are deployed to further optimize the technical and economical behaviour of ESSs. Nevertheless, it is obvious that in the upcoming years, the complementarity of the different forms of renewable energy production will play a crucial role in the global energy transition in its entirety. It is precisely in the coupling of various renewable energies that their advantage will become all the more apparent – both in terms of the economic and the ecological balance [181]. In the following section, hybridization as an upward solution for the intermittent nature of solar energy will be discussed in detail.

4 Solar hybridization

Nowadays, the most common hybrid solar systems are based, either on the hybridization of solar technologies in-between (i.e. PV with CSP considering different configurations) [63, 182, 183], or on a solar system coupled with other renewable technologies (e.g. wind, geothermal, etc.) [181, 184–190] as shown in Figure 1.20. In this section, we will start with reviewing the literature on PV-CSP hybrid technologies classified in two main types as described in Figure. 1.20, followed by a discussion of some new hybridization concepts. Then, we will assess the technical and economical interest of these technologies via a detailed comparison. Finally, we will introduce the novelty and interest of our work for the scientific community. We will focus on the hybridization of PV with CSP, since this route has significant potential for coupling the technical and economic advantages from both technologies. In fact, such option may contribute to improve the power quality, grid stability and renewable penetration in the grid compared to PV standalone plants [44, 63, 73, 191–204].

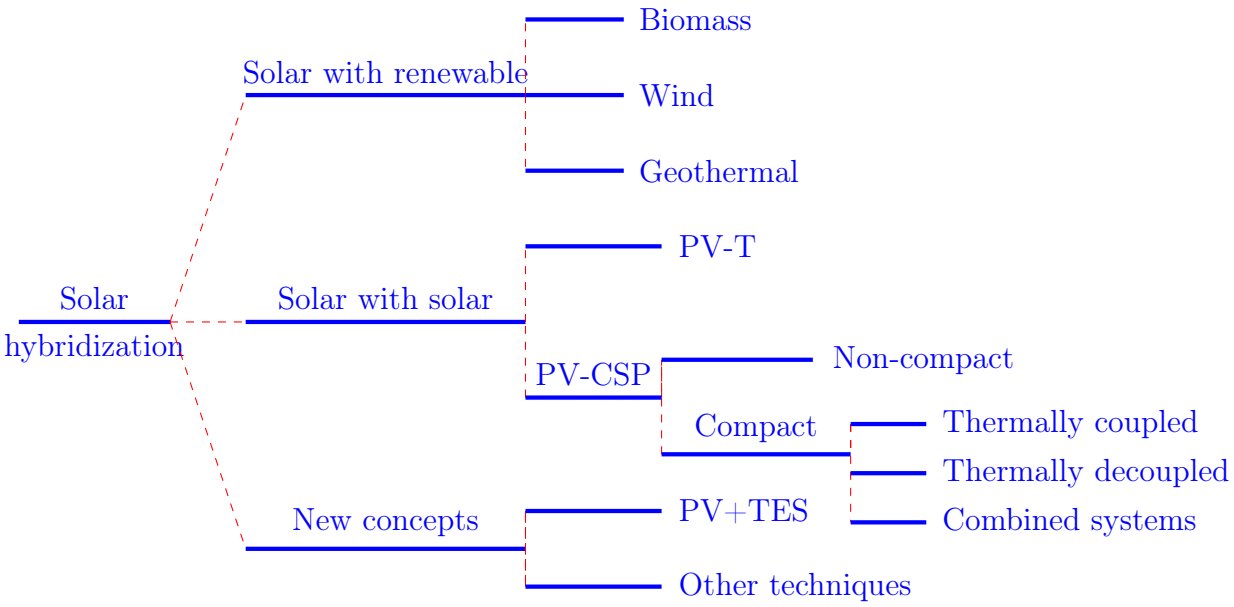

Figure 1.20: Classification of different solar hybridization techniques.

4.1 Non-compact PV-CSP hybrid systems

The *non-compact* PV-CSP classification was first introduced in [63], as two separated systems, usually located close to each other and only connected via the electrical grid to supply either a variable or a baseload energy demand as shown in Figure 1.21. One of the features of this strategy is that PV and CSP are mature technologies, and their combination poses few technical problems. Therefore, the scientific community has mainly focused on 1) design optimization, i.e. the power distribution between PV and CSP, 2) assessment of the techno-economic performance of a hybrid strategy compared to stand-alone technologies, and 3) selection of an adequate dispatch strategy of TES regarding PV and CSP operations.

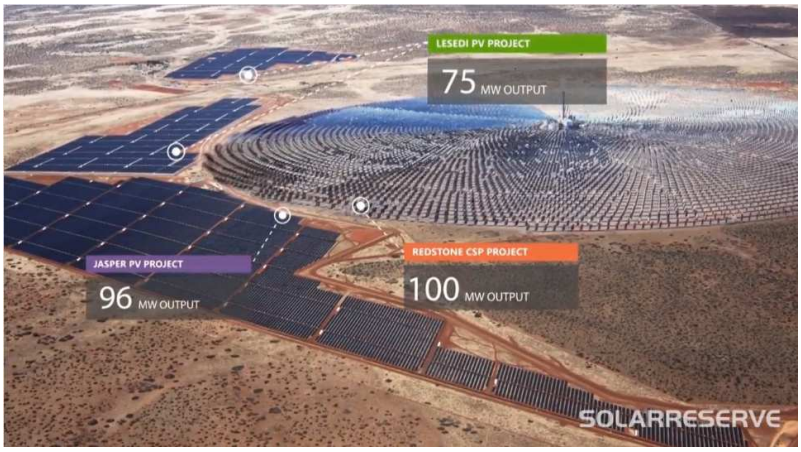

Figure 1.21: South-Africa's largest renewable energy project **Redstone** CSP project, adjacent to the 75 MW and 96 MW PV solar power projects successfully developed and implemented by SolarReserve [27].

Despite differences in system design, the majority of techno-economic studies confirmed the superiority of *non-compact* PV-CSP hybrid plants over standalone technologies, described with higher CFs and lower LCOE [63, 73, 205]. While for large capacities ($>$ 50 MW) *non-compact* systems present a very attractive solution, they may not be suitable for microgrids ($<$ 10 MW). In [192] only a 2% increase in the LCOE was obtained in comparison to a PV-battery configuration. Table 1.4 summarizes the main works conducted on existing *non-compact* plants for electricity generation during the last five years. Since the main trend of the CSP market is on developing PTC and CRs technologies, we found identical orientation for the *non-compact* hybrid plants as seen in Table. 1.4. The choice of the CSP technology along with the plant capacity directly affects the LCOE of the plant. CR and PTC plants with $\approx$ 270 MW capacity offer the lowest LCOE ($<$ 60 \$/MWh). Nonetheless, owing to the high level of flexibility a *non-compact* PV-CSP hybrid plant may offer, cogeneration of electricity with hydrogen production or water desalination have been capturing the interest of numerous researches recently [71, 211–214]. For example, in [211, 212] minimum levelized costs of hydrogen (LCOH) were obtained with a PV-CSP system regarding a standalone PV plant, with values of 4.04 \$/kg and 9.4 \$/kg respectively. Chile presents an ideal market opportunity for the integration of PV-CSP hybrid systems (see Table 1.4). However, Chile has begun to face serious problems of water scarcity. The integration of a multi-effect-distillation (MED) system into a PV-CSP plant was proposed in [71, 213, 214]. The first results show that due to the complexity of the operating conditions, a CSP + PV+ MED plant can be subject to different targets depending on which product is most relevant to produce, i.e. freshwater, electricity, or heat.

Table 1.4: Summary of works related to existing *non-compact* PV-CSP hybrid plants.

Ref.	**Locations**	**Plant Capacity** (MW)	**CSP techno.**	**TES** (h)	**CF** (%)	**LCOE** ($/MWh)
[73]	Morocco	300	PTC	14	92.4	109.00
[67]	Chile	130	CR	14	90.34	77.22
[206]	China	273	PTC	—	—	55.50
[76]	South-Africa	130	PTC	14	88	121.00
[64]	Chile	210	CR	17.5	88	124.6
[70, 207]	Chile	270	CR	13	—	52.59
[69]	Chile	50 – 150	CR	14.7	89.9	152.10
			PTC	14.1	81.8	123.20
[208]	Chile	—	CR	11.7	—	118.78
[209]	China	10	CR	16	—	140.00
[210]	Morocco	800	CR	—	—	70.00

In several *non-compact* plants the storage of the fluctuating PV electricity was carried out using expensive BESSs [71, 73, 192, 193, 197, 206, 215, 216]. The possibility of storing electricity as heat may seem thermodynamically counterintuitive; yet, it presents promising economic features. Using an electrical heater, then converted heat will be stored in the TES unit integrated into the plant [217–220]; a configuration that helps to decrease the LCOE by 19% in comparison to a conventional plant. The 800 MW Noor Midelt hybrid solar plant will be the first solar project in the world to combine PV as well as CSP with TES instead of PV + BESS. This combination presents an optimal mix to deliver electricity for the day and for five hours after sunset at 70 $/MWh [210].

Although *non-compact* plants offer a tremendous opportunity when it comes to low-cost plants, all with highly stable and on-demand power output, the use of the solar spectrum remains the same as for standalone technologies. More importantly, side-by-side installations of PV and CSP consume significant space and thus have a large land footprint. Therefore, *compact* PV-CSP hybrid technology is designed to overcome the above shortcomings by making full utilization of solar energy.

4.2 Compact PV-CSP hybrid systems

As the name indicates *compact* hybrid systems consist of coupling the two technologies into a single system [63] as depicted in Figure 1.22. Conversely to *non-compact* systems, the *compact* configuration raises some additional technical difficulties. Therefore, work on *compact* technologies focuses more on system design and technical challenges [44, 78, 79, 194, 195, 198–203, 221–225]. *Compact* hybrid systems can be classified into thermally coupled [78], thermally decoupled [79] or a combination of both strategies [63].

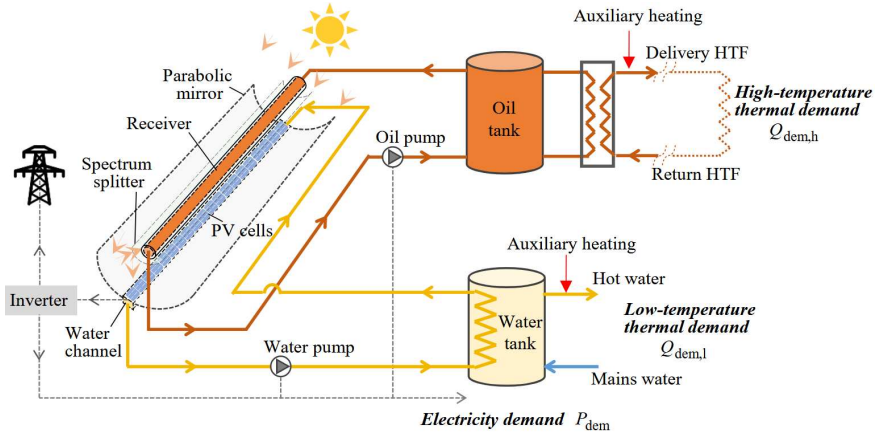

Figure 1.22: Schematic description of a *compact* hybrid plant with a PTC as a CSP system. PV cells are located on the outside of the heat collector with vacuum on surrounding the line tube or combined heating and power provision for dairy applications [28].

4.2.1 Thermally coupled systems

PV cells tend to warm up under solar illumination, rejecting thermal losses into the environment due to their fundamental inability to efficiently convert the broad solar spectrum into electricity. Those losses can be harvested using a wasted heat recovery (WHR) system, also known as the PV-topping [78]. A thermal collector bonded to the rear surface of PV cells recovers part of the losses for power generation using a thermal or CSP subsystem, while PV cells directly convert the part of the solar spectrum within the cell bandgap into electricity. Thermally coupled PV-CSP hybrid systems can be further distinguished into low, medium and high operating temperature systems.

① Low-temperature WHR systems (LT-WHR)

The LT-WH recovered from PV cells can be collected to directly generate electricity and heat mainly for domestic application [226] or in building integrated PV thermal (BIPVT) configuration [227]. Cui et al. and Lamnatou et al. [226, 228] reviewed the state-of-art of PV-T systems operating at low temperatures (< 60 °C). Widyolar et al. [29] developed a novel PVT collector which replaces the traditional packaging materials with a low-cost non-imaging optics and replaces sheet-and-tube heat exchange materials with a low cost and thermally efficient aluminium minichannel, depicted in Figure 1.23. Si solar cells are attached to the top and bottom of the minichannel using a thermally conductive and electrically isolating double-sided tape that isolates the cells from the aluminium minichannel absorber while allowing heat to be transferred into the absorber. The glass tube is filled with argon gas to reduce the internal convection coefficient inside the tube and minimize heat losses from the hot solar cells. Results demonstrated 57.4% thermal efficiency and 12.3% electric efficiency at ambient temperature and a maximum temperature around 80 °C.

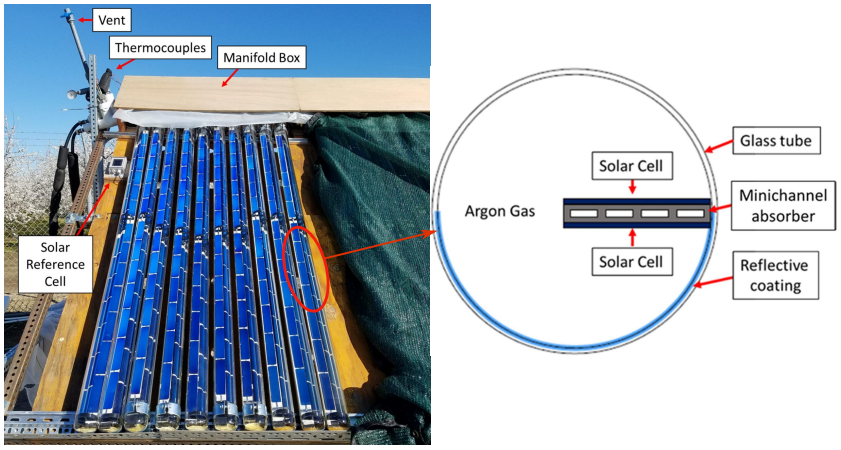

Figure 1.23: Experimental test platform with mounted PVT collectors with a close look into the front-facing cross-sectional view of PVT collector [29].

② Medium-temperature WHR systems (MT-WHR)

The MT-WHR systems have immense potential in the applications of absorption cooling, thermoelectric generation, organic Rankine cycle (ORC) power generation, etc. In MT-WHR systems the working-fluid temperatures range between 60 and 90 °C [226]. RayGen developed an ultra efficient cost-effective solar CR plant, via the combination of a PV receiver with thermal hydro [30, 229–231] shown in Figure 1.24. Low-cost heliostats focus sunlight onto a small ultra-high efficiency 1 m^2 PV array entirely covered with triple-junction (TJ) solar cells [232]. Unlike traditional storage systems that use electricity to heat water, thermal hydro uses a temperature gradient to generate power between two covered reservoirs, a heated (92 °C) and a cooled one (2 °C). The difference in temperature between the two reservoirs of water (90 °C) is exploited to drive an ORC turbine to create electricity.

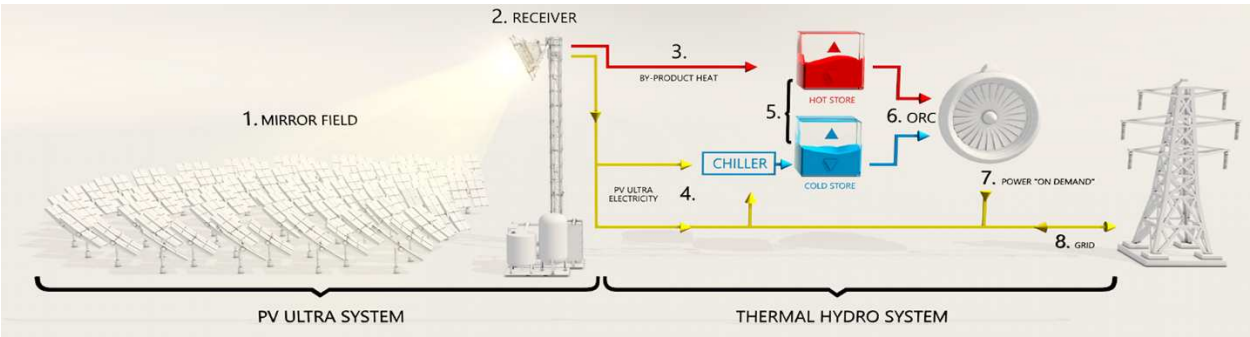

Figure 1.24: Schematic description of Raygen's PV-Ultra thermally coupled plant, with a PV receiver located at the top of the tower and an ORC for power generation [30].

Han et al. [203, 204] investigated the behaviour of a CR with a similar configuration; however, instead of covering the entire receiver area, only the core region of the receiver is covered with InGaP/InGaAs/Ge solar cells [115] (i.e. where high and relatively uniform flux density distribution occurs). The solar cells are cooled using R134a fluid. An

annular receiver is used to collect the non-uniform outermost part of the light distribution. Results showed that the overall solar-to-electricity efficiency can be theoretically increased from 32.8% for the dense array system (DA-CPV) to 34.8% for the hybrid system, when the concentration increases from 500 to 2 000 suns [203]. Sarafraz et al. [233] assessed the energetic performance of a dual receiver including a steam generator based on a CR and a CPV/T receiver for the co-production of steam, electricity and hot water/air. The results showed that the system thermal efficiency is improved from 28% to 36% when the solar concentration ratio increases from 10 to 1500.

③ High-temperature WHR systems (HT-WHR)

It is well known that the Carnot cycle efficiency is maximized with the highest possible heat source temperature. Therefore, increasing the temperature generally increases the overall cycle efficiency. However, in the HT-WHR system, as the solar cell temperature increases, the efficiency of solar cells decreases. These two facts lead to tough physical and engineering challenges for the development of the HT-WHR hybrid system. To date, few research works have discussed the behaviour and application prospects of HT-WHR systems. Ju et al. [78] reviewed different HT-WHR technologies based on concentration level. Most recently, Vaillon et al. [117] reviewed the progress of solar cells tested in the laboratory under thermal stress (temperatures up to 500 °C), in addition to the fundamental physics governing the thermal sensitivity of solar cells and the main criteria determining the ability of semiconductor materials to survive HT. To date, Perl et al. [116] were the first to experimentally investigate the output performances of GaAs and AlInGaP III-V solar cells up to high temperatures (over a temperature range of 25 - 400 °C) and under high concentration. Steiner et al. [118, 234] studied the resilience of III-V cell technologies in a tandem configuration. First results demonstrated a 15 % efficiency at 400 °C over a concentration range of 300 - 1000 suns of a dual junction GaInP/GaAs solar cell. Vossier et al. [224, 225] investigated the theoretical output performances of a PV-topping system operating at HT ($\sim$ 400 °C). Results showed that a 10% decrease in the efficiency occurs when considering realistic cell parameters, i.e. when including series resistances and non-radiative recombination. Regardless of the decline of cell efficiency with temperature, there is a noticeable improvement in the total (PV + thermal) hybrid electrical power production due to the improved efficiency of the turbine with increasing temperature at high concentrations.

4.2.2 Thermally decoupled systems

As the name indicates, a thermally decoupled system or spectral beam splitting (SBS) approach offers an alternative to the previously described strategy, in which the solar cells and the thermal collector are decoupled [79, 235–238], as illustrated in Figure 1.25. In particular, this technology has instigated a large number of numerical and experimental researches [44, 194, 198, 201, 221, 223, 236, 239–249], considering different filtering techniques, aiming to provide the *SBS* technology into the solar market. Among the different filtering techniques, only three have been in continued

progress during the last 6 years: liquid absorptive filters, dichroic filters and PV cells as filters.

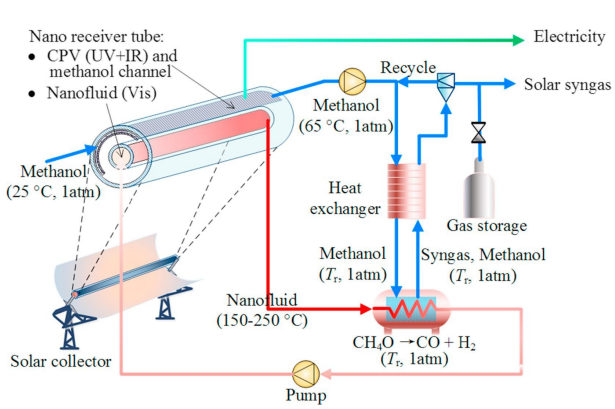

(a) Liquid absorptive filters [245]

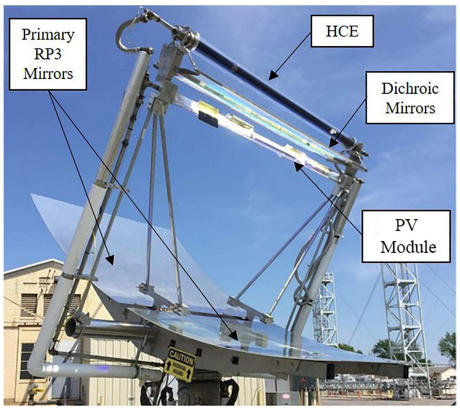

(b) Dichroic filters [194]

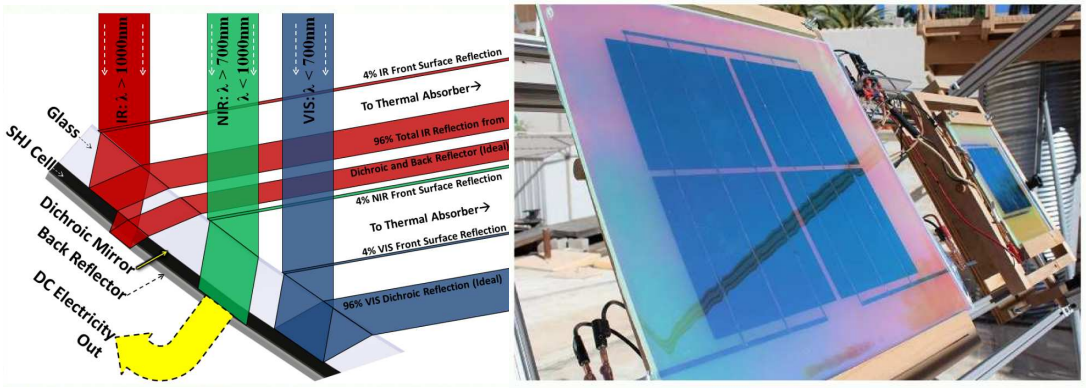

(c) PVMirror [250]

Figure 1.25: Classification of the *SBS* PV-CSP hybrid systems: (a) concentrated sunlight is channeled by the nanofluid inside the thermal collector located in the middle of the PTC, (b) SBS Retrofit Installed and On-Sun at the University of Tulsa, and (c) PVMirror prototypes being tested on tracker with a schematic description of the splitting spectrum principle.

⇝ **Liquid absorptive filters** are liquids with or without nanoparticles able to absorb solar radiation of a certain spectral range [237, 238, 251, 252]. Part of the spectrum is absorbed by the liquid as thermal energy as depicted in Figure 1.25(a). In this example, the concentrated sunlight is channeled by a nanofluid to produce (150 - 250 °C) heat. The rest of the solar radiation suitable for electricity generation by the PV cells passes through the nanofluid. The use of suspended nanoparticles increases efficiencies compared to conventional HTFs. However, the stability of nanofluids at HT and ultraviolet light is not optimized for long-term operation.

⇝ **Dichroic filters** are optical filters with nearly zero coefficient of absorption that reflect part of the spectral bands and transmit the rest. In Figure 1.25(b), the

dichroic mirror split the incoming spectrum and redirect the PV effective wavelengths down to the PV module underneath it. The remaining photons are transmitted to the existing thermal collector [194]. Due to the excellent spectral splitting effect, stable working performance, mature processing technology, dichroic filters are widely utilized in PV/CSP hybrid systems [79, 194].

⇝ **PV cells as filters** use the optical properties of semiconductors. Photons with energy lower than the cell energy bandgap can pass through the PV cell, while energy higher than the energy bandgap is absorbed by the PV cell. The technology is known as PVMirrors [195, 196, 250, 253–256] in Figure 1.25(c). PVMirror acts as a concentrator, SBS and a high-efficiency PV converter. However, it is difficult and expensive to manufacture high-transmittance PV cells at present. In [195, 196, 253, 255], it has been confirmed that the addition of filters increases the system's cost by 10%. Meanwhile, the hybrid system has increased its annual energy output by 53% [195]. While most studies are concerned with the technicality of the systems as summarized in Table 1.5, Fisher et al. [253] investigated the economical viability of the PVMirror technology depicted in Figure 1.25(c). The LCOE decreased by more than 15% relative to CSP while maintaining full dispatchability.
Today, the world's first solar plant based on the use of PVMirrors instead of conventional mirrors on the heliostat field of an SPT plant is being developed in Seville and is known as BLUESOLAR technology [257]. This technology will generates heat that can be economically stored at an LCOE varying around 42 – 47 €/MWh.

Mojiri et al. [235], Ju et al. [79], Liang et al. [237], and Kumar et al. [258] reviewed various SBS approaches for PV/T and PV-CSP applications and discussed the research trends, technical obstacles, and vital future research for the performance improvement of the different systems with the SBS technology. In Tables 1.5 and 1.6 a summary of the main work conducted on SBS systems is given. Similarly to the PV-topping Si cells are used for low operating temperatures, whereas III-V single junction and MJ cells are more suitable for HTs. Moreover, an increase of the hybrid system conversion efficiency relative to individual technologies can be noted, this increase is more or less related to the choice of the cell technology along with the filtering technique. It is worth mentioning that most of the reported studies considered the use of PTC as a CSP subsystem for their high technical maturity and the flexibility the system offers when it comes to integrating different *SBS* filters.

Table 1.5: List of recent works conducted on *SBS* hybrid systems using a wide variety of PV cell technologies and filtering techniques.

Year	Ref.	PV Cell technology	Filtering technique	CSP technology	T_{HTF} (°C)	T_{cell} (°C)	η_{PV} (%)	$\eta_{th.}$ (%)	$\eta_{hyb.}$ (%)	$\eta_{conv.}$ (%)
2018	[239]	c-Si	Dichroic	PTC	355	40	—	—	23 '$\eta_{PV} + \eta_{th.\ elec}$'	22 'PV'
		CdTe			385			—	22 '$\eta_{PV} + \eta_{th.\ elec}$'	18 'PV'
		GaAs			365			—	29 '$\eta_{PV} + \eta_{th.\ elec}$'	23 'PV'
		InGaP			405			—	27 '$\eta_{PV} + \eta_{th.\ elec}$'	19 'PV'
	[223]	Si	Nanofluid	PTC	200	—	—	76.5	80.8 '$\eta_{PV} + \eta_{th.}$'	62 'PV/T'
	[259]	c-Si	Nanoparticles		300	108	11.7	64	75.7 '$\eta_{PV} + \eta_{th.}$'	—
		GaAs			305	110	17.9	53	70.9 '$\eta_{PV} + \eta_{th.}$'	
	[44]	InGaP	PV cells	PTC	600	40	5.8	52.6	22.6 '$\eta_{PV} + \eta_{th.\ elec}$'	14 'PV'
		InGaP/GaAs					9.1	45.9	23.7 '$\eta_{PV} + \eta_{th.\ elec}$'	23 'PV'
	[222]	Si	Gold & ITO particles + fluid	PTC	110	50	5	61	66 '$\eta_{PV} + \eta_{th.}$'	—
2019	[201]	InGaP/GaAs	Suspended particles	PTC	600	30	4	69	19 '$\eta_{PV} + \eta_{th.\ elec}$'	—
	[260]	InGaP/InGaAs/Ge	Nano-fluid	PTC	167	25	15.4	75.9	20.5	17.8 'CPV/T'
	[261]	Si	Beam filter	PTC	265	—	24.2	54.5 'η_{TC}'	31.2	25 'PV'
	[262]	c-Si	Multi-layer Ge/Nb_2O_3	CLFR*	334	30	21.6	19.73	26.7 '$\eta_{PV} + \eta_{th.\ elec}$'	25 'CPV'
	[263]	Si	$Ag/CoSO_4$-1	LFR	—	25	5.3	53.1	58.4 '$\eta_{PV} + \eta_{th.}$'	15.9 'CPV'
	[264]	p-Si	Dichroic	—	—	36	18.5	4.2	22.7	18.5
	[265]	c-Si	Multi-layer	CLFR	300	30	21.1	18.07	25.8 '$\eta_{PV} + \eta_{th.\ elec}$'	24.5 'CPV'
	[245]	m-Si	Nanofluid	PTC	200	25	33.7	75.5 'η_{chem}'	36.3	25.9 'CPV'

T_{cell}: cell temperature, η_{PV}: efficiency of PV subsystem in the hybrid configuration, $\eta_{th.}$: the thermal efficiency of the hybrid system, $\eta_{th.\ elec} = 2/3\,\eta_{Carnot}\,\eta_{th.}\,\eta_{HX}\,\eta_{PB,\ net}$: thermal to electric efficiency of the hybrid system, η_{HX}: heat exchange losses (0.9), $\eta_{PB,\ net}$: parasitic losses (0.9), η_{hyb}: the overall efficiency of the hybrid system, $\eta_{conv.}$: efficiency of conventional PV, CSP or PV/T system, c-Si: Crystalline-silicone, p-Si: Polycrystalline-silicon, m-Si: multicrystalline-silicon, * Compact Linear Fresnel Reflector , η_{TC}: Thermochemical , η_{chem}: solar to fuel efficiency, WSF: wavelength-selective filter.

Table 1.6: List of recent works conducted on *SBS* hybrid systems (continued).

Year	Ref.	PV Cell technology	Filtering technique	CSP technology	T_{HTF} (°C)	T_{cell} (°C)	η_{PV} (%)	$\eta_{th.}$ (%)	$\eta_{hyb.}$ (%)	$\eta_{conv.}$ (%)
2020	[194]	Si	Dichroic Mirror	PTC	—	35 - 45	—	—	18	15 'CSP'
	[199]	MJ [266]	Beam filter	PTC	—	86	21	—	—	—
	[200]	m-Si	Dichroic	PTC	250	92	14.9	74.4 '$\eta_{opt.}$'	29.3	16.5 'CPV'
	[267]	m-Si	Nanofluid	FL	—	—	13.1	10.97	24.1 '$\eta_{PV} + \eta_{th.}$'	16.3 'PV' [268]
	[198]	m-Si	Dichroic	PTC	374	40	10	50	60 '$\eta_{PV} + \eta_{th.}$'	17.5 'PV' 64 'PTC'
	[252]	Si	$Ag/CoSO_4$-PG	—	—	—	4.56	79.4	83.96 '$\eta_{PV} + \eta_{th.}$'	15.76
		GaAs		—	—	—	5.5		84.9 '$\eta_{PV} + \eta_{th.}$'	14.9
	[269]	Si	$Ag/CoSO_4$-PG	LFR	77	37	7.6	46.2	53.9 '$\eta_{PV} + \eta_{th.}$'	43.5 'CPV/T'
	[270]	Si	Multi-layer Ge/SiO_2	CLFR	300	30	19.4	19.9	24.2 '$\eta_{PV} + \eta_{th.\ elec}$'	—
2021	[271]	m-Si	Ethylene Glycol	—	—	35	10	30	40 '$\eta_{PV} + \eta_{th.}$'	18 'PV'
	[272]	Si	Nanofluid	LFR	—	30	29.6	18.5	48.1 '$\eta_{PV} + \eta_{th.}$'	—
	[273]	c-Si	WSF	PTC	—	30	19.9	—	—	18.2 'CSP'
	[274]	c-Si	PV cells	SPT	50	—	6.2	46	52.2 '$\eta_{PV} + \eta_{th.}$'	—

T_{cell}: cell temperature, η_{PV}: efficiency of PV subsystem in the hybrid configuration, η_{hyb}: the overall efficiency of the hybrid system, $\eta_{conv.}$: efficiency of a conventional PV or CSP system, c-Si: Crystalline-silicone, p-Si: Polycrystalline-silicon, m-Si: multicrystalline-silicon, WSF: wavelength-selective filter, FL: Fresnel Lens.

4.2.3 Combined systems

The ultimate challenge of the aforementioned hybrid technologies is to combine all the desired properties into a single structure to obtain the best output performances of both subsystems. Nowadays, PV-topping systems working at HTs using today's best cell technologies are less likely to tolerate high operating temperatures for long durations in comparison with conventional Si systems (e.g. 20 – 25 years [275]). To date, only a limited number of studies have discussed the ability of III-V solar cells to support HTs for various durations: up to 37 days with GaInP cell technologies [276] and up to 200 hours with MJ cells [118]. These first results may encourage research towards HTs. Yet, they highlight the fact that expensive cell technologies are likely to operate effectively under HTs [117], a cell category that still struggles to reach the solar market under low operating temperatures. In the meantime, the SBS strategy faces the limitation of the partial utilization of the solar spectrum regardless of the choice of the filtering techniques. As a result, the combination of PV-topping and SBS remains of high technical interest to improve the overall system performances with decreased costs. Ju et al. [63] reviewed some possible combined configurations between the technologies to enhance the operating temperature of HTFs without sacrificing the PV efficiency or discarding the LT heat generated in the PV cells. Most recently, Weinstein et al. [31] described the operation of a novel hybrid electric and thermal solar (HEATS) receiver, a schematic diagram of which is shown in Figure 1.26(a). The incident solar spectrum is split using a spectrally selective light pipe (SSLP) coating. The light pipe reflects high-energy photons towards the PV module while absorbing the remaining fraction of the solar spectrum. The modelling indicates that the HEATS receiver can achieve a total electrical efficiency of 26.8% when a Si PV cell is used and 28.5% when a GaAs PV cell is used, with over 75% dispatchability in both cases. Notably, these efficiencies are higher than if the HEATS receiver was replaced with just a PV cell or a purely thermal receiver [31].

Within the same context, Codd et al. [32] experimentally investigated the performances of an advanced version of a spectral-splitting transmissive-CPV (tCPV) module coupled to a dimple plate cavity thermal receiver, as depicted in Figure 1.26(b). Approximately 71% of photons below the bandgap energy of the cell, conventionally wasted as heat or otherwise not captured, are transmitted through the CPV cells. Thereby, the HTF can attain high temperatures without sacrificing the efficiency of the cells or discarding the low-temperature heat generated in the PV cells. This combined hybrid technology shows several advantages: high electrical efficiency, low temperature (< 100 °C) heat, and high temperature (> 100 °C) heat, all three at a levelized cost of heat (LCOHe) that is competitive with natural gas prices.

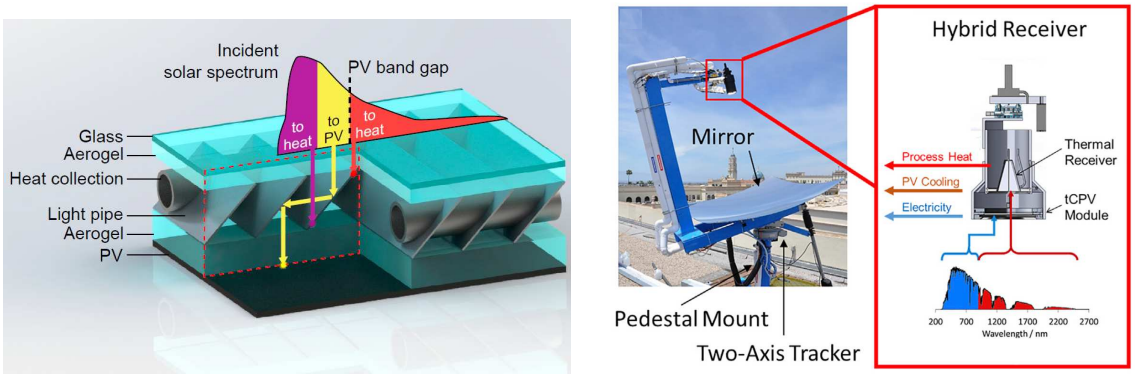

(a) (b)

Figure 1.26: Example of two combined systems: (a) The HEATS receiver using light pipes to direct the effective energy within the PV cell bandgap [31]. (b) The tCPV/T hybrid system, were sunlight is concentrated by the paraboloidal mirror on the 2-axis tracker and directed to the hybrid receiver. There, the tCPV module converts a portion of the high-energy photons to electricity and LT heat, while transmitting IR wavelengths to a thermal receiver, where it is absorbed and converted to HT heat [32].

4.3 New concepts

In this section, the focus will be brought onto some exotic solutions that offer either full utilization of the solar spectrum or cost-competitive technologies or offer both.

4.3.1 Photovoltaic with thermal energy storage

We aforementioned the possibility to use TES to store the overproduced electricity via a PV subsystem in a *non-compact* PV-CSP hybrid plant. Therefore, Gordon et al. [33] investigated the idea of power-to-heat-to-power generation using a PV plant with a TES unit. They evaluated the thermodynamic and economic benefit of an oversized PV plant operating during the day to meet electrical demand. During this time, the overproduced electricity is stored as heat in cost-effective molten salts to expand the production beyond daylight, as shown in Figure 1.27(a). The need for low investments (i.e. Si PV systems and molten salts as HTFs) make the PV-TES approach a promising solution; however, the low conversion efficiency of solar energy (i.e. conversion of solar radiation into electricity, then conversion of electricity into heat using an electrical heater, to finally convert heat into electricity using a power block) may slow down the development of this strategy. A recent study conducted by Schöniger et al. [34] compared three different technologies, CSP+TES, PV+ BESS and PV+TES, using three cost scenarios to cover uncertainty in future costs as shown in Figure 1.27(b). For short storage periods, PV+BESS comes first as the most economical solution then, CSP+TES becomes competitive after 2 – 3 h and 4 – 10 h for the current cost and low-cost case studies, respectively (Figure 1.27(b)). Regardless of the cost scenarios, the specific cost of a PV+TES plant remains higher than that of a CSP+TES. Thereby it is advisable to investigate further the ability of these technologies to take a large

part in the future of solar electricity production.

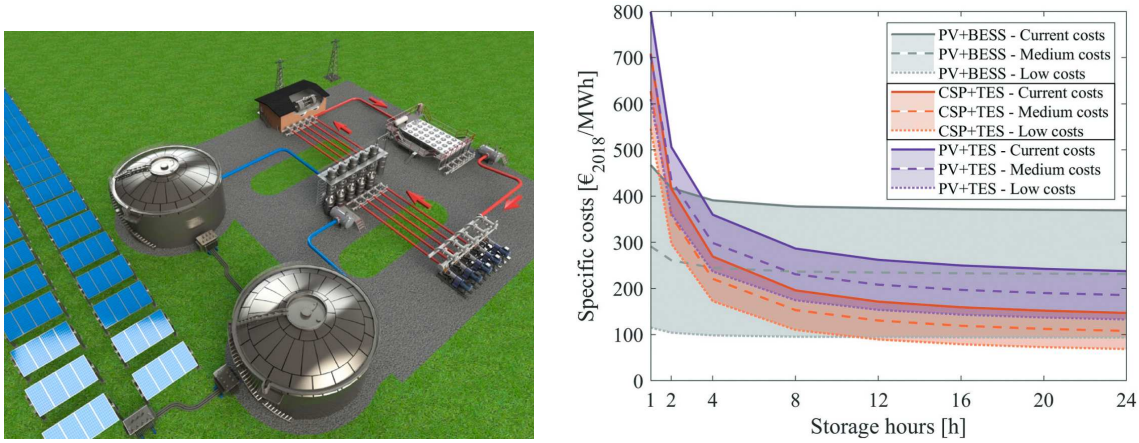

(a) (b)

Figure 1.27: (a) A sketch of a PV+TES hybrid plant using molten salt as a HTF [33], (b) Variation of the specific costs of three different technologies with the TES duration, with consideration of different cost scenarios [34].

4.3.2 Ultra-high temperature systems

The research work of Datas et al. [35, 36, 277–279] addresses the possibility of storing energy at extremely HTs up to 2000 °C using intermittent resources, mainly PV, CSP or wind (see Figure 1.28). These systems rely on a novel latent heat thermal energy storage (LHTES) technology using silicon-based alloys as new PCMs, with one of the highest energy densities within the range of 1000 – 2000 kWh/m^3 and melting points far above 1000 °C [280]. The main attraction in the proposed systems lies in their simplicity and modularity compared to conventional CSP plants due to the absence of moving parts (i.e. turbine). The stored energy in the LHTES can be converted into electricity on demand using:

- A thermophotovoltaic technology (TPV), that is, thermally radiated photons are absorbed in a low-bandgap semiconductor and excite electron-hole pairs, which are selectively collected to produce an electric current [281] (see Figure 1.28(a)).
- A thermionic-photovoltaic converter (TIPV) [282] composed of three main elements: the emitter (cathode), the anode and the PV cell. The cathode is directly heated by the PCM, which then emits two types of heat carriers, electrons and photons. Electrons are collected in the anode and produce an external electric current. Photons pass through the anode and are absorbed by an infrared-sensitive PV cell, which generates additional electricity (see Figure 1.28(b)).

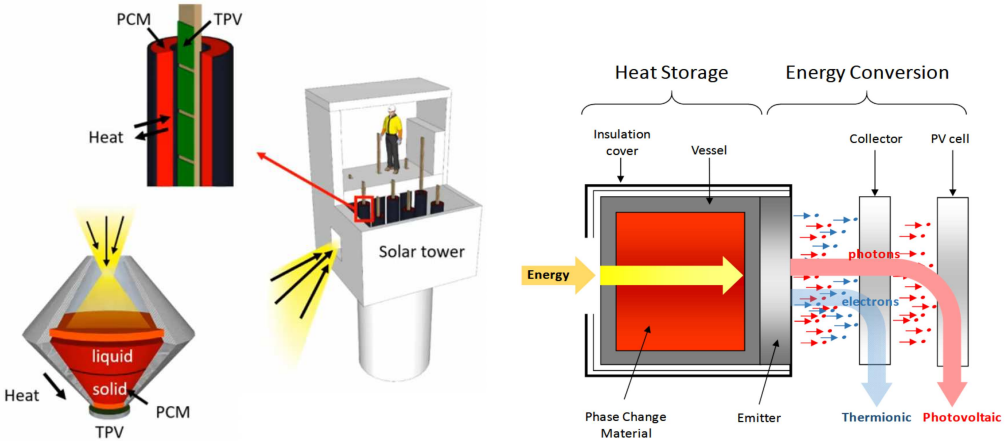

(a) (b)

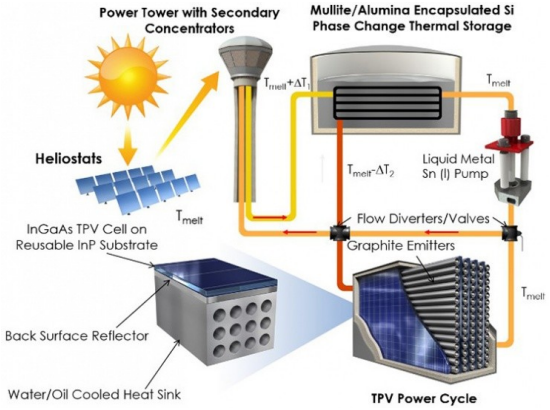

(c)

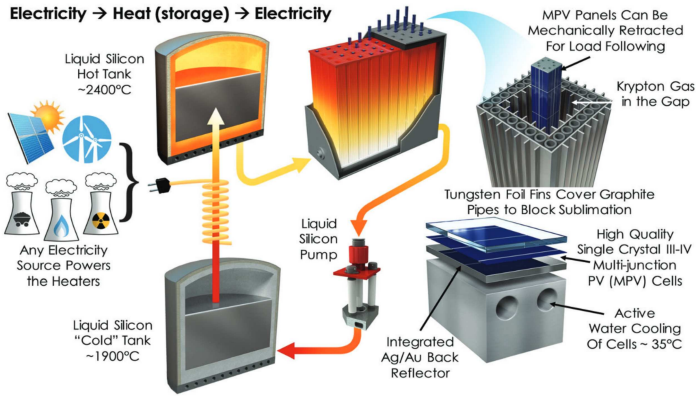

(d)

Figure 1.28: Schematic description of three different technologies operating at very high temperatures: (a) the AMADEUS unit located at the top of the SPT with a close-up view of the individual unit where the heated Si exchanger with the PCM and the TPV unit [35], (b) very much inspired by the AMADEUS project with the additions of TIPV unit [36], (c) conceptual layout of a utility-scale TPV system. The red and white arrows on the pipes indicate the flow path for charging (red) and discharging (white) TES [37], and (d) another integration of the TPV system, using electricity from any source to be converted to heat via joule heating, which is then transferred to Si [38].

The two configurations are highly suited for high operating temperatures because they are based on the direct emission of electrons and photons through space, eliminating the need for a working fluid and moving parts. Another potential application for TPV has been proposed in the context of solar energy conversion and specifically as a power cycle for CSP illustrated in Figure 1.28(c), instead of a turbine-based heat engine [37]. Solar energy collected via the heliostats field is concentrated onto a receiver made of graphite located at the top of a tower, where liquid metal Sn is used as a primary HTF. The collected heat via Sn is stored using low-cost Si PCM as a storage medium. To produce electricity Sn is circulated from the TES tank to the TPV power cycle. The system concept combines the surpassing economic advantages of TES with the potential for low cost and high performance derived from TPV cells fabricated on reusable substrates, with a high reflectivity back reflector for photon recycling [37]. Similarly, Amy et al. [38] proposed a thermal energy grid storage using multi-junction PV as a heat engine and Si as a TES medium as illustrated in Figure 1.28(d). First experimental results showed the ability of this technology to provide a great potential in terms of efficiency, cost reduction and storage energy density.

4.3.3 Other technologies

In an attempt to reduce thermal heat rejection PV cells suffer from, Haviv et al. [39] introduced the concept of luminescent solar power (LSP) depicted in Figure 1.29(a). Solar radiation is concentrated on a photo-luminescent (PL) absorber that absorbs the high-energy photons and after thermalization, emits low-energy photons with a high EQE at high temperatures (above 500 °C). A diffusive surface at the back of the PL absorber, together with a highly reflective coating at the front face directs the PL toward the PV cell's side. The emitted photons, combined with the transmitted ones, drive the adjacent PV cell. In this configuration, PV cells operate nearly as efficiently as under direct illumination but with minimal excessive heat that is recovered using the PL absorber.

Fan et al. [40] proposed a concentrated photochemical–photovoltaic–thermochemical (CP-PV-T) system depicted in Figure 1.29(b). Photons with energy surpassing the PV cell bandgap energy are stored in the chemical bonds directly by the photochemical process while energy within the cell bandgap is efficiently converted into electricity. Finally, photons with energy below the bandgap are used in the thermochemical reactor by the methanol decomposition reaction, thereby guarantying a full utilization of the solar spectrum. Numerical results demonstrated the increased utilization of the solar spectrum at the first 600 nm, from 44.01% with CPV-T to 80.68% with the CP-PV-T system. Similarly, Kashyap et al. [41] presented a general hybrid concept to achieve full-spectrum solar energy harvesting and storage to provide thermal energy both during the day and night. Figure 1.29(c) illustrates a sketch of the proposed system composed of a molecular storage material (MSM) and localized phase change material (L-PCM) that enables to reach the phase-transition temperature at low solar flux and minimum heat loss. One of the main advantages of this technology is the unlimited range of possible combinations of PCM and MSM materials to achieve higher

energy densities, therefore opening up various avenues for harvesting solar energy at high efficiency and low operation cost for a large spectrum of applications.

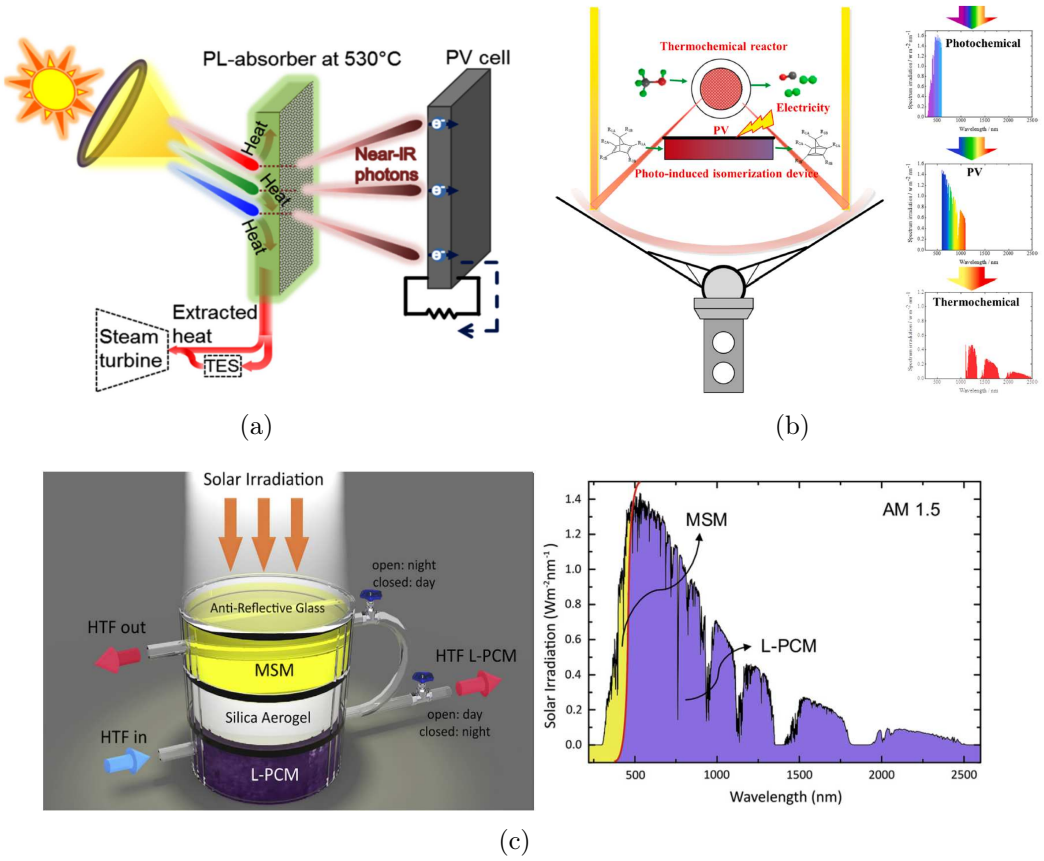

Figure 1.29: Innovative approaches for a full utilization of the solar spectrum: (a) Illustration of the LSP concept. The red-shifted PL emission is then coupled to a PV cell with a matching bandgap, while the residual heat (at 530 °C) is stored and transferred to a heat engine [39], (b) Sketch of full-spectrum solar energy utilization system with a schematic diagram of the cascade utilization of sunlight [40], and (c) Illustration of the molecular and phase-change hybrid. The hybrid consists of a MSM and a L-PCM separated by a silica aerogel to maintain the necessary temperature difference [41].

Summary

This chapter provided at first a brief overview of solar radiation components commonly used for power generation. Then the focus was on describing the operating principle of two main solar technologies, PV and CSP. A detailed up to date review of both technologies was provided. Since the 1980s, both PV and CSP technologies have improved in conversion efficiency and cost. However, the lack of dispatchability that accompanies both solar technologies present an Achilles' heel against the wide integration of solar technologies. With the recent launch of the net-zero emission policy, the world is now mostly directed into combining different solar technologies and energy storage technologies to highly increase the share of solar electricity in the grid, and expand power production beyond daylight. This chapter also contained a short introduction to new concepts using solar technologies in some uncommon configurations that seem rather unrealistic to present; however, all commercial plants started decades ago with ideas that seemed unpractical and highly complicated. From the literature review focused on previous research on the topics related to the present work, it can be said that there is a lack of studies that specifically explore the *compact* integration of PV-CSP hybrid plants considering large-scale plants under ground measured meteorological conditions.

Chapter 2

Energy assessment of large-scale *compact* PV-CSP systems

In this chapter, the question of whether or not large-scale compact PV-CSP hybrid technologies can outperform a conventional CSP plant will be addressed. To answer this question, section 1 describes the operation of the CSP plant considered as a case study as well as the compact systems. In section 2, a presentation of the mathematical model for all components is provided. In section 3, the impact of different operating conditions on the daily and yearly performance of the two compact PV-CSP hybrid plants is conducted. For a wide range of test scenarios and with ground measured meteorological data, the superiority of compact PV-CSP systems over the standalone CSP plant is highlighted. Finally, section 3.2.2 summarizes the main findings and presents an opening to the next chapter. The results presented in this chapter have been published in Applied Energy [283].

Introduction

According to the literature review that has just been presented, *compact* PV-CSP hybrid systems are an attractive way to overcome the problem of intermittency inherent to solar energy for several reasons. First, this technique allows more efficient use of the solar spectrum. Secondly, the different possibilities of combinations between the two technologies widen the scope of application and the choice of technologies to be used. However, the extent to which *compact* PV-CSP hybrid plants may outperform conventional solar plants is still unclear. In particular, the implementation of a large-scale *compact* hybrid PV-CSP plant still presents some challenges due to the lack of experimental results at the prototype scale. These results show contradictory predictions regarding the influence of some operating parameters on the systems output performances. Therefore, the choice of an appropriate metric to evaluate the benefits of these technologies remains relevant. System efficiency has been used in the past [224, 225] but does not describe the instantaneous change in electrical energy produced under realistic operating conditions. Accordingly, we use the annual energy production in this study to accurately assess the interest of these hybrid technologies, as some

studies have proven that a high conversion efficiency does not always translate into high energy production [284].

1 Systems description

In this section, a detailed description of the studied systems based on the example of a large-scale CR plant is given, followed by a schematic illustration of the hybrid strategies based on the CR plant, the *one-sun* and the *high-temperature* approaches. The choice of a CR plant can be justified by the direct access to a large number of technical and meteorological data available on site.

1.1 THEMIS CR plant

THEMIS CR plant is an R&D facility located at Targassonne, in the south of France. The particularity of this location lies in its high altitude (1700 m), which favours the reception of direct solar radiation with low atmospheric dispersion. The original THEMIS heliostat field consisted of 201 heliostats [285]; today, only 107 heliostats positioned north of the receiver and displayed in an amphitheatre layout [1] [286] are used as shown in Figure 2.1. A single heliostat is composed of nine modules (i.e. a set of mirrors): eight main modules of 3.62 m × 1.79 m, and one module of 2.46 m × 0.83 m filling the central gap left by the tracking system, as shown at the bottom right of Figure 2.1. The solar tower has height of 100 m, the receiver is located 86 m above the ground, and its dimensions are set equal to 4 m × 2 m. Table 2.1 lists the most important characteristics of THEMIS plant considered in this study [287–289].

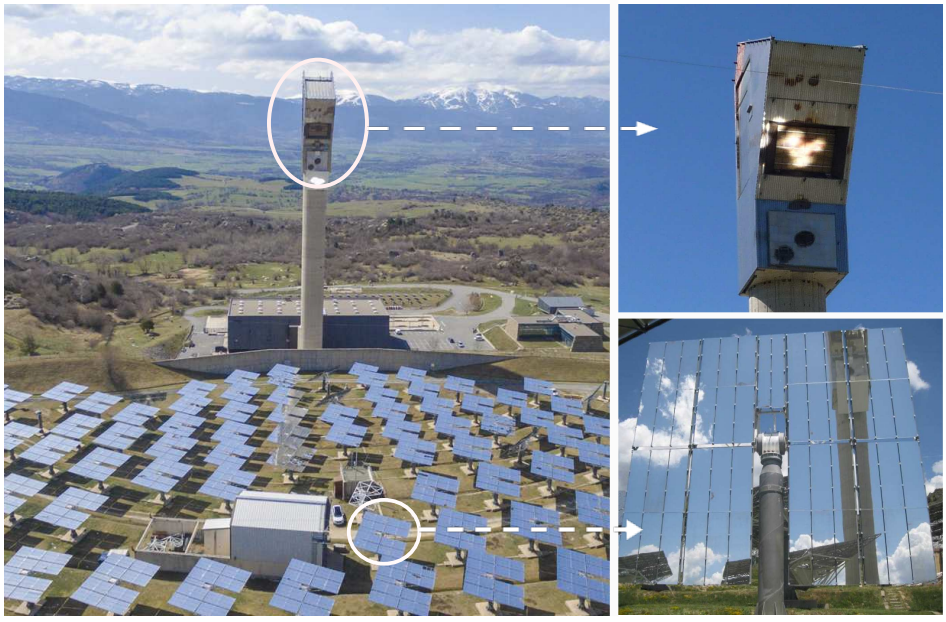

Figure 2.1: **THEMIS** CR plant with a close look at the receiver at the top of the tower and one of the heliostat in the solar field.

[1] The land is slightly sloping, between 6 and 18 °, ideal for a tower plant.

Table 2.1: **THEMIS** power plant input parameters of the model.

Heliostat field	
Number of Heliostats N_{hel}	107
Heliostat reflective area, S_{hel}	53.7 m^2
Mirror reflectivity, ρ_{Mir}	0.9 [287, 290–297]
Central Receiver	
Area, S_{rec}	8 m^2
Operating temperature, T_{rec}	400 °C
Absorptivity, α	0.95
Surface emissivity, ε	0.9
Convective heat loss coefficient, h_{conv}	10 W/m^2K [298]

1.2 *One-sun* strategy

The ***one-sun (1S)*** *compact* PV-CSP hybrid system considered in this work is mainly inspired by Holman et al. [195, 196, 253], and is schematically illustrated in Figure 2.2. The conventional mirrors used in the solar field are replaced by PV heliostats including, a back reflector, thus allowing sub-bandgap photons to be reflected onto the thermal receiver. Here, we assume GaAs solar cells from Alta Devices (that currently hold the world record for single-junction solar cells [299]) to be integrated onto the heliostats. The fraction of incident solar energy absorbed by the PV cells ($\sim$ 64%) is calculated from the spectral reflectance curve shown in Figure 2.8, with the remaining fraction being sent to the receiver. Unlike other hybrid strategies, the *1S* approach offers the inherent advantage of converting a large fraction of the diffuse light.

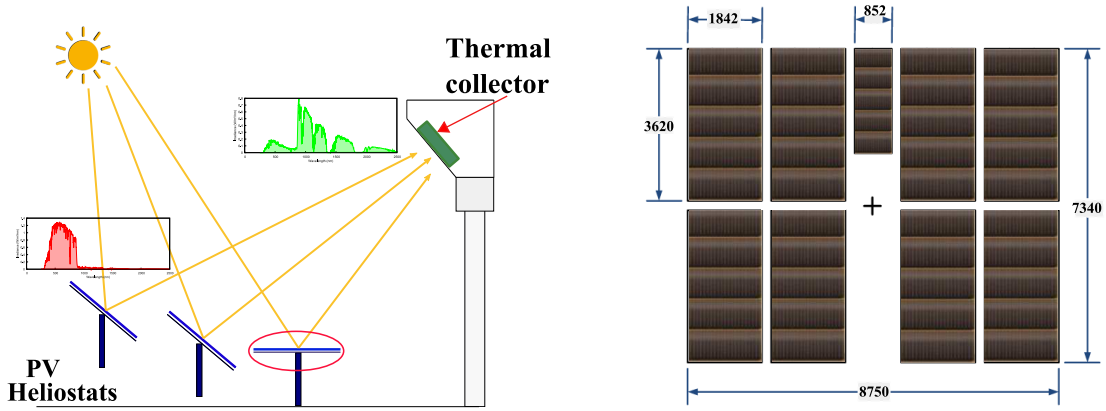

Figure 2.2: Schematic description of the *1S* hybrid approach with a close look at a PV heliostat entirely covered with highly reflected GaAs solar cells (dimension in mm).

1.3 *High-temperature* strategy

Unlike the ***1S*** strategy, the High-temperature (***HT***) approach does not involve any modification of the heliostat field but uses PV cells as the outer part of an integrated receiver, thermally bonded to a thermal receiver beneath it, as depicted in Figure 2.3. The heat generated by sub-bandgap photons and thermalised electrons is transferred to the HTF, which is assumed to be at a temperature close to but below 400 °C (a value coherent with early long-duration characterizations of *HT* GaAs PV cells [116]).

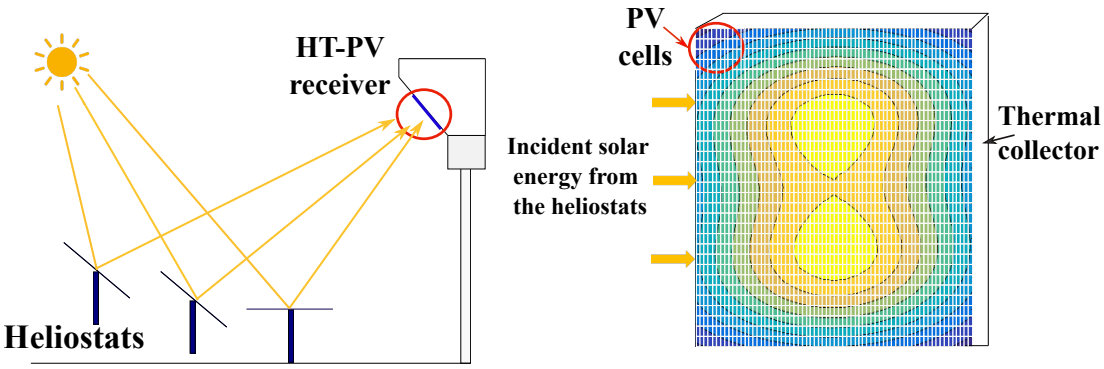

Figure 2.3: Schematic of the *HT* hybrid approach with a close look at the PV receiver entirely covered with solar cells (represented by the small blocks separated with white lines). The different contour color represent the concentration level over the receiver varying between 20 to 1500 suns.

2 Model description

We developed a predictive model under MATLAB R2016b providing the energy output for each strategy on an annual basis to compare the performance of both hybrid plants described above with a standalone CSP plant. The schematic diagram of the multiphysics model is shown in Figure 2.4. The model takes as inputs:

- The geographical coordinates for the location of interest (altitude, longitude, latitude),
- The local time,
- Several important meteorological parameters: temperature, wind speed, and irradiation (DNI, DHI and GHI). The latter was measured on-site considering one almost complete year (2018): the missing and low-quality data (8 days out of 365 days) were replaced with equivalent irradiation data measured during previous years. These data were selected after identifying similar days (DNI level and variation) and were implemented in the data-set following the procedure described in [300],
- The heliostats position regarding each other and the tower as well as the receiver main characteristics.

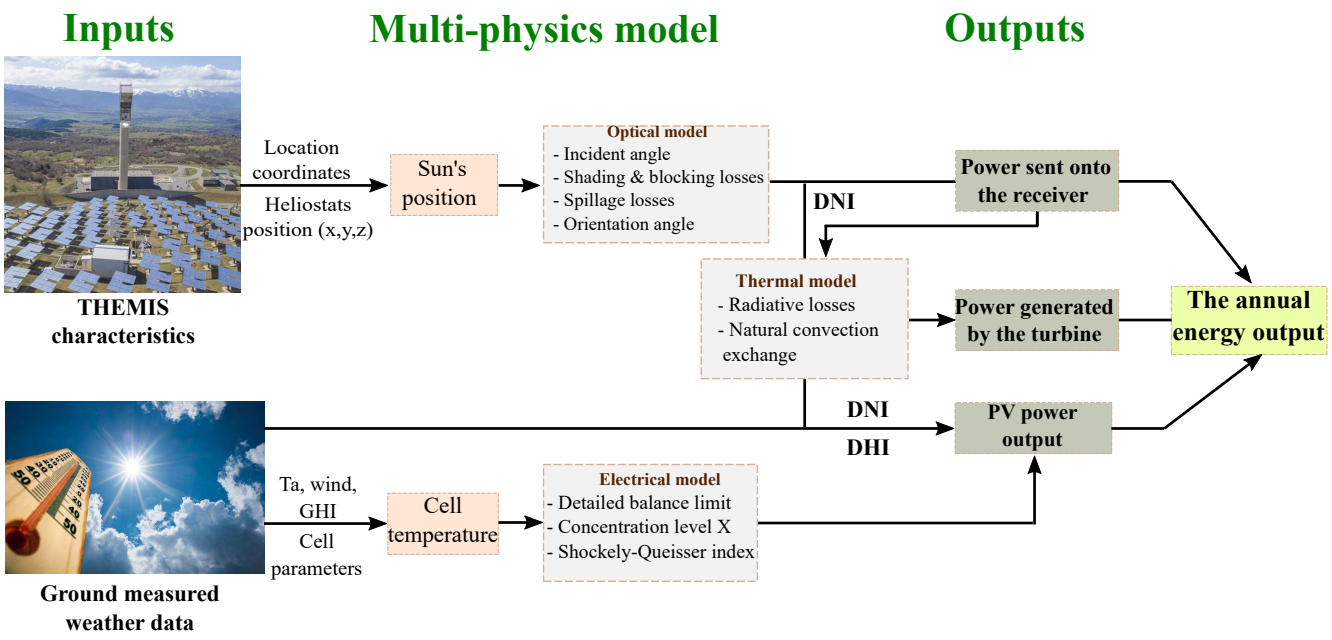

Figure 2.4: Schematic diagram of the multiphysics model used to assess the annual energy output of the three solar technologies.

The model computes the sun's position described with three important angles shown in Figure A.1 and the set of equations (A.1), (A.2), and (A.3) at every time step throughout the year using the SPA[2] NREL program [302]. Then, the heliostat field optical efficiency, taking into account different losses is determined with regard of the sun position (Figure 2.6(a)). The power absorbed and reflected by each individual heliostat is then calculated, considering the spectral reflectance $R_{PV}(\lambda)$ (measured over the AM 1.5D solar spectrum curve according to ASTM G173-03 [303] considering wavelength ranging between 250 and 2500 nm) of the GaAs cells [42] used as PV heliostats in the *1S* approach (see Figure 2.8) or a mean mirror reflectivity value of 90% (see Table 2.1) for the *HT* approach and conventional CSP plant. The electrical and thermal output of the PV and CSP subsystems are calculated applying a set of equations (*vide infra*) describing the optical, electrical and thermal behaviour of each strategy investigated (Figure 2.4). The annual energy output is finally calculated for six different time steps of 1, 5, 10, 15, 30 and 60 min. The following assumptions are adopted in the model:

1. The HT solar cells are supposed to be at a fixed temperature of 400 °C.

2. **GaAs** single-junction solar cells are employed in both hybrid systems.

3. The receiver is described by a set of basic parameters (temperature, absorptivity, emissivity, and convective heat loss coefficient), without specifying any particular material, geometry, or coating.

[2]Solar Position Algorithm: first introduced in [301] and later revised in [302], achieves uncertainties in the range of ±0.0003 ° for the time period from year 2000 to 6000 [302].

4. The thermophysical properties of HTFs and used materials are temperature independent.

5. No TES is considered in this first analysis. Nevertheless, the objective of the concept is obviously to store the heat energy collected by the thermal receiver to produce power after sunset.

In the following paragraphs, the model is described in detail, from the input parameters to the functioning of the three sub models.

2.1 Solar resource

The present study was carried out using ground measured data at Targassonne (42 °30N, 2°E) considering different time resolutions. THEMIS plant is located in a region

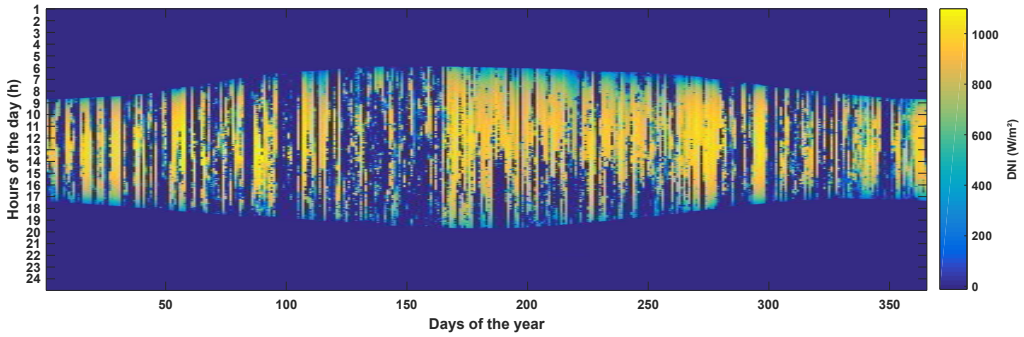

(a) DNI

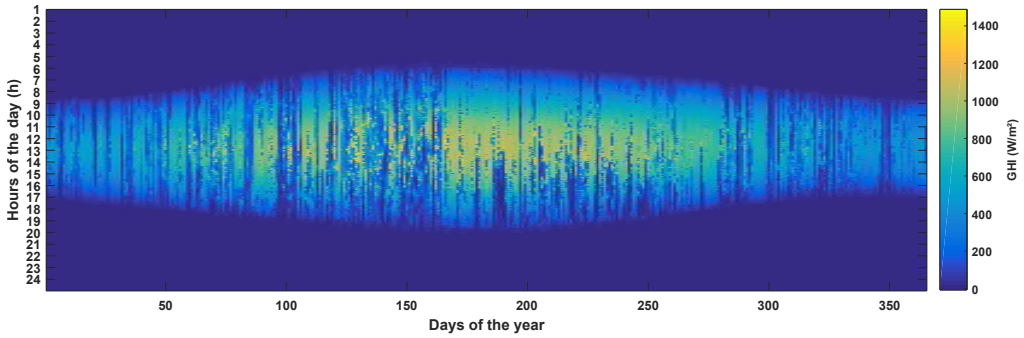

(b) GHI

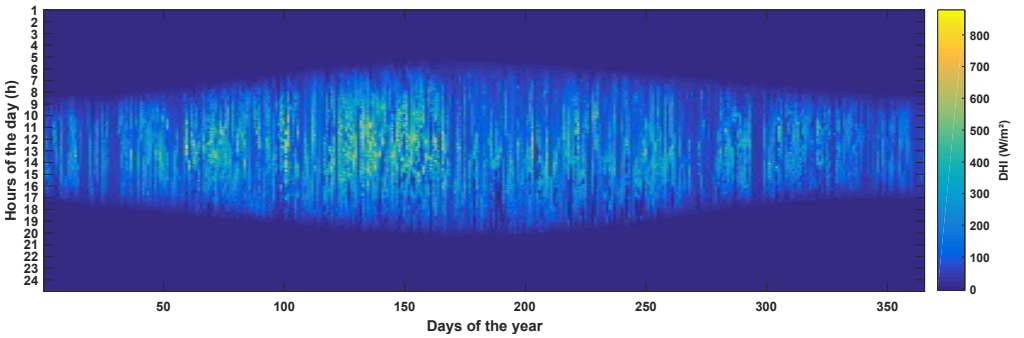

(c) DHI

Figure 2.5: Hourly (a) DNI, (b) GHI, and (c) DHI for the whole year of 2018 in Targassonne.

with low ambient temperatures on average ($\sim$ 8 °C) and low mean wind speed (which limits the time of non-operation due to excessive wind). Figure 2.5 shows hourly totals of DNI, GHI and DHI for each day of 2018. The seasonality for DNI and GHI is apparent, with shorter days and high values for the winter season. In spring, cloud covers are more common, days are longer, and radiation levels are greatly reduced. The yearly totals are 1592 kWh/m^2-year for GHI and 1785 kWh/m^2-year for DNI, a record in France [304]. The DHI resource is generally much smaller since it accounts for irradiation from the ground and reflected by the clouds.

2.2 Optical model

The instantaneous optical efficiency of the heliostat field takes into account the various loss mechanisms depicted in Figure 2.6(a), and is calculated for a given heliostat as [218]:

$$\eta_{hel} = \rho\, \eta_{tra}\, \cos\theta\, \eta_{sh}\, \eta_{blo}\, \eta_{spil} \tag{2.1}$$

where ρ refers to the heliostat reflectivity, whose value depends on the type of system considered, η_{tra} is the atmospheric transmission between the heliostat and the receiver (which is assumed equal to 1 in this study). $\cos\theta$, η_{sh}, η_{blo} and η_{spil} are the main sources of optical losses in the heliostat field: $\cos\theta$ is the cosine of the angle formed between the normal to the heliostat surface and the incident rays calculated using Eq. (4.5) as reported in [305], η_{sh} is the fraction of the heliostat surface shaded by adjacent heliostats, η_{blo} is the fraction of the reflected sunlight blocked by adjacent heliostats, and η_{spil} refers to the fraction of reflected sunlight missing the receiver due to heliostat tracking errors, unsuitable aiming strategies, etc....

As an example, Figure 2.6(b) represents the total efficiency of THEMIS heliostats field on the 21st December at noon. These results illustrate that heliostats located on both edges of the solar field are less efficient, as a consequence of their orientation relative to the receiver.

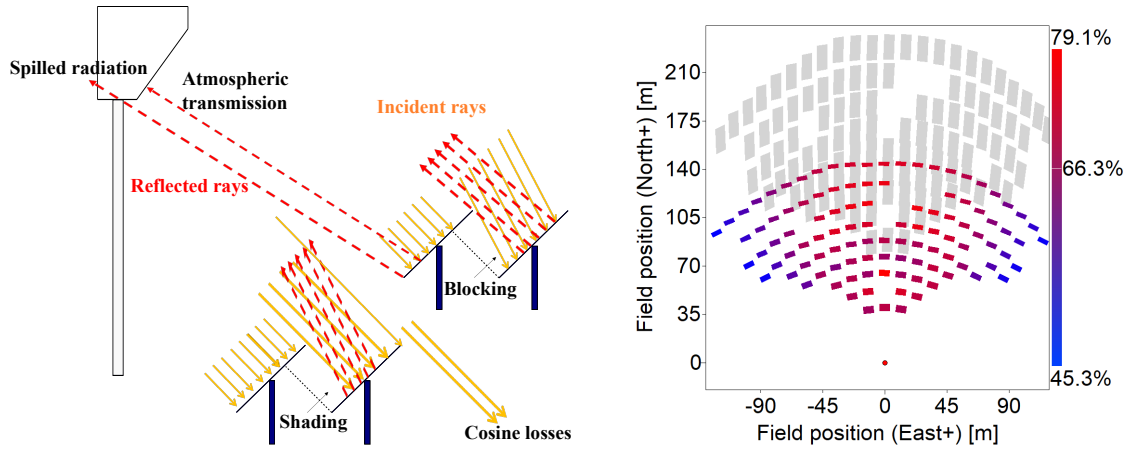

Figure 2.6: (a) Schematic description of the main optical losses of the heliostat field, (b) SolarPILOT plot showing THEMIS heliostat field overall efficiency.

For a given heliostat field configuration at a given location, the $\cos\theta$ effect depends only on the sun position in the sky by the following equation [305]:

$$\cos 2\,\theta = \sin\alpha\,\cos\lambda - \cos\alpha\,\sin\lambda\,\cos\left(\theta_H - \gamma_s\right) \tag{2.2}$$

The incident angle θ can be extracted from Eq. (4.5) as follows:

$$\theta = \cos^{-1}\left[\frac{\sqrt{2}}{2}\left(\sin\alpha\,\cos\lambda - \cos\alpha\,\sin\lambda\,\cos\left(\theta_H - \gamma_s\right) + 1\right)^{1/2}\right] \tag{2.3}$$

here α and γ_s are the solar altitude (see Eq. (A.2)) and the solar azimuth angle which, are measured clockwise on the horizontal plane from the projection of the sun's central ray to the south-pointing coordinate axis (see Eq. (A.3)). Both angles are calculated according to the solar time and the heliostat location on earth using the SPA program. λ and θ_H are respectively the heliostats target angle and the heliostats facing angle which is measured anticlockwise on the horizontal plane from the south-pointing coordinate axis to the heliostats position. The latter angles vary with heliostats position on the solar field as follow [305]:

$$\begin{cases} \lambda = \arctan\left(\dfrac{\sqrt{x_{pos}^2 + y_{pos}^2}}{z_{tower}}\right) \\ \theta_H = \arctan\left(\dfrac{y_{pos}}{|x_{pos}|}\right) \end{cases} \tag{2.4}$$

where, x_{pos}, y_{pos} and z_{tower} are the heliostat coordinate following the direct axis (x,y,z) the position of the receiver above the ground (z_{tower}) being equal to 86 m.

The identification of shading losses was carried out via Solar Power Tower Integrated Layout and Optimization Tool (SolarPILOT) software [3] [306] using as an input the heliostats positions along with the receiver characteristics. First, 11 days along the year were chosen, and for each day 23 different instants (i.e. each instant represents a particular position of the sun translated as elevation and azimuth angles) were selected as shown in Figure 2.7. The selected points encapsulate the path of the sun throughout the year at Targassonne. For the 253 (11 x 23) data points the shading losses of each heliostat on the solar field were identified and stored in a text file. Then, the shading losses at each instant of the year were estimated using a built-in Matlab interpolation function. The use of the interpolation function can be justified by the fact that manual entry of values takes a considerable amount of time. For example, entering the 253 data points took an average of about half an hour, as it is necessary to verify that the selected hours are sufficient to describe the sun's path at a given date. Furthermore, since the calculations were performed with different time resolutions, it would be both inefficient and time-consuming to carry out this process by hand. More importantly,

[3] A software package developed by the NREL to generate solar field layouts and characterizes the optical performance of CSP tower systems.

using a theoretical formula will introduce additional parameters to be calculated in the algorithm and thus increase the time of the calculations, which already range from 2 hours to 5 days with 60 minute and 1-minute time resolution, respectively.

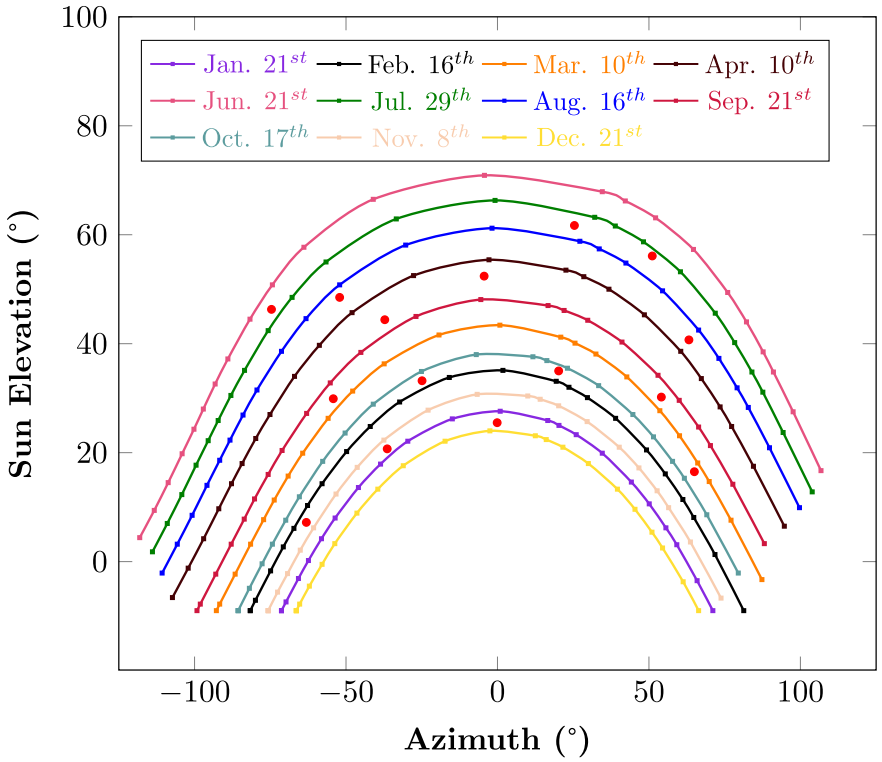

Figure 2.7: The sun course at Targassonne described as the variation of the elevation angle as a function of the azimuth angle at 253 different data-points over the year 2018. Eleven days for eleven months out of the twelve and considering 23 different moment each day, that represent different hours during the same day.

Therefore, to verify the accuracy of the values obtained via the interpolation function, we calculated the relative difference between interpolated values and those obtained with SolarPILOT. To do this, we considered 15 different data points over the year represented by the red dots in Figure 2.7 and summarized in Table 2.2. The selected data points have the particularity of being located between the 11 continuous plots representing different days in Figure 2.7. The reason for that is that the interpolation function will guarantee a very high prediction of the shading losses of data points located on the lines, whereas important differences may occur when the data points are in-between the lines. As can be seen in Table 2.2 the relative difference is overall lower than 1%. The initial data points were increased from 153 to 253 to reduce the relative difference and raise the capability of the interpolation function to predict shading losses over the whole year.

Table 2.2: The mean shading loss and relative difference between SolarPILOT values and the interpolation function over the whole heliostat field (data: year 2018).

	SolarPILOT	**Interpol. Funct**	**Relative difference (%)**
March 5^{th}	0.845	0.844	0.12 %
May 10^{th}	1.000	1.000	0.00 %
July 20^{th}	1.000	1.000	0.00 %
November 15^{th}	0.972	0.965	0.72 %
April 21^{st}	1.000	1.000	0.00 %
May 5^{th}	1.000	1.000	0.00 %
January 10^{th}	0.984	0.983	0.10 %
March 15^{th}	0.827	0.829	0.24%
October 20^{th}	1.000	1.000	0.00 %
August 25^{th}	1.000	1.000	0.00 %
February 20^{th}	1.000	1.000	0.00 %
September 28^{th}	0.973	0.975	0.21 %
September 15^{th}	0.995	1.000	0.50 %

2.2.1 *1S* approach

In this strategy, the heliostat reflectivity is calculated as the ratio between 1) the power reflected by the PV heliostat, computed as the integration of the spectral reflectivity of the PV mirrors multiplied by the spectral distribution of sunlight over the solar range (250 - 2500 nm) and 2) the total solar power impinging the heliostats (i.e. the integration of the spectral distribution of sunlight over the solar range) (see Figure 2.8):

$$\rho_{1S} = \frac{\int_{250}^{2500} R_{PV}(\lambda) f(\lambda) d\lambda}{\int_{250}^{2500} f(\lambda) d\lambda} \tag{2.5}$$

where $f(\lambda)$ refers to the spectral distribution of the incoming sunlight (λ being the wavelength of solar radiation, expressed in nm).

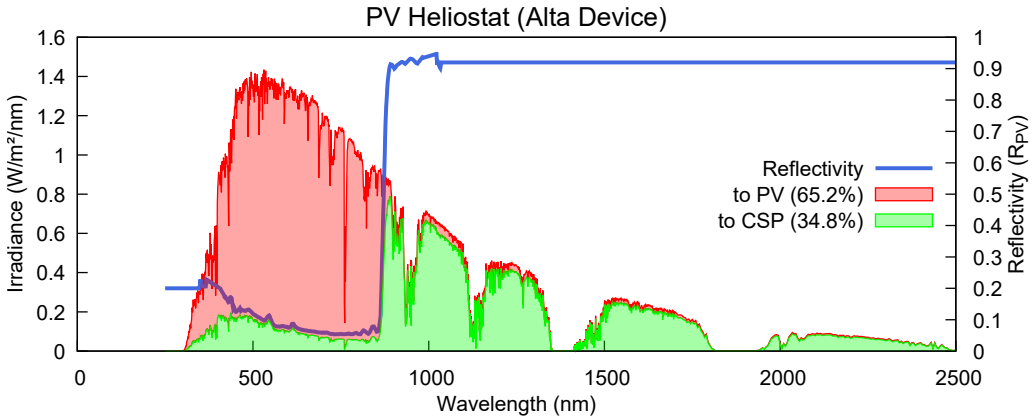

Figure 2.8: Measured spectral reflectance of GaAs solar cell (blue: cell reflectivity [42], red: power absorbed by PV, green: power sent to CSP).

It is important to mention that there is no spectral variation considered in this study, we only considered using the AM1.5G spectral distribution according to ASTM G173-03 [303].

The optical flux sent onto the thermal receiver by the heliostat field is calculated as the sum of the optical flux sent by each PV heliostat. The total optical flux at a given time t can then be computed as:

$$P_{rec,\ 1S}(t) = \sum_{i=1}^{N_{hel}} \eta_{hel,\ 1S}(t)\, S_{hel}\, DNI(t) \tag{2.6}$$

2.2.2 *HT* approach

For both the *HT* approach and the conventional CSP plant, the reflectivity of each heliostat is taken equal to the mirror reflectivity given in Table 2.1:

$$\rho_{HT} = \rho_{CSP} = \rho_{Mir} \tag{2.7}$$

The total optical flux sent onto the receiver is calculated as:

$$P_{rec,\ HT}(t) = P_{rec,\ CSP}(t) = \sum_{i=1}^{N_{hel}} \eta_{hel,\ Mir}(t)\, S_{hel}\, DNI(t) \tag{2.8}$$

2.2.3 Model validation

As no experimental data are available for the proposed whole system at the current stage, the validation of the model is done separately for the PV and CSP subsystems. The optical efficiency of the original THEMIS plant (including 201 heliostats and a four m side-squared receiver) was estimated with SolarPILOT and compared to the optical efficiency measured on-site March 21st 2018 at noon [287]. The simulated optical efficiency was found equal to 0.82 in comparison to 0.84.

2.3 Electrical model

For a precise estimation of the PV output of a system, one has to take into account the temperature and illumination dependence of the PV technology used. In the detailed balance limit [307, 308], the current-voltage curve of an ideal PV cell can simply be computed using equation (1.12) given in chapter 1:

$$J(V) = J_{ph} - J_0 \left[\exp\left(\frac{q\,(V + J\,R_s)}{n\,k_B\,T_{cell}}\right) - 1\right] - \frac{V + J\,R_s}{R_{sh}} \tag{2.9}$$

The radiative recombination current density is calculated in the detailed balance limit as [307]:

$$J_0(V) = \frac{2\,\pi}{h^3\,c^2} \int_{E_g}^{\infty} \frac{E^2\,dE}{\exp\left(\dfrac{E - \mu}{k_B\,T_{cell}}\right) - 1} \tag{2.10}$$

where h and k_B are respectively the Planck and Boltzmann constants, c the speed of light and E_g the bandgap of the PV cell used. E refers to the energy of photons, while T_{cell} is the temperature of the PV cells, whose value is a function of the strategy considered. μ is the chemical potential.
Rewriting Eq. (1.3) with consideration of (EQE = 1) and under concentration the J_{ph} can be expressed as:

$$J_{ph} = q\,X \int_{E_g}^{\infty} f(E)\,dE \tag{2.11}$$

Because of the wide range of operating temperatures considered in this work, one has to take into account the temperature dependence of the bandgap, which can be described by the following equation [136]:

$$E_g(T) = E_g(0\text{ K}) - \frac{\alpha^{'}\,T_{cell}^2}{T_{cell} + \beta'} \tag{2.12}$$

where $E_g(0)$ is the bandgap energy at 0 K and $\alpha^{'}$ and $\beta^{'}$ are material dependent constants, whose values are reported in Table 2.3.
The bandgap for semiconductor alloys can be determined by the following linear superposition [309]:

$$E_g(A_{1-x}B_x) = (1-x)\,E_g(A) + x\,E_g(B) - x\,(1-x)\,P \tag{2.13}$$

here $A_{1-x}B_x$ is the alloy composition and P (eV) is an alloy dependent parameter that accounts for deviations from the linear approximation. Table 2.3 summarizes a set of parameters used to identify the bandgap energy of different alloy composition based on GaAs, GaP and InP.

Table 2.3: Bandgap parameters of the cell technologies used in the *HT* hybrid approach.

Parameters	**GaAs** [136]	**GaP** [309]	**InP** [309]
$E_g(0\text{ K})$ (eV)	1.519	2.350	1.424
$\alpha^{'}$ (eV/K)	5.405×10^{-4}	5.771×10^{-4}	3.63×10^{-4}
$\beta^{'}$ (K)	204	372	162
P (eV)	—	0.65	
R_s ($\Omega\,\text{cm}^2$)		0	

Finally, the PV efficiency is calculated as the ratio between 1) the maximum electrical power extractable from the PV cell (referred to as the maximum power point given in Eq. (1.9)) and 2) the incident solar power P_{in} absorbed by the PV receiver , the value of which is a function of the strategy considered:

$$\eta_{PV} = \frac{V_{mpp} \times J_{mpp}}{P_{in}} \tag{2.14}$$

Providing a realistic estimate of the electric production of the PV modules rather than an idealized one requires this model to be altered to better describe the different ranges of temperature and illumination.

2.3.1 *1S* approach

The PV output in the *1S* approach is calculated assuming that the PV efficiency is independent of the DNI (a specific calculation shows that the gap in PV efficiency between the extreme DNI values throughout the year, ranging from 300 W/m^2 to 1094 W/m^2, is less than 0.1 % absolute). The temperature dependence of the PV cell efficiency is estimated applying the following equation [218]:

$$\eta_{1S}(T_{cell}) = \eta_{ref}\ [1 + \beta_{ref}\,(T_{cell}(t) - T_{ref})] \tag{2.15}$$

where η_{ref} refers to the reference PV efficiency in standard test conditions (STC) (25 °C and 1 sun illumination), calculated by solving Eq. 2.14, β_{ref} is the GaAs temperature coefficient, while T_c and T_{ref} are the cell and reference temperatures. The cell temperature is calculated as a function of the meteorological parameters, namely GHI, ambient temperature and wind speed, using [310]:

$$T_{cell}(t) = T_{amb}(t) + (T_{NOCT} - T_{a,NOCT})\,\frac{GHI(t)}{G_{NOCT}}\,\frac{U_{NOCT}}{U(t)}\left(1 - \frac{\eta_{1S}(T_c)}{\tau\,\alpha}\right) \tag{2.16}$$

where T_{amb} is the ambient temperature, $(\tau\,\alpha)$ is the effective transmittance-absorptance of the PV module, U the heat transfer coefficient calculated using the equation reported in Table 2.4 where v_{wind} is the wind speed, GHI the global irradiation, U_{NOCT} and G_{NOCT} the heat transfer coefficient and the global irradiation at the nominal operating cell temperature (NOCT) given in Table 2.4.

Table 2.4: Main parameters of the PV cell used in the *1S* hybrid approach.

Reference operating conditions	**GaAs**	**InGaP**
Temperature coeff. of power, β_{ref}	-0.08 (%/K) [311]	-0.02 (%/K) [44]
Reference temperature, T_{ref}	25 °C	
U= $5.67 + 3.86\,V_{wind}$		
$\tau\,\alpha$	0.8 [217]	
NOCT conditions [312]		
T_{NOCT} = 46 °C	T_{NOCT} = 20 °C	
U_{NOCT} = 9.53 W/m^2 K	G_{NOCT} = 800 W/m^2	

By replacing η_{1S} expression in Eq. 2.16 we obtain:

$$T_{cell}(t) = \frac{T_{amb}(t) + (T_{NOCT} - T_{a,NOCT})\,\frac{GHI(t)}{G_{NOCT}}\,\frac{U_{NOCT}}{U(t)}\,\left[1 - \frac{\eta_{ref}}{\tau\,\alpha}\,(1 - \beta_{ref}\,T_{ref})\right]}{1 + \frac{\eta_{ref}\,\beta_{ref}}{\tau\,\alpha}\,(T_{NOCT} - T_{a,NOCT})\,\frac{GHI(t)}{G_{NOCT}}\,\frac{U_{NOCT}}{U(t)}} \tag{2.17}$$

A precise estimation of the solar resource impinging each heliostat should take into account that 1) each heliostat does not strictly face the sun but is rather positioned at mid-angle between the sun and the receiver located at the top of the tower 2) PV heliostats offer the inherent advantage of converting a fraction of diffuse sunlight, which is a function of the panel orientation and the DHI. The total PV power generated at a given time t can thus be calculated as:

$$P_{PV,\ 1S}(t) = \sum_{i=1}^{N_{hel}} \zeta_{SQ,\ 1S}\,\eta_{1S}(t)\,[P_{dir}(t) + P_{dif}(t)] \tag{2.18}$$

where $\zeta_{SQ,\ 1S}$ translates the ability of a given cell technology to approach its own theoretical limit [313], and will be detailed in section 2.3.3.

The direct solar power impinging each individual PV heliostat can then be written:

$$P_{dir}(t) = S_{hel}\,cos\theta(t)\,\eta_{blo}(t)\,\eta_{sh}(t)\,DNI(t) \tag{2.19}$$

Whereas, the diffuse solar power intercepted by each heliostat at a given time t is [314]:

$$P_{dif}(t) = \frac{[1 + cos\beta(t)]}{2} S_{hel} DHI(t) \tag{2.20}$$

where β is the angle formed between the normal to each individual heliostat and the ground given in Eq. (2.21) [315].

$$\sin\beta = \frac{(z_{tower} - z_{pos}) + \sin\alpha}{2\,\cos\theta} \tag{2.21}$$

here, z_{pos}, α and θ are the heliostat height from the ground, the sun elevation and the incident angle, respectively.

2.3.2 *HT* approach

The *HT* strategy implies radically different operating conditions for the PV cells: the cell temperature is assumed constant and equal to 400 °C. Practically, adjusting the HTF flow rate to the incoming concentrated solar power should allow this condition to be satisfied [283]. Additionally, the temperature dependence of PV cell properties has been shown to reduce significantly with increasing sunlight concentration, relaxing the need for a rigorous temperature dependence formalism accounting for the variations in the operating temperature the PV receiver may be exposed to in reality [116, 118].

The PV efficiency in the *HT* approach is thus calculated as a function of temperature and sunlight concentration solving Eq. (2.14), assuming a cell temperature of 400 °C and a concentration ratio of sunlight given by:

$$X(t) = \frac{P_{rec,\ HT}(t)}{1000 \times S_{rec}} \tag{2.22}$$

For the *HT* strategy, the optical flux sent onto the receiver is used to quantify the concentration level in Eq. (2.22), which is then used to compute the PV output. The PV output power is finally calculated as:

$$P_{PV,\ HT}(t) = \zeta_{SQ,\ HT}\, \eta_{HT}(t)\, \eta_{th}(t)\, P_{rec,\ HT}(t) \tag{2.23}$$

where η_{th} is the thermal efficiency, which will be described in more detail in section 2.4, while $\zeta_{SQ,\ HT}$ translates the ability of a realistic *HT* cell technology to approach its own theoretical limit.

2.3.3 From ideal to realistic solar cells

Realistic PV cells are likely to be affected by several limiting mechanisms (series resistance losses, non-radiative recombination, imperfect absorption...) precluding them to achieve the ideal efficiency derived previously in the radiative limit. To better account for these losses, we choose to alter the PV model by introducing a corrective coefficient, referred to as ζ_{SQ}, translating the ability of a given cell technology to practically approach its own theoretical limit [313]:

$$\zeta_{SQ} = \frac{\eta_{PV,\ exp}}{\eta_{PV,\ SQ}} \tag{2.24}$$

where $\eta_{PV,\ exp}$ is a realistic efficiency value measured experimentally, while $\eta_{PV,\ SQ}$ is the theoretical upper limit for the corresponding PV cell technology [12].
This fixed parameter is thus used as a way to quantify how a particular cell technology will deviate from the ideal PV efficiency, because of internal loss mechanisms (the dependence to external operating conditions, such as temperature or illumination, being taken into account in the model, as described previously). Typical values of ζ_{SQ} may vary considerably, depending on the cell technology or the operating conditions to which the cells are submitted experimentally. On the one hand, GaAs has been proven to experimentally reach very high conversion efficiencies, currently exceeding 29% under 1 sun conditions [299], making this cell technology a good candidate for approaching unity values of ζ_{SQ} under one-sun operation. On the other hand, experimental data regarding the high-temperature operation of GaAs cells remain scarce, and the rare experimental characterizations of comparable cell technologies show ζ_{SQ} values of ~ 0.35 [116, 118]. To explore the impact of the PV cell efficiency on the performance of the hybrid system, we thus select 3 different values of ζ_{SQ} for each strategy considered, corresponding to 3 operational scenarios. Because there is a huge gap in

the industrial maturity of these cell technologies (high-temperature solar cells are still in their infancy, while conventional 1 sun GaAs solar cells have benefited from decades of research and development, culminating with the 29.1% world-record efficiency for single-junction solar cells), the ζ_{SQ} value associated with each of these scenarios varies depending on the strategy considered:

- **Optimistic scenario**:
  - *1S approach*: The PV efficiency is supposed to be equal to the record GaAs *cell* efficiency reported in the literature [102], leading to ζ_{SQ} of 0.9.
  - *HT approach*: We assume a similar ζ_{SQ} value of 0.9, with a corresponding experimental efficiency of $\sim 30\%$.
- **Realistic scenario**:
  - *1S approach*: The PV efficiency is supposed to be equal to the record GaAs *module* efficiency reported in the literature [103], leading to ζ_{SQ} of 0.76.
  - *HT approach*: We assume $\zeta_{SQ} = 0.65$, a median value between the optimistic and pessimistic ζ_{SQ} values considered in this work.
- **Pessimistic scenario**:
  - *1S approach*: The PV efficiency is taken equal to the experimentally measured efficiency of large dimension SunPower Silicon flat panels [103]. This scenario thus accounts for a possible degradation in the typical efficiency of mass-produced, large-scale PV modules, leading to ζ_{SQ} of 0.7.
  - *HT approach*: We assume the use of *HT* PV cells with efficiencies equivalent to the one reported in previously published experimental work [116, 225], leading to a ζ_{SQ} value of 0.4.

The ζ_{SQ} indices associated with each scenario considered are reported in Table 2.5, together with the corresponding experimental efficiencies.

Table 2.5: Summary of the ζ_{SQ} values considered in this work for the two hybrid strategies investigated, considering GaAs solar cells.

1S approach	$\zeta_{SQ,\ 1S}$	$\eta_{PV,\ exp}$	Reference	$\eta_{PV,\ SQ}$	Reference
Optimistic scenario	0.9	29.3%	[102]		
Realistic scenario	0.76	25.1%	[103]		
Pessimistic scenario	0.7	22.8%	[103]		
				33.3%	[316]
HT approach	$\zeta_{SQ,\ HT}$	$\eta_{PV,\ exp}$	Reference		
Optimistic scenario	0.9	29.7%	”		
Realistic scenario	0.65	21.45%	”		
Pessimistic scenario	0.4	13.2%	[116, 225]		

2.3.4 Model validation

For the PV subsystem, the model validation was conducted on the PV parameters used for both hybrid technologies. Considering the optimistic scenario reflecting the operation of *state-of-the-art* GaAs PV cells from Alta Devices and an ambient temperature of 25 °C, the difference between the experimental efficiency (29.1%) [102] and simulated efficiency (29.4%) was found to be equal to -1.02%. The *1S* PV efficiency is thus coherent with recent measurements on advanced PV cells.

A second validation was performed on the open-circuit voltage of the cell. The electrical validation was conducted for GaAs and AlGaInP solar cells. The V_{oc} for both GaAs and AlGaInP technologies considered in this work were calculated assuming an illumination equivalent to 500 suns and an operating temperature of 400 °C. The calculated values, reported in Table 2.6 show a good agreement with the experimental measurement performed by Perl et al. in similar conditions [317].

Table 2.6: Validation of the electrical model under 400 °C and 500 suns.

Parameter	Cell technology	Model	Experimental [317]	Deviation
V_{oc} (V)	GaAs	0.655	0.67	2.3%
	AlGaInP	0.92	0.93	1.1%

2.4 Thermal model

The thermal exchanges are modelled assuming convective and radiative heat losses between the receiver surface and the environment (the other sides of the receiver are supposed to be perfectly insulated, and the heat conduction losses are neglected). The thermal efficiency of the receiver is calculated as [14]:

$$\eta_{th}\, P_{rec}(t) = \alpha\, P_{rec}(t) - P_{loss} \tag{2.25}$$

$$\eta_{th}(t) = \alpha - \frac{\overbrace{\varepsilon\, \sigma\, S_{rec}\, (T_{rec}^4 - T_{sky}^4)}^{P_{rad}} + \overbrace{h_{conv}\, S_{rec}\, (T_{rec} - T_{ref})}^{P_{conv}}}{P_{rec}(t)} \tag{2.26}$$

where P_{loss} is the power loss due to convection and radiation ($=P_{conv} + P_{rad}$), α, ε and σ are the absorptivity, the surface emissivity of the thermal receiver, and Stefan-Boltzmann constant, while h_{conv} is the convective heat transfer coefficient, computed using the physical properties of air [298], and T_{sky} is the sky temperature (calculated as $= 0.0552\, (T_{amb})^{1.5}$ [318]). If the numerator of this equation is basically independent upon the strategy considered, the thermal efficiency is also function of the optical flux sent onto the receiver by the heliostats field. Consequently, η_{th} will necessarily vary significantly depending on the approach investigated, the optical flux in the *1S* strategy ($P_{rec,\ 1S}$) is noticeably lower than the corresponding optical fluxs in the *HT* ($P_{rec,\ HT}$) and conventional CSP approaches ($P_{rec,\ CSP}$).

Due to the constantly variable nature of the DNI, the operation considers the limitations of starting up the receiver through a set of control parameters:

1. A minimum DNI value is required, set at 300 W/m^2 [319], along with positive values of the sun elevation,

2. A minimum thermal power is required for the turbine to operate, set at 30% of the receiver thermal power available at Spring equinox (see Eq. (2.27)), March 21st 2018 at noon [319].

$$P_{mim\ pb,\ 21March} = 0.3\, P_{nom\ pb,\ 21March} \tag{2.27}$$

where, $P_{nom\ pb,\ 21March}$ is the nominal thermal power available at the PB on March 21st 2018, given as follows:

$$P_{nom\ pb,\ 21March} = \eta_{pb}\, P_{th\ utile,\ 21March} \tag{2.28}$$

where $P_{th\ utile,\ 21March}$ is expressed using Eq. (A.7).
Table 2.7 summarizes different values of power calculated on March 21st 2018 at noon for both hybrid technologies and the standalone CSP plant, more details are given in Appendix A. As can be seen, the size of the turbine is highly dependent on the amount of energy impinging the receiver. As a result, the turbine of the *1S* strategy is the smallest since more than half of the energy output available for the heliostat field

is first used by the PV heliostats, and only the remaining fraction can be converted effectively into heat at the top of the tower.

Table 2.7: The different power output computed March 21st 2018 at noon.

	1S	*HT*	Conven. CSP
$P_{rec,\ 21March}$ (kW)	1920		4967
$P_{th\ utile,\ 21March}$ (kW)	1743	4312	4685
$P_{nom\ pb,\ 21March}$ (kW)	650	1607	1746
$P_{mim\ pb,\ 21March}$ (kW)	195	482	524

The electrical power generated by the turbine is calculated assuming a turbine operating at 2/3 of the Carnot limit (an assumption practically describing the operation of realistic turbines over a wide range of CSP-relevant temperatures [44, 182, 262, 320, 321]). The Carnot efficiency η_{Carnot} is calculated based on the thermal stream operating temperature T_{rec} and assuming a constant cold reservoir temperature T_{ref} of 25°C:

$$\eta_{Carnot} = 1 - \frac{T_{ref}}{T_{rec}} \tag{2.29}$$

The electrical power generated by the turbine can be estimated for the *1S* and CSP approaches using Eqs. (2.30) and (2.31):

$$P_{CSP,\ 1S}(t) = \frac{2}{3}\,\eta_{Carnot}\,\eta_{th}(t)\,P_{rec,\ 1S}(t) \tag{2.30}$$

$$P_{CSP,\ CSP}(t) = \frac{2}{3}\,\eta_{Carnot}\,\eta_{th}(t)\,P_{rec,\ CSP}(t) \tag{2.31}$$

The use of an integrated receiver in the *HT* strategy requires the PV power produced by the *HT* receiver to be subtracted from the optical flux sent by the heliostats field in order to estimate the thermal power, as described in Eq. (2.32):

$$P_{CSP,\ HT}(t) = \frac{2}{3}\,\eta_{Carnot}\,\left[\eta_{th}(t)\,P_{rec,\ CSP}(t) - P_{PV,\ HT}(t)\right] \tag{2.32}$$

2.5 Annual Energy calculation

The energy flows associated with the different contributions discussed previously are simply calculated as a summation over a whole year:

$$Q_i = \sum_{t=1}^{t=K_t} P_i(t)\,\delta(t) \tag{2.33}$$

where P_i refers to the power associated with the parameter of interest at a given time t, $\delta(t)$ is the time step (either 1 or 5 minutes) and K_t is the total number of time steps over the year (K_t=525600 for $\delta(t) = 1$ min, 105120 for $\delta(t) = 5$ min).
The disparity observed in the results being systematically less than 2 %, and because of the significant increase in the calculation time associated with the 1 min time-step (from ∼1.5 days per calculation with a 5 min time-step against ∼5 days with a 1 min time-step), we select a default time resolution of 5 minutes in the rest of this work. The nature of the solar plant considered in this study precludes any global validation of the model since 1) THEMIS power plant was used as a solar facility delivering electricity to the grid but no operation data is available that would have allowed a direct solar-to-electricity validation 2) the key components of the hybrid strategies investigated here are currently not mature enough for being integrated in an operational power plant.

3 Results & Discussions

Results presented in the following section describe the influence of various design parameters on the annual and daily output performances of the two PV-CSP *compact* hybrid plants in comparison to a standalone CSP technology.

3.1 Yearly performances

3.1.1 Impact of cell performances

Figure 2.9 shows the distribution of the annual energy output for the two-hybrid systems as well as for the conventional CSP plant, and for the 3 operational scenarios described above.

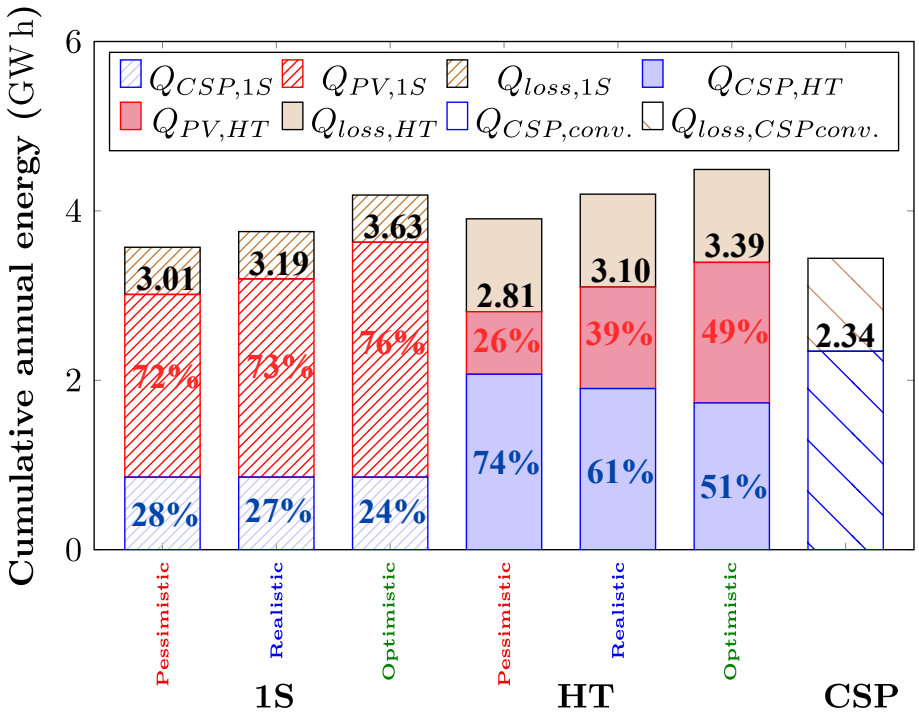

Figure 2.9: Annual cumulative energy production for the two hybrid approaches & the conventional CSP plant, considering the pessimistic, realistic, and optimistic operation scenarios all at a constant temperature of 400 °C.

Regardless of the operational scenario considered, we observe a noticeable difference between the energy output of the hybrid strategies, and the energy output of the CSP conventional plant, with a relative gain in energy ranging from 20% (in the case of the *HT* approach in the pessimistic scenario) to 55% (*1S* approach in the optimistic scenario). These numbers confirm the intrinsic superiority of the two *compact*-hybrid approaches investigated over conventional CSP plant, owing to the increased capacity of the *1S* approach to convert diffuse radiation (the extra-energy output associated with the conversion of diffuse solar radiation representing $\sim$ 414MW h (14%) over a full-year operation), and the improved ability of the *HT* approach to efficiently use high-energy photons (that are commonly wasted as heat and rejected to the environment, in conventional PV systems).

The two-hybrid strategies demonstrate opposite trends regarding the share between PV and CSP production, suggesting that the nature of the PV cells, the operating conditions to which they are exposed, and their ability to practically approach their own theoretical limits, has tremendous effects on the performance of the hybrid systems. Increased PV efficiency obviously leads to higher system performance, independent of the hybrid technology considered. However, in the *1S* strategy, the improvement in the PV cell efficiency induces a net increase in the PV output without affecting the CSP operation, which translates into very modest changes in the share between PV and CSP depending on the operational scenario considered. Conversely, the improvement in the PV cell efficiency in the *HT* approach simultaneously leads to a net increase in the power output, together with a significant change in the balance between the energy output of the two converters. This speculative scenario is based upon a dramatic improvement in the *HT* cell technology and will require numerous technological and scientific barriers (that will be discussed in detail in the final section) to be overcome. It should also be stressed that the amount of thermal losses at the receiver level appears to be significantly lower in the *1S* strategy, as a consequence of the prevalence of reflection losses, that scale proportionally to the optical flux sent to the receiver.

3.1.2 Impact of cell technology

The choice of the PV cell technology may alter dramatically these first conclusions, the amount of optical flux absorbed by each converter (in the *1S* approach) or the PV temperature dependence (in the *HT* approach) being correlated to the electronic gap of the PV cell. Figure 2.10 show the energy fluxes associated with the two-hybrid

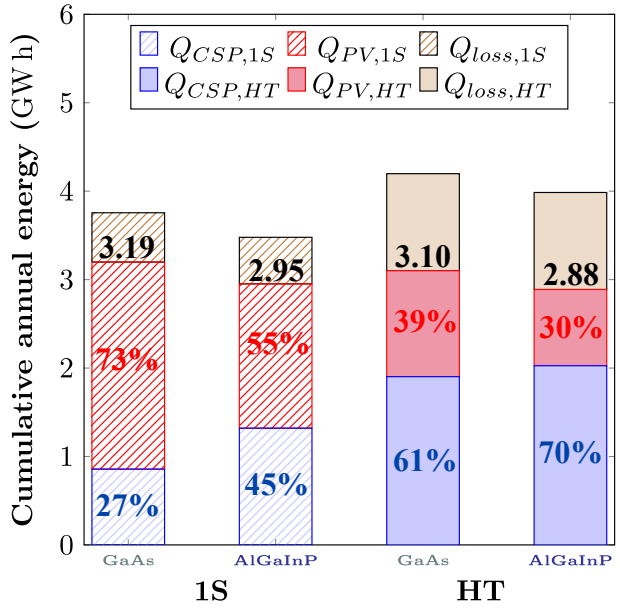

Figure 2.10: Annual cumulative energy production for the two hybrid approaches, considering the realistic operation scenario, and for two different cell technologies.

strategies assuming AlGaInP solar cells as PV converters, and considering a realistic operational scenario (with ζ_{SQ} values estimated following similar assumptions as the ones formulated in the case of GaAs (see Table A.2 for the exact numerical values,

as well as the corresponding references supporting them)). For improved clarity, the energy shares associated with hybrid plants involving GaAs solar cells are also represented. The numerical values corresponding to the energy fluxes in the pessimistic and optimistic scenarios are reported in Table A.3.

If opting for a high-bandgap material as PV cell technology in the *1S* approach leads to an improved balance in the energy output of each converter, it is worth noticing that the total energy delivered by the system is noticeably lower in comparison with hybrid systems involving GaAs solar cells. In the *HT* approach, the use of high-bandgap cells deteriorates both the total energy output of the system and the balance between CSP and PV, relative to the GaAs case, suggesting that the improved temperature resistance of such material does not allow counterbalancing its fundamentally lower efficiency under 1 sun condition.

3.1.3 Impact of the HTF outline temperature

The operating temperature of the thermal receiver constitutes a key parameter, affecting the amplitude of thermal losses, the turbine efficiency, as well as the PV output in the *HT* approach involving a PV module acting as a thermal receiver. Figure 2.11 shows the different energy fluxes associated with the three strategies investigated, considering a turbine inlet temperature of 300, 400 and 500 °C, and assuming a realistic operational scenario (the numerical values for the other operational scenarios being reported in Table A.3).

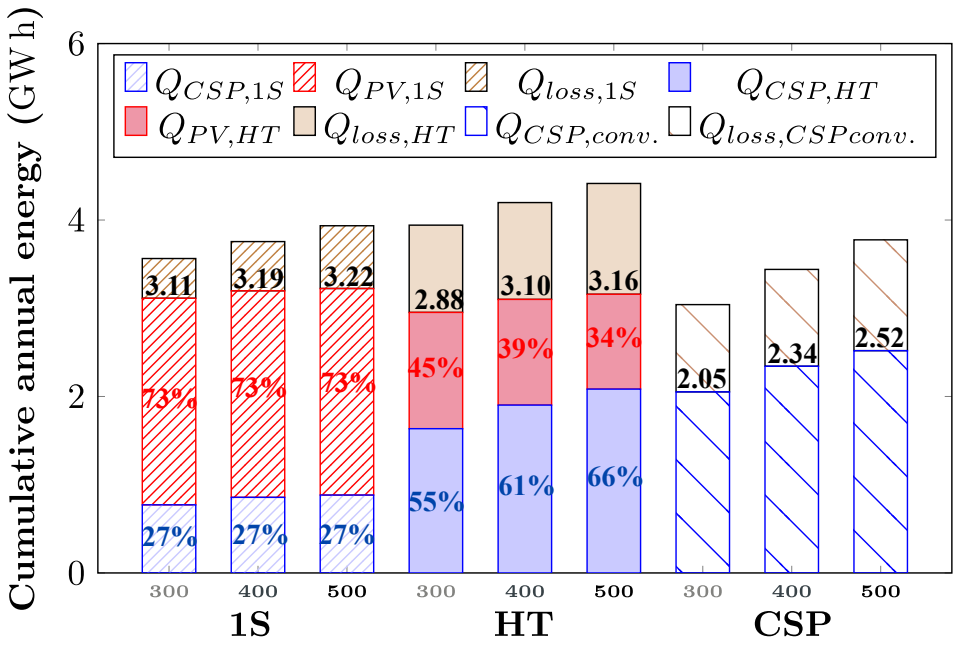

Figure 2.11: Annual cumulative energy production for the two hybrid approaches & the conventional CSP plant, in the realistic operation scenario, and for different temperature of the HTF.

Overall, the energy output for the three systems considered here increases steadily with increasing temperature. However, the temperature dependence of the energy out-

put changes noticeably depending on the approach: while conventional CSP plants show an improvement in the energy output approaching 23% between 300 and 500 °C, the net gain in energy output appears to be far more modest with the two-hybrid approaches (respectively 3.5 and 7% with the *1S* and *HT* strategies).

As a result, the benefit associated with *compact*-hybrid strategies over the conventional CSP plant decreases as the operating temperature is increased (the net gain in energy between *compacts* and CSP plants shifting from ∼50% to less than 25% in this temperature range). The underlying reasons explaining these trends are however different: the global temperature dependence of an integrated PV-CSP receiver stems from the competing temperature dependence of the PV and CSP converters: while the efficiency of the thermal converter increases with turbine inlet temperature, the PV output drops, principally because of the detrimental effect of temperature on V_{oc}, resulting in a less favorable temperature dependence relative to the conventional CSP plant. On the contrary, the decoupling between PV and CSP in the *1S* approach does not induce any penalty in the PV output for increasing turbine inlet temperature. However, the use of PV heliostats in the *1S* approach implies that only a fraction of the incident solar power is sent onto the receiver: the gain in the energy output with increasing temperature thus scales with the fraction of the incident power absorbed by the thermal receiver.

3.1.4 Variation of the annual production with DNI resource

Figure 2.12 shows the electric energy output production of the three strategies investigated here, as a function of the DNI value and over a year, in Targassonne.

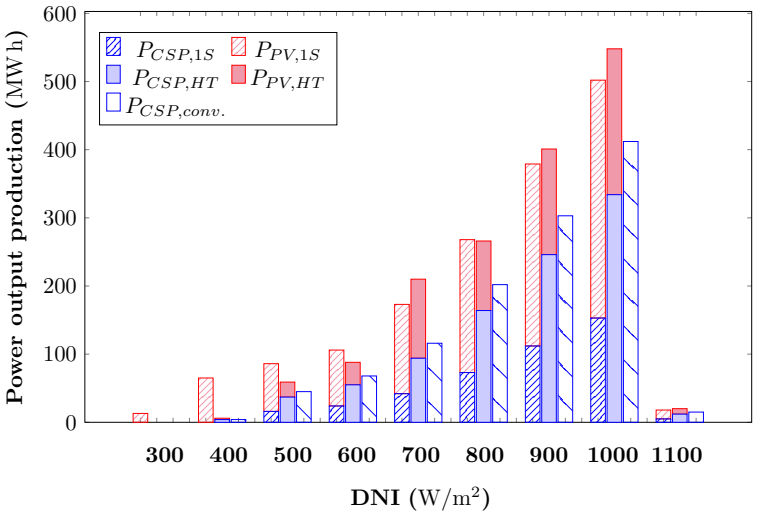

Figure 2.12: Variation of the power output with the DNI for the three strategies considered.

As can be seen, the electrical output changes consistently with the solar irradiance value: the higher the DNI, the higher the fraction of the total electrical energy produced by the CSP converter. However, at low DNI values, the CSP production remains very

low or even absent, as the power production of a CSP plant is highly dependent on the amount of DNI resource available for the HTF. A problem that equally affects the *HT* approach and the standalone CSP plant, whereas the *1S* strategy may overcome these conditions in locations with high DHI resources. As such, this suggests that the distribution of a particular site's DNI over a year should provide valuable insight into the most appropriate hybrid strategy to implement in a given location.

3.2 Daily performances

Two types of days were chosen to compare the operation of the two-hybrid plants regarding the conventional CSP plant using 60 minutes as a time step. Due to the absence of any TES facility and the fact that the studied systems are not engaged to supply a given amount of power during the day, the impact of time resolution on the behaviour of the two-hybrid technologies in comparison to the conventional plant is irrelevant as discussed by Zurita and al. [197].
To better visualize the impact of time steps on the input parameters, Figure D.4 shows the three components of the solar irradiance, DNI, GHI and DHI, using two time steps 5 min (Figures 2.13(a) and 2.13(b)) and 60 min (Figures 2.13(c) and 2.13(d)) at Targassonne. These data are plotted for a clear-sky day (April 17^{th}) with high levels of DNI with a maximum DNI of 1034 W/m^2, and a cloudy day (June 17^{th}) characterized by rapid and abrupt variations of the DNI, with a consequent drop during some hours in the mid-afternoon from 850 W/m^2 to 416 W/m^2. In the case of a clear-sky day, an increase of the time resolution has a negligible impact on the variation of the solar components profiles (Figures 2.13(a) and 2.13(b)). However, for a cloudy day, the increase of the time step results in a smoother profile for the three solar components (Figure 2.13(d)) that will highly impact the operation of the thermal receiver and the TES unit.

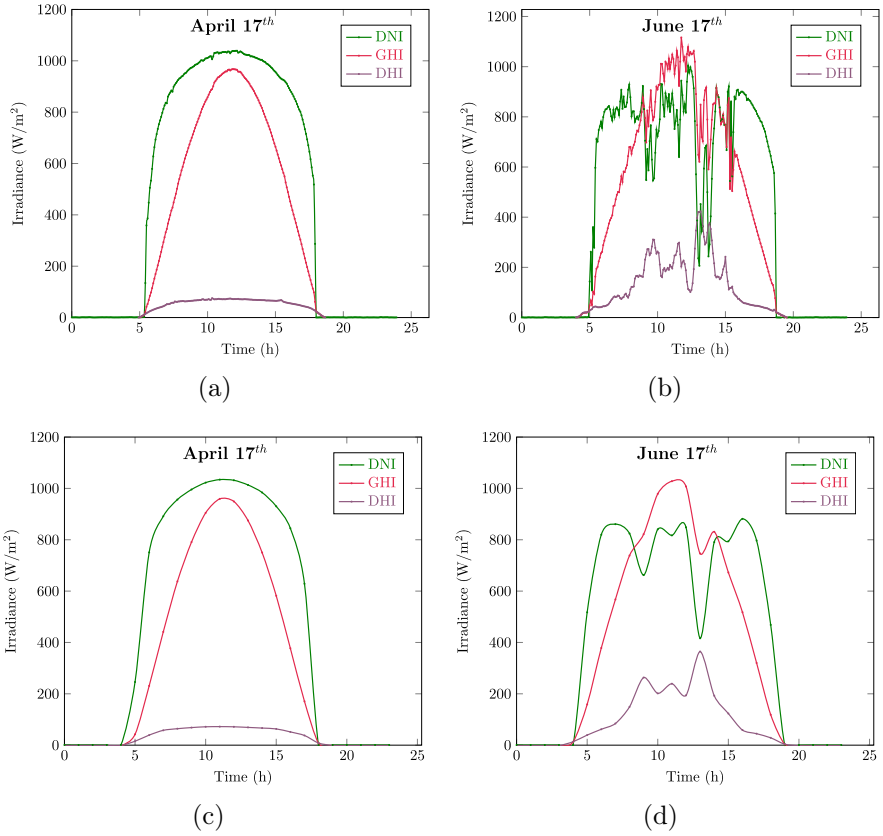

Figure 2.13: Solar irradiance components at two different days a clear-sky day (April 17^{st}) and a cloudy day (June 17^{st}) with two time resolutions: (a) and (c) 5 min, and (b) and (d) with 60 min.

3.2.1 Daily operation of hybrid plants

The variation of the daily power output for the hybrid strategies and the conventional CSP plant is shown in Figure 2.14, along with the DNI profile, for the two above days. Since similar tendencies were observed for the three cell scenarios, we focus on the realistic case study with GaAs as a cell technology and with the three solar technologies operating at 400 °C.

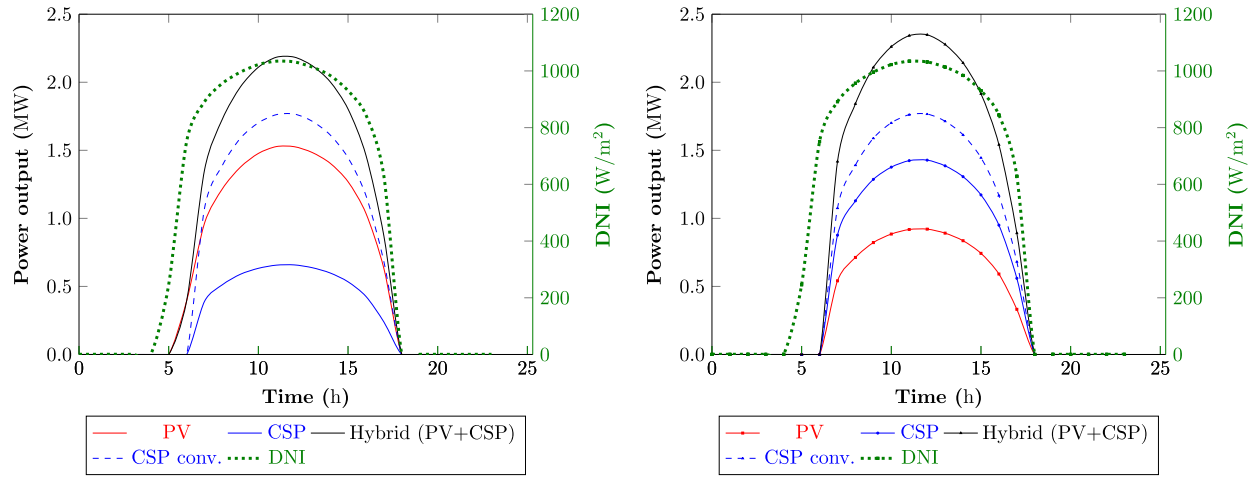

(a) *1S* (b) *HT*

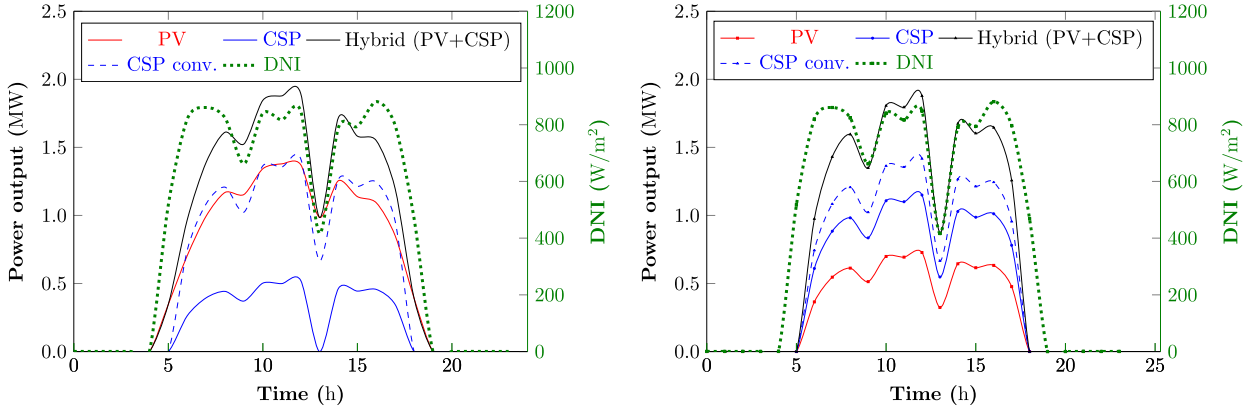

(c) *1S* (d) *HT*

Figure 2.14: Daily power output variation and DNI profile for the two hybrid strategies considering a time resolution of 60 min, for a clear-sky day (April 17^{th}): (a) and (b), and for a cloudy day (June 17^{th}): (c) and (d).

It can be noticed that:

- The daily power generation of both hybrid strategies exceeds that of the conventional CSP plant, regardless of the meteorological conditions. However, it is worth noticing that the hybrid strategy showing the best performances over the standalone CSP plant depends on the DNI pattern. The *HT* approach demonstrates the best performance during clear-sky days (Figure 2.14(b)), with an improvement in the power output of 24.5% relative to the CSP power output while only 19.8% increase of the power output is achieved with the *1S* hybrid system, mainly because of the small amount of DHI available this day (Figure 2.13(c)). For a cloudy day, both hybrid technologies show similar improvements in power production. For the *1S* approach, an increase of 25.3% relative to the CSP power output is noted, as a result of the improved ability of the PV heliostats to better handle the variable solar resource (the turbine operation being penalized by intermittent start-and-stops for DNI values close to 300 W/m^2 as explained in section 2.4) in addition to the increased amount of DHI resource (Figure 2.13(d)). A 24.2% increase is noticed with the *HT* strategy as the standalone CSP plant is operating under similar conditions for the receiver and the power block unit as the *HT* approach.

- With the existence of a threshold DNI value below which the turbine is assumed not to operate, the response of the different plants to the daily variation of DNI differs noticeably. This translates into an extended operation time of the *1S* approach over the course of the day, thanks to the increased capacity of the PV heliostats to convert the DHI solar radiation close to sunrise or sunset. As can be seen in Figure 2.13(d), during a clouding day, the DHI resource is available minutes before the DNI, resulting in more power generation of the *1S* strategy.

3.2.2 Impact of shading on PV heliostat

In our model, the description of shading losses was performed differently for the *1S* approach involving the use of PV heliostats compared to the *HT* approach and the conventional CSP plant. To account for shading impact, in a simplified yet close to reality description, two different scenarios were considered:

1. An ideal case where the shading effect was described similarly as for the conventional heliostats field. In this case study, the fraction of the PV power loss is strictly proportional to the shaded area as shown in Figure 2.15.

2. A more realistic case where the PV power loss is not linear anymore and follows a step function (Figure 2.15). In this scenario, the PV power loss does not vary linearly with the shaded fraction of the panel, but follows a staircase behaviour characterized by abrupt variation in the PV output for specific values of the shading.

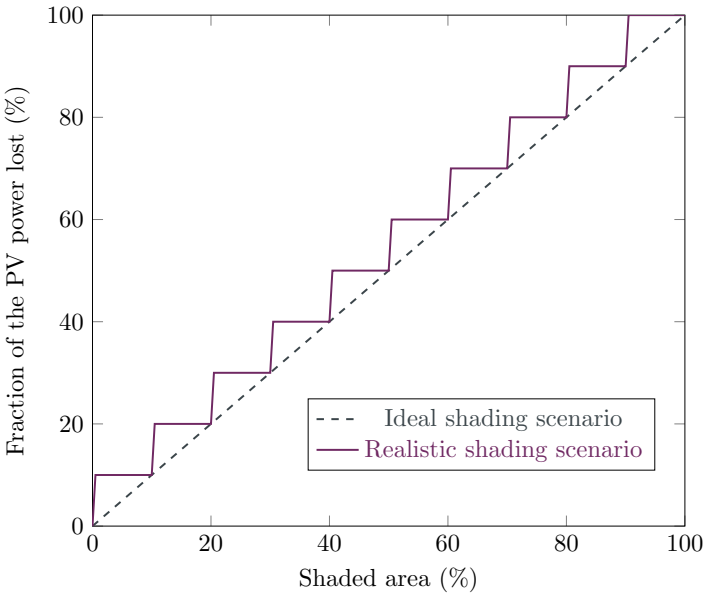

Figure 2.15: Schematic description of the two case studies for the description of the impact of shading losses on the PV power production of the *1S* hybrid strategy.

Figures 2.16(a) and 2.16(b) show the daily PV power output (left axis) and the difference between the ideal and real power production (right axis) during two days, April 17^{th} and June 17^{th}, respectively. Regardless of the type of day considered, at the beginning and end of the day, the absolute difference is negligible. For example, for a clear-sky (Figure 2.16(a)), the absolute power difference varies from 3.84% in the early hours of the morning to 4.2% at the end of the day. As the sun rises, the power difference between the real and ideal case studies becomes more significant, resulting in the emergence of three peaks for both days.

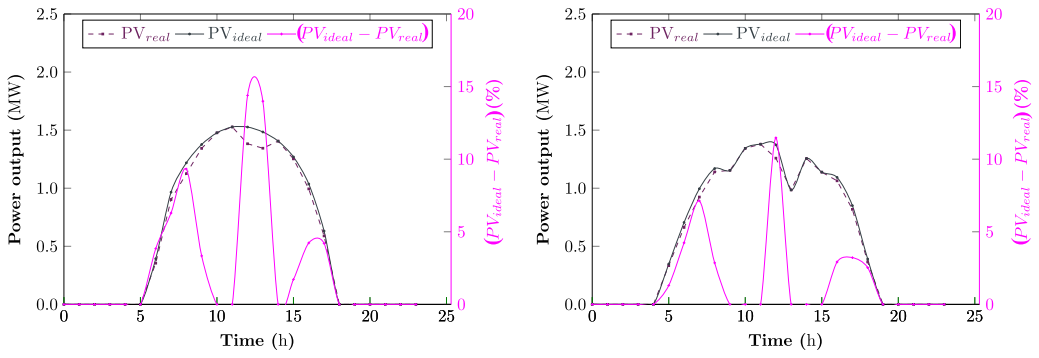

(a) *April 17th* (b) *June 17th*

Figure 2.16: Daily PV power output variation and the for the *1S* hybrid strategy considering a time resolution of 60 min and the realistic operation scenario, for: (a) a clear-sky day (b) and a cloudy day.

Table 2.8 summarizes the annual PV production considering the two shading loss scenarios in addition to the relative difference. Regardless of the operating scenarios of

the cells, the relative difference between the ideal and real case study remains constant and equal to 3.4%. This is mainly due to the independent description of the shading scenario and the cell operation case study considered.

Table 2.8: The PV annual energy production for the two shading scenarios and the relative difference in comparison to the ideal case study for the three cell scenarios.

	Ideal case (MWh)	**Real case** (MWh)	Relative difference (%)
Optimistic scenario	2870.8	2773.0	
Realistic scenario	2424.2	2341.7	3.4 %
Pessimistic scenario	2232.8	2156.8	

Summary

In this work, we have developed a multiphysics optical, electrical, and thermal model of the main PV-CSP *compact* hybrid strategies, based upon their integration in a real solar tower plant. Our motivation here was to precisely assess the performance of two different *compact* hybrid strategies when practically implemented into a large-scale solar plant, taking into account realistic plant parameters and ground-measured meteorological data over a full-year operation. From the first obtained results, several important conclusions can be drawn:

- If the superiority of PV-CSP *compact* hybrid plants over conventional CSP plants was left unclear to date, the present model tends to confirm that this family of hybrid approaches systematically demonstrates higher energy output than their pure solar thermal counterparts. The gap between PV-CSP *compact* hybrid systems and conventional CSP plants tends to grow substantially with increasing PV efficiency.

- Both hybrid strategies show an unbalanced share between the energy output of PV and CSP subsystems. Improving the ability of PV cells to approach their theoretical limit through R&D efforts will impact the system performance in different ways: an improvement in the PV efficiency of the *1S* system will lead to a net gain in the energy output of the plant, without improving the balance with the CSP subsystem. On the other hand, *HT* systems will benefit from an improvement in cell technology, both in terms of energy output and balance between PV and CSP subsystems.

- The comparison of hybrid systems encompassing two widely used PV cell materials and characterized by rather different bandgaps (1.4 eV in the case of GaAs and 2 eV in the case of AlGaInP) suggests that tailoring the electronic gap of the cell to ensure a relatively satisfying balance between PV and CSP may lead

to lower energy output. This implies that the optimal optoelectronic properties of the PV cells used in both approaches should stem from a compromise between net energy output of the system and balance between PV and CSP, a point left for future investigations.

☞ The benefit in the energy output associated with PV-CSP *compact*-hybrid systems tends to reduce as the operating temperature of the CSP converter increases. There is currently a significant body of research dedicated to the development of high-temperature CSP plants [94, 322], that could translate into higher CSP efficiency shortly, thus lowering even more the energy gap one may observe between PV-CSP *compact* hybrid and conventional CSP plants. In the meantime, the lifetime of PV cells is known to decrease significantly with increasing operating temperature, and the development of efficient and reliable *HT* modules operating at temperatures of several hundreds of degrees will necessarily require this reliability issue to be successfully addressed.

☞ The fact that the *1S* hybrid technology enables the use of DHI resources contrary to the *HT* and conventional CSP plants broadens the area of deployment of such technology. Therefore, additional studies should be conducted to investigate further the behaviour of the three technologies under different climatic conditions around the world (Targassonne presents a good balance between a solar resource, ambient temperature and wind speed, but remains less intended for the integration of solar technologies, in contrast with Africa and Middle-east [27]).

☞ The impact of shading on the PV production output of the *1S* strategy may present a technical problem that should be addressed properly. In this work, we proposed a simplified description of the problem to quantify the impact of shading losses on the overall production. A detailed study, accounting for the size of the heliostat field, the technology considered for the CSP plant and the electrical wiring considered between the cells covering the PV heliostats may result in different conclusions. It is worth pointing out that the THEMIS heliostat field results in reduced shading losses throughout the year, thanks to the slope between the rows.

Several additional remarks are in order:

As already stated previously, there is a large gap in the technological maturity of the two types of PV converters considered in this work. Flat-panel single-junction GaAs solar cells are already produced at an industrial scale and show very high efficiency, both at the cell and module level [103, 299], this cell technology will thus require modest research efforts before its integration into *1S* hybrid power plants, which will mainly consist in ensuring the most efficient spectrum-splitting possible and adequate wiring between the cells to repress the negative impact of shading effects. Conversely, the development of efficient *HT* solar cells is currently highly speculative, despite promising first attempts [116, 118, 317]. Major progress will need to be achieved, both at the cell and module levels, before considering their integration into *HT* hybrid power plants. At the cell level, it is still unclear how real PV cells are likely to approach their own theoretical limits. Better understanding the physics of solar cells at a temperature of several hundreds of degrees above ambient has already instigated some first research efforts that will need to be pursued toward understanding how *HT* cells should be designed and tailored to the extreme conditions to which they will be exposed. At the module level, the development of integrated PV receivers comprising hundreds or thousands of PV cells operating at very high temperature and concentration levels will necessarily raise numerous issues: how to handle large solar fluxes or temperature gradients across the *HT* module? How to optimize the electrical interconnection scheme between the thousands of PV cells typically comprised in a *HT* integrated receiver?

Finally, the ability of these approaches to significantly improve the dispatchability of solar electricity in comparison to standalone technologies, which indeed constitutes a key motivation in the development of PV-CSP *compact*-hybrid solar plants, will have to be assessed with the integration of some EES systems. For that purpose, in the following chapter, we propose to compare five different solar technologies (fixed-tilt PV, single-axis tracking PV, CR, *1S* and *HT*) by selecting 14 locations representative of the diversity of climate around the world, as well as two dispatching strategies of the TES integration, to supply a baseload and variable load demand.

Chapter 3

Compact PV-CSP hybrid plants integrating TES using two dispatch priorities

In this chapter, the behaviour of the two compact hybrid technologies integrating TES systems will be assessed using two dispatch strategies controlled by solar resource availability and TES status. The output performances of these systems will be studied under different weather conditions, considering constant load demand profiles over a full year of operation and using satellite data. Calculations are performed using the multiphysic model presented in chapter 2.

Introduction

For solar technologies without any storage system, the production of solar electricity is constrained by the availability of the solar resource, thus precluding any dispatchable electricity production strategy. Without storage, the system is unable to absorb excess energy when it is available. As a result, there is no stored energy to draw upon when there is a shortage of solar radiation, leading to the necessity to provide other means (e.g. fuel motor) to compensate for the mismatch between solar production and electricity demand. For example, in California, 15% of the solar power output is curtailed during the spring months as electricity demand is relatively low (because of moderate temperatures decreasing heating and cooling demand), and solar production is relatively high [323]. Conventional solutions typically involve the integration of electrochemical batteries to store the overproduced PV even if alternative storage solutions are currently being investigated (see chapter 1).

The energetic and economic reliability of *non-compact* PV-CSP hybrid technologies have been shown for various plant configurations involving either TES or BESS [73, 218, 324, 325] over the last six years, mainly in locations with very important solar resources (e.g. Chile, Morocco,...). Conversely, the ability of *compact* PV-CSP hybrid systems to outperform conventional solar plants remains poorly documented. The scarcity of

data motivates the need for investigating the ability of different solar technologies to meet constant load demand in different locations around the world.

1 System description

The evaluation of the technical performances of the different solar technologies under investigation is based upon THEMIS solar plant geometry. However, THEMIS heliostats field layout is not a typical arrangement for commercial CRs, due to the high optical losses resulting from heliostats located at the edges and the external rows of the solar field, relative to the receiver (see Appendix C). A modified layout of the heliostat field was adopted here, based on a polar disposition of the heliostats (the right display of the heliostat field in Figure 3.1) where heliostats are arranged in a radially staggered configuration north of the receiver tower (where heliostats located at the edges as well as in the last two rows are removed to increase the heliostat field efficiency). This configuration demonstrated higher optical efficiencies relative to the arrangement involving circular rows around the tower [326, 327]. This configuration is detailed in Appendix C.

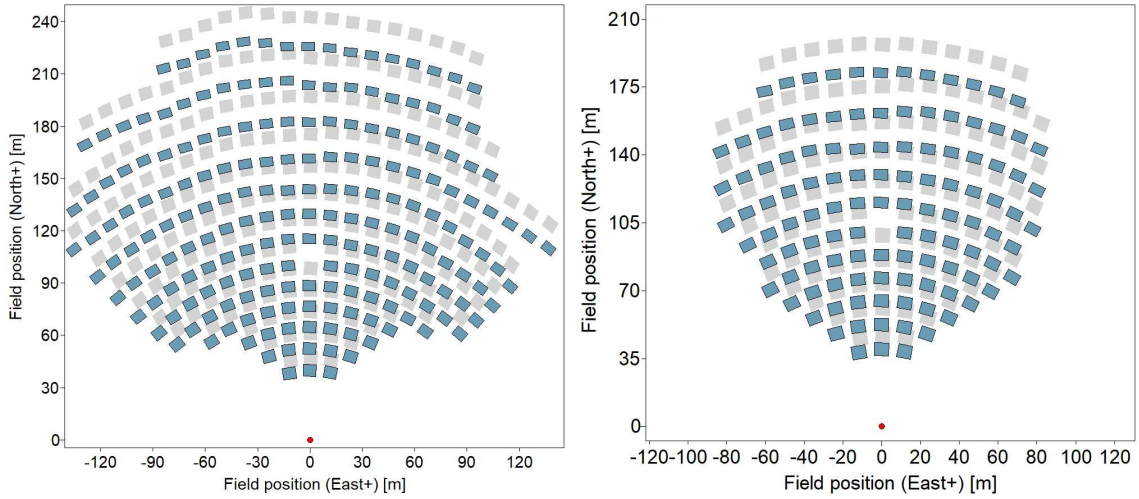

Figure 3.1: THEMIS original heliostat field layout accounting 201 heliostats (left graph) and the enhanced layout accounting 116 heliostat (right graph) (the red dot represents the location of the solar tower).

1.1 Conventional CR plant

Figure 3.2 provides a schematic description of the conventional CR plant considered in this study with the three main components:

- **Heliostat field:** 116 heliostats following the course of the sun during the day to concentrate the collected energy onto a central area at a thermal receiver located at the top of the tower (see Figure 3.2).
- **TES unit:** a two-tank "direct" TES system including a hot and a cold storage tank (see Figure 3.2). In a "direct" storage system, the HTF and the storage

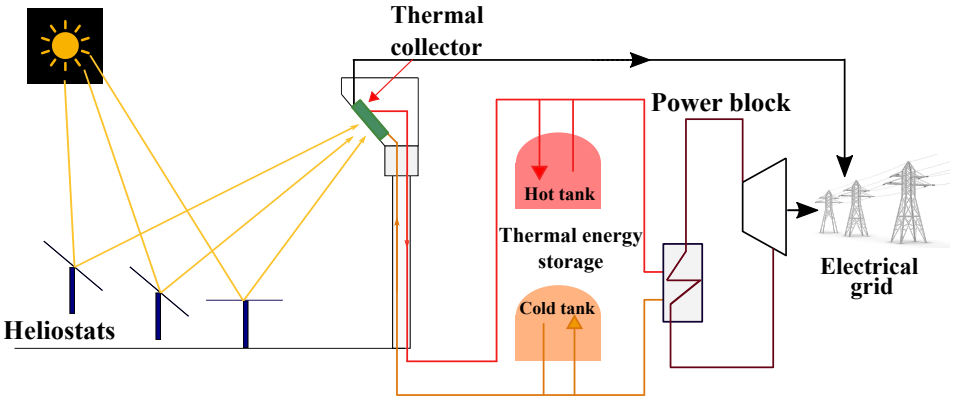

Figure 3.2: Schematic of a conventional CR plant with integrating two-tank direct TES.

fluid are the same, and therefore no intermediate heat exchanger is needed as shown in Figure 3.2. The energy surplus is stored in the hot tank by filling it with the heated HTF in a process known as *charging*. Then the HTF is taken from the hot tank in the process of *discharging* and used for power generation in the power block.

- **Power block (PB):** a conventional thermal PB consists of a heat exchanger (i.e. steam generator), a steam turbine, a generator and a cooling system. In this study, each solar technology has an identical gross power of 1 MWe and a nominal efficiency denoted by η_{pb}, given as $(2/3\,\eta_{Carnot})$, varying between 37 and $\sim$ 43 % depending on the HTF temperature (see Table 3.1), while the temperature of the cold reservoir is assumed to be constant and equal to 25°C. The receiver temperature is set at 400 °C for the *HT* approach, a temperature level consistent with the high-temperature cell characterizations reported elsewhere [234]. The temperature is set at 560 °C for the other approaches involving conventional receivers. The minimum turbine load was set at 30 % of the gross power. The main design parameters of the CSP plant and the PB are presented in Table 3.1.

Table 3.1: Design parameters of the CR subsystem plant and PB.

CSP plant	HTF	
Number of heliostats N_{hel}	116	
Heliostat field total reflective area (m^2)	6079	
Design receiver temperature (°C)	400	560
Design condition DNI (W/m^2)	950	
Power block		
Gross power output (MWe)	1	
Minimum output condition	30 %	
Nominal thermal efficiency	37.2 %	42.8 %

1.2 PV-CSP compact hybrid plants

The working principles of the two *compact* hybrid systems have been detailed in chapter 2. The model is modified to take into account the fact that the energy collected via the CSP subsystem will be either used instantly to meet the electrical demand or stored using the TES unit for later use. Figures 3.3(a) and 3.3(b) show a schematic description of the *HT* and *1S* hybrid systems respectively. The dark dashed lines represent the different possibilities of using the generated electricity, depending on the dispatch strategies chosen. The details are given in section 3.

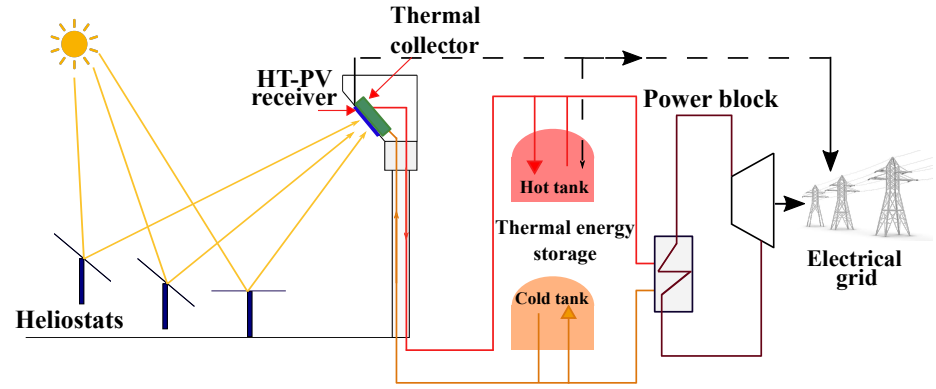

(a)

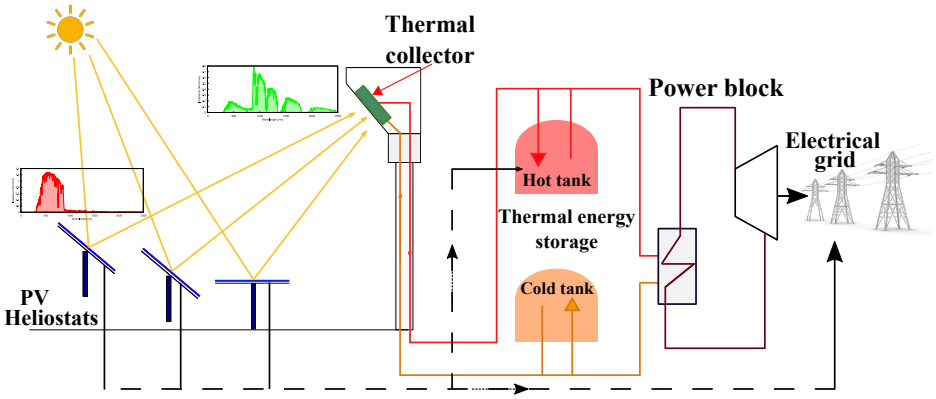

(b)

Figure 3.3: Schematic description of the two-compact hybrid plants integrated with a two-tank direct TES: (a) *HT*, and (b) *1S*.

2 Sites characteristics

The selected sites are classified into three groups according to their mean irradiation level:

- **Very high irradiation**: This category accounts mainly for deserted and semi-arid locations with very high DNI profiles along the year as shown in Figure B.2, with a yearly total of DNI ranging from around 2400 to 3700 kWh/m^2-yr (Table 3.2).
- **Medium irradiation**: This category accounts mainly for locations with moderate DNI values (Figure B.3) ranging from around 1400 to less than 2400 kWh/m^2-yr (Table 3.2).
- **Low irradiation**: This category accounts low DNI distribution (< 1400 kWh/m^2-yr) as shown in Figure B.4.

Table 3.2: Meteorological data for the 15 selected locations.

	Very high irradiation		
Country	**Chile**	**Australia**	**South Africa**
Description	**Antofagasta**	**Ghan NT**	**Bokpoort**
Latitude (°)	-23.43	-25.27	-28.73
Longitude (°)	-70.4	133.76	21.99
Altitude (m)	2646	398	953
ς_{fix}(°)	22.2	23.5	29.3
γ_{fix} (°)	0	0	0
Yearly total of DNI (kWh/m^2-yr)	3752	3004	2991
Yearly total of GHI (kWh/m^2-yr)	2722	2342	2299
Yearly total of DHI (kWh/m^2-yr)	382	450	460
	Very high irradiation		
Country	**Morocco**	**USA**	**Algeria**
Description	**Ouarzazate**	**Phoenix**	**Tamanrasset**
Latitude (°)	30.93	33.45	22.79
Longitude (°)	-6.94	-112.07	5.52
Altitude (m)	1135	330	1367
ς_{fix} (°)	28	29.9	21.5
γ_{fix} (°)	180	180	180
Yearly total of DNI (kWh/m^2-yr)	2741	2474	2348
Yearly total of GHI (kWh/m^2-yr)	2173	2078	2266
Yearly total of DHI (kWh/m^2-yr)	507	537	721

Continued on next page

Table 3.2 – continued from previous page

			Medium irradiation
			Medium irradiation
Country	**Spain**	**UAE**	**Brazil**
Description	**Sevilla**	**Abu-Dhabi**	**Porto Naci.**
Latitude (°)	37.39	24.4	-10.7
Longitude (°)	-5.98	54.7	-48.4
Altitude (m)	17	6	231
ς_{fix} (°)	32.8	22.9	10.7
γ_{fix} (°)	180	180	0
Yearly total of DNI (kWh/m^2-yr)	1983	1765	1624
Yearly total of GHI (kWh/m^2-yr)	1781	2064	1883
Yearly total of DHI (kWh/m^2-yr)	607	865	757
			Medium irradiation
Country	**Ecuador**	**USA**	**France**
Description	**Quito**	**Boston**	**Targassonne**
Latitude (°)	-0.2	42.36	42.49
Longitude (°)	-78.5	-71.06	1.99
Altitude (m)	2800	10	1600
ς_{fix} (°)	0	36.2	36.3
γ_{fix} (°)	0	180	180
Yearly total of DNI (kWh/m^2-yr)	1409	1395	1387
Yearly total of GHI (kWh/m^2-yr)	1916	1370	1515
Yearly total of DHI (kWh/m^2-yr)	930	737	593
			Low irradiation
Country	**China**	**India**	**Germany**
Description	**Lanzhou**	**Andheri**	**Jülich**
Latitude (°)	35.86	20.59	50.91
Longitude (°)	104.19	78.96	6.38
Altitude (m)	1838	248	86
ς_{fix} (°)	31.7	19.6	41.7
γ_{fix} (°)	180	180	180
Yearly total of DNI (kWh/m^2-yr)	1306	1300	1123
Yearly total of GHI (kWh/m^2-yr)	1564	1744	1184
Yearly total of DHI (kWh/m^2-yr)	746	824	594

2.1 Solar databases

To perform a rigorous comparison between the different solar technologies, the accurate knowledge of incoming solar radiation at selected locations is of great importance. Meanwhile, the difficulty to access ground-measured meteorological data over selected locations directed us towards satellite-based models referred to as solar databases (SDB). Satellite-based models typically use empirical or physical radiation models that estimate the irradiation using cloud properties derived from satellite radiance and then calculate GHI and DNI obtained in a radiative transfer model [328]. Nowadays, several products are available, making the selection of an appropriate dataset rather intricate, as each database applies for different locations, temporal resolutions, and methods of error calculation [329–331].

In the following, only two SDBs are compared to the ground-measured data at Targassonne namely 1) Photovoltaic Geographical Information System (PVGIS), an instantly downloadable and free database providing the direct, diffuse and reflected irradiance on inclined PV plane [332] and 2) Solcast, [333] a database providing GHI and DNI data in addition to the global tilted, both for fixed-tilt and single-axis tracking systems. Since Solcast is a very recent product (available since 2015), only a limited documentation and sparse validation exist at this point [333, 334].
Table 3.3 summarizes the main characteristics of both SDBs. Here, the year 2016 is selected to compare hourly GHI, and DNI data from the two SDBs to the ground measured data retrieved from on-site measurements in Targassonne, details about the measurement tools used are given in Appendix B.

Table 3.3: Summary of the main characteristics of the two solar databases.

Database	**Solcast** [335]	**PVGIS** [330]
Temporal resolution (min)	5, 10, 15, 30, 60	60
Spatial resolution (km)	1 – 2	4 – 6
Availability of the data	2007 – to date	2005 – 2016
Components	GHI, DNI, DHI EBH , GTI	I_b, I_d, I_{refl}
Coverage	Global	Europe, Africa, Middle East

EBH: Direct Horizontal Irradiance (W/m^2).
GTI: Global Tilted Irradiance (W/m^2).
I_b: Direct irradiance on the inclined PV plane (W/m^2)
I_d: Diffuse irradiance on the inclined PV plane (W/m^2).
I_{refl}: Reflected irradiance on the inclined PV plane (W/m^2).

Figure 3.4 depicts measured against estimated GHI hourly values from the two SDBs. In the case of PVGIS, measurement points appear to be significantly more scattered compared to Solcast. This difference could be explained by the high spatial resolution of PVGIS compared to Solcast. More importantly, the estimation of the GHI resource is performed indirectly with PVGIS from the I_{refl} using Eq. (4.4) detailed in

chapter 4. The indirect estimation will require precise knowledge of the surface albedo and the optimized tilt considered for the PV panels. Thus, increasing the percentage error to accurately estimate the GHI resource using PVGIS.

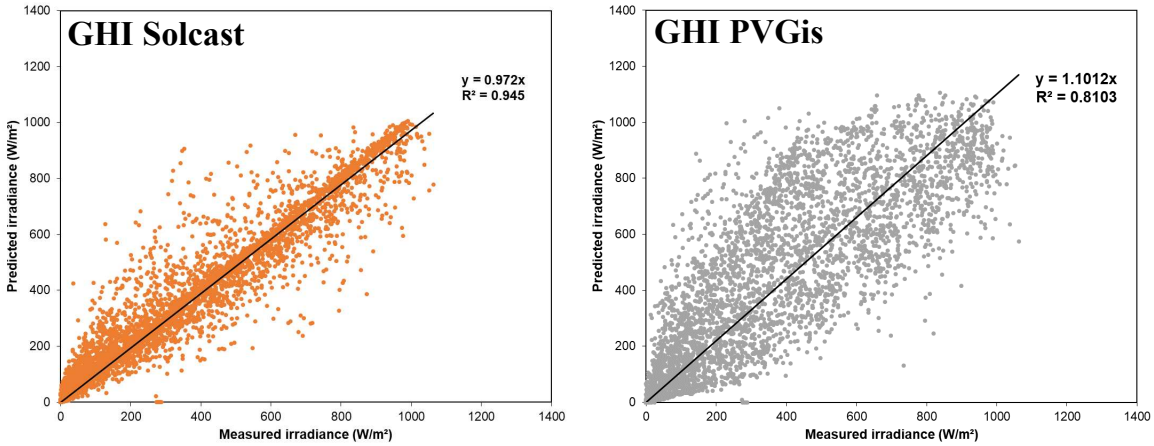

Figure 3.4: Hourly estimates of GHI from Solcast and PVGIS compared to measured data at Targassonne. The regression line is shown in black, with results in the form of y =a x; R is the correlation coefficient.

Figure 3.5 is similar to Figure 3.4, but for DNI data. The two plots reveal much more scatter around the diagonal than in Figure 3.4, which could be expected because DNI is more sensitive to cloudiness and aerosols than GHI [328]. Additionally, as the prediction of DNI values is conducted indirectly from the GHI values, inaccurate estimation of a parameter can strongly affect the output results. Solcast displays less scatter than PVGIS with a relatively improved correlation parameter (about 0.85 vs, 0.66 respectively). The shape of the regression line is discussed in more detail in section 6 of the Appendix.

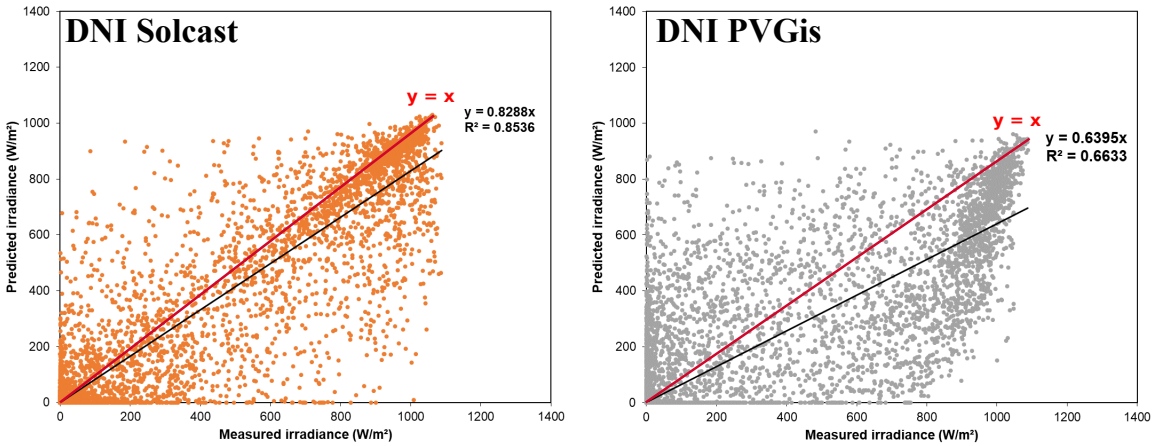

Figure 3.5: Hourly estimates of DNI from Solcast and PVGIS compared to measured data at Targassonne. The red line shows y =x curve, along which each data point should ideally be perfectly aligned with.

The criteria used to evaluate the forecast accuracy are based on the evaluation of two statistical indicators: (1) the mean bias error (MBE), defined as the average forecast error representing the systematic error of a forecast model to underestimate or overestimate the irradiation components (Eq. (3.1)) and (2) the root mean squared error (RMSE), defined as the mean of the square root of the error between the forecasted value and the measured value (Eq. (3.3)) [336]:

$$MBE(\mathrm{W/m^2}) = \frac{\sum_{i=1}^{N}(I_{pred,i} - I_{meas,i})}{N} \tag{3.1}$$

$$MBE(\%) = \frac{MBE(\mathrm{W/m^2})}{\frac{\sum_{i=1}^{N} I_{meas,i}}{N}} \times 100\% \tag{3.2}$$

$$RMSE(\mathrm{W/m^2}) = \sqrt{\frac{\sum_{i=1}^{N}(I_{pred,i} - I_{meas,i})^2}{N}} \tag{3.3}$$

$$RMSE(\%) = \frac{RMSE(\mathrm{W/m^2})}{\frac{\sum_{i=1}^{N} I_{meas,i}}{N}} \times 100\% \tag{3.4}$$

where I stands for the irradiance components (GHI and DNI in ($\mathrm{W/m^2}$)). The subscript i, *pred* and *meas* refer to the ith value of the daily solar irradiation, the predicted and measured daily solar irradiation values, respectively, and N is the total number of available data points.
For both GHI and DNI, the performance statistics displayed in Table 3.4 confirm the better results obtained by Solcast.

Table 3.4: Statistical indicators for the hourly GHI and DNI irradiation values.

	Mean irradiance ($\mathrm{W/m^2}$)	MBE ($\mathrm{W/m^2}$)	MBE (%)	RMSE ($\mathrm{W/m^2}$)	RMSE (%)
GHI					
Measured	181	—	—	—	—
Solcast	184	2	**1**	62	**34**
PVGIS	220	38	21	139	77
DNI					
Measured	227	—	—	—	—
Solcast	192	-34	**-15**	141	62
PVGIS	159	-68	-30	223	98

Solcast appears to overestimate the GHI resource, resulting in positive biases (MBE) of 2%. In contrast, the magnitude of model errors (RMSE) is larger for PVGIS for GHI and DNI by (77 and 98% versus 34 and 62%, respectively with Solcast). For DNI, both SDBs underestimate the MBE with values varying in the range of -15 – -30%. The highest biases can be attributed to the significant impact of poor cloud detection

[328], which results in more scatter points, as depicted in Figure 3.5.

From the results mentioned above, it can be noted that Solcast is more suitable to provide the solar data required for the study conducted in this thesis. Furthermore, in addition to solar components, Solcast provides access to temperature and wind velocity data that are important to accurately describe the variation of cell temperature with ambient air characteristics as described in Chapter 2.

3 Storage integration modes

The integration of storage systems within a particular solar technology will highly impact the plant dispatchability as well as its affordability. In this section, two main dispatch strategies will be described and assigned to the studied solar technologies. The first strategy is to set priorities for the PV output production to cover the demand over the electrical energy generated by the remaining subsystems (either direct CSP production, or indirect electricity generation using the thermal energy from the storage). This configuration is commonly used in *non-compact* PV-CSP hybrid plants, as it enables to take advantage of the PV system cost-effectiveness [337]. The second strategy optimizes the operation of the PB, by minimizing the turbine shutdowns and maximizing PB operating hours. Bousselamti et al. [74] demonstrated that high capacity factors, low LCOE, and low dumped energy can be achieved by implementing this dispatch strategy in *non-compact* PV-CSP hybrid plant. For the five solar technologies, control parameters of the TES and BESS were applied to monitor the state-of-charge (SOC) of the storage systems (i.e. the volume fraction of the HTF that can be *charged* and *discharged* in the storage tank) as summarized in Table 3.5. The initial SOC of both storage systems is set at SOC_{min}. The SOC values are used to

Table 3.5: Control parameters for the SOC of the two storage systems.

Storage technology	**TES**	**BESS**
SOC_{min}	2%	20%
SOC_{max}	98%	100%
η	100%	96%

identify the allowable power inside the hot tank given by the following equations:

$$P_{SOCmax} = \frac{SOC_{max}\, E_{TES}}{\delta t} \tag{3.5}$$

$$P_{SOCmin} = \frac{SOC_{min}\, E_{TES}}{\delta t} \tag{3.6}$$

where E_{TES} is the TES thermal capacity expressed in MWh and δt the time step between two measurements (expressed in hours).

Table 3.6 summarizes the main parameter notations used in this chapter.

Table 3.6: Main parameter notations used in the following chapter.

P_{load}	The electrical load demand
P_{th}	The hourly thermal power after accounting for convective and radiative losses available at the receiver
P_{rec}	The initial thermal power available at the receiver
P_{avai}	The available thermal power after accounting for PV power
P_{need}	The needed thermal power to complement the electrical load
$P_{pv,\ gr}$	The PV output power by the PV subsystem
$P_{csp,\ gr}$	The CSP output power by the CSP and TES subsystems
$P_{pv,\ dum}$	The amount of surplus PV power curtailed
$P_{rec,\ dum}$	The amount of excess power available at the solar field
$P_{pv,\ def\ dum}$	The amount of surplus PV definitely curtailed after recovering part of surplus PV using the EH with the **DS2**
$P_{TES,\ pb}$	The amount of energy from TES to the PB unit
P_{recov}	The amount of suplus PV power recovered using the electric heater
P_{rej}	The amount of surplus PV power curtailed equal to $P_{pv,\ dum}$

3.1 PV-CSP *compact* hybrid systems

After computing the PV power output and the power impinging the receiver using Eqs. (2.23), (2.18), (2.6), and (2.8), respectively, we then evaluate the thermal power available at the inlet of the PB or TES at each time-step (i), for both hybrid technologies. For the *1S* strategy, it can be expressed as:

$$P_{th,\ 1S}(i) = \eta_{th,\ 1S}\, P_{rec,\ 1S}(i) \tag{3.7}$$

For the *HT* hybrid approach, part of the power impinging the receiver is first harvested by the PV module, as depicted in Figure 3.6, hence the power available for the HTF is noted as P_{avai} and is given by:

$$P_{avai}(i) = \eta_{th,\ HT}\, P_{rec,\ HT}(i) - P_{pv,\ HT}(i) \tag{3.8}$$

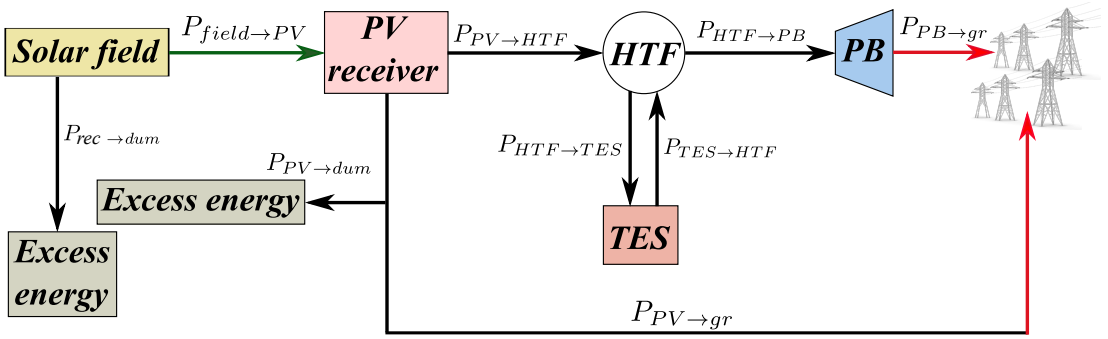

Figure 3.6: Simplified *HT* PV-CSP hybrid model, containing the four components of the plant. The input to the system is the amount of power impinging the receiver from the solar field (green arrow). The output is the electrical power released directly from the PV receiver into the electrical grid and the output power from the PB unit (red arrow). The blocks are connected by the power flows between them. The excess energy branch represents the energy that is discarded from the system when it cannot be stored or used for power generation.

The relation between the described power flows is shown in Figure 3.6. To fulfill the electrical demand, two alternative paths are possible, either directly from the PV receiver ($P_{pv,\ gr}$), or from the PB ($P_{pb,\ gr}$), the latter using the thermal power either directly from the HTF or the TES (indicated as $P_{HTF\to PB}$ and $P_{TES\to HTF}$ on the power flow diagram, respectively).

In the following sections, the two dispatch strategies (DS) will be explained for the *1S* hybrid plant; the same conditions apply for the *HT* hybrid strategy.

3.1.1 Prioritize PV output: DS1

The hybrid plant first operation scheme is based on the delivery of a given electrical demand P_{load} (either constant or variable). We assume that the overproduced PV electricity cannot be stored (no electrochemical storage, nor any possibility to store the excess PV electricity as heat in the TES using an electric heater (EH)). As a consequence, PV electricity has priority in the electrical grid over electricity generation from CSP and TES, which operate as a back-up of PV. This dispatch strategy will be referred to as **DS1** in the upcoming sections.

Figure 3.7 shows a flowchart describing the operation mode of the *1S* hybrid plant, where P_{pv} is the PV output, P_{SOC} is the SOC of the hot tank, P_{need} is the amount of power needed to fulfil P_{load}, $P_{min,\ pb}$ is the net minimum allowable power output from the turbine defined as 30% of the PB nominal output P_{pb}. The index *dum* stands for the amount of power curtailed from PV and heliostat field separately (see Eqs. (3.9) (3.10)) and *gr* for the amount of energy supplied to the electrical grid via the PV, CSP or TES subsystems, respectively. The operation modes considered in this work follow the steps described below:

1. If the PV output is above P_{load}, the PV system can cover the demand, and the surplus PV output is curtailed (Eq. (3.9)). In this case, the CSP subsystem is shut down, and the energy available for the HTF is sent to the hot tank. If the TES is full, the heliostats are defocused, and the optical energy collected by the heliostat field noted as $P_{rec,\ dum}$ in Figure 3.7 is lost.

$$P_{pv,\ dum}(i) = P_{pv}(i) - P_{pv,\ gr} \tag{3.9}$$

$$P_{rec,\ dum}(i) = P_{rec}(i) - [P_{SOCmax} - P_{SOC}(i-1)] \tag{3.10}$$

2. If the PV output is below P_{load}, the PV power is entirely injected into the electrical grid, and the energy required to bridge the gap between the PV electricity available and P_{load}, noted P_{need} (Eq. (3.11)), is provided either by the CSP or by the TES subsystem. If P_{rec} exceeds both P_{need} and $P_{min,\ pb}$, the power delivered by the turbine noted $P_{csp,\ gr}$, is given by Eq. (3.12). The extra thermal energy can either be stored as heat in the TES or spilt if the hot tank attains P_{SOCmax}.

$$P_{need}(i) = \frac{P_{load} - P_{pv,\ gr}(i)}{\eta_{pb}} \tag{3.11}$$

$$P_{csp,\ gr}(i) = \eta_{pb}\, P_{need}(i) \tag{3.12}$$

3. If P_{rec} is not sufficient to fulfill the power demand, then the hot tank is discharged to power the turbine. If the TES does not have enough energy (i.e. the SOC of the TES is close to its minimum value P_{SOCmin} (Eq. (3.6)), then the available power is used to charge the hot tank.

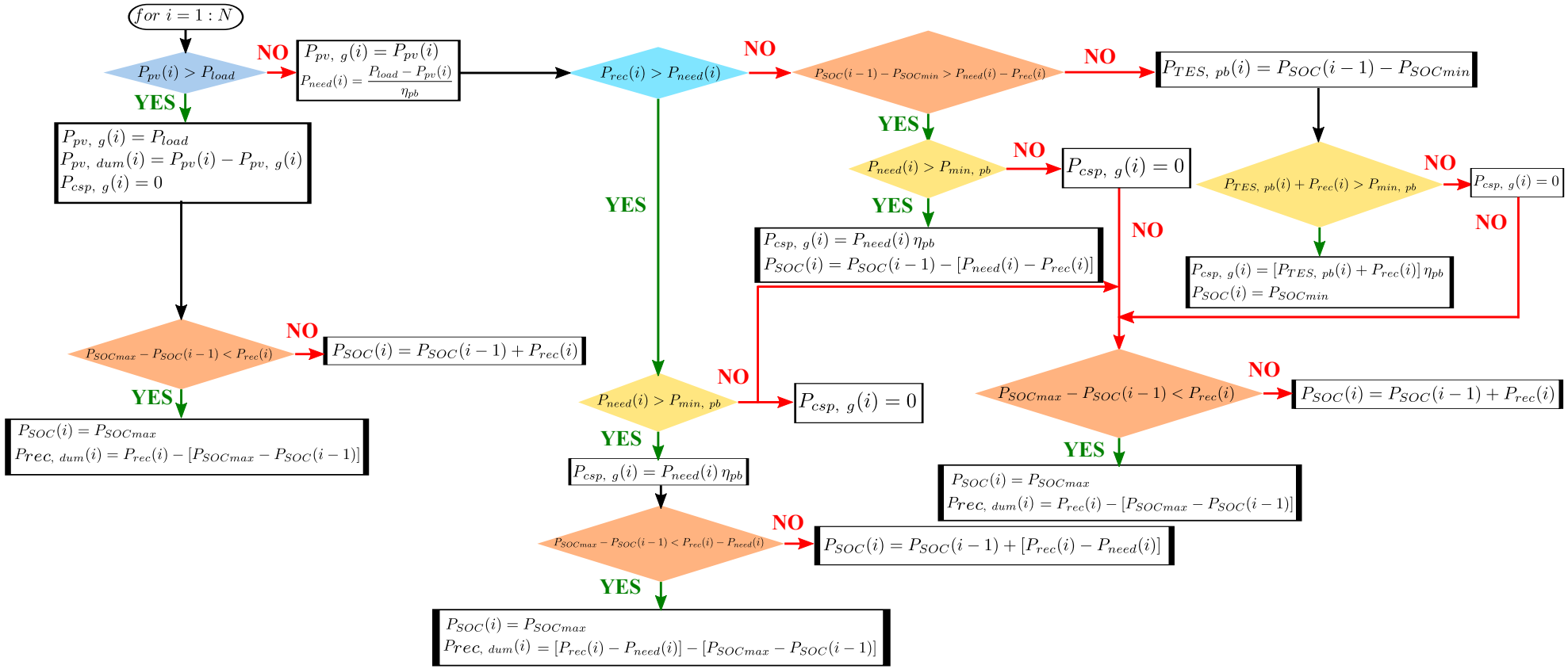

Figure 3.7: Flowchart of the operational strategy **DS1** of the *1S* hybrid plant. The initial conditions regarding the load demand are highlighted in blue, the yellow colors indicates the operation of the PB and finally orange color is associated with the TES SOC evaluation.

4. If the sum of P_{rec} and the energy available in the TES tank denoted $P_{TES,\ pb}$ and described by (Eq. (3.13)) is sufficient to complete the demand, then the $P_{csp,\ gr}$ is given by Eq. (3.14); otherwise, P_{rec} is used to charge the hot tank and the CSP+TES contribution is nil.

$$P_{TES,\ pb}(i) = P_{SOC}(i-1) - P_{SOCmin} \tag{3.13}$$

$$P_{csp,\ gr}(i) = \eta_{pb}\ [P_{TES,\ pb}(i) + P_{rec}(i)] \tag{3.14}$$

As can be seen in Figure 3.7, prioritizing PV production is the simplest dispatch strategy for the PV subsystem of a *compact* PV-CSP hybrid plant. However, this approach may not be technically and economically efficient due to PV curtailments and the non-optimized operation of the PB unit. Turbine startup and shutdown is one of the most critical aspects of a CSP plant operation, as the turbine must be shutdown only if it remains offline for a sufficient amount of time (for 2 to 3 hours) to avoid the turbine lifetime reduction.

For the above-mentioned reasons, a second dispatch strategy aiming at minimizing the dumped energy is developed and evaluated.

3.1.2 Minimize the energy dumped: DS2

Compared to the first dispatch strategy, an EH is integrated into the hybrid plant (Figure 3.8). The EH converts excess PV power (otherwise curtailed) to produce heat. The heat is then absorbed by the HTF and stored in the hot tank. The EH operates as a new heat resource for the TES, which is beneficial for the flexibility and dispatchability of the hybrid system.

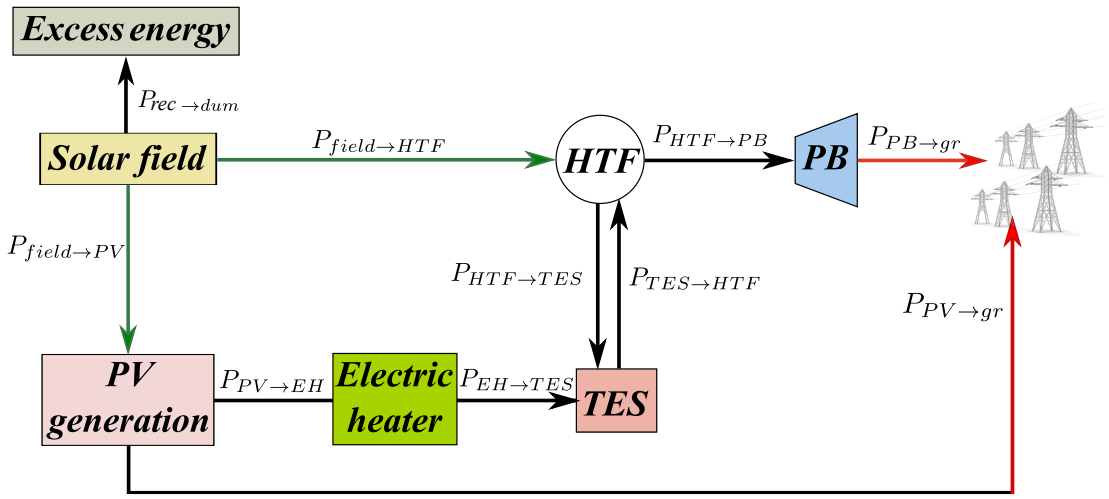

Figure 3.8: Simplified *1S* PV-CSP hybrid model, containing the four plant components.

Each dispatch strategy and technology discussed in this work has a specific set of conditions, i.e., the use of available solar energy, the minimum power needed to power the turbine, etc., depending on the system under consideration. Thus, to simplify the reading of this chapter, only the main steps are detailed here, with the corresponding flowcharts in the Appendix B.

Figure B.5 shows a detailed flowchart describing the operation mode of the *HT* hybrid plant. It can be noticed that when the PV output is above P_{load}, priority is for PV as for the **DS1**. In this case, the energy impinging the receiver P_{avai} (Eq. (3.8)) is used to charge the hot tank. However, instead of dumping the overproduced PV electricity, it can be converted into heat via the EH without losses (i.e. conversion efficiency of 100%). Thus, a condition is added to verify the SOC of the TES system. If the hot tank is not fully charged, $P_{pv,\ dum}$ is used for charging the hot tank; otherwise, the PV surplus will be curtailed (Eq. (3.15)).

$$P_{pv,\ def\ dum}(i) = P_{pv,\ dum}(i) - [P_{SOCmax} - P_{SOC}(i)] \tag{3.15}$$

If the PV output is below P_{load}, three possibilities may occur:

1. If P_{avai} exceeds P_{need} and $P_{min,\ pb}$, the CSP contribution is the same as in Eq. (3.12) and the PV power is entirely injected into the grid as well. At the same time, the SOC of the hot tank is verified. If the TES is fully charged to its maximum value, then energy coming from the thermal receiver is spilt.

2. When P_{avai} still exceeds P_{need} but P_{need} is below $P_{min,\ pb}$, the PB operates at its minimum rate to fulfill part of the load. $P_{csp,\ gr}$ is given by Eq. (3.16), whereas the remaining energy is provided by the PV output (Eq. (3.17)). The TES will be charged using the remaining thermal energy available at the receiver after accounting for $P_{min,\ pb}$, and then using the overproduced PV electricity.

$$P_{csp,\ gr}(i) = \eta_{pb}\, P_{min,\ pb} \tag{3.16}$$

$$P_{pv,\ gr}(i) = P_{load} - P_{csp,\ gr}(i) \tag{3.17}$$

3. If P_{avai} is below P_{need}, then the TES discharges at a minimum rate to supply the demand while PV is used to supplement the TES (Eq. (3.17)). If the TES does not have enough energy to meet the required demand, the available energy from the heliostat field at the hot tank inlet is used to charge the TES, and the PV power is fully fed into the power grid.

The same operating modes apply to the *1S* hybrid approach. The only difference is that P_{avai} should be replaced by P_{rec}.

3.2 Conventional CSP plant

In the case of a conventional CSP plant, after accounting for optical and thermal losses, part of the solar irradiation available in the solar field is recovered by the HTF as expressed in Eq. (3.18). This power is then used to generate electricity using the PB unit; however, when the PB is operating at full capacity and the TES is fully charged, part of this power has to be curtailed, as illustrated in Figure 3.9. For the standalone CSP plant, the required thermal energy is first deduced from Eq. (3.19), and is compared with the thermal output available at the receiver.

$$P_{th,\ csp}(i) = \eta_{th,\ csp}\, P_{rec,\ csp}(i) \tag{3.18}$$

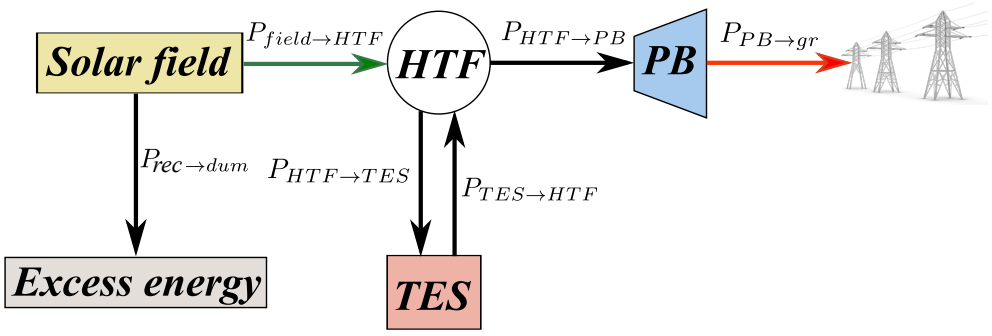

Figure 3.9: Simplified CSP conventional model, containing the four plant components.

$$P_{need} = \frac{P_{load}}{\eta_{pb}} \tag{3.19}$$

Figure B.6 shows a flowchart describing the operation mode of a standalone CSP plant. The operation modes considered in this work follow the steps described below:

1. If $P_{rec,\ csp}$ is above P_{need}, part of the energy available at the receiver is used to cover the demand (Eq. (3.20)), while the surplus energy is used to charge the hot tank. If the TES is fully charged, the energy reflected by the heliostat field is spilt.

$$P_{csp,\ gr}(i) = \eta_{pb}\, P_{need} \tag{3.20}$$

2. If $P_{rec,\ csp}$ output is below P_{need}, then the hot tank is discharged to supply P_{need}. When the energy available in the hot tank is not sufficient to supply the required demand, then the sum of $P_{TES,\ pb}$ (Eq. (3.21)) and $P_{rec,\ csp}$ is used to supplement the electrical demand; if the sum is not sufficient, then $P_{rec,\ csp}$ is stored as heat in the TES.

$$P_{TES,\ pb}(i) = P_{need} - P_{rec,\ csp}(i) \tag{3.21}$$

4 Performance parameters

According to the previous equations and dispatch strategies, the model needs several technical parameters to assess the performance of each solar technology: the annual energy output of each component and the recovery factor.

4.1 Energy output

The annual energy output (Q) of each plant component is simply given by the following equations:

$$Q_{pv,\ gr}(i) = \sum_{i=1}^{8760} P_{pv,\ gr}(i)\,\delta t \tag{3.22}$$

$$Q_{csp,\ gr}(i) = \sum_{i=1}^{8760} P_{csp,\ gr}(i)\,\delta t \tag{3.23}$$

$$Q_{TES,\ gr}(i) = \sum_{i=1}^{8760} P_{TES,\ gr}(i)\,\delta t \tag{3.24}$$

$$Q_{BESS,\ gr}(i) = \sum_{i=1}^{8760} P_{BESS,\ gr}(i)\,\delta t \tag{3.25}$$

4.2 Recovery factor

For the two PV-CSP *compact* hybrid plants, the rejected power can be used to heat the HTF through the EH device and provide extra energy in the storage. The recovery ratio is used to estimate the system capacity to recover the energy rejection of the PV system. The recovery ratio is defined as the ratio between the power recovered from the PV system (P_{recov}) (defined as the difference between the power originally dumped and the PV power recovered (Eq. (3.27))) and the power rejection of the PV system (P_{rej}) (Eq. (3.28)), and it is calculated by:

$$\eta_{recov} = \frac{\sum_{i=1}^{8760} P_{recov}(i)}{\sum_{i=1}^{8760} P_{rej}(i)} \tag{3.26}$$

where, P_{recov} and P_{rej} are given by:

$$P_{recov}(i) = P_{pv,\ dum}(i) - P_{pv,\ def\ dum}(i) \tag{3.27}$$

$$P_{rej}(i) = P_{pv,\ dum}(i) \tag{3.28}$$

5 Results & discussion

The simulation is based on satisfying a constant baseload demand ranging from 0.5 to 1 MWe with different TES capacity values [0:20 MWh_t].

5.1 Impact of time resolution

5.1.1 Daily performance

Figures 3.10 and 3.11 show the daily power generation of the *1S* and *HT* hybrid plants, respectively for January 13^{th}, 2018 in Antofagasta (CL) using five different time steps. Both hybrid plants operate to provide a base demand of 0.7 MWe with 10 MWh_t of TES.

- Figure 3.10 shows that the variability of the maximum PV output of the *1S* hybrid plant (purple curve) is reduced as the time step increases, due to the significantly reduced variability of shading losses, as the sun position is averaged at every time step. This results in less fluctuating PV output during the early hours of the day when using small time steps between 5 and 30 minutes (Figures 3.10(a), 3.10(b), 3.10(c) and 3.10(d)), which shift the CSP contribution after sunset with a 60-minute time resolution.

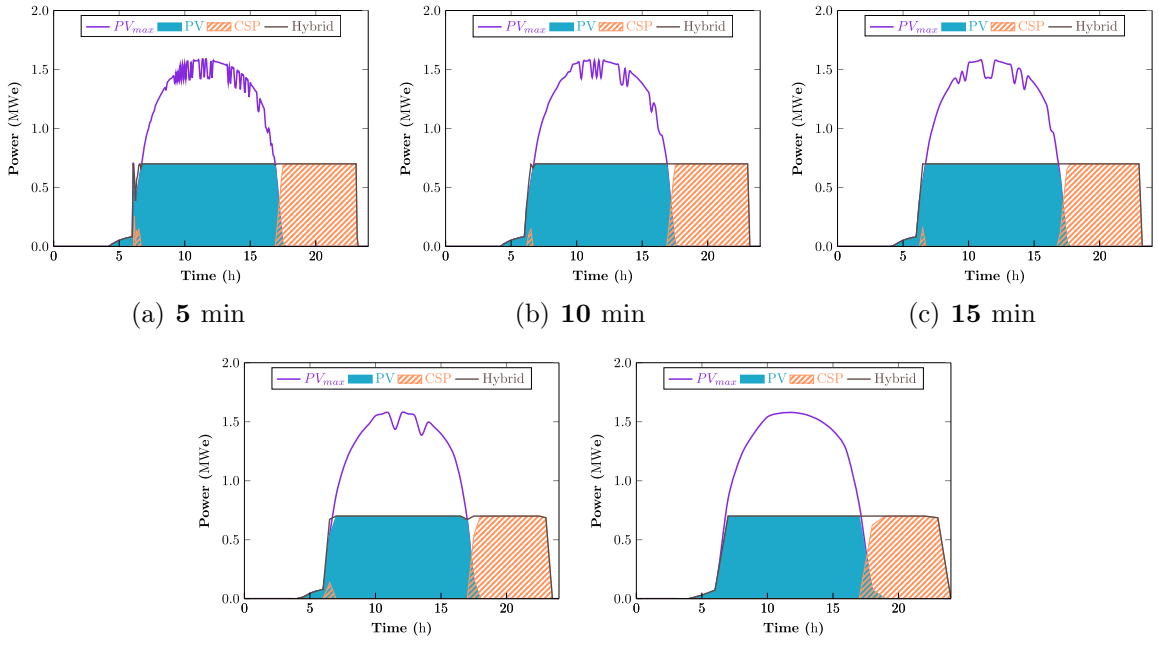

(a) **5** min (b) **10** min (c) **15** min

(d) **30** min (e) **60** min

Figure 3.10: Operation profile of the *1S* plant at **Antofagasta** January 13^{th}, 2018 for different time steps: (a) **5** min, (b) **10** min, (c) **15** min, (d) **30** min, and (e) **60** min.

- For both hybrid plants, the PV contribution, shown in blue (see Figures 3.10 and 3.11), varies marginally with increasing time step; at the same time, the CSP contribution is shifted to the night hours; which can be explained by the fact

that CSP is less solicited because PV production is sufficient to supplement the demand.

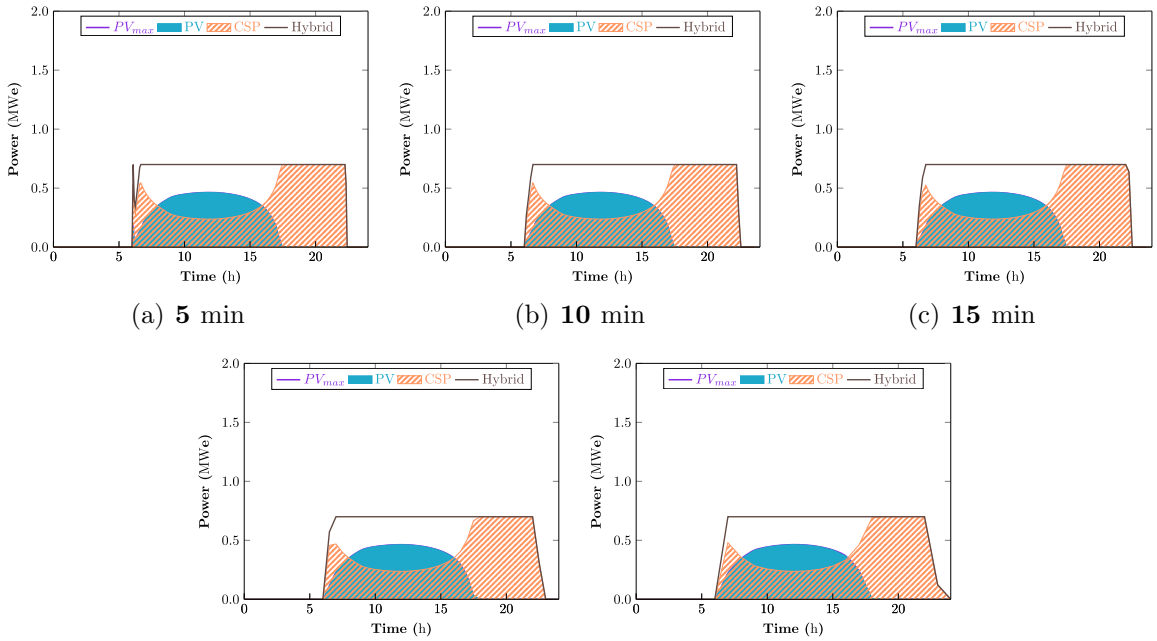

(a) **5** min (b) **10** min (c) **15** min

(d) **30** min (e) **60** min

Figure 3.11: Operation profile of the *HT* plant at **Antofagasta** January 13th, 2018 for different time steps: (a) **5** min, (b) **10** min, (c) **15** min, (d) **30** min, and (e) **60** min.

5.1.2 Yearly performance

Tables 3.7 and 3.8 present the total annual generation of each component of the hybrid plants as well as the conventional CSP plant, using different time steps together with the relative differences in comparison to the 5-minute results at two locations: Antofagasta, located in the Atacama Desert in northern Chile and Targassonne, presented earlier (see Chapter 2).

It is found that the annual production of the two *compact* hybrid systems and the CSP plant is overestimated as the time step increases in Antofagasta, with a maximum increase of 2% with the 60-minute data (Table 3.7), while in Targassonne, the yearly production of the three technologies is barely affected by the time resolution, with an underestimation of the annual generation with the 60-minute data of 1.2%, 0.8% and $\sim$ 2% for the *HT*, *1S* and conventional CSP plant, respectively (Table 3.8). This difference can be explained by the variation of the available solar resource with time resolution during highly variable days in both locations (see Figure B.14(a)), while minor differences can be noticed during clear-sky days (see Figure B.14(b)).

A relative difference of 3% may seem significant, but it can provide an enormous gain in computational time to study the best configuration and production conditions for the proposed solar technologies. A time resolution of 5 minutes requires around 7 hours to estimate the annual energy output of the solar technologies, compared to

Table 3.7: Annual total energy and relative differences with respect to 5 min results using different time steps for the two-hybrid and the standalone CSP plant at Antofagasta (CL).

Technology	Time step	Annual generation (MWh)			Relative difference (%)		
		PV	CSP	*Hybrid*	PV	CSP	*Hybrid*
HT	5 min	1125	2556	3681	—	—	—
	10 min	1122	2556	3678	0.24%	0.00%	0.07%
	15 min	1126	2559	3684	0.06%	0.10%	0.09%
	30 min	1139	2572	3712	1.27%	0.64%	0.83%
	60 min	1164	2605	3769	3.43%	1.92%	2.38%
1S	5 min	2442	1386	3828	—	—	—
	10 min	2439	1385	3824	0.14%	0.03%	0.10%
	15 min	2445	1386	3831	0.12%	0.01%	0.08%
	30 min	2472	1391	3862	1.21%	0.37%	0.91%
	60 min	2516	1401	3917	3.02%	1.12%	2.33%
Standalone CSP	5 min	—	3811	—	—	—	—
	10 min	—	3808	—	—	0.08%	—
	15 min	—	3815	—	—	0.10%	—
	30 min	—	3842	—	—	0.81%	—
	60 min	—	3897	—	—	2.24%	—

Table 3.8: Annual total energy and relative differences with respect to 5 min results using different time steps for the two-hybrid and the standalone CSP plant at Targassonne (FR).

Technology	Time step	Annual generation (MWh)			Relative difference (%)		
		PV	CSP	*Hybrid*	PV	CSP	*Hybrid*
HT	5 min	531	1594	2124	—	—	—
	10 min	531	1593	2124	0.03%	0.04%	0.02%
	15 min	531	1593	2123	0.01%	0.06%	0.04%
	30 min	530	1591	2121	0.08%	0.19%	0.16%
	60 min	519	1581	2099	2.23%	0.82%	1.17%
1S	5 min	1993	713	2705	—	—	—
	10 min	1993	713	2706	0.04%	0.01%	0.02%
	15 min	1994	711	2706	0.08%	0.17%	0.01%
	30 min	1996	709	2705	0.17%	0.53%	0.02%
	60 min	1991	693	2684	0.08%	2.79%	0.79%
Standalone CSP	5 min	—	2099	—	—	—	—
	10 min	—	2098	—	—	0.03%	—
	15 min	—	2097	—	—	0.09%	—
	30 min	—	2093	—	—	0.30%	—
	60 min	—	2060	—	—	1.86%	—

27 minutes with a time resolution of 60 minutes (see Table 3.9). More importantly, since the model does not precisely describe the operating controls of the PB unit, i.e., turbine startup and shutdown, consideration of a 60-minute time resolution can be highly justified [197], since the following operating conditions require a high level of description for the variability of the DNI resource, especially in locations with highly variable solar resources such as Targassonne.

Table 3.9: Variation of simulation time with increased time step.

Time step	Simulation time
5 min	7h 6min 3s
10 min	3h 6min 7s
15 min	2h 2min 18s
30 min	57min 2s
60 min	27min 30s

5.2 Impact of dispatch strategy

5.2.1 Daily performance

Figures 3.13 and 3.14 illustrate the power flow in the two *compact* PV-CSP hybrid plants with TES, including the power output of the PV and CSP sections, the overall hybrid plant output, the hot tank SOC, and the unmet power for four consecutive days (March 20^{th} – 23^{rd}, 2018) in Andheri (IN) (Figure 3.12), with the two dispatch strategies considered to provide a baseload demand of 0.5 MWe with 20 MWh_t of TES.

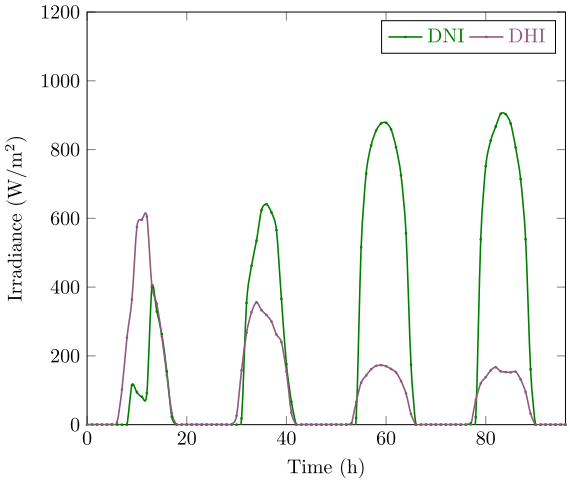

Figure 3.12: Solar resource components during four successive days (March 20^{th} – 23^{rd}, 2018) at **Andheri**.

- During the first two days of operation, the DNI was quite low (Figure 3.12), the hot tank was at its minimum level (P_{SOCmin}), and the required load could not be met regardless of the dispatch strategy considered (Figures 3.13 and 3.14). However, since the excess PV is used to charge the TES with the **DS2** strategy, after sunset, the *1S* hybrid plant can operate for a few additional hours compared to the **DS1** strategy, i.e., 2 hours on March 20^{th} and 4 hours on March 21^{st} (Figure 3.13(b)), a difference that stems from the large amount of energy available to charge the TES hot tank on March 21^{st} as shown in Figure 3.12. On the other hand, no difference can be noted between the two dispatch strategies for the *HT* plant (Figure 3.14) due to the absence of surplus PV and the lack of solar resource to charge the hot tank to expand production (Figure 3.12).
- Since the daily PV production of the *1S* hybrid plant is five times that of the *HT* hybrid plant (see Table 3.10), during the day, only PV provides the needed demand, and the excess power from the PV mirrors is stored in the TES (Figure 3.13(b)). Fewer hours of unmet supply are observed with the **DS2** strategy (Figures 3.13(b)), the excess energy being more effectively used to cover demand during nighttime hours for the *1S* hybrid strategy. In Figure 3.13(b), it can be seen that there is enough energy inside the hot tank to supply the demand until the early morning hour of the fourth day since the hot tank does not discharge to its minimum level.

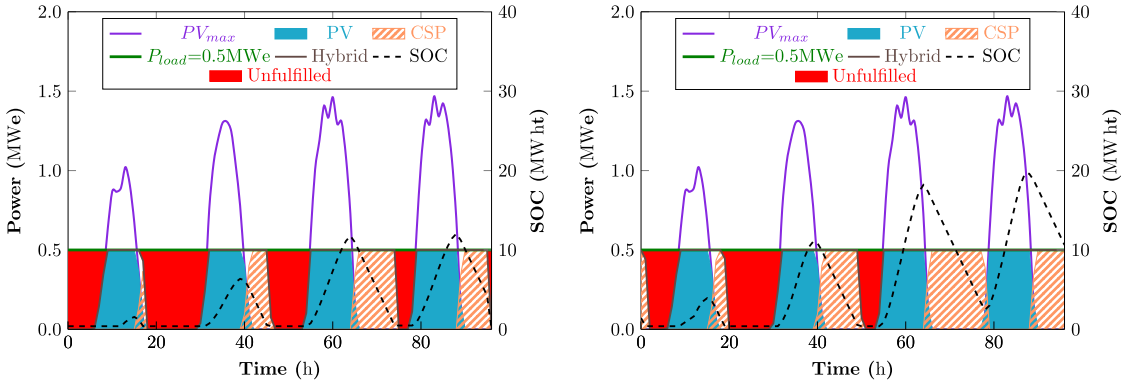

(a) **DS1** (b) **DS2**

Figure 3.13: Dispatchability of the *1S* hybrid plants considering a baseload profile of 0.5 MWe during four successive days (March 20^{th} – 23^{rd}, 2018) at **Andheri** with a 20 MWh_t TES using the two dispatch strategies: (a) **DS1** and (b) **DS2**.

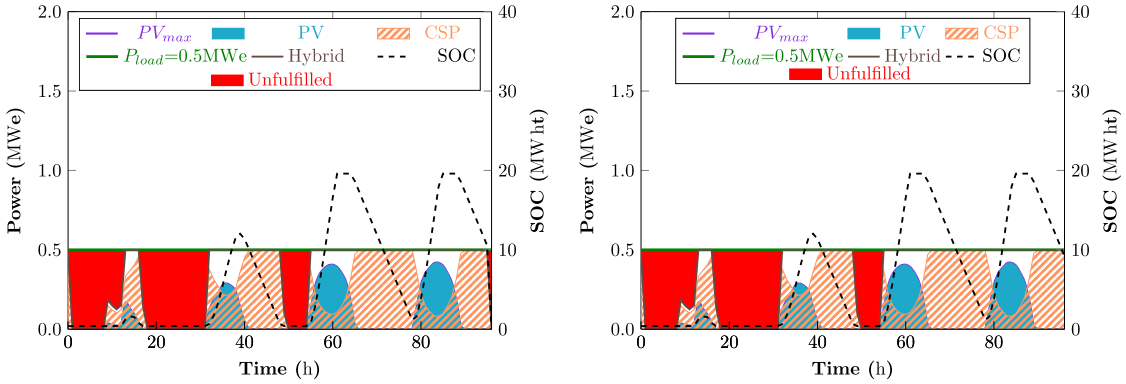

(a) **DS1** (b) **DS2**

Figure 3.14: Dispatchability of the *HT* hybrid plants considering a baseload profile of 0.5 MWe during four successive days (March 20^{th} – 23^{rd}, 2018) at **Andheri** with a 20 MWh_t TES using the two dispatch strategies: (a) **DS1** and (b) **DS2**.

Table 3.10: Daily total production March 21^{st}, 2018 at Andheri for a baseload demand of 0.5 MWe with 20 MWh_t for the TES system.

Hybrid technology	$Q_{PV\,max}$	Q_{PV}	**DS1** Q_{CSP}	**DS1** Q_{Hybrid}	**DS2** Q_{CSP}	**DS2** Q_{Hybrid}
			(MWh)			
1S	**9.45**	4.78	2.56	7.35	3.50	8.28
HT	**1.81**	1.81	6.19	8.00	6.19	8.00

- On the highly irradiated days (22^{nd} and 23^{rd}), the **DS2** provides continuous load supply without any interruption using the two-hybrid plants (Figures 3.13(b) and 3.14(b)). However, the demand was fully satisfied using the **DS1** strategy for the *HT* hybrid plant, as shown in Figure 3.14(a), as a result of the abundant amount of DNI resource (Figure 3.12) available at the receiver inlet.

5.2.2 Yearly performance

Figure 3.15 illustrates the annual energy production of the two-hybrid plants and for the 15 locations selected with the two dispatch configurations, for a baseload demand of 0.5 MWe with 20 MWh_t of TES.

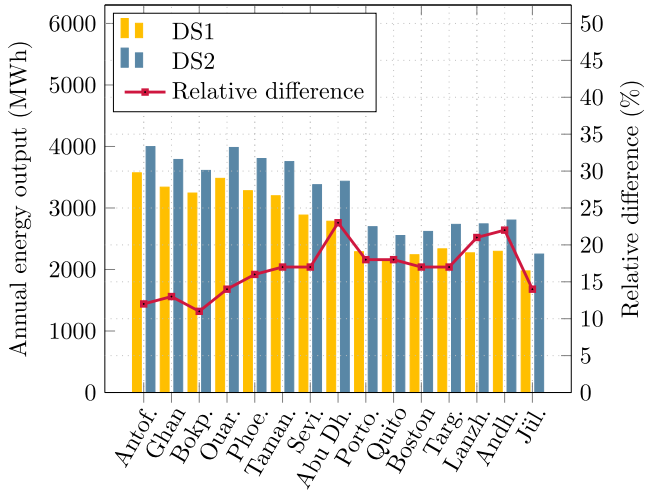

(a) *1S*

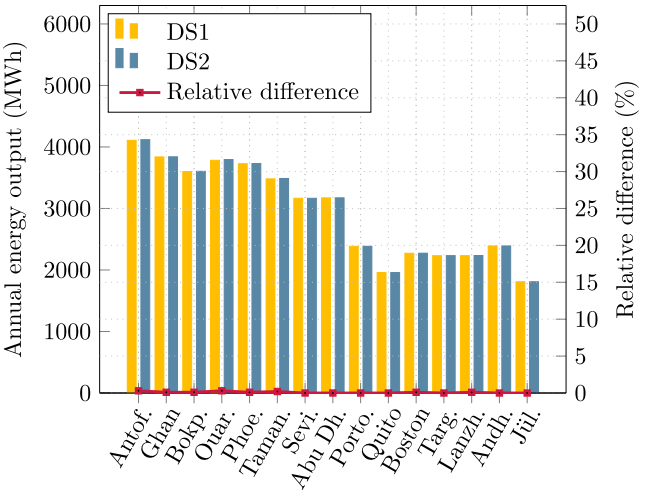

(b) *HT*

Figure 3.15: Annual total generation (left axis) and relative differences (right axis) using the two dispatch strategies in the selected locations for the: (a) *1S*, and (b) *HT* hybrid plants for a baseload of 0.5 MWe with 20 MWh_t of TES.

It is found that using the **DS2** approach with the *1S* hybrid plant results in an average increase of 17% in the annual energy output, with a maximum of 23% recorded in Abu Dhabi (Figure 3.15(a)), while no significant improvement is observed in the case of the *HT* hybrid plant (Figure 3.15(b)). This improvement in the energy output of the 1S approach stems from the ability of the **DS2** strategy to recover excess PV electrical energy in the form of heat, unlike the **DS1** strategy.
As an example, Figure 3.16 shows the monthly CSP production of the hybrid plants implementing the two operation modes in Abu Dhabi (UAE).

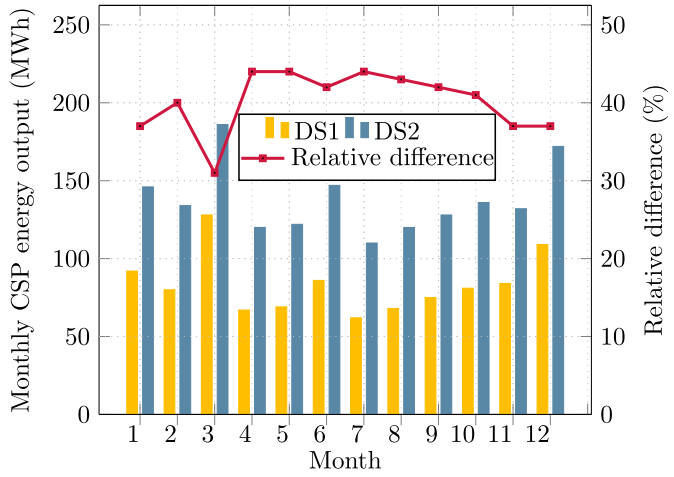

(a) *1S*

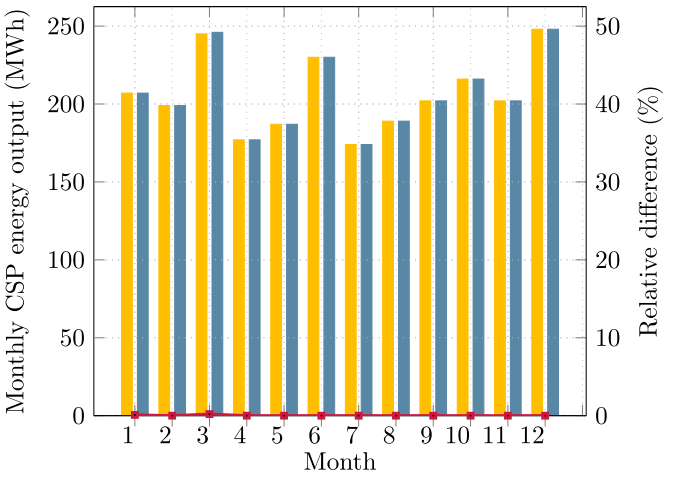

(b) *HT*

Figure 3.16: Monthly CSP production implementing **DS1** and **DS2** approaches, and the relative difference on the monthly production of the two-hybrid plants at Abu Dhabi: (a) *1S*, and *HT*.

The results for the *1S* hybrid plant show that the **DS2** approach is favourable for CSP production for all months of the year, with a maximum of 44% during the summer months and a minimum of 31% in March (Figure 3.16(a)). This sudden decrease is directly related to 1) a large amount of energy available for the PV mirrors (i.e., DNI resource shown in Figure 3.17) and 2) the low electrical demand (0.5 MWe). The combination of these two factors results in a higher amount of excess PV that cannot be efficiently recovered using the **DS2** approach since there is no room for additional energy in the hot tank. On the other hand, there is no significant increase in the monthly output of the *HT* hybrid plant (Figure 3.16(b)), which is consistent with the annual results presented in Figure 3.15(b).

The amount of dumped energy is simply the sum of PV and CSP dumped electrical energy. To ensure the coherence of this indicator, the thermal energy dumped from

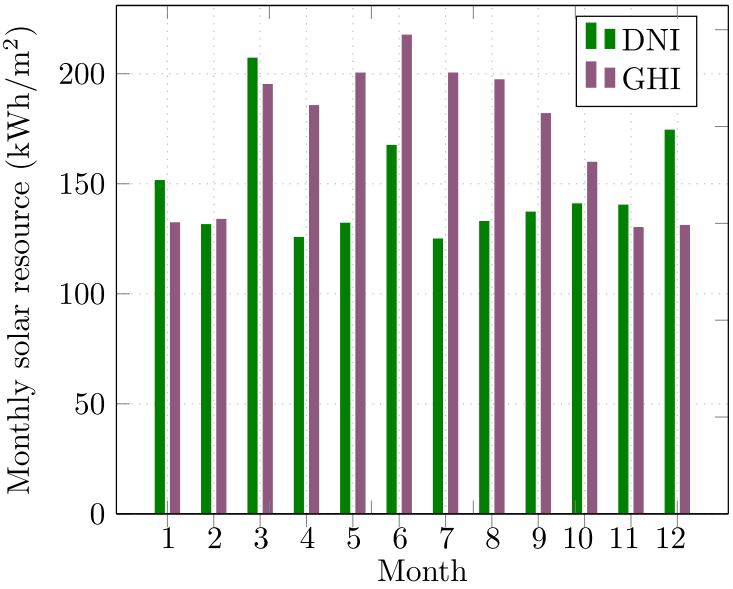

Figure 3.17: Monthly solar resource distribution of Abu Dhabi.

the CSP converter is translated into electrical energy:

$$Q_{dum}(i) = \sum_{i=1}^{8760} Q_{dum,\ pv}(i) + \eta_{pb} \sum_{i=1}^{8760} Q_{dum,\ csp}(i) \tag{3.29}$$

Additionally, Figure 3.18(b) shows that the receiver experiences some energy curtailments with the **DS2** approach, which is related to the fact that recovering the excess PV (Figure 3.18(a)) allows the hot tank to charge rapidly, thus leaving a small amount of room for the thermal energy impinging the heliostats to charge the hot tank. By increasing the value of P_{load} while keeping the storage capacity constant, the PV curtailments of the *1S* hybrid plant decrease (Figure 3.19(a)), resulting in 100% recovery of excess PV with the **DS2** (Figure 3.19(b)). For the *HT* hybrid plant, increasing P_{load} causes the elimination of energy curtailments at the receiver level for every month of the year, regardless of the dispatch strategy considered (Figures 3.19(a) and 3.19(b)).

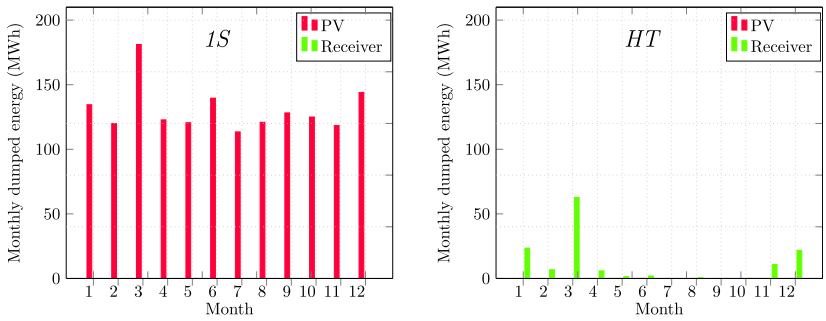

(a) **DS1**

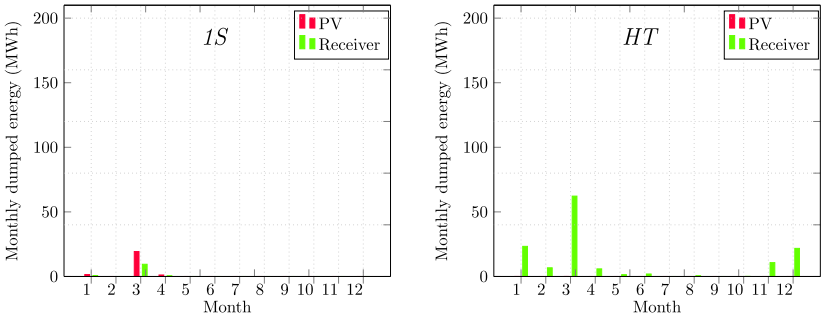

(b) **DS2**

Figure 3.18: Monthly dumped energy of the PV and CSP subsections of the two-hybrid plants: *1S* (left plot), *HT* (right plot), using the two dispatch strategies at Abu Dhabi for a baseload demand of 0.5 MWe and a 20 MWh_t of TES: (a) **DS1**, and (b) **DS2**.

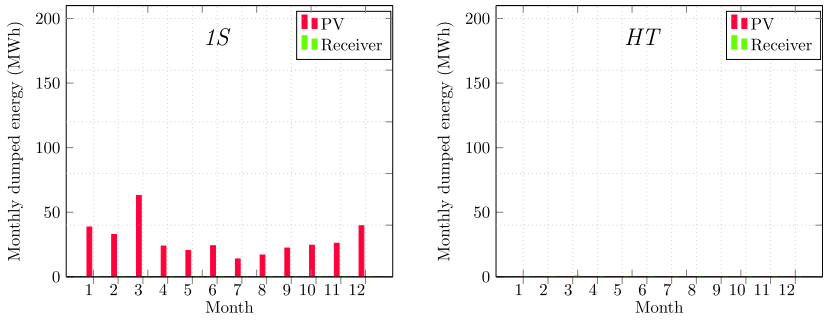

(a) **DS1**

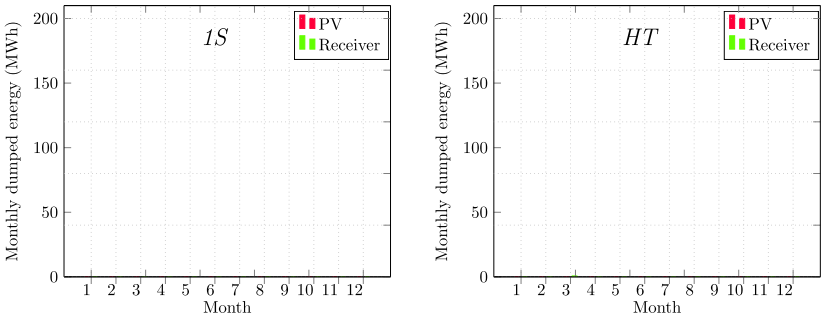

(b) **DS2**

Figure 3.19: Monthly dumped energy of the PV and CSP subsections of the two-hybrid plants at Abu Dhabi for a baseload demand of 1 MWe and a 20 MWh_t of TES: (a) **DS1**, and (b) **DS2**.

Figure 3.20 shows the annual energy dumped from the two-hybrid plants at the 15 locations. The use of the **DS2** within the *1S* hybrid plant results in less energy curtailments regardless of location (Figure 3.20(a)). As mentioned earlier, no significant difference can be observed between the two dispatch strategies with the *HT* hybrid plant (Figure 3.20(b)).

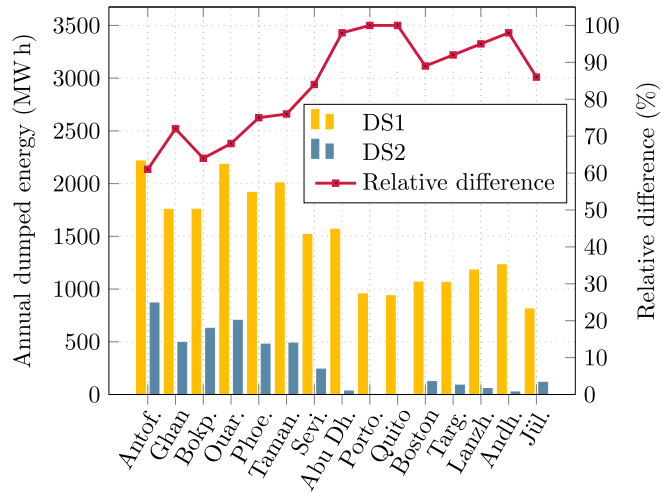

(a) *1S*

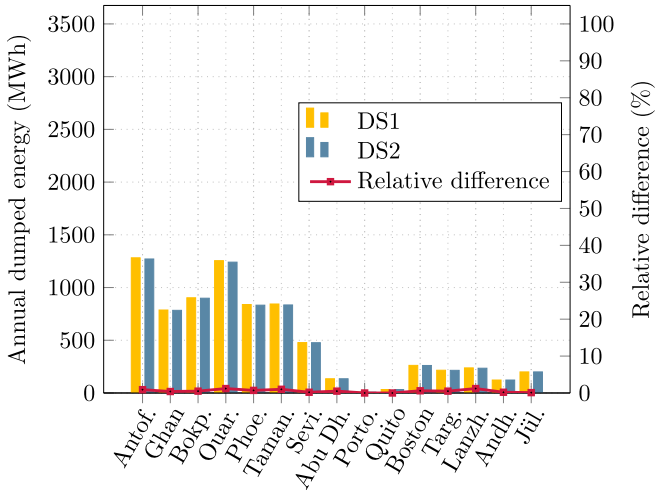

(b) *HT*

Figure 3.20: Annual dumped energy (left axis) and relative differences (right axis) using the two dispatch strategies in the selected locations to supply a baseload demand of 0.5 MWe with 20 MWh_t of TES for the: (a) *1S*, and (b) *HT* hybrid plants.

To further highlight the advantage of the **DS2** approach over **DS1** approach, Figures 3.21 and 3.22 show the alterations of the recovery ratio (η_{recov}) as a function of P_{load} and TES capacity for the *1S* and *HT* hybrid plants, respectively. We observe that the η_{recov} ratio increases with increasing P_{load} and storage capacity, varying more significantly for the *1S* hybrid plant than for the *HT* approach.

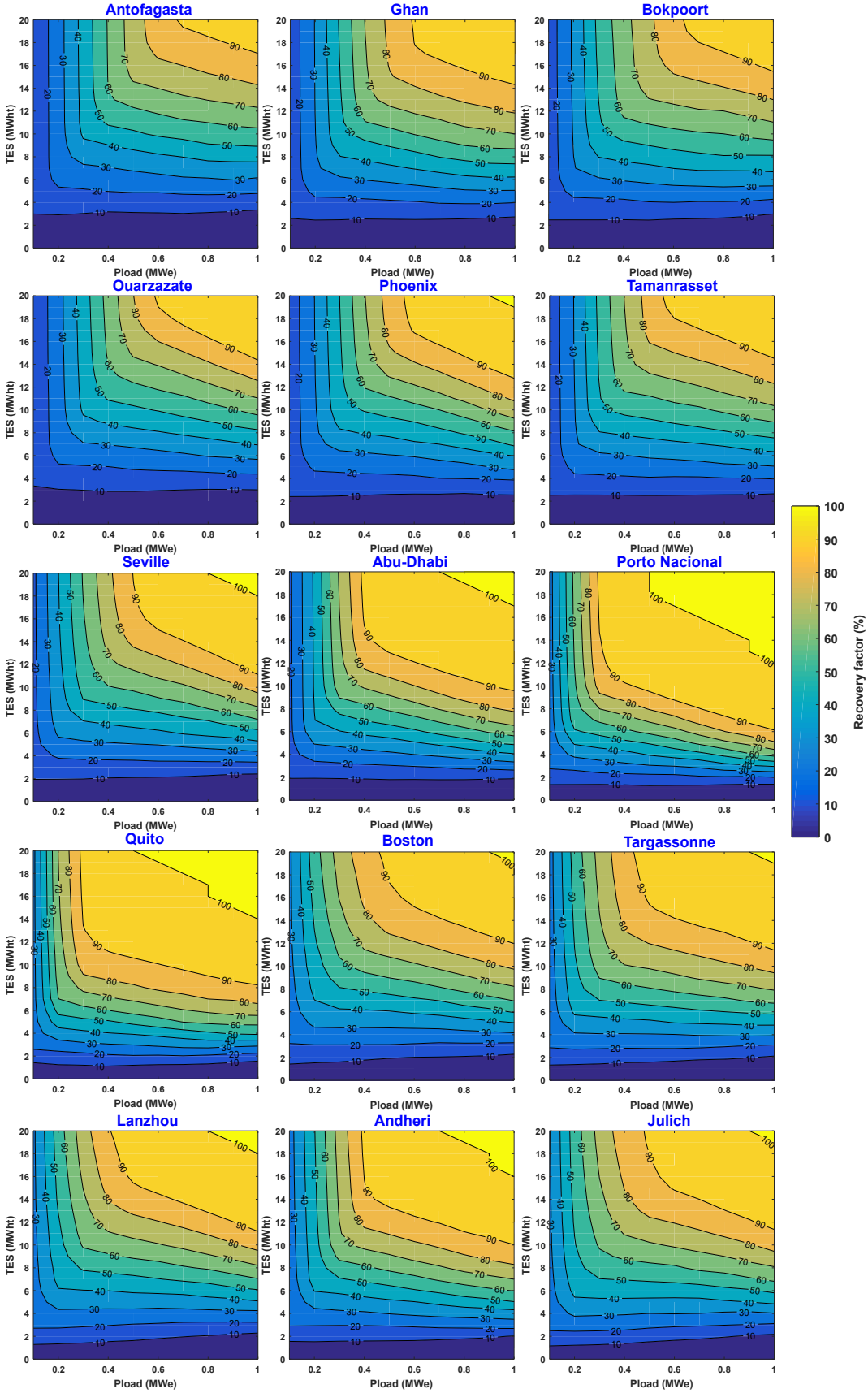

Figure 3.21: Recovery ratio of the *1S* hybrid plant at the selected locations considering the **DS2**.

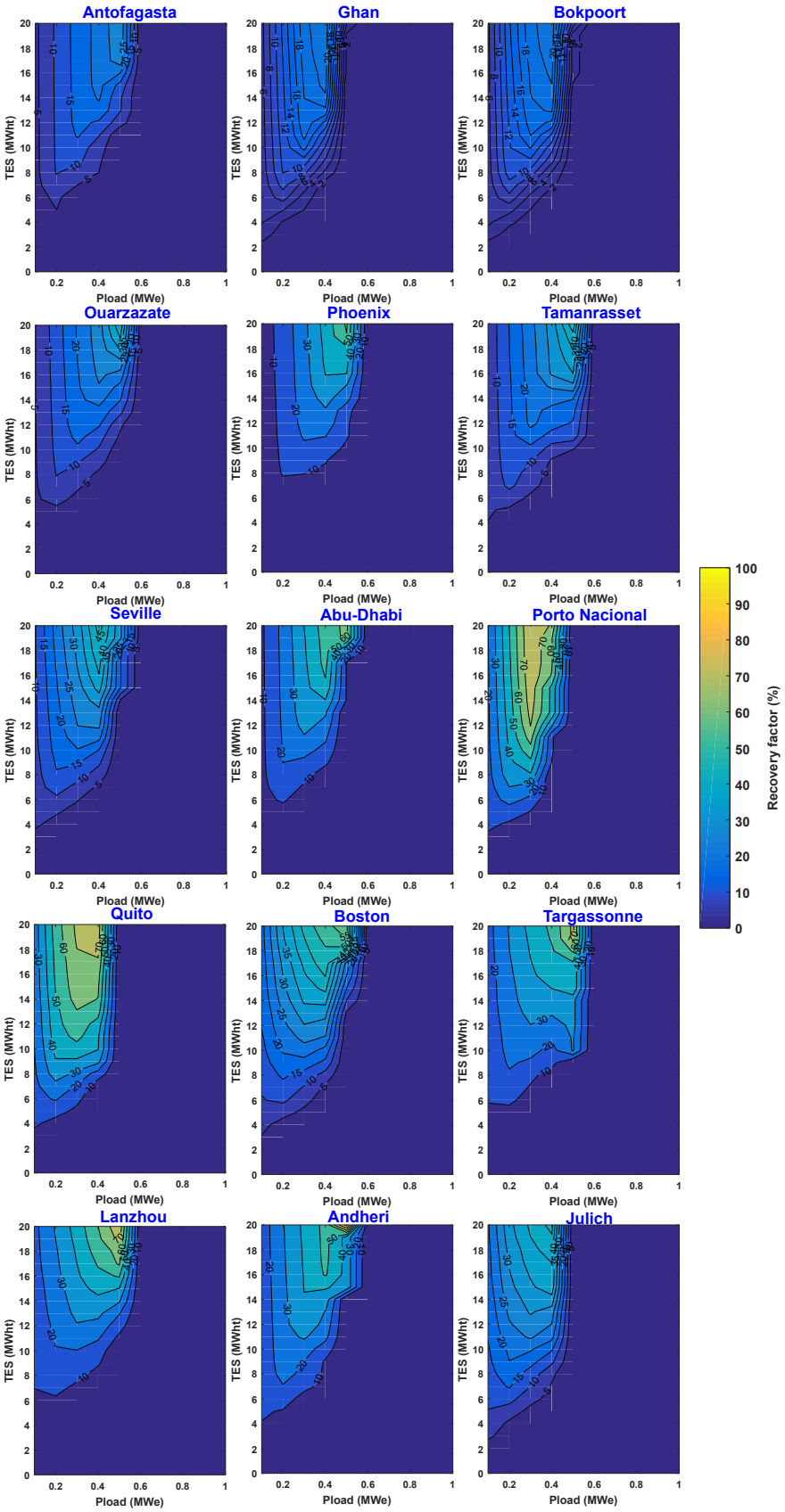

Figure 3.22: Recovery ratio of the *HT* hybrid plant at the selected locations considering the **DS2**.

For a more visible illustration, Figures 3.23 and 3.25 illustrate the variation of the η_{recov} ratio with the TES capacity of the two-hybrid plants for four different load demand values at three different locations, Ghan in northern Australia, a location with very high solar resource, Seville located in the southwestern Iberian Peninsula with a medium solar resource, and finally Jülich the location with the lowest DNI profile (see Table 3.2).

- Regardless of the location considered, the recovery ratio increases linearly with increasing TES capacity, up to an inflexion point above which the improvement in the recovery ratio varies smoothly. For example, in Ghan, when the *1S* hybrid plant is operated to provide an electrical demand of 0.2 MWe, the hot tank overflows with thermal energy (Figure 3.24(a)), i.e. only half of the thermal energy in the hot tank is discharged, leaving the hot tank at three times P_{SOCmin}. Therefore, neither the abundant DNI resource (Figure B.16) nor the excess PV energy can be recovered, which explains the stable behaviour of the recovery factor with increasing storage capacity.

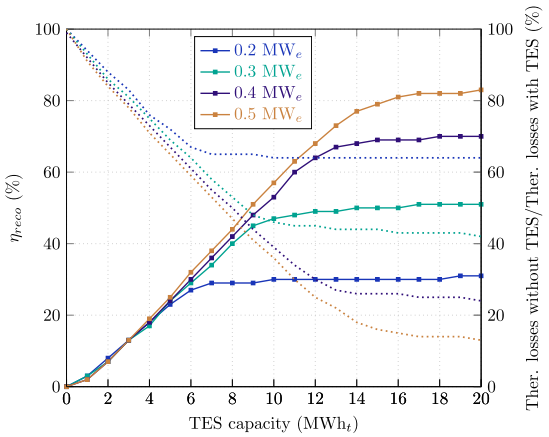

(a) Ghan (AU)

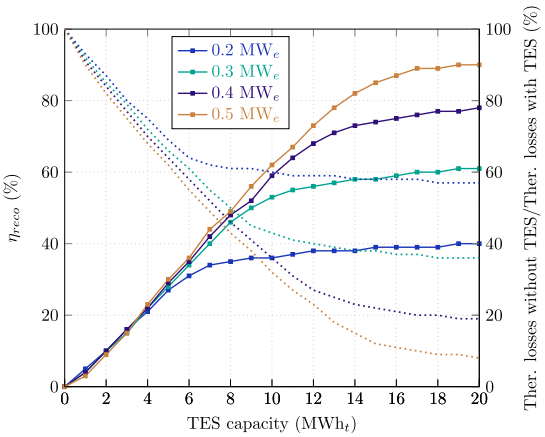

(b) Seville (ES)

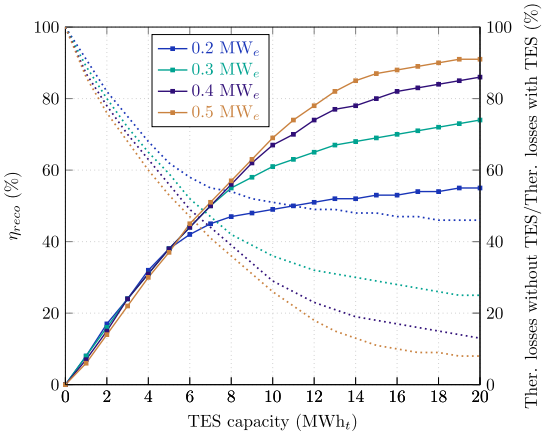

(c) Jülich (DE)

Figure 3.23: Variation of the recovery ratio with increasing TES capacity for different P_{load} values of the *1S* plant at: (a) Ghan, (b) Seville, and (c) Jülich.

By doubling the electrical demand, the PV generation is used more effectively during daytime, and as a result, the hot tank discharges much more efficiently, reaching P_{SOCmin}(=0.24 MWh) during the five days of operation, as shown in Figure 3.24(b). At Jülich, the near-constant region is less visible (Figure 3.23(c)), primarily due to the poor weather conditions that do not allow efficient charging or discharging of the TES hot tank for both electrical demands (Figure 3.24).

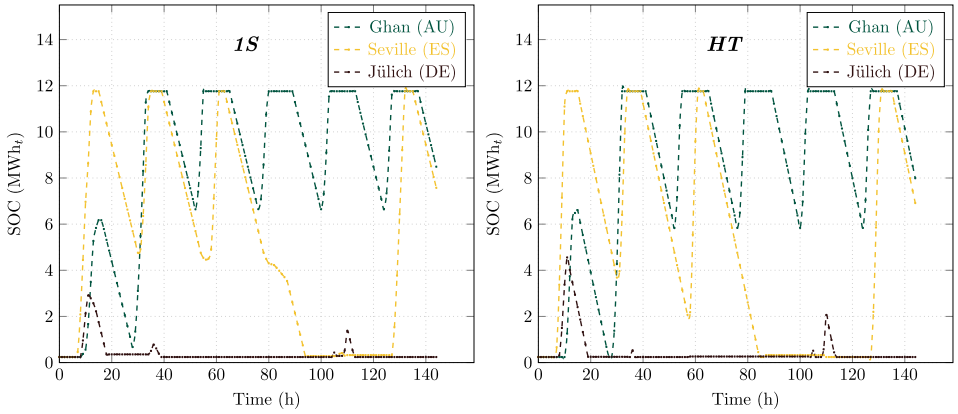

(a) 0.2 MWe

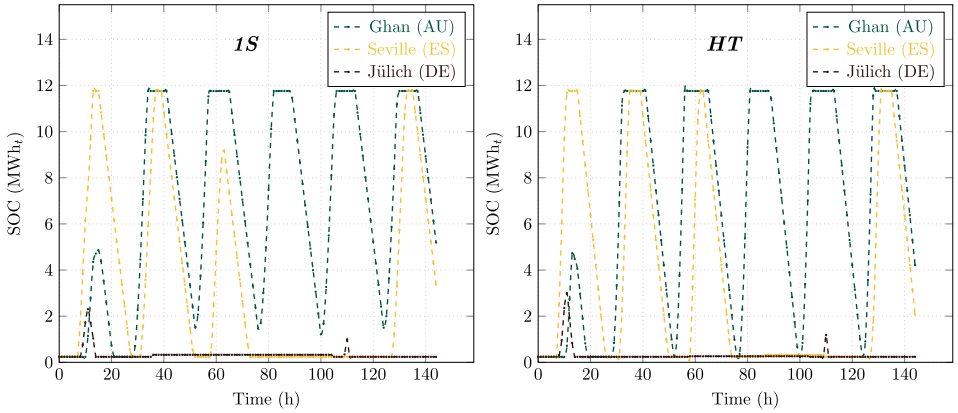

(b) 0.4 MWe

Figure 3.24: The instantaneous capacity of the solar salt in the hot tank at three locations and for the *1S* (left graph) and *HT* (right graph) hybrid plants for two baseload demands with 12 MWh$_t$ during six successive days (January 1^{st} – 6^{th}, 2018).

- For the *HT* hybrid plant, we find that the recovery ratio remains nil for low TES capacities because charging of the hot tank is subject to certain priorities, i.e., excess CSP energy is first used to charge the TES and only when additional space is available can surplus PV energy be recovered with the **DS2** as shown by the dotted line in Figure 3.25. In Seville, for a baseload demand of 0.5 MWe, the recovery ratio remains nil when the storage capacity increases from 0 to 12 MWh$_t$, as the TES unit is fully charged by the abundant thermal energy from the heliostat field. Between 12 and 20 MWh$_t$ the recovery ratio increases according to a staircase function due to the sudden decrease in the amount of energy recovered from the PV receiver, from 0.134 MWh to 0.09 MWh, respectively. The two steps

in Figure 3.25, can be justified by the quasi-constant variation in the amount of PV rejected after recovery (see Figure B.28) due to the charging priority of the hot tank, which translates into a continuous linear decrease of thermal energy curtailments since the hot tank is being charged efficiently with surplus energy from the solar field. For the *1S* hybrid plant, the thermal losses experience a near-constant variation for high storage capacities (see Figure B.29), which explains the lack of any steps for the variation in the recovery ratio (Figure 3.23).

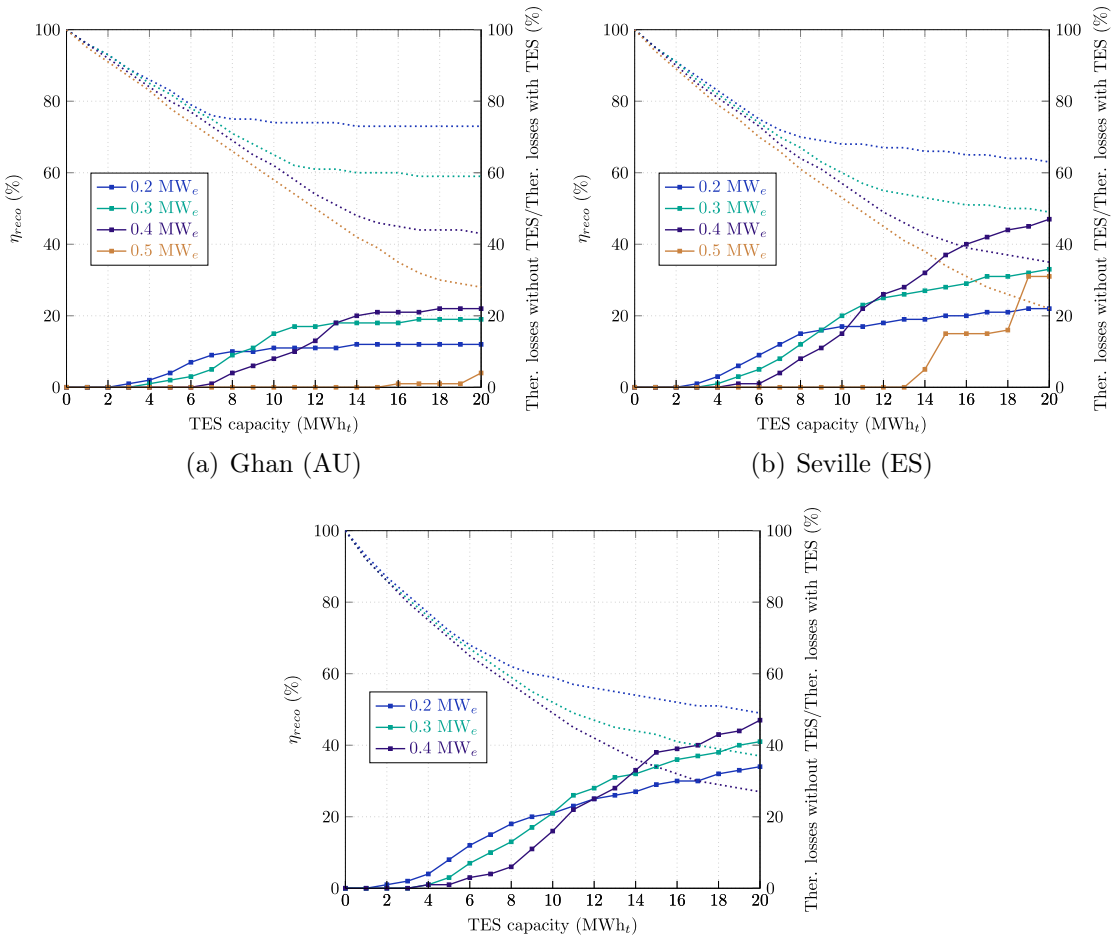

(a) Ghan (AU)

(b) Seville (ES)

(c) Jülich (DE)

Figure 3.25: The variation of the η_{recov} ratio with increasing TES capacity for different P_{load} values of the *HT* plant at: (a) Ghan, (b) Seville, and (c) Jülich.

Figure 3.26 illustrates the variation of excess PV curtailed after recovery with increasing TES capacity at the three selected locations. It can be noticed that the variation of η_{recov} of the two-hybrid plants follows the same variations of the excess PV. However, the different shapes observed between the *1S* and the *HT* hybrid plant can be explained by the nature and the amount of excess energy recovered by each of the hybrid plants.

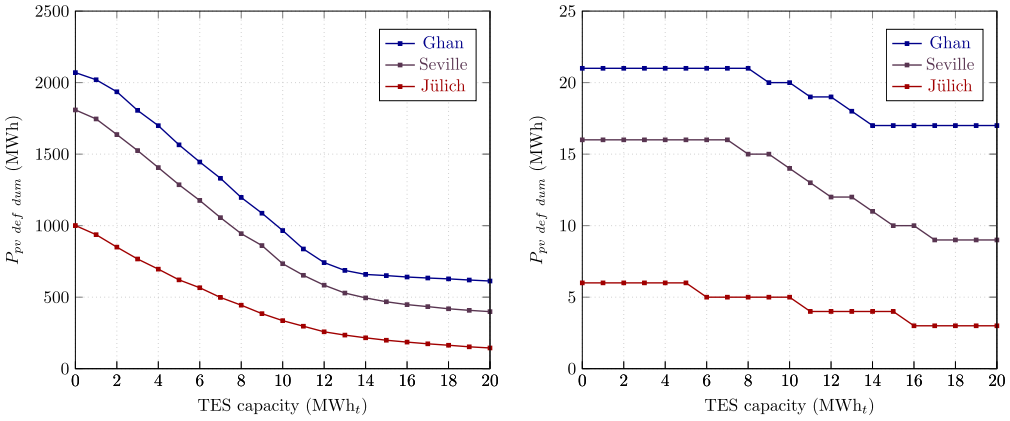

(a) *1S* (b) *HT*

Figure 3.26: The variation of excess PV definitely dumped $P_{pv,\ def\ dum}$ as a function of TES capacity at the three locations to supply a baseload demand of 0.4 MWe.

Summary

In this chapter, we have described how the integration of TES within the two-hybrid plants can be achieved using two dispatch strategies. The first aims to maximize the use of PV generation when it is available. The second offers two additional advantages over the first dispatch strategy. First, when PV production is less than the electrical demand, priority is given to the CSP and TES to minimize the turbine shutdown and thus maximize the operation of the PB unit, i.e., PV is used to complete the demand. Second, it provides the opportunity to recover excess PV energy via an electric heater feeding the TES to reduce the power rejection and meet the load demand. Different locations in the world were selected, and Solcast SDB meteorological data were used. From the first results obtained, several important conclusions can be drawn:

- ☞ Choosing a 60-minute time step will result in an overestimation or underestimation of approximately 2% of the total annual output of the two-hybrid plants and the standalone CSP system. Time steps between 10 and 15 minutes also provide a good balance between computational time and capturing the realistic behaviour of both subsystems. However, since the goal of this study is to investigate the energy capabilities of the *compact* PV-CSP hybrid plants versus other solar technologies under different weather conditions, the consideration of a 60-minute time resolution is valid as long as we identify the limitations of the model and the results obtained.

- ☞ The use of the **DS2** approach proved to be well suited to the *1S* hybrid plant as it increases the overall productivity of the plant while maintaining a good load demand matching, especially for low baseload demand profiles. In contrast, the use of **DS2** with the *HT* plant proved to be less attractive. Therefore, in what follows, the comparison between the different solar technologies will be conducted by considering **DS2** as a dispatch strategy for both hybrid plants.

With the integration of the TES system in the two-hybrid plants, it is worthwhile

to identify the efficiency of the proposed systems compared to standalone technologies, namely CSP and conventional PV plants, to identify the main pros and cons. In the following chapter, we try to identify the position of hybrid technologies compared to conventional technologies under different operating conditions.

Chapter 4

Solar technologies with storage systems: which technology in which location?

In this chapter, the behaviour of the two compact hybrid technologies will be assessed and compared to three conventional solar technologies integrating energy storage systems (TES and BESS). The impact of different weather conditions on the performances of the solar technologies will then be evaluated, by considering constant load and variable load demand profiles along a whole year of operation and using high accuracy satellite-based data. Calculations are performed using the model presented in the previous chapter.

Introduction

The comparison of performance indicators of *non-compact* PV-CSP hybrid plant with conventional solar technologies has been widely discussed recently, including the economic reliability of hybridizing the two subsystems. Zurita et al. [324] investigated the techno-economic feasibility of *non-compact* hybrid plant compared to conventional plants with different storage technologies by considering the implementation of four different dispatch strategies. The results showed that designing solar power plants to achieve a minimum LCOE may not be the most appropriate approach when a certain level of supply needs to be guaranteed, especially for baseload and nighttime dispatch strategies. More importantly, PV-CSP hybrid plants (with or without BESS) were found to be the most competitive option when long-duration storage is required in baseload demand case study, as they represent the only option that can reach capacity factors above 85% with moderate costs [324]. In the same optic, Behar et al. [70] conducted a comparison between different solar technologies used for integration in existing copper mining plants located in Chile. The results indicated that a standalone PV and a *non-compact* PV-CSP hybrid plant present good opportunities for integration into the existing mining plants. Meanwhile, further efforts are needed to reduce the capital costs of CSP technology to make it attractive as an energy source for the copper mining industry. As the working principle of the two-hybrid configuration, *non-compact*

and *compact*, is completely different, it is difficult to conclude regarding the technical interest of the proposed hybrid technologies compared to standalone plants. Therefore, in this chapter, we propose to answer the question of whether or not *compact* hybrid plants can achieve the highest production performance with a certain level of supply guarantee, considering different demand profiles (baseload and variable profile at some of the selected locations), and solar resource conditions. In this context, five technology combinations are compared: the *1S* hybrid plant, the *HT* hybrid plant, a CSP-TES plant, a PV-BESS plant with lithium-ion batteries, and a PV-TES plant. The performance indicators evaluated in this work are the annual energy production, the capacity factor (CF), the demand factor (DF) and the loss of power supply probability (LPSP).

1 Conventional PV plants

The conventional PV power plant includes PV panels, an inverter and two different storage facilities (see Figures 4.1 and 4.2). Two PV plants with mono-crystalline-Si as a cell technology were studied and compared. The first PV plant consists of a fixed-tilt module configuration, whereas the second PV configuration uses a single-axis tracking system allowing a maximization of the power output. Table 4.1 summarizes the main parameters of the conventional PV plant.

Table 4.1: Main parameters of both conventional PV plant.

Reference operating conditions	
Cell technology	mono-Si
Temperature coeff. of power, β_{ref}	-0.35 (%/K) [338]
Area of the PV module, A_{pv}	2 m^2
Number of fixed PV modules, $M_{mod,\ fix}$	3050
Number of single axis PV modules, $M_{mod,\ 1axe}$	3040
η_{inver}	0.978 [73, 206, 217, 218, 325]
$\eta_{PV,\ exp}$	20.5% [103]
f_{lpv}	0.9

1.1 Fixed-tilt PV plant

For the fixed tilted PV system, the tilt angle (i.e. the angle at which the panels are mounted relative to horizontal) is noted ς_{fix} and is taken equal to the location latitude as it maximizes the annual PV energy production [339–342].
The power output of a PV plant at each time step can be given by [73]:

$$P_{pv}(i) = M_{mod}\, A_{pv}\, \eta_{inver}\, f_{lpv}\, G_{inc}(i)\, \eta_{pv}(i) \tag{4.1}$$

where, M_{mod}, A_{pv}, η_{pv}, η_{inver}, and f_{lpv} are the number of PV modules, the area of each PV module, the PV module efficiency computed using Eq. (2.15), the inverter efficiency, and finally the derating factor accounting for soiling of the panels, wiring

losses, shading, snow cover, ageing and other secondary losses. The cell temperature is estimated using Eq. (2.16), replacing the GHI value by the global tilted solar radiation G_{inc}, which is better suited here because it accounts for ground reflected irradiation given by the following equation [343]:

$$G_{inc}(i) = DNI(i)\,\cos(\theta) + R_d\,DHI(i) + I_{refl}(i) \tag{4.2}$$

where R_d is the ratio between the average daily diffuse solar radiation on a tilted surface, to that on a horizontal surface. The isotropic sky model [344] assumes that all the diffuse solar radiation is uniformly distributed over the sky, i.e., it is independent on the azimuth and zenith angles [344]. In this limit, R_d can simply be written as:

$$R_d = \frac{1 + \cos(\varsigma_{fix})}{2} \tag{4.3}$$

I_{refl} is the irradiation reflected by the ground calculated by Eq. (4.4), which depends on the albedo of the surface, that is comprised between 0 and 1 [345].

$$I_{refl}(i) = \frac{1 - \cos(\varsigma_{fix})}{2}\,\rho\,GHI(i) \tag{4.4}$$

The angle of incidence θ is extracted from the relationship between the orientation of the module (characterized by ς the tilt angle and γ_s the surface azimuth angle (see Table 3.2)) and the sun's position for a given location (α the solar altitude (Eq. (A.1)), and γ the solar azimuth angle (Eq. (A.3))); it can be calculated as follow [43]:

$$\cos(\theta) = \sin(\alpha)\,\cos(\varsigma_{fix}) - \cos(\alpha)\,\cos(\gamma - \gamma_s)\,\sin(\varsigma_{fix}) \tag{4.5}$$

where γ_s is the surface azimuth angle that specifies the direction on the horizon towards which the PV panels are facing [43] as shown in Figure A.1. Values are found between -180 and 180 °.

1.2 Single-axis tracking PV plant

For a plane rotated around a horizontal north-south axis, the angle of incidence is expressed as [43]:

$$\cos(\theta) = \left(\cos^2(\theta_z) + \cos^2(\delta)\,\sin^2(\omega)\right)^{1/2} \tag{4.6}$$

where θ_z, δ and ω are the zenith angle, the solar declination and the hour angle respectively described in Appendix A.
The tilted angle of a single-axis tracking system is given by [43]:

$$\tan(\varsigma) = \tan(\theta_z)\,|\cos(\gamma - \gamma_s)| \tag{4.7}$$

where γ_s can take two values depending on the sign of the sun azimuth angle [43]:

$$\gamma_s = \begin{cases} 90° & \text{if } \gamma > 0 \\ -90° & \text{if } \gamma \leq 0 \end{cases} \tag{4.8}$$

It is worth mentioning that the literature documentation on f_{lpv} is very scarce with values varying around 0.8 [218, 346], as a result, we decided to consider using PVsyst software to identify the exact value of f_{lpv} at a given location (Porto Nacional) (more details on the validation with PVsyst will be given in section 5), then the obtained value was using among the input parameters in our model. After adding the global losses of PVsyst, the value of f_{lpv} was found to be equal to 0.93. Table 4.2 summarizes the annual energy output obtained using PVsyst and our model. As can be seen in Table 4.2, the relative difference is lower than 1%.

Table 4.2: Annual energy production of a fixed-tilt PV plant located in Porto Nacional (BR) and the relative difference between PVsyst and our model.

f_{lpv}	Annual energy generation (MWh)		
	PVsyst	Model	Relative difference (%)
0.93	1629	1619.5	0.58 %

Overestimating losses due to soiling, wiring and shading, which are accounted for in the derating factor, will result in significant differences that do not describe the behaviour of actual PV installations. Meanwhile, considering a derating factor of 0.9 for both PV configurations may present an optimistic case study rarely encountered in the literature, but with efforts to address the different loss mechanisms, it could be achieved in the coming years. Therefore, we consider a derating factor of 0.9 for both PV configurations and all 15 locations.

1.2.1 PV with thermal energy storage

The combination of PV with TES has been suggested recently as an alternative way of storing the extra energy produced by PV panels [33]. In this unusual configuration, electricity is transformed into heat via an electric heater almost without losses (100 % conversion efficiency) (Figure 4.1). However, to make thermal storage for electricity storage competitive, the efficiency loss of energy transformation from electricity to heat and back has to be compensated by the cost advantages of the TES and the PV modules.

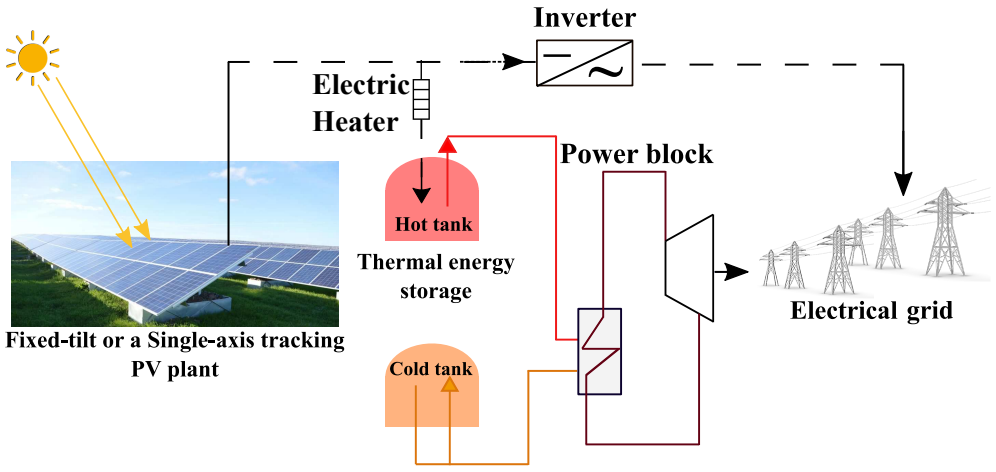

Figure 4.1: Schematic description of the conventional PV plant integrated with TES.

1.2.2 PV with battery energy storage system

The introduction of BESS in PV power generation is an effective solution to the shortcomings of PV power generation, due to the ability of BESS to transfer energy effectively and smooth out the PV power output quickly. When the PV output power is greater than the load demand, the surplus PV power is stored in the battery for a time-shifted use when the PV output power cannot meet the load demand (Figure 4.2). In this study, a Li-ion battery is assumed as the BESS technology with a maximum discharge rate of 96%.

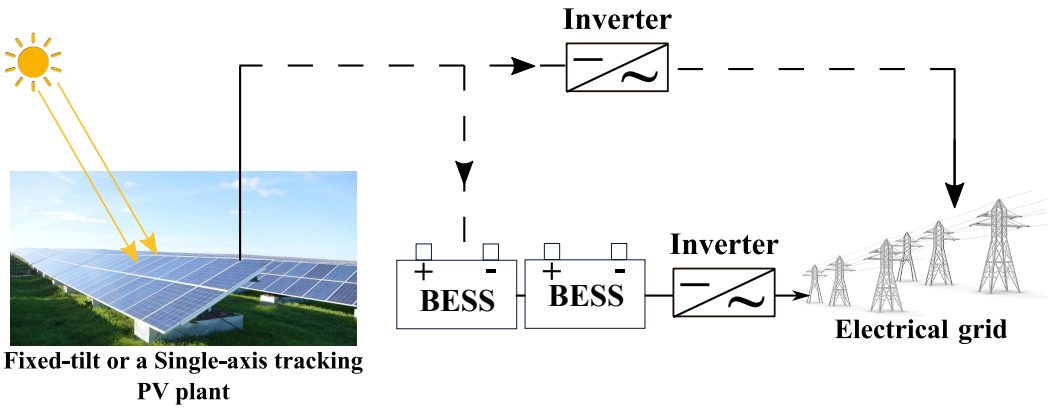

Figure 4.2: Schematic description of a conventional PV plant with BESS using Li-ion.

2 Storage integration modes

2.1 Conventional PV with TES

Here the integration of TES in a conventional PV plant (fixed-tilt or a single-axis tracking technology) is discussed, choosing an operating strategy that aims to minimize energy curtailments and promote PB unit operation, referred to as **DS2** approach in section 3.1.2 of chapter 3. Figure 4.3 depicts the power dispatch strategy and key components of a PV-TES plant.

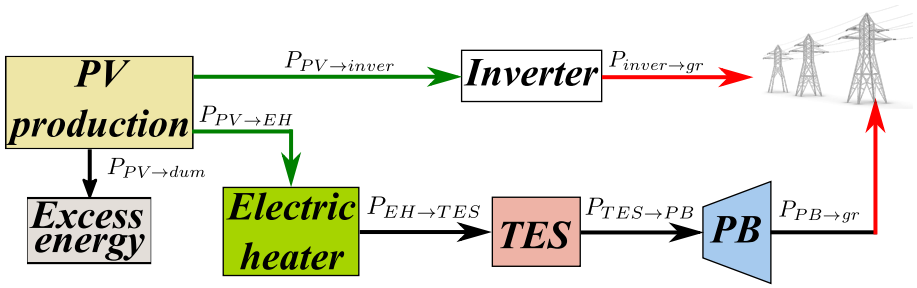

Figure 4.3: Simplified PV with TES model, containing the four plant components.

Figure B.7 shows a flowchart describing the operation of a PV-TES plant. The operation modes considered in this work follow the steps below:

1. If P_{pv} is above P_{load}, PV generation is sufficient to cover the load, while the surplus PV power is used to charge the hot tank. If the TES is fully charged, the surplus energy from the PV plant is spilt (Eq. (4.9)).

$$P_{pv,\ dum}(i) = [P_{pv}(i) - P_{pv,\ gr}(i)] - [P_{SOCmax} - P_{SOC}(i-1)] \tag{4.9}$$

2. If P_{pv} output is below P_{load}, the PV power is entirely sent into the electrical grid, and the hot tank is discharged at a minimum rate to supply P_{need} (Eq. (3.11)).

$$P_{TES,\ gr}(i) = \eta_{pb}\, P_{need}(i) \tag{4.10}$$

3. If the TES does not have enough energy to supply P_{need} but has enough energy to power the PB at a minimum rate, then $P_{TES,\ gr}$ is given by equation (4.11). If there is not enough energy available at the hot tank inlet to provide P_{need} and power the turbine at a minimum rate $P_{min,\ pb}$, then the SOC of the TES remains unchanged (Eq. (4.12)) while all PV power is sent to the grid (see Figure B.7).

$$P_{TES,\ gr}(i) = \eta_{pb}\ [P_{SOC}(i-1) - P_{SOCmin}] \tag{4.11}$$

$$P_{SOC}(i) = P_{SOC}(i-1) \tag{4.12}$$

2.2 Conventional PV with BESS

The integration of a BESS into a conventional PV plant presents a practical solution for rapid response to instant fluctuations in the PV outputs as opposed to a TES system that may require as much as 1 – 2 hours before the turbine starts operating [27]. Figure 4.4 illustrates the main power flows associated with the operation of a PV-BESS plant.

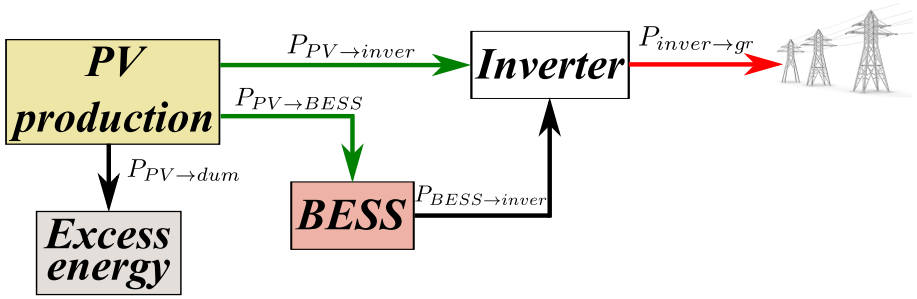

Figure 4.4: Simplified PV with BESS model, summarizing the main power flows.

There are two operation modes of a PV-BESS plant described in Figure B.8.

1. If the PV production is sufficient to cover the load, the required amount of electrical energy is sent to the electrical grid while the BESS is charged with the excess PV energy. The values of P_{SOCmax} and P_{SOCmin} are calculated using the same equations as for a TES system (Eqs. (3.5) and (3.6)), the only difference being the values of SOC_{min} and SOC_{max} of the BESS given in Table 3.5.

2. If the PV production is below the load, then all PV production is sent to the grid. If the electrical energy available in the BESS is sufficient to complement the direct PV production, the demand is fulfilled by both the PV and the BESS. If the BESS cannot meet P_{need} (Eq. (4.13)) entirely, then the BESS is discharged but is constrained so that the battery level never drops below its minimum value. In this case the $P_{BESS,\ gr}$ contribution is given by Eq. (4.14).

$$P_{need}(i) = \frac{[P_{load} - P_{pv,gr}(i)]}{\eta_{BESS}} \tag{4.13}$$

$$P_{BESS,\ gr}(i) = \eta_{BESS}\ [P_{SOC}(i-1) - P_{SOCmin}] \tag{4.14}$$

3 Electrical load profiles

Two case studies were considered in this chapter: a constant baseload demand curve, regardless of the selected location and a variable load curve for several locations, when available (which is the case for only 10 [347–354] out of the 15 locations selected (Figure 4.5)). Most demand data represent the demand profile of an entire region of a selected country. For Bokpoort (RSA) and Lanzhou (CH), data were reported in scientific papers without any specific details about the source of the obtained data. Figure 4.5 shows the monthly averages of the normalized electrical load for the ten different locations. There are three easily distinguishable tendencies in the load profiles. In the case of Targassonne, the electricity peak consumption occurs in December and February. A decrease can be noticed until June, after which the consumption begins to increase. Lanzhou (CN) has a different consumption structure. There is no winter peak in their data, yet the country has a summer peak in July. Bokpoort and Phoenix also show peak consumptions in July and August, respectively. For the remaining locations, only minor differences can be noticed throughout the year.

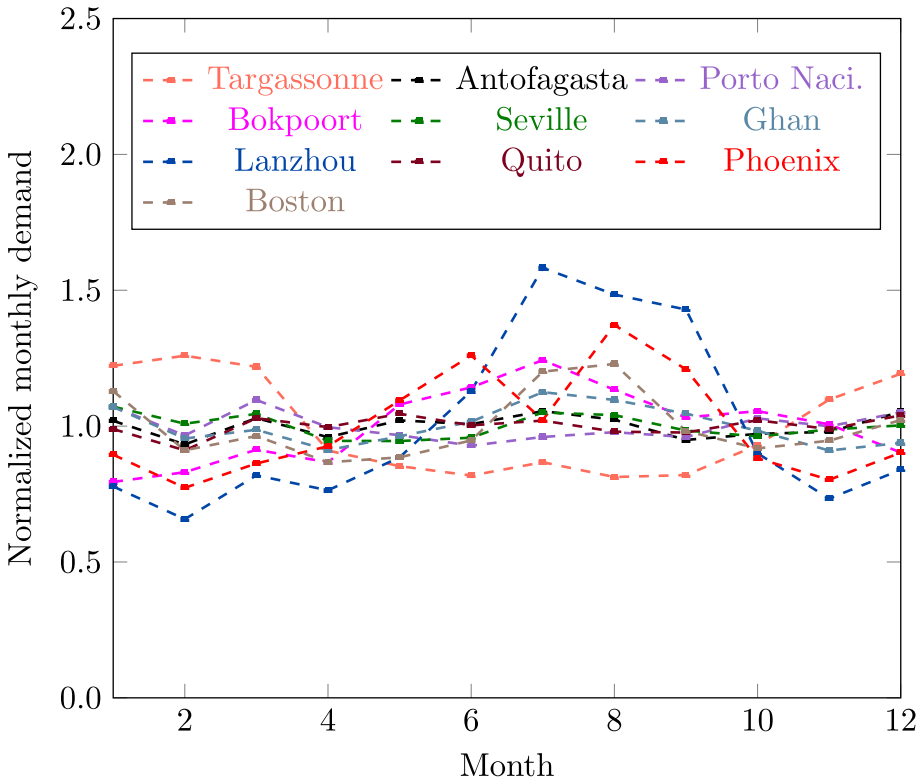

Figure 4.5: Monthly average values of the normalized electric load at ten locations.

4 Performance parameters

According to the previous equations and dispatch strategies, the model needs a series of technical parameters to assess the performance of each of the solar technologies in addition to the annual energy output of each component (see section 4.1): capacity factor, demand factor and loss of power supply probability.

4.1 Capacity factor

The capacity factor of a plant is defined as the ratio between the electrical energy effectively injected to the grid and the theoretical energy delivered by the power plant operating continuously at the nominal peak power, over one year. The definition can be expressed as follows [337]:

$$CF = \frac{Q_{act}}{8760\, P_{pb}} \tag{4.15}$$

4.2 Demand factor

The demand factor (DF) is defined as the ratio between the electrical energy produced by the plant and the energy demanded by the electrical grid. The DF is given by:

$$DF = \frac{Q_{act}}{8760\, P_{load}} \tag{4.16}$$

4.3 Loss of power supply probability

The loss of power supply probability (LPSP) is proposed to describe the power-supply reliability of the different power plants, and is defined as the fraction of the time during which the power plant is not able to satisfy the load demand. The LPSP is calculated according to [355] as:

$$LPSP = \frac{\sum_{i=1}^{8760} t_{un,\ i}\,(P_{avai} < P_{load})}{\sum_{i=1}^{8760} t_{0,\ i}} \tag{4.17}$$

where, $t_{un,\ i}$ is the annual time under power failure (when the available electricity is unable to satisfy the load demand) and $t_{0,\ i}$ is the total operation time during year i, respectively.

5 Model validation

One of the main advantages of Solcast SDB is the possibility to access directly the G_{inc} irradiation for each locations. Figure 4.6 shows a comparison of Solcast estimated and theoretical G_{inc} irradiance computed using Eq. (4.2). The daily variation of the G_{inc} at the two locations shows a good matching between Solcast values and the theoretical equation (Eq. (4.2)). More importantly, the annual resource also show small differences (3%) reported in Table 4.3. This difference can be explained by the ignorance of some information concerning the calculation of the sun position used by Solcast, i.e. the sun azimuth and zenith angles (see Eqs. (A.2) and (A.1)), whereas, in our model, we use the SPA program for the calculation of the above angles [301]. Nevertheless, the computational burden can be drastically reduced by considering the direct use of Solcast values from 20 minutes to less than one second, as a result of the calculation of additional solar angles (i.e., δ, ω and γ_s).

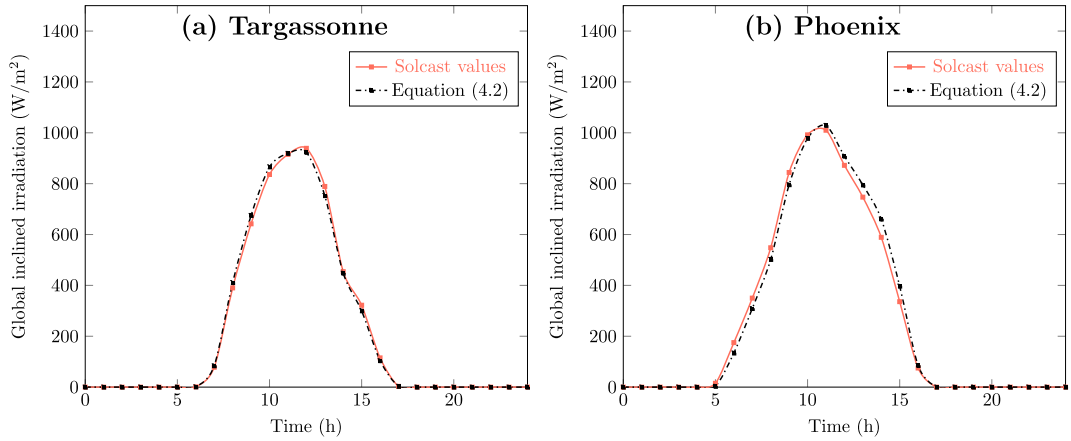

Figure 4.6: Comparison between estimated global irradiance on a tilted surface using Solcast database and Eq. (4.2) at two different locations: (a) Targassonne (FR) and (b) Phoenix (USA).

Table 4.3: Comparison between the annual G_{inc} irradiance estimated using Solcast and the theoretical expression (Eq. (4.2)) at two different locations Targassonne and Phoenix.

Locations	G_{inc} (kWh/m^2-yr) Solcast	Eq. (4.2)	Relative difference (%)
Targassonne (FR)	1716	1663	3%
Phoenix (USA)	2325	2377	2%

The model validation was conducted with PVsyst, a simulation software aimed at designing the optimal configuration of PV systems and estimating the amount of electrical energy generated [356], to validate the daily and yearly PV output, considering two different locations. PVsyst is an engineering software dedicated to the design of solar plants, which includes a solar database which has been largely validated elsewhere [357, 358].

Table 4.4 summarizes the main input parameters simulated via PVsyst at the two locations.

Table 4.4: Main parameters of the conventional PV plant used for validation.

Locations	M_{mod}	A_{pv} (m^2)	η (%)
Porto Nacional	2500	2.061	19.42 %
Antofagasta	2470		19.69 %

Figures 4.7(a) and 4.7(b) show the PV output power of fixed-tilt and single-axis tracking plants, respectively. Validations were done considering the operation of the plant in January the 1^{st} at Antofagasta (CL) and Porto Nacional (BR). The validation figures show good agreement in general regardless of the location.

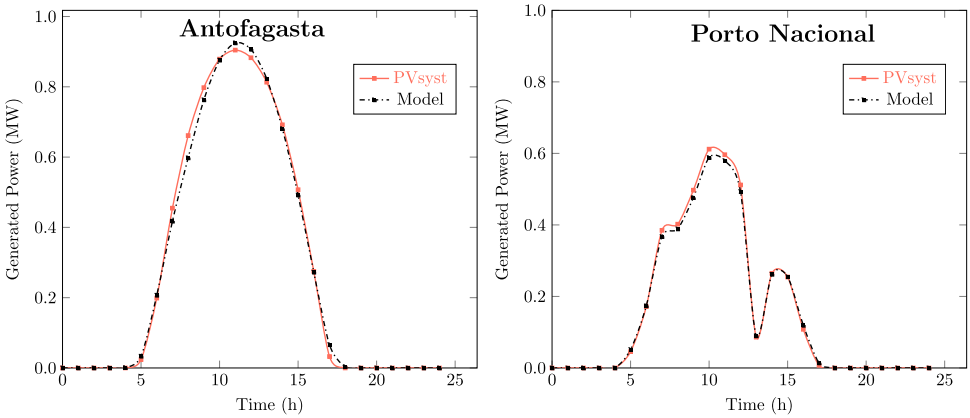

(a) *Fixed-tilt plant*

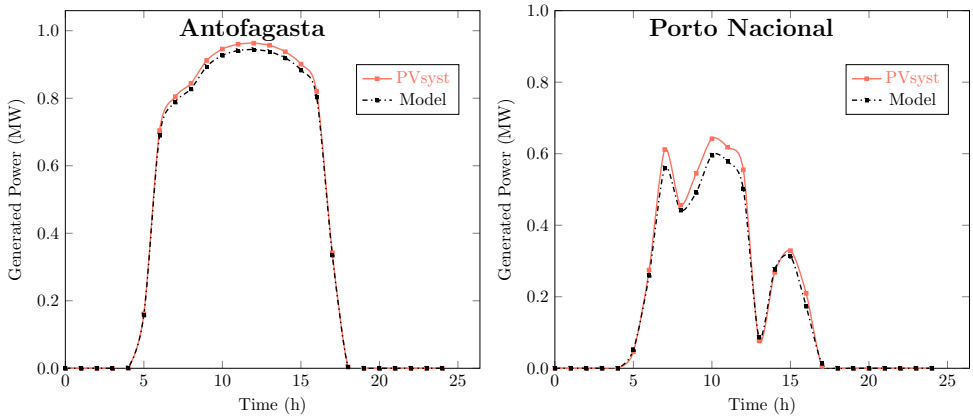

(b) *Single-axis tracking plant*

Figure 4.7: Comparison between the proposed model and PVsyst output power for the two PV plants at January the 1^{st}: (a) Fixed-tilt and (b) single-axis tracking.

Table 4.5 summarizes the annual PV production for both technologies. It can be noticed that regardless of the location considered, PVsyst values match the results of the proposed model when considering a fixed-tilt PV configuration, with a difference lower than 2% (1.89% for Porto Nacional and 1.14% in Antofagasta). On the other hand, in the case of a single-axis tracking PV configuration, the difference increases up to $\sim$ 7% in Porto Nacional, which can be explained by the difference in the derating factor f_{lpv}. PVsyst estimates the overall system losses at 0.93, whereas, in our model, we considered a value of 0.9, which brings the difference between PVsyst and the proposed model to 7% while using a f_{lpv} equal to 0.93 brings the difference to only 0.6%.
The relative difference of 3% in f_{lpv} does not fully justify the difference found between PVsyst and our model. Furthermore, PVsyst provides a detailed description of several loss parameters detailed in [359] and shown in the array loss diagram in Figure B.15. The addition of the losses highlighted in red (Figure B.15) corresponds to a total loss of 4%, which may explain the additional difference.

Table 4.5: Comparison between model output energy generation and PVsyst output of the two PV conventional plants considering different locations.

PV technology	Locations	Annual energy generation (MWh)		
		PVsyst	Model	Relative difference (%)
Fixed-tilt	Porto Nacional	1629	1598	1.89%
	Antofagasta	2480	2452	1.14%
Single-axis	Porto Nacional	1935	1804	6.78%
	Antofagasta	2953	2895	1.96%

A derating factor of **0.9** was considered for each location, and the location-dependence of the soiling losses (which should translate into different derating factor for each site) was thus neglected.

6 Results & discussion

6.1 Impact of weather conditions

6.1.1 Maximum annual energy production

Table 4.6 shows the maximum annual energy generation (i.e., the maximum energy production that could be sent to the power grid without any storage losses) of each component of the two-hybrid plants, as well as the overall output production for the five solar technologies and for the 15 selected sites.

Table 4.6: The yearly maximum electricity generation of the five solar technologies at the 15 selected locations.

Location	Maximum annual electricity generation (MWh)								
	CSP	***1S***			***HT***			**PV$_{Fix}$**	**PV$_{1axis}$**
		PV	CSP	Hybrid	PV	CSP	Hybrid		
Antofagasta	5182	4018	1769	**5787**	1164	4241	**5405**	3096	3840
Ghan	4417	3622	1473	**5095**	990	3645	**4635**	2669	3168
Bokpoort	4298	3566	1430	**4996**	965	3549	**4514**	2658	3142
Ouarzazate	4833	4017	1648	**5665**	1089	3962	**5051**	2580	2955
Phoenix	4357	3730	1463	**5192**	981	3591	**4572**	2387	2723
Tamanrasset	4128	3818	1385	**5204**	930	3404	**4334**	2518	2918
Seville	3463	3257	1139	**4396**	778	2871	**3649**	2120	2377
Abu Dhabi	3114	3355	992	**4347**	698	2610	**3308**	2260	2544
Porto Nacional	2235	2548	686	**3234**	501	1890	**2391**	1984	2303
Quito	1855	2515	574	**3089**	419	1572	**1991**	2020	2378
Boston	2393	2523	778	**3302**	539	1995	**2534**	1719	1848
Targassonne	2302	2655	740	**3395**	519	1928	**2447**	1847	1984
Lanzhou	2338	2680	768	**3448**	527	1943	**2470**	1896	2014
Andheri	2375	2756	767	**3522**	533	1983	**2516**	1870	2034
Jülich	1877	2190	593	**2783**	424	1582	**2006**	1487	1581

Some observations can be noted:

- The maximum potential energy production of the *1S* hybrid plant exceeds that of the four other solar technologies (Table 4.6). This superiority of the *1S* approach can be explained by its ability to harness a larger fraction of the solar resource, owing to its capacity to use diffuse radiation. Figure 4.8 shows the average diffuse and direct fraction for the selected locations. We can notice that the amount of diffuse incident energy increases as the direct incident energy contribution decreases as we move to less irradiated locations. In addition, the percentage of diffuse energy contribution remains non-negligible in the selected locations, with a minimum value of 11% recorded in Antofagasta and a maximum of 47% in Quito. The imperfect matching between the direct incident energy available in the 1S and the HT approaches stems from discrepancies in the description of the shading losses (see chapter 2).

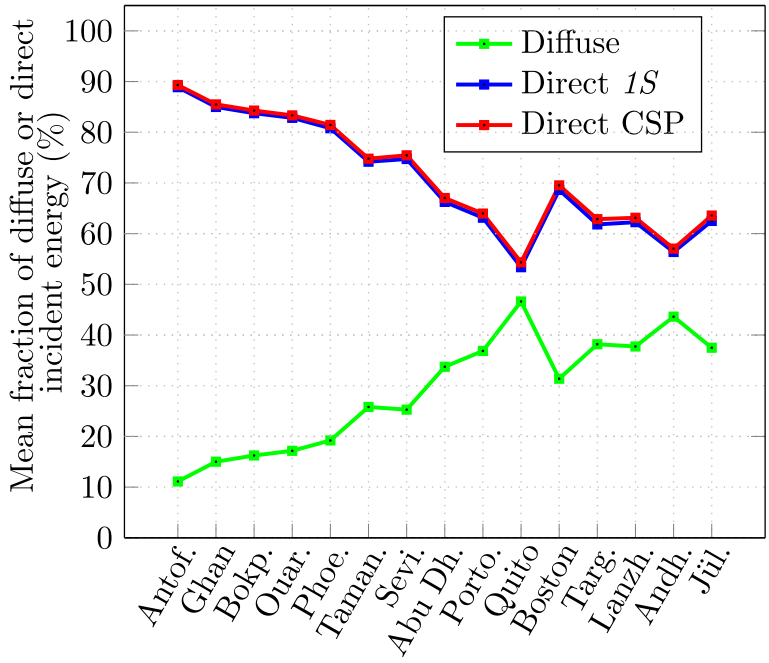

Figure 4.8: The mean fraction of direct irradiation used by a conventional CSP and *HT* hybrid plant and diffuse and direct irradiation of the *1S* hybrid plant for the 15 locations.

- The maximum electricity production of the *HT* hybrid plant exceeds that of a conventional CSP plant by an average of 5% across the 15 locations. This increase is related to the additional contribution of the PV receiver to the overall output of the *HT* plant. The CSP contribution is lower than that of the conventional CSP plant (Table 4.6), due to the low operating temperature of the PV receiver (400 °C instead of 560 °C), which results in a low conversion efficiency of the PB (see Table 3.1) and thus a lower CSP production.
  Notably, the annual energy improvement varies differently among the selected sites. For example, in locations with higher direct fractions, such as Antofagasta or Ouarzazate (89% and 84%, respectively (Figure 4.8)), the relative energy gain is only 4%, while the highest energy gain (7%) is observed in locations such as Quito and Porto Nacional (54% and 64% respectively (Figure 4.8)). Unlike the *1S* hybrid plant, this cannot be explained by the nature of the solar resource used since the *HT* and the conventional CSP plants use only the DNI resource. We, therefore, calculated an additional parameter to understand this difference, namely the performance factor (PF), which translates the ability of the two solar power plants to approach the theoretical maximum production if all the energy available at the solar field was recovered by the receiver without any loss (see Eq. (4.18)).

$$PF = \frac{E_{act,\ max}}{E_{theo,\ max}} = \frac{E_{act,\ max}}{Total\ annual\ DNI \times Collection\ area} \tag{4.18}$$

Figure 4.9 illustrates the variation of the PF of the two solar plants together with the relative difference. We can see that in highly irradiated locations, the *HT* hybrid plant allows for better utilization of the available solar resource at the PV receiver, which is reflected in a minimum relative difference of 4% in Antofagasta and Ouarzazate versus 7% in Porto Nacional and Quito (Figure 4.9). Therefore, the PF shows that the difference in maximum energy production is explained by the solar irradiation used for the two-hybrid plants.

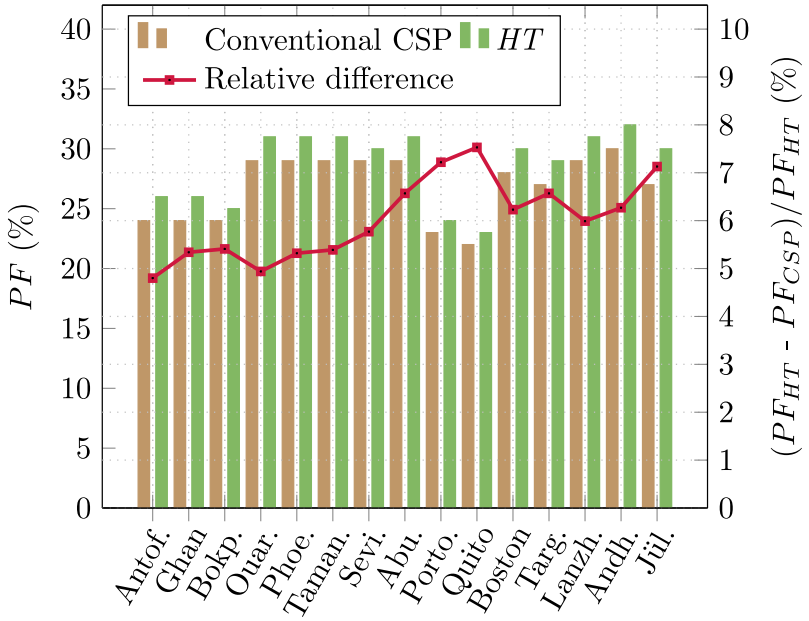

Figure 4.9: The performance factor of the conventional CSP and the *HT* hybrid plants at the selected locations along with the relative difference between the two technologies.

- As expected, the maximum annual production of a 1Axis tracking PV plant is higher than that of a fixed-tilt plant, with a maximum relative energy gain ranging from 19% in Antofagasta to 6% in Jülich (Figure 4.10). This difference arises primarily from the difference between the $G_{inc,\ fix}$ and $G_{inc,\ 1axis}$ depicted in Figure 4.10.
  Additionally, the maximum potential production of the two conventional PV plants remains the lowest compared to the output production of the three other solar technologies regardless of the location considered (Table 4.6).

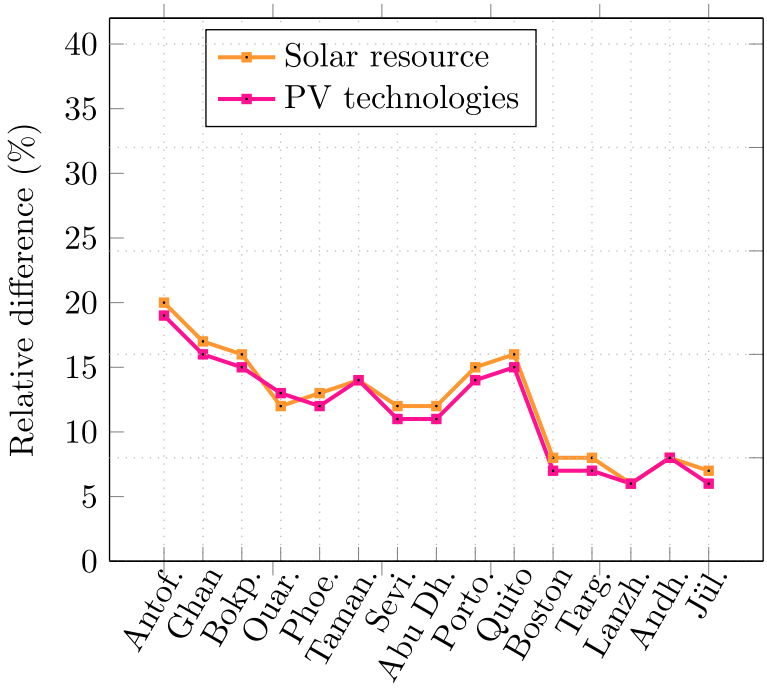

Figure 4.10: The relative difference between the solar irradiation at the two inclined PV mounting 1Axis-PV and Fixed-PV plants (orange plot), and the maximum yearly generation of the PV production (pink plot).

6.1.2 Annual energy effectively supplied to the electrical grid

Figure 4.11 illustrates the maximum potential (light bars) and actual (dark bars and dashed lines) energy production of the seven solar plants for the 15 locations. The actual energy output is obtained for a base case scenario where the solar plants are required to meet a constant electrical demand of 0.2 MWe throughout the year, using a TES capacity of 10 MWh_t (equivalent to 10 h, as 1 MWh_t is equal to 1 h) and a BESS capacity of 4.2 MWhe (corresponding to 4.2 h as 1 MWh_e is equal to 0.42 h, the nominal power of the turbine being considered as a reference value to size the storage).

- In general, locations with higher DNI are more likely to experience higher energy curtailment. For example, Antofagasta experiences the highest levels of energy curtailment, ranging from 44% to 70% depending on the solar technology considered (Table 4.7); for the two-hybrid technologies as well as the conventional CSP plant, an average energy curtailment of 55% is noticed (Table 4.7). Indeed, the TES hot tank reaches its maximum energy level more quickly due to the abundance of solar resources available at the receiver, thus preventing the plant from significantly increasing the plant energy output under the given circumstances. For the conventional PV plants, an average energy curtailment of 55% was observed with the 1Axis-PV plant using both storage technologies, while the lowest energy curtailment of 44% was recorded with a Fixed-PV plant (Table 4.7).

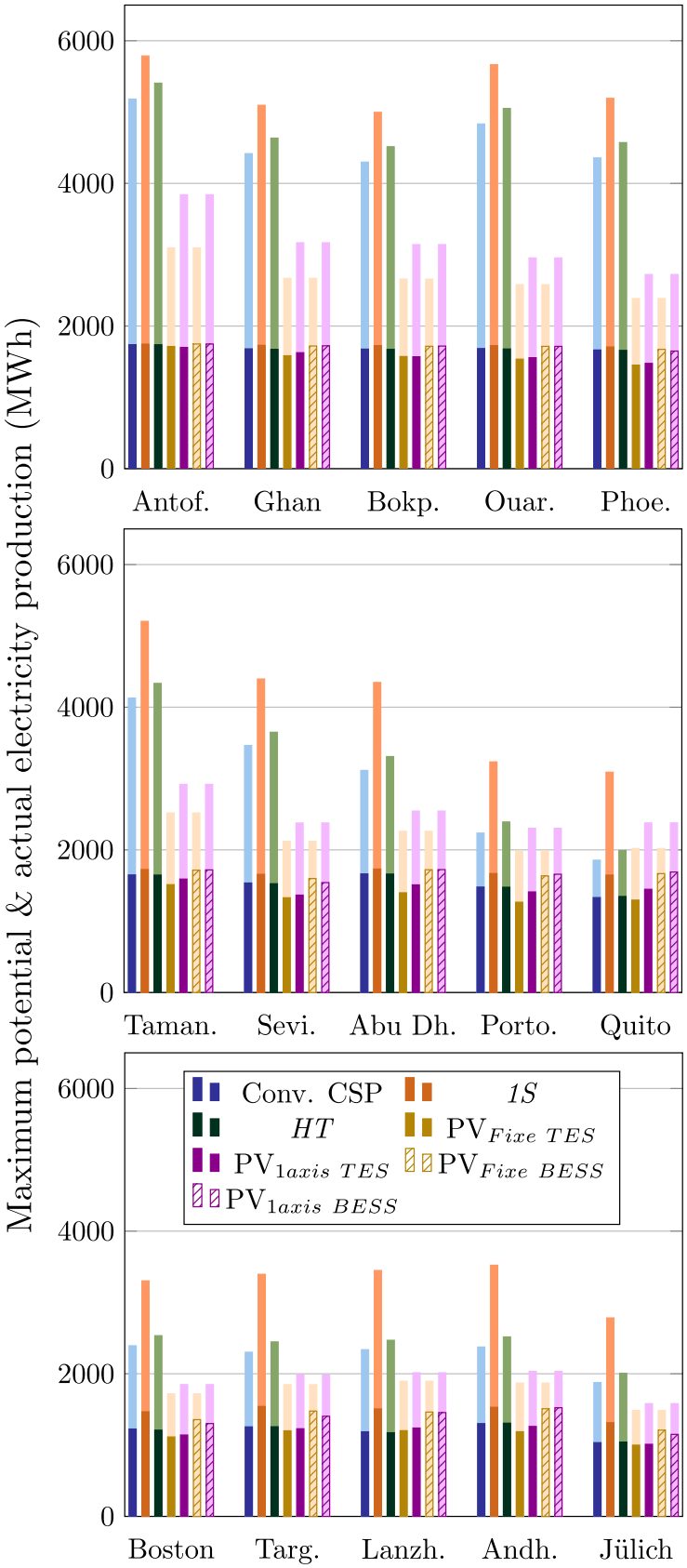

Figure 4.11: The maximum potential (light colors) and actual (dark colors and dashed bars) annual electricity production of the seven solar technologies for the 15 locations for a baseload demand of 0.2 MWe using 10 MWh_t TES and 4.2 MWhe BESS capacities.

Table 4.7: Percentage of energy curtailments of the seven solar approaches at the selected locations.

Location	Percentage of energy curtailments (%)						
	CSP	*1S*	*HT*	***Fixed-PV***		***1Axis-PV***	
				TES	BESS	TES	BESS
Antofagasta	66	70	68	45	56	44	54
Ghan	62	66	64	41	49	36	46
Bokpoort	61	65	63	41	50	35	45
Ouarzazate	65	70	67	41	47	34	42
Phoenix	62	67	64	39	46	30	39
Tamanrasset	60	67	62	40	46	32	41
Seville	56	62	58	37	43	25	35
Abu Dhabi	47	60	50	38	41	24	32
Porto Nacional	34	48	38	36	39	18	28
Quito	28	47	32	36	39	17	29
Boston	49	56	52	35	38	21	30
Targassonne	45	55	49	35	38	20	29
Lanzhou	49	56	53	37	39	23	28
Andheri	45	57	48	36	38	19	25
Jülich	45	53	48	33	36	19	27

6.2 Impact of storage capacity with a constant demand

Figure 4.12 illustrates the maximum potential amount of electrical energy and the actual energy sent to the power grid of the seven solar approaches at three locations only, for better visualisation of the main results. Ouarzazate, one of the sites with the highest DNI resources, Abu Dhabi, an intermediate case study, and finally Jülich, with the lowest DNI profile (see chapter 3). Three storage capacities are compared: 0, 2 and 10 MWh_t for a minimum and maximum electrical demand of 0.2 and 1 MWe, respectively. The operating energy yield, i.e. the ratio between the energy currently produced and the maximum potential energy output of a solar plant, is also reported in Figure 4.12.

In general, regardless of the value of electrical demand considered, increasing the capacity of the TES expands solar generation while decreasing the difference between solar technologies. In the case where solar plants are expected to provide a high baseload demand of 1 MWe over the entire year of operation, even without any storage facilities, we can note that the amount of energy actually produced remains much more significant than for a base demand of 0.2 MWe under similar conditions, due to the efficient utilization of the maximum available potential, which directly translates into a minimization of energy curtailments. Nevertheless, all four PV configurations achieve near 100% with small storage capacities in highly irradiated locations such as Ouarzazate (Figure 4.12(a)). Whilst without storage, the plants located in Abu Dhabi and Jülich can fully use the maximum potential of energy (Figures 4.12(b) and 4.12(c)) due to the reduced energy potential in these two locations, which makes it easier to

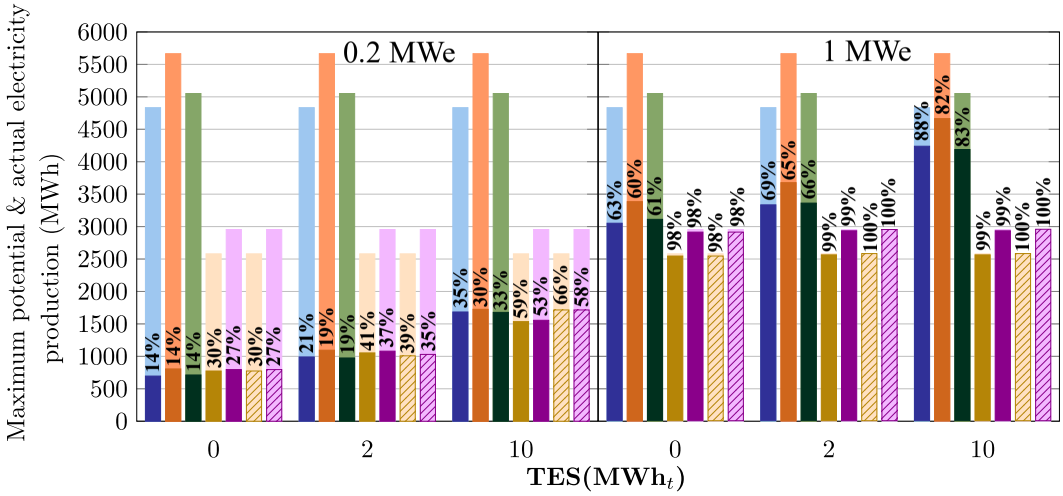

(a) **Ouarzazate**

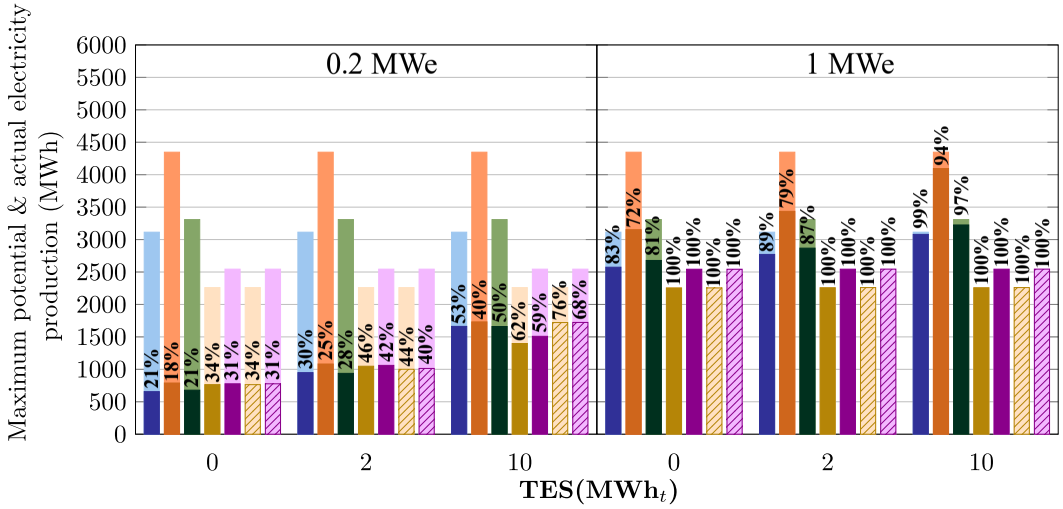

(b) **Abu Dhabi**

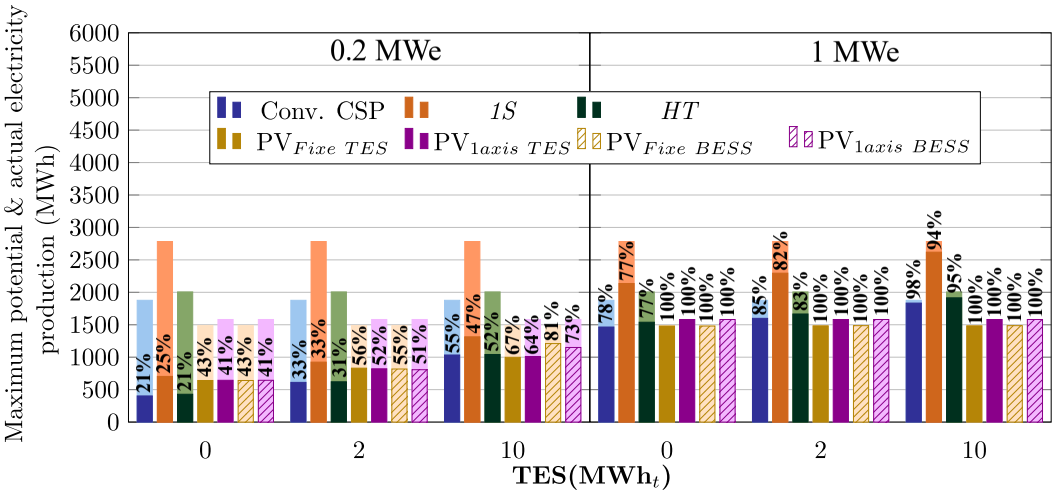

(c) **Jülich**

Figure 4.12: The maximum potential (light colors) & actual (dark and dashed colors) electricity production of the seven solar technologies considering two baseload demands of 0.2 and 1 MWe at three locations: (a) Ouarzazate, (b) Abu Dhabi and (c) Jülich.

approach the 100% utilization of the plant production. On the other hand, a storage capacity of 10 MWh_t is not sufficient to reach the maximum potential of the hybrid plants as well as the conventional CSP plant in Ouarzazate (Figure 4.12(a)). That can be explained by the large amount of available resources for conversion, regardless of the different possible operating conditions of the plants. These initial observations show that there are several trade-offs to consider to fully exploit the potential of a solar power plant at a given location under specific conditions.

Figure 4.13 illustrates the demand factor (DF) for the three locations mentioned above, with three different storage capacities and two baseload demands.

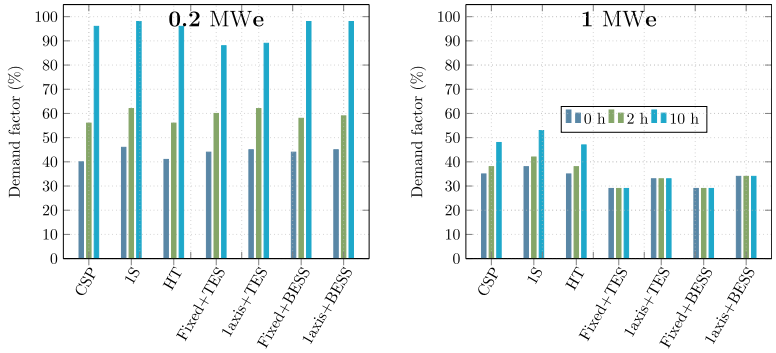

(a) **Ouarzazate**

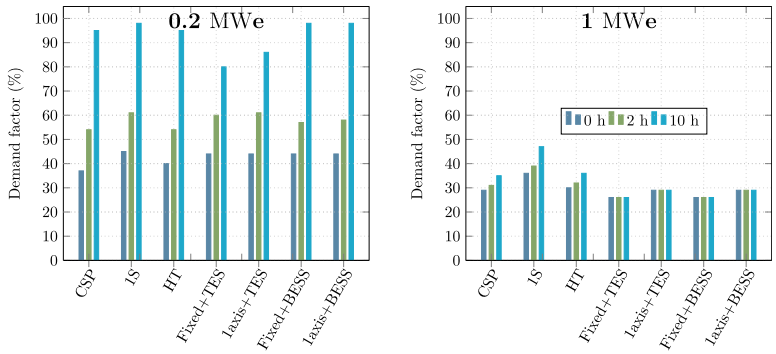

(b) **Abu Dhabi**

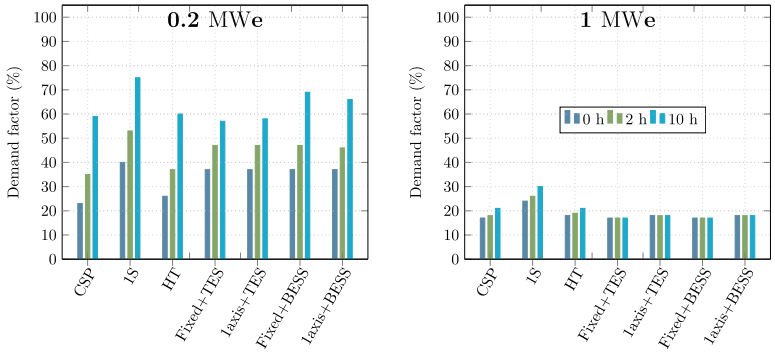

(c) **Jülich**

Figure 4.13: Variation of the DF of the seven solar technologies for three values for the storage capacity with the consideration of two baseload demand values (0.2 MWe left graph) and (1 MWe right graph) at: (a) Ouarzazate, (b) Abu Dhabi, and (c) Jülich.

Although a baseload demand of 0.2 MWe uses the solar plant capacity less effectively, it ensures the highest DF because the plant operates for a longer period of the year to supply a low energy demand (see Eq. (4.16)). In Ouarzazate and Abu Dhabi, the majority of the solar plants have very high DFs with 10 MWh_t storage capacity, except for the two conventional PV plants with TES, 87.60% and 88.79% in Ouarzazate (Figure 4.13(a)) compared to 79.81% and 86.51% in Abu Dhabi (Figure 4.13(b)) for a Fixed and 1Axis PV plant, respectively. This can be explained by the lack of excess PV to efficiently charge the hot tank, which results in lower operating hours. Whereas at Jülich, the lack of solar resource implies a different variation in DF with the increasing capacity of TES (Figure 4.13(c)). At Jülich, the *1S* hybrid plant provides the highest DF, regardless of the storage capacity, with a maximum of 75% with 10 MWh_t.
Increased baseload demand allows for more efficient use of the PV potential during the day, which results in a decrease in the energy available at the inlet of the TES unit. This, therefore, explains the negligible difference between the DFs of the three locations with increasing storage capacity (Figure 4.13). However, since the annual energy output of the two conventional PV plants is the lowest among the remaining technologies, it is challenging for the PV plants to provide a baseload of 1 MWe throughout the year, especially in less irradiated locations, which is a direct consequence of choosing to compare similar collection areas and not the nominal power output of the plants.

The above results are limited to a particular case study that turns out to be in favour of certain technologies under the above conditions. To verify these initial observations, Figures 4.14, 4.15 and 4.16 present the variation of the different performance parameters as a function of a wide range of P_{load} and the TES capacity values in Ouarzazate for the seven solar plants.
As can be seen, the annual energy production, as well as the CF, increases with increasing P_{load} and TES capacity for all solar technologies, while the annual dumped energy decreases. However, this increase varies differently for a given technology:

- For solar plants with the presence of the CSP subsystem, the increase of the annual energy production is gradual with increasing P_{load} and TES capacity (Figure 4.14); since excess PV is effectively recovered via the TES unit for the hybrid technologies, while heliostats are less often defocused when the storage is fully charged for the conventional CSP plant.

- As expected, the *1S* hybrid plant has the highest annual energy output for a maximum demand of 1 MWe and 20 MWh_t of TES. At the same time, the increase in electrical demand results in a decrease in DF from 99.59% to 59.60% (corresponding to an increase of the LPSP from 0.41% to 40.4%), due to the increase in the amount of energy demanded by the electrical grid, from 1752 MWh to 8760 MWh when P_{load} increases from 0.2 MWe to 1 MWe (see Eq. (4.16)). Therefore, it is much more difficult for the *1S* hybrid plant to meet the demand given the plant's limited capabilities and the variability of the solar resource. Similar trends are observed for the *HT* hybrid plant as well as the conventional CSP plant (Figure 4.14).

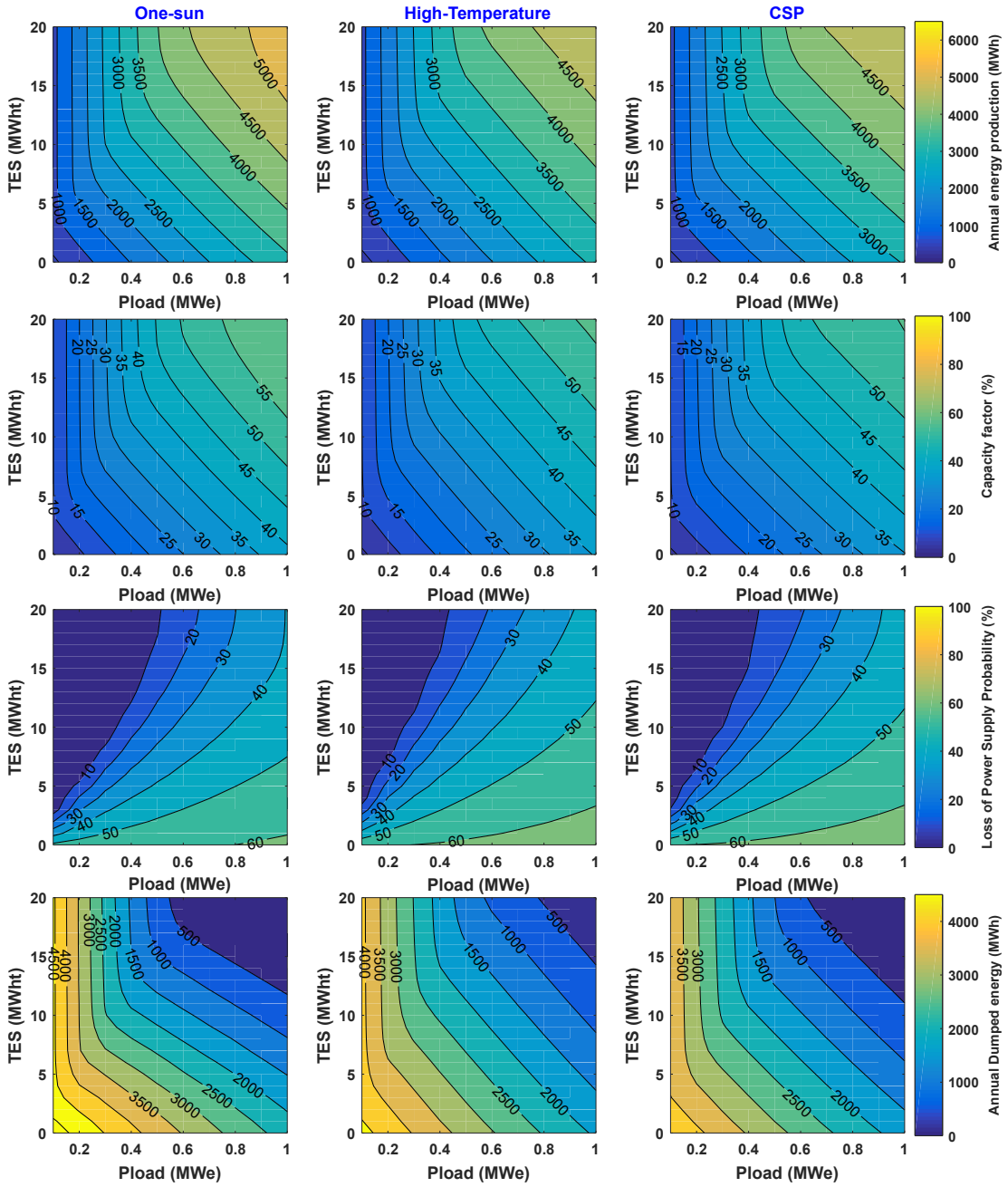

Figure 4.14: Annual energy production, CF, LPSP and the annual dumped energy the receiver and the PV subsystem of the two hybrid plants and the conventional CSP plant in Ouarzazate.

- For a fixed P_{load} and increasing storage capacity, we can notice that beyond 5 MWh_t TES, and 4 MWhe BESS, the three performance parameters, namely annual energy, CF and LPSP, remain constant for the two PV mounting configurations with integrated TES and BESS systems presented in Figures 4.15 and 4.16, respectively. By increasing the storage capacity for a given demand value, the contribution of the storage system in the overall production is increased up to a given storage capacity value. Above this limiting storage value, the storage cannot be exploited any longer and no further improvement in the main energy parameters is observed.

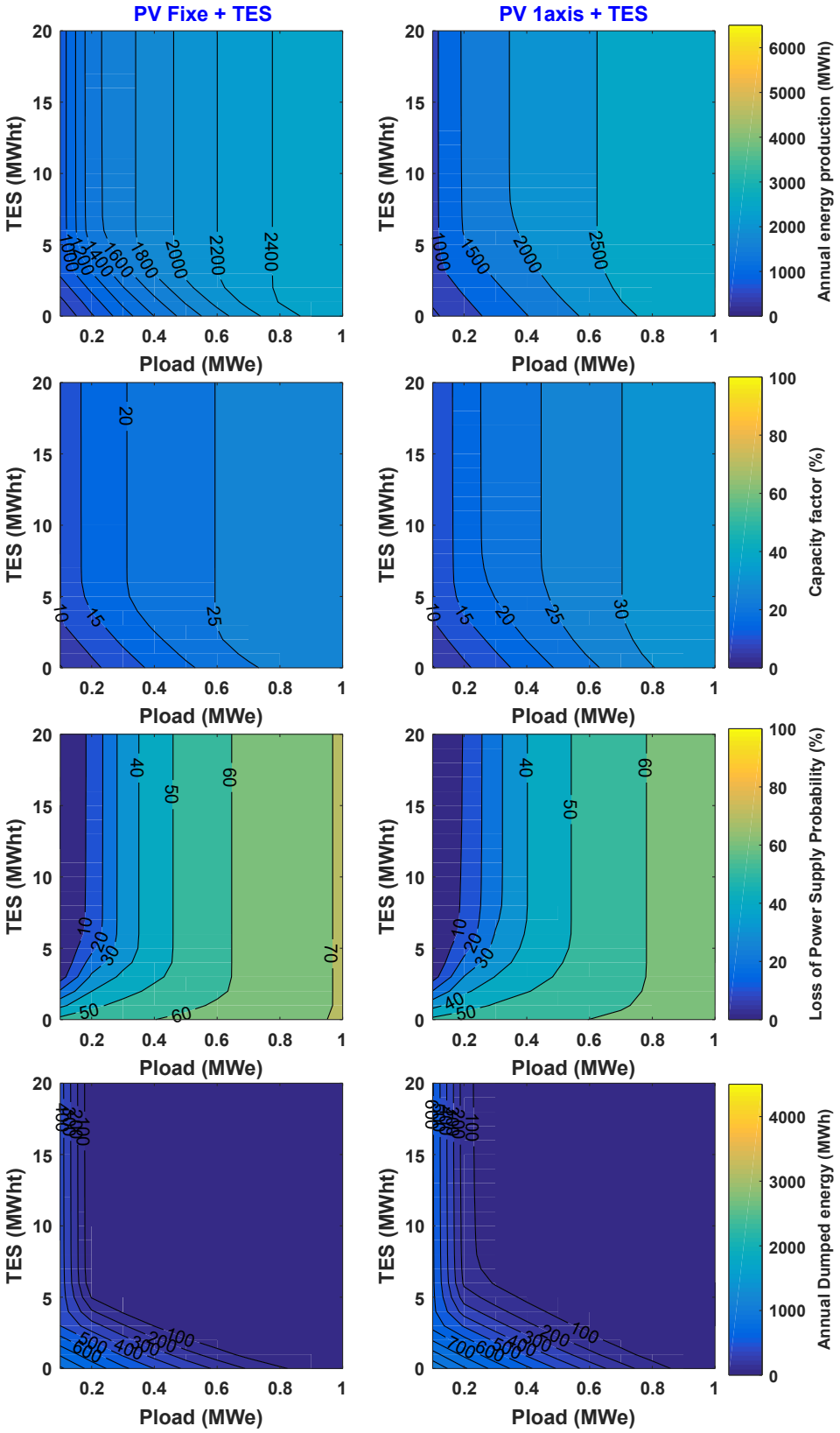

Figure 4.15: Annual energy production, CF, LPSP and the annual dumped energy the receiver and the PV subsystem of the two conventional PV plants integrating TES system in Ouarzazate.

More importantly, the storage capacity at which the performance parameters become stable decreases with increasing P_{load} as a consequence of the decreasing amount of energy available for storage (Figure B.17). For example, for a baseload demand of 1.3 MWe, the contribution of the storage system equals zero (Figure B.17), eliminating the need for any storage facility. This is a consequence of the choice to compare solar technologies considering the same collection area rather than the same nominal power. Similar trends can be noticed for the other technologies, but the storage capacity at which the performance parameters becomes stable differs between the technologies (Figures 4.14 and 4.16). This difference can be explained on the one hand by the higher conversion efficiencies of both hybrid plants as well as the conventional CSP plant compared to the PV systems, and on the other hand by the high amount of energy available for utilization, either from the excess PV or at the receiver, which results in a non-negligible amount of energy to be recovered via the storage unit, even at very high P_{load} values (Figure B.18).

- From Figure 4.16, it can be noticed that PV + BESS installations show a slightly higher output performance compared to the PV + TES systems. This is due to the higher conversion efficiency of the BESS unit (96% vs. 42% for the PB unit) and the lack of restrictions on battery operation, unlike the PB (i.e., 30% of the nominal power of the turbine).

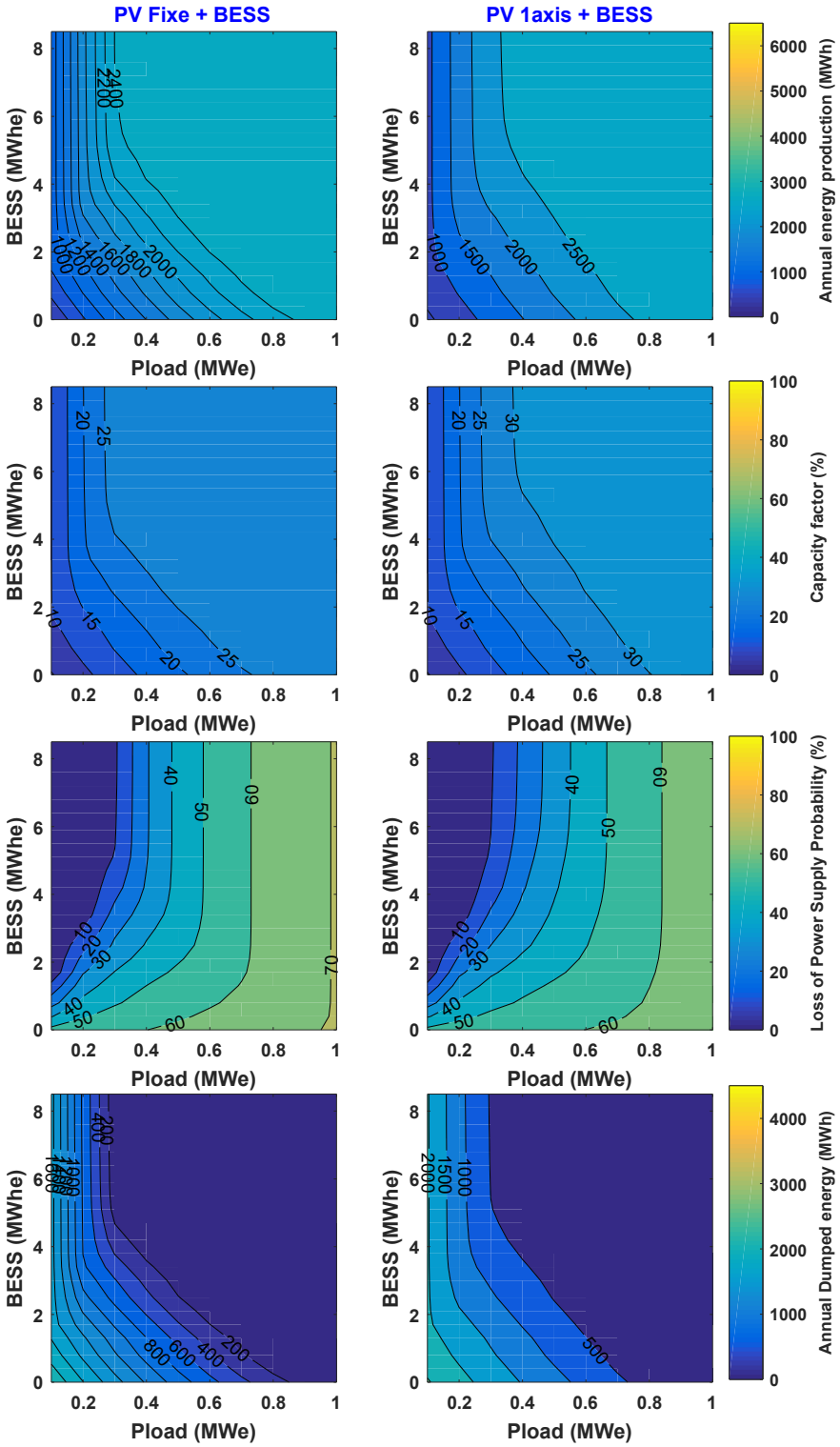

Figure 4.16: Annual energy production, CF, LPSP and the annual dumped energy the receiver and the PV subsystem of the two conventional PV plants with integrating BESS system in Ouarzazate.

Similar trends can be observed at the other locations (see Appendix B). Nevertheless, the annual production, as well as the remaining performance parameters, are highly correlated with the location considered.

6.3 Impact of the variable demand strategy

To evaluate the difference between a constant and a variable electrical demand profile, the load profiles collected for the ten locations previously discussed in the section 3 were subjected to a re-normalization procedure aiming to fit the energy production with the electrical demand. It should be mentioned that the following normalization technique was proposed by a colleague, Freddy Ordonez.
The proposed method starts with the definition of a unit-less load parameter denoted W, defined as the ratio between an actual electrical demand over a year of operation to the constant electrical demand over the same period (Eq. (4.19)).

$$W(p) = \frac{\sum_{i=1}^{8760} Electrical\ load(i)}{P_{iload}(p) \times 8760} \tag{4.19}$$

where, p is the number of load values studied varying between 0.2 and 1 MWe.
For example, in the case of a baseload demand of 0.5 MWe from a power plant at Targassonne, the parameter W will be given as follows:

$$W(0.5\text{MW}) = \frac{4.76E+08\ MWh}{365\ days \times 24\ hours/day \times 0.5\text{MW}} = 1.09E+05 \tag{4.20}$$

Table 4.8 summarizes the annual overall demand and the unit-less load parameter of the selected locations.

Table 4.8: Unit-less load parameter at the selected locations for a baseload of 0.5 MWe.

Location	$\sum_{i=1}^{8760} Electrical\ load(i)$ (MWh)	W
Antofagasta	7.74E+07	1.77E+04
Ghan	7.15E+07	1.63E+04
Bokpoort	1.30E+08	2.97E+04
Phoenix	1.02E+08	2.34E+04
Seville	2.55E+08	5.81E+04
Porto Nacional	5.54E+08	1.27E+05
Quito	2.30E+07	5.24E+03
Boston	1.23E+08	2.82E+04
Targassonne	4.76E+08	1.09E+05
Lanzhou	2.14E+11	4.88E+07

Once the load parameter is identified for a given location, the equivalent value of P_{load} is the ratio of the instantaneous demand to the unitless load parameter, given by the equation (4.21) as:

$$P_{load}(i) = \frac{Electrical\ load(i)}{W} \tag{4.21}$$

Figure 4.17 shows the monthly variation in load for the ten given locations for a constant baseload of 0.5 MWe. It can be seen that most sites fluctuate similarly throughout the year around 0.5 MWe following the monthly distribution shown in Figure 4.5.

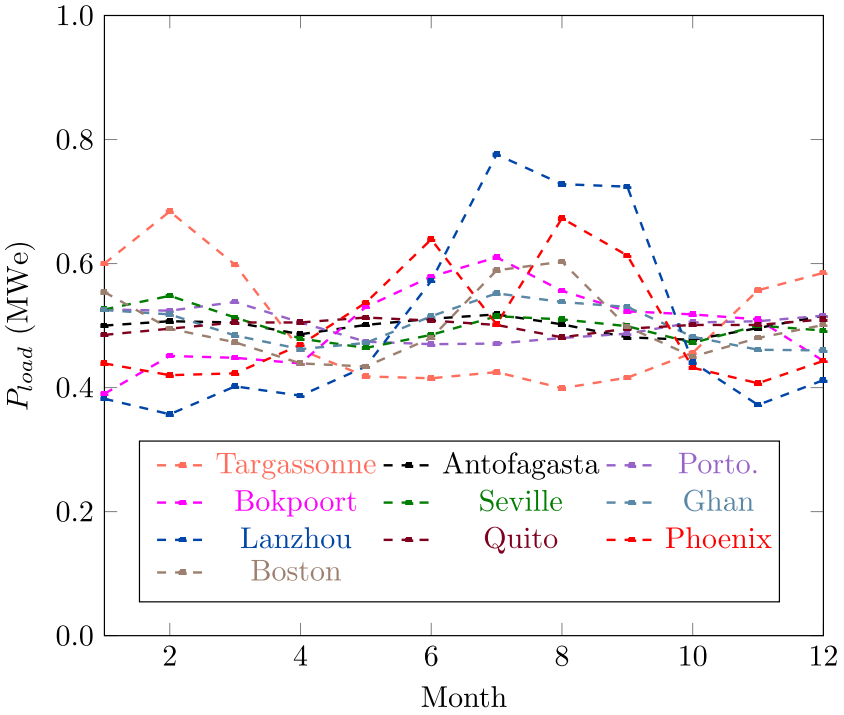

Figure 4.17: Monthly average values of P_{load} at the ten locations obtained for a P_{iload} of 0.5 MWe.

6.3.1 Daily performance

As an example of the performance of technology combination, Figure 4.18 illustrates the dispatchability of the seven solar plants on two consecutive days, January 8^{th} and 9^{th}, with relatively good solar availability, at Antofagasta. The calculation assumes a baseload demand of 0.5 MWe, 14 MWh_t of TES and 6 MWhe of BESS. In Figure 4.18(a), 4.18(b), 4.18(d), 4.18(e), 4.18(f) and 4.18(g), the purple line represents the PV generation, a fraction of which is sent onto the electrical grid, the rest being either stored in BESS or TES, or curtailed. In Figure 4.18(a), the baseload capacity is primarily supplied using the PV power during the day, while the energy available at the receiver inlet and the surplus PV power is used to charge the TES to its maximum level. The TES complements the production until early in the morning. When the TES is fully discharged (i.e., the hot tank reaches P_{SOCmin} (see Figure B.5) and no PV power is available, P_{load} cannot be fully satisfied for a short time (Figure 4.18(a)). The *1S* hybrid plant undergoes a large number of power curtailments during the operation, both at the receiver level and the PV output. Conversely, the *HT* hybrid plant PV power production is fully used to cover the demand, as shown in Figure 4.18(b) but the PV production by itself is not sufficient to fulfill the demand, which is satisfied by the CSP subsystem during daytime, and by the energy contained in the thermal

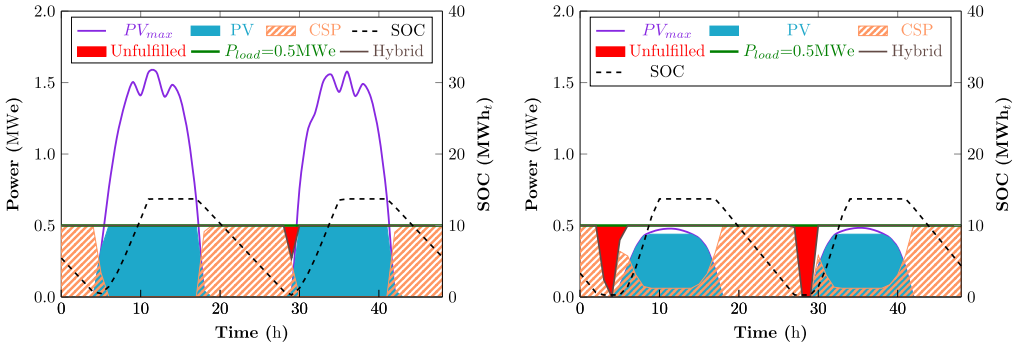

(a) *1S* (b) *HT*

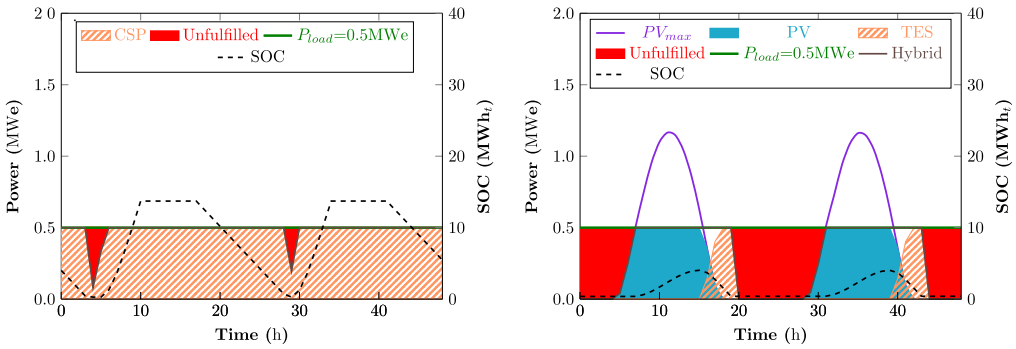

(c) **CSP** (d) **Fixed-PV + TES**

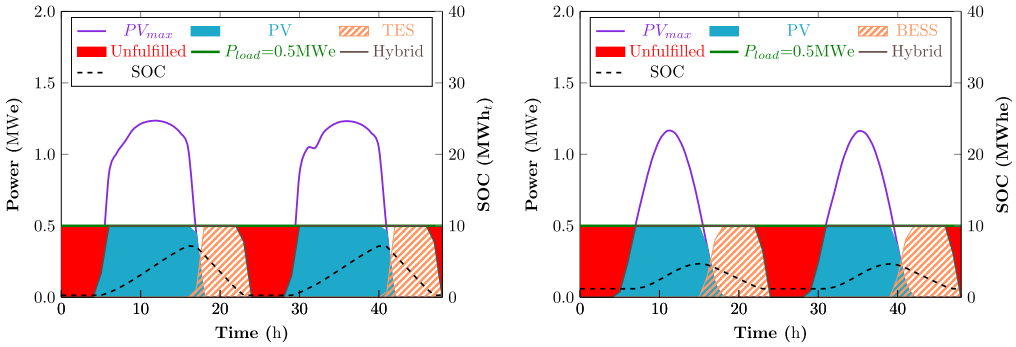

(e) **1Axis-PV + TES** (f) **Fixed-PV + BESS**

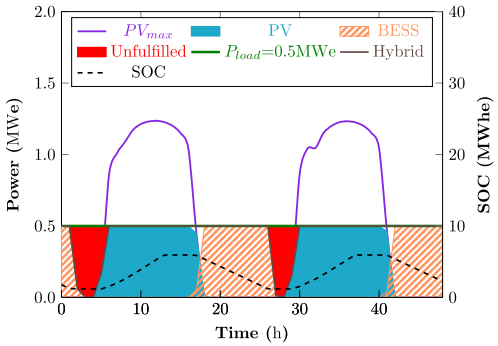

(g) **1Axis-PV + BESS**

Figure 4.18: Dispatchability of the seven solar plants considering a baseload profile of 0.5 MWe for two selected days (January 8^{th} and 9^{th}, 2018) at Antofagasta with a TES capacity of 14 MWh$_t$ and a BESS capacity of 6 MWhe.

storage after sunset. Despite this, demand cannot be fully met throughout all day, and the *HT* plant must shut down during several hours (one hour early in the morning of January 8^{th} and two hours early on January 9^{th} as shown in Figure 4.18(b)). In Figure 4.18(c), the conventional CSP plant also presents a high level of demand fulfilment, but its generation is slightly reduced relative to the *1S* plant during the early hours of the day due to the lack of energy in the hot tank. Therefore, the PB can only be powered by the thermal energy available at the receiver (in the *1S* hybrid systems this is provided by the PV plant, as illustrated in Figure 4.18(a)).

Figures 4.18(d) and 4.18(e) show the dispatchability of the PV+TES plant, with both types of PV mounting systems. With fixed panels, the PV plant only maintains maximum power for a few hours around noon, and the TES system complements the production after sunset until the TES is completely discharged (Figure 4.18(d)). In contrast, the PV production with tracked panels results in more intensive use of the PV power generation throughout the day by supplying the load while charging the hot tank with the excess PV, resulting in extended use of the TES. This difference is more relevant at highly irradiated locations such as Antofagasta due to the increase in PV production, which will result in the availability of more energy to charge the TES system. Under similar conditions, the single-axis PV+TES plant provides an additional 244 MWhe energy for the storage in Antofagasta, compared to 16 MWhe in Jülich.

Finally, Figures 4.18(f) and 4.18(g) shows the operation of the PV-BESS plant with the two PV configurations. During sunlight hours, both PV mounting systems, fixed-PV (Figure 4.18(f)) and 1axis PV (Figure 4.18(g)) provide the net power demand as for PV+TES plants while charging the BESS with excess PV energy. After sunset, the BESS is discharged at a minimum rate to provide the baseload. The BESS unit covers a greater amount of operation during the night compared to the TES system.

Figures 4.19 illustrates the dynamic performance of the seven solar plants, operating as load tracking plants in Antofagasta under conditions identical to those of the aforementioned case study (Figure 4.18). Minor differences are noted for the *1S* hybrid plant, where the demand was fully met since less power was required early in the morning of January 9^{th} (0.43 MWe instead of 0.5 MWe) as shown in Figure 4.19(a). The conventional CSP plant experiences a similar situation (Figure 4.19(c)) during the first hours of operation January 9^{th}. For the *HT* hybrid plant, we notice that the TES discharge less quickly during the early morning hours under a tracking load profile (Figure 4.19(b)), as the electrical demand is 12% lower than in the case of a baseload demand. Finally, no significant difference can be noted for the conventional PV plants with both storage systems using a tracking load strategy as shown in Figures 4.19(d), 4.19(e),4.19(f) and 4.19(g).

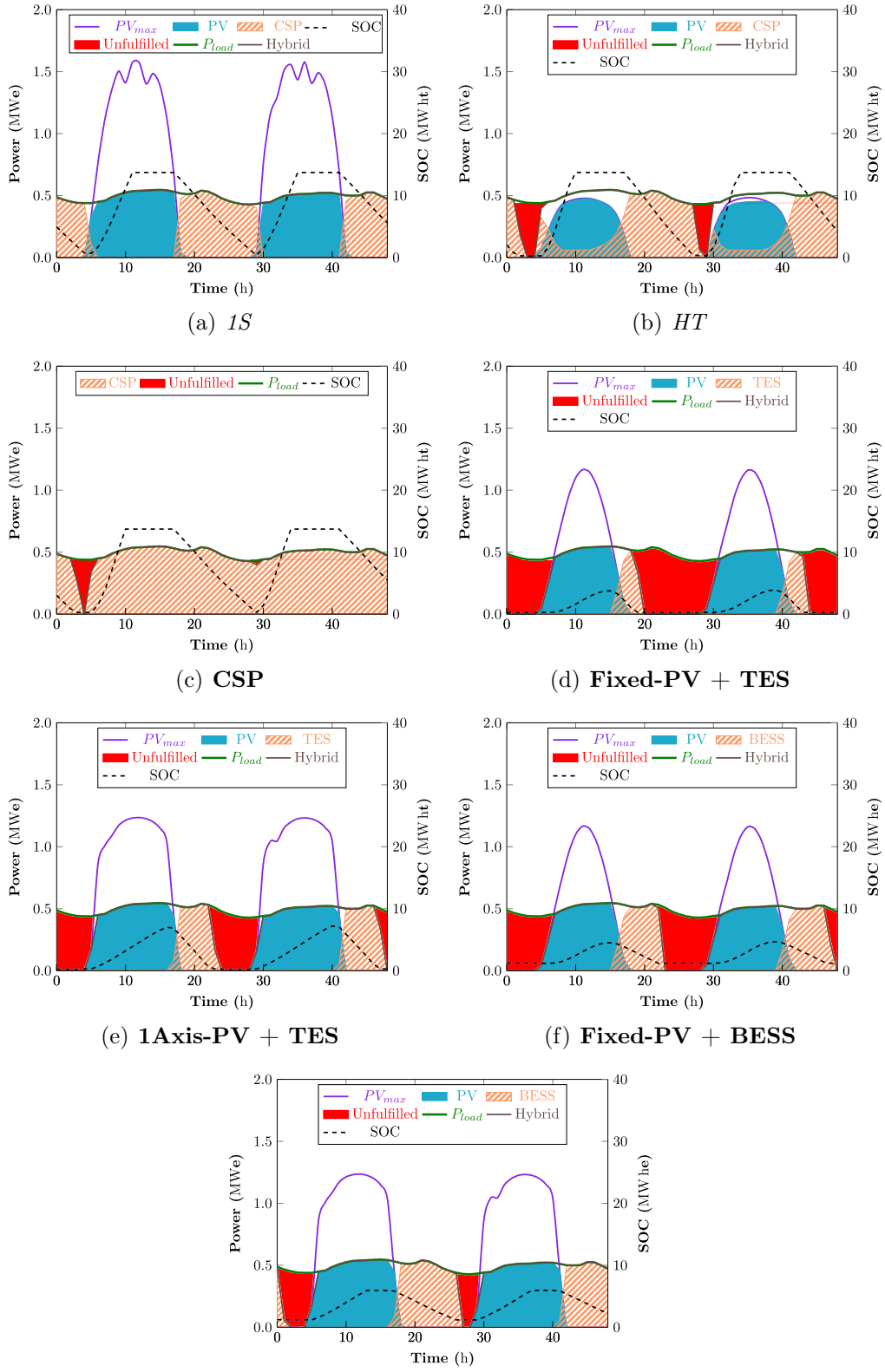

(a) *1S* (b) *HT*

(c) **CSP** (d) **Fixed-PV + TES**

(e) **1Axis-PV + TES** (f) **Fixed-PV + BESS**

(g) **1Axis-PV + BESS**

Figure 4.19: Dispatchability of the seven solar plants considering a load tracking strategy during two successive days at Antofagasta with 14 MWh_t for the TES system and 6 MWhe for the BESS.

6.3.2 Yearly performance

Tables 4.9 and 4.10 summarize the annual energy contribution of the *1S* and *HT* hybrid plants components as well as the different power losses, respectively, at the ten locations for the two load case scenarios considering a baseload of 0.5 MWe and 14 MWh_t of TES. In general, we find that the two-hybrid technologies behave differently depending on the load demand scenario considered:

Table 4.9: Annual performance of the *1S* hybrid plant at the selected locations for a baseload demand of 0.5 MWe with 14 MWh_t TES capacity.

	Baseload				**Tracking-load**			
Location	PV_{gen}	CSP_{gen}	PV_{dum}	CSP_{dum}	PV_{gen}	CSP_{gen}	PV_{dum}	CSP_{dum}
	(MWh)				(MWh)			
Antofagasta	1868	1962	689	442	**1932**	1940	669	448
Ghan	**1888**	1794	398	259	1882	1769	432	275
Bokpoort	**1854**	1667	467	306	1823	1579	585	359
Phoenix	1815	1808	482	284	**1840**	1807	451	291
Seville	1736	1525	274	164	**1853**	1476	260	165
Porto Nac.	1591	1098	7	4	**1641**	1080	3	2
Quito	1571	961	24	12	**1613**	944	25	12
Boston	1454	1076	172	97	**1523**	1041	168	103
Targassonne	**1587**	1066	143	81	1580	1024	194	104
Lanzhou	**1496**	1126	168	87	1481	1090	227	107

Table 4.10: Annual performance of the *HT* hybrid plant at the selected locations for a baseload demand of 0.5 MWe with 14 MWh_t TES capacity.

	Baseload				**Tracking-load**			
Location	PV_{gen}	CSP_{gen}	PV_{dum}	CSP_{dum}	PV_{gen}	CSP_{gen}	PV_{dum}	CSP_{dum}
	(MWh)				(MWh)			
Antofagasta	1156	2448	6.56	1776	1160	**2501**	3	1723
Ghan	990	**2442**	0.46	1195	982	2438	7	1191
Bokpoort	965	**2345**	0.62	1193	941	2273	21	1263
Phoenix	979	2300	1.55	1280	961	**2355**	12	1227
Seville	778	2055	0.13	810	778	**2138**	0.2	728
Porto Nac.	501	1822	0.00	69	501	**1829**	0.00	63
Quito	419	1455	0.00	118	418	**1459**	0.06	114
Boston	539	1516	0.51	476	535	**1551**	3	442
Targassonne	519	**1535**	0.09	393	516	1509	2	418
Lanzhou	526	**1460**	1	481	509	1430	11	512

- In the case of the *1S* hybrid plant, PV generation is most affected by a tracking-load profile due to the abundant PV potential that a *1S* hybrid plant can have compared to the *HT* hybrid system. It was found that a tracking load profile is favourable for PV production and thus leads to a reduction in PV surplus at most of the selected locations, except for four sites, Ghan, Bokpoort, Targassonne and Lanzhou (Table 4.9), which are characterized by the higher variation in the load profile over the course of the year (Figure 4.17). To understand the behaviour of the following sites, Figure 4.20 shows the monthly variation in the amount of dumped PV energy. Regardless of location, a tracking load profile shows higher amounts of PV curtailment, especially during months when electrical demand is less than 0.5 MWe (Figure 4.20), resulting in slightly lower PV and CSP generation (Table 4.9), the hot tank being less able to store the extra energy.

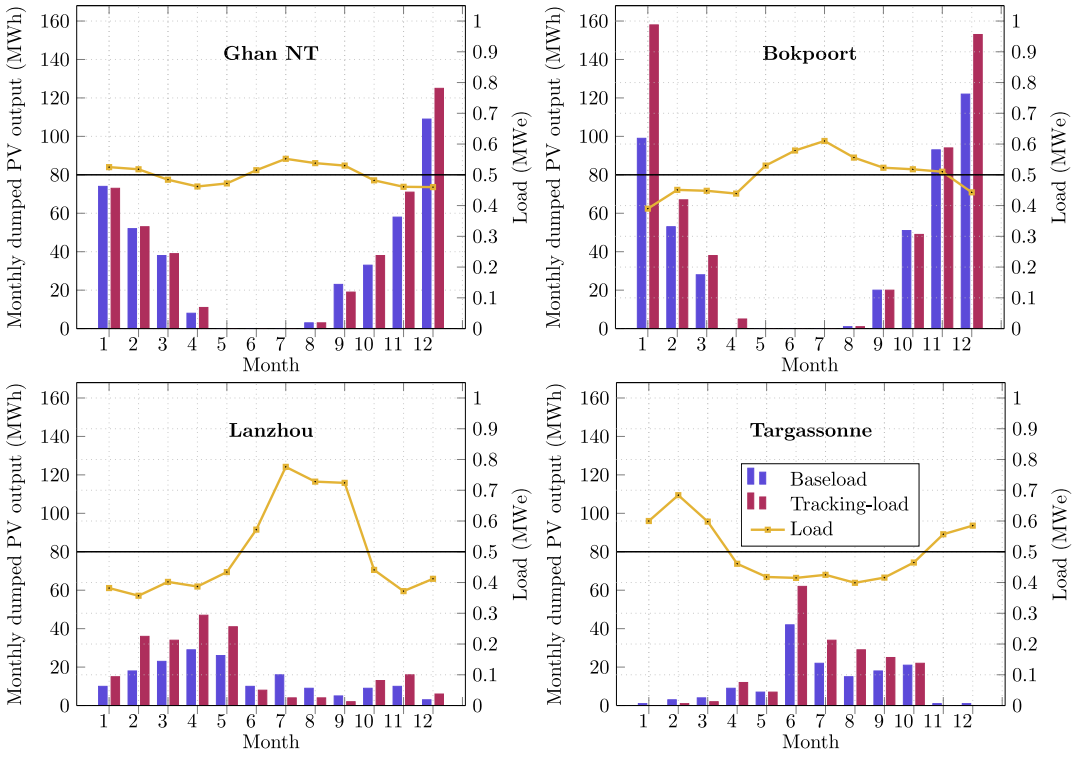

Figure 4.20: Monthly excess PV implementing the two load case scenarios (left axis), and the load profile (right axis) at four locations of the *1S* hybrid plant with 14 MWh_t TES capacity. The black line shows the baseload demand of 0.5 MWe.

- For the *HT* hybrid plant, a tracking load profile will increase the operation of the CSP+TES subsystem in locations with a stable demand profile, such as Antofagasta (Table 4.10). However, a sudden increase in PV surplus can occur at these locations, which is counterbalanced by a decrease in the amount of thermal energy dumped from the solar field (Table 4.10). This can be explained by the dispatch strategy followed to fill the hot water tank, which consists of using the energy from the solar field first, then the PV surplus (see Figure B.5).

Figure 4.21 shows the total annual energy production obtained for the two demand scenarios as well as the relative difference for the ten sites using the two-hybrid plants.

Under the given demand and storage capacity conditions, the impact of a tracking demand profile is limited, with the variation in energy production over a year of operation not exceeding 4%, with a maximum of 3.38% and 2.88% for the *1S* (Figure 4.21(a)) and *HT* (Figure 4.21(b)) hybrid plants, respectively at Bokpoort. With a variable load profile, grid operators are forced to take the PB offline or back online quickly to balance supply and demand. However, this operation quickly becomes expensive as it presents a risk of turbine life impairment and can result in financial penalties if the plant operators cannot guarantee the demand second-by-second. More importantly, the consideration of a variable load profile makes voltage and frequency management more difficult [360].

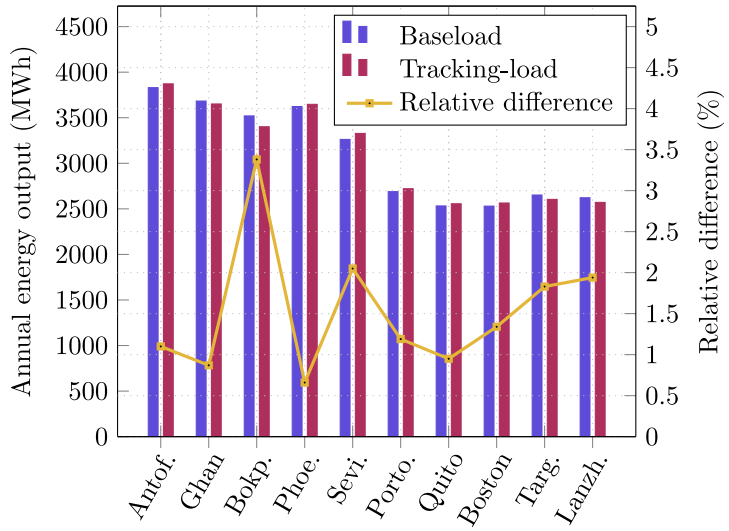

(a) *1S*

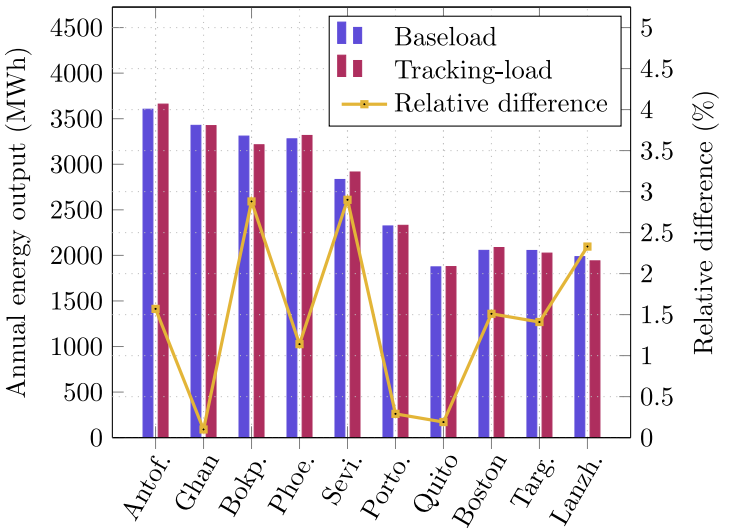

(b) *HT*

Figure 4.21: Annual total generation (left axis) and relative difference (right axis) using the two demand strategies in ten locations for the: (a) *1S*, and (b) *HT* hybrid plants with 14 MWh_t TES capacity.

Finally, similar trends were observed for the other solar plants studied, as shown in Figures B.30 and B.31 in the Appendix B.

Summary

Several important conclusions can be drawn from the initial results:

☞ First, to analyze the effect of hybridization of *compact* PV-CSP plants at fifteen different sites around the world, we began by identifying the maximum annual energy production of the solar plants. Considering the five solar plant technology analyzed, it turned out that the *1S* hybrid plant has the highest maximum annual energy potential, regardless of the site of implementation. In places where DNI resources are abundant such as Antofagasta, there is only a relative difference of 7% between the two-hybrid plants, a relative difference that increases with the decrease in DNI resources with a maximum of 36% in Quito. Since a conventional CSP plant needs a high DNI resource to provide a significant amount of energy, when we move towards locations with a low DNI profile, we not only reduce the annual energy production of the plant but also the relative difference between the annual production of a conventional CSP and a 1-axis PV plant, from 39% in Ouarzazate (MAR) to 3% in Porto Nacional (BR). While with a fixed-tilt PV plant, the relative difference between the annual energy production of the conventional CSP plant and the fixed-tilt PV configuration ranges from 47% in Ouarzazate to 9% in Quito (ECU).

☞ Next, the effect of an increase in the baseload electrical demand and storage capacity of the seven solar approaches was analyzed. The increase in base load and storage capacity led to an increase in annual energy production, as the share of CSP in overall hybrid plant production increased with a consequent expansion of TES capacity. However, this increase also led to a reduction in DF. On the other hand, the lowest reduction in DF occurred within the PV + BESS plants. More importantly, it was found that the variation in performance parameters is highly dependent on the location as well as the solar plant under consideration. Therefore, each technology has a target range in which a good compromise can be found between the different performance parameters to ensure an LPSP below 10%.
Table 4.11 summarizes the different values of P_{load} and storage capacity based on each location. We can see that the required storage capacity increases while the electrical demand decreases for locations with low DNI resources. Mainly because supplying a relatively small P_{load} is more likely with a hybrid power plant than with standalone technologies (i.e., CSP and PV), resulting in a significant amount of unused energy that can be stored efficiently by having a large storage capacity.

Table 4.11: Target range for baseload demand and TES capacity for a LPSP below 10% at the 15 locations and the different solar plants.

Location		Solar power plants						
					PV + TES		PV + BESS	
		1S	*HT*	CSP	Fixed	1Axis	Fixed	1Axis
Antofagasta	P_{load}	≤ 0.5	≤ 0.4	≤ 0.5	0.2	0.2	≤ 0.3	≤ 0.4
	TES	≥ 14	≥ 12	14	≥ 6	≥ 5	4.2	5.9
Ghan	P_{load}	≤ 0.4	≤ 0.3	0.3	0.2	0.2	0.2	0.3
	TES	≥ 12	≥ 11	10	6	6	3	4.7
Bokpoort	P_{load}		0.3				0.2	
	TES	9	11	10	7	7	3	3
Ouarzazate	P_{load}		0.3				0.2	
	TES	9	11	10	7	10	3	3
Phoenix	P_{load}		0.3				0.2	
	TES	9	12	11	8	10	3	3
Tamanrasset	P_{load}		0.3			0.2		0.3
	TES	9	13	13	9	7	3	5.1
Seville	P_{load}	0.3				0.2		
	TES	12	13	13	20	14	3.8	5.1
Abu Dhabi	P_{load}		0.3				0.2	
	TES	9	11	10	7	10	3	3
Porto Nacional	P_{load}				0.2			
	TES	7	16	16	5	7	3.4	3.4
Quito	P_{load}				0.2			
	TES	7	20	20	20	9	3.4	3.4
Boston	P_{load}				0.2			
	TES	15				20		
Targassonne	P_{load}				0.2			
	TES	12				20		
Lanzhou	P_{load}				0.2			
	TES	13				20		
Andheri	P_{load}				0.2			
	TES	15				20		
Jülich	P_{load}				0.2			
	TES				20			

☞ Finally, the impact of a variable load profile on the annual energy production was evaluated at ten sites to approximate realistic operating conditions. An average relative difference of less than 2% was found for the seven solar plant technologies compared to the constant demand profile over a year of operation. This difference does not accurately describe the day-to-day behaviour of the plants under instantaneous solar resources variability, which is more critical for solar plants operating to meet a variable demand profile. In the electricity market, most solar plants adjust their supply primarily based on economic criteria, namely tracking the price of electricity and ensuring that the plant meets the demand during

evening peak hours. In [324] Zurita et al. demonstrated the techno-economic reliability of different solar technologies with TES and BESS as storage facilities operating to supply a baseload demand, highlighting the effectiveness of a baseload demand strategy over a variable load.
The recovery ratio of the *HT* hybrid plant obtained with a tracking-load electrical profile at locations with low load variations throughout a year of operation showed increased values compared to the baseload demand case study as a result of the better use of excess PV energy (Figure B.26). For the *1S* hybrid plant, only small differences were noted when considering the operation under a tracking-load profile (Figure B.27).

Conclusions & Future work

The present work consists of a detailed study on the combination of photovoltaic and concentrated solar power systems in a *compact* hybrid plant. The objectives of this work were to determine (1) whether or not a *compact* PV-CSP hybrid plant is more viable than a conventional CSP plant, (2) identify the impact of a particular storage dispatch strategy on the performance parameters of the *compact* hybrid plants, and (3) understand where *compact* hybrid plants stand today relative to stand-alone solar plants integrating thermal and electrochemical storage systems.
These objectives were addressed in several steps. First, a complete review of the literature was conducted in order to fully understand how the two types of technologies (PV and CSP) work in a stand-alone and hybrid configuration, followed by an analysis of what the hybridization of these two technologies represents, both technically and practically, so that the benefits of each can be taken advantage of. Second, a new multiphysics model was developed. The main improvements that have been made concern the assumptions, namely the detailed description of the optical losses of the solar field, the variation of the cell efficiency with the variation of the ambient temperature and wind velocity, the use of on-site meteorological data, and the description of the main physical parameters. Then, two *compact* hybrid plants were evaluated, the *one-sun* and the *high-temperature* plants. Initially, the analysis was limited to the evaluation of the annual energy production of the hybrid plants, then the study was extended by considering different performance parameters, namely the plant capacity factor, the loss of power supply probability and the amount of curtailed energy.

Concluding remarks

From the calculations obtained, it was possible to verify that:

- *Compact* PV-CSP hybrid systems can effectively outperform the conventional solar tower plant. Nevertheless, the gap between the two *compact* hybrid plants and the stand-alone solar tower plant tends to widen considerably with the increase in PV efficiency. At the same time, the benefit in the energy generation associated with PV-CSP *compact* hybrid systems tends to decrease as the operating temperature of the heat transfer fluid increases. Significant research is currently being devoted to the development of high-temperature CSP plants, which may result in higher CSP efficiency shortly, thus diminishing even more the energy gap one may observe between PV-CSP *compact* hybrid plants and conventional CSP plants.

The development of the *HT* hybrid power plant depends heavily on the ability to develop highly efficient solar cells that can operate at high temperatures for long durations. Finally, the fact that the *one-sun* hybrid technology allows the use of diffuse solar resources contrary to the *high-temperature* and conventional CSP plants widens the deployment range of such technology. Therefore, the annual production of the studied technologies must be evaluated taking into account various locations worldwide, since Targassonne has a good balance between the solar resource and the transparency of the sky, but remains less suitable for the integration of solar technologies, unlike Chile, Africa and the Middle East.

☞ To optimally use the electrical and thermal energy supplied by the PV and CSP subsystems in *compact* PV-CSP hybrid plants, it is mandatory to implement a dispatch strategy to organize the priority of operation of different subsystems. For this purpose, in the second part of this work, two dispatch strategies have been compared; **DS1** where PV production is prioritized and **DS2** where PV curtailments are reduced using an electric heater to store the overproduced PV energy as heat in TES, so that the performance of the two hybrid plants in terms of annual energy production and energy curtailments can be analyzed.
The use of **DS2** has proven to be a good fit for the *1S* hybrid plant as it increases the overall productivity of the plant while maintaining good load demand response, especially for low baseload demand profiles. On the other hand, no significant difference was noted on the overall annual production of the *HT* hybrid plant with the two dispatch strategies because the excess PV of this hybrid plant is limited. This different behaviour resulted in different recovery ratio values for the two *compact* hybrid plants. To extend the study beyond the case of Targassonne, which was found to be less favorable to the integration of the proposed hybrid plants compared to Antofagasta, with a relative difference of 54% in annual energy production with the plant *HT*. Therefore, in this section, a wide range of weather conditions was selected (15 sites around the world). The results indicate that the choice of a particular storage strategy is strongly correlated to the plant technology considered but less to the location of implementation.

☞ Regardless of the location considered, the *1S* hybrid plant show the highest maximum energy production compared to conventional CSP and PV plants. However, in locations with a high solar resource (DNI $>$ 2500 kWh/m^2/year), the *1S* hybrid plant remains the least optimal solution, since it suffers the highest amount of energy reductions with a maximum of 70% in Antofagasta, compared to 44% with the single-axis PV tracking + TES plant.
Regarding storage systems, the combination of PV technology with BESS presents greater simplicity and modularity than TES systems coupled to CSP. On the other hand, BESS have a shorter useful life and therefore need to be replaced more frequently. TES and BESS systems have the advantage of making energy production independent of the solar resource, allowing better control of the plant and extending the production time. This allows delivering a constant output power, which favours the production in nominal conditions, allowing better

maintenance of the turbines and better performance of the power block.
Finally, the impact of a tracking load demand on the performance parameters of the different solar plants was evaluated at ten sites. Regardless of the plant, an average relative difference of less than 5% of the annual energy production was found compared to the constant demand profile over a year of operation.

Scientific contribution

To our knowledge, there is no work to date evaluating the annual energy production of *compact* PV-CSP hybrid systems with changing weather conditions and for a large-scale solar power plant. In this work, we focus on providing results that describe the operation of a real solar plant while delivering the possibility to cover a wide range of operating conditions. Instead of approximating the annual production of the plants based on the given conversion efficiency of the PV subsystems of both *compact* hybrid plants and a simplified description of the main parts of a CSP subsystem, the intention is to develop a detailed model and formulate it as a combination between three main components of a hybrid plant, namely, thermal, electrical and optical. This model offers the possibility to compare the proposed hybrid plants with existing technologies while keeping the run-time as small as possible to study different case studies.

Future works

The present thesis work can be further refined by considering and investigating cases that time constraints did not allow to take into account and that are discussed below.

- ☞ Similar research approaches involving larger heliostat fields representative of current commercial solar plants (e.g. PS10 in Seville [326] and Cerro Dominador in Antofagasta [64] with **624** and **10 600** heliostats respectively) could be investigated. Since, THEMIS heliostat field represents a very particular case study, due to the elevation between rows that resulted in nil blocking losses and negligible shading losses throughout the year of operation. Therefore, the consideration of a larger field will allow to approach commercial plants and to verify the functioning of the proposed hybrid plants.
  There is a wide range of configurations to study, both in terms of heliostat field arrangements and solar receiver types. For the *1S* hybrid plant, it would remain interesting to consider an external receiver, i.e. a panel of parallel aligned tubes usually arranged like a cylinder, rather than a flat receiver, i.e. where tubes are arranged like a rectangle [361], as it offers better thermal performance and remains more suitable with circular fields [362]. For the *HT* hybrid plant, the focus should be on optimizing the layout of the heliostat field, considering a radial staggered display or a cornfield, were heliostats are only located in face of the tower and not surrounding it.

- ☞ The main interest of a *compact* PV-CSP hybrid plant is to combine the low cost of

PV technology with the low cost and efficient TES facility of the CSP plant. The use of expensive III-V solar cells can be justified by their ability to efficiently convert the solar spectrum energy available; however, the high cost of these technologies may present an additional challenge in the face of the widespread development of *compact* PV-CSP hybrid systems. Therefore, the use of silicon as a cell technology will be of much higher financial benefit for the *1S* hybrid technology. For the *HT* hybrid plant, it remains difficult to consider other cell technologies since temperatures up to 400 °C are less favourable for silicon-based cells; therefore, the use of III-V solar cells will be preferred.

☞ Another important comparison has to be conducted between the two main families of PV-CSP hybrid plants, namely *non-compact* and *compact* plants. In addition to the techno-economic evaluation, the study must take into account the environmental evaluation via the assessment of the carbon footprint. The comparison can be made on two different sites with completely different weather conditions, e.g., Atacama desert (CH) and Seville (ES). One of the main reasons encouraging the carbon footprint evaluation is that one of the arguments in favour of the *compact* hybrid plant is related to their expected small footprint.

☞ As the new CSP designs move towards higher operating temperatures [363] with falling particles, supercritical CO_2, etc., the use of other HTFs will more certainly affect the thermal behaviour of the fluid. Today molten salts are used, but they still present a large number of challenges that limit their utilization regardless of their low cost. Also if we can use much lower cost fluids with better thermal properties it will increase the quality of the heat exchange while keeping the low cost of investment.

☞ The consideration of other CSP technologies may present a new set of insights into how *compact* plants can operate at large scale and also increase their suitability for different configurations. Today, parabolic trough collectors (PTCs) have been studied for both hybrid approaches [29, 44, 194]. This technology remains much more mature, flexible, and less expensive than the remaining CSP technologies [364]. One of the main input parameters of our model is the position of the solar reflectors, in our case the heliostats, but it could also be the PTC positions; to obtain this information, we can, for example, use the System Advisor Model (SAM) software [365] and retrieve the proposed positions for a given plant capacity. Furthermore, to validate the results obtained with our model, we can conduct a comparative study between SAMs and our model.

☞ The impact of shading losses is a common problem for conventional flat PV panels that can pose a challenge in the development of the *1S* hybrid strategy. For this, a detailed description like the one performed for the impact of the non-uniform flux density distribution for the *HT* plant is needed. This study can be conducted using existing models for conventional PV plants and extended to the case of PV mirrors. The main difficulty is the large number of solar cells that need to be

connected to efficiently cover the PV mirrors. For this purpose, the heliostat should be considered as a small block and each block as a PV module. Then, the interconnection of the modules constitutes a PV array in a conventional PV field. To simplify the study, we can consider silicon as cell technology for the PV mirrors, which can be practical as the size of current commercial cells used in PV modules varies between 18 to 21 cm.

☞ The use of a conventional PV plant with a BESS seemed attractive to cover baseload demand. However, the possibility of combining the PV plant with two storage units BESS + TES in the same plant would be of high interest. The BESS would cover production shortcomings from the PV plant instead of turning on the turbine for only a short duration, while the priority of the TES would be to supply the load after sunset. The capacity of the BESS may be very small compared to the TES, yet sufficient to endure effective charging and discharging cycles. This study will require some changes in the modelling of conventional PV power plants and the storage priorities.

☞ Depending on the operating condition of the different solar plants, we acknowledged that a significant amount of electricity is curtailed. This problem can be avoided by extending the energy supply to heat and not only electricity; in this way, the unused surplus energy will be used more efficiently. Instead of using the excess PV energy as heat to charge the TES, it can be used to provide electrical demand of some equipment of the plant, for example, powering the electrical demand of the heliostats, while the excess thermal energy can be used to cover hot water demands on the building. The extension of the study to the supply of thermal and electrical energy will increase the capacity factor of the plant without increasing its size, but only by better scheduling of the different parts of the plant.

☞ The effect of daily startups on the turbine performance and lifetime was not considered in this thesis. Due to the nature of the dispatch strategy implemented, both the compact and standalone plants do not operate continuously during the year but experience daily startups instead. Therefore, a study of the impact of these frequent startups on the degradation of the power block needs to be performed. In large-scale power plants operations based on steam cycles, the turbine block needs some time to reach the nominal operating point at startup or to adjust its output to different demand levels during operation. In our model, these delays were not fully accounted for and we assumed that the plant was able to adjust its output quickly enough to reach the desired power at the planned hours in the predefined dispatch strategy.
In our model, we consider that when the TES is fully charged, the heliostats are defocused; however, to keep the receiver warm while the hot tank is full, a small part of the heliostats remain must focused. Incorporating this into our model will allow us to avoid turning on the electric heater for long periods when free energy is available.

☞ Finally, future efforts should focus on model improvement through increased fidelity, reduced computational load, and additional capabilities. Our initial multiphysics model used a one to five-minute time resolution for weather data, which we have had to increase to hourly time steps. However, solar resource transients occur on the scale of minutes or even seconds, such as a cloud passing over the heliostat field. While modelling the annual performance of a CSP system to the nearest minute is quite challenging with current computational resources, or at least tedious for design iteration, we can investigate and understand how these performance degradations due to transients impact the predicted production at the 10- or 15-minute time scales.

Appendix A

Useful parameters for energy evaluation

1 Sun position

The sun's position in the sky at any moment relative to an observer on Earth is defined by three angles:

- The solar elevation angle is the angle between the sun's rays and the horizon (Figure A.1), expressed as [366]:

$$\sin(\alpha) = \sin(\delta)\,\sin(\phi) + \cos(\delta)\,\cos(\phi)\,\cos(\omega) \tag{A.1}$$

where δ, ϕ and ω are the solar declination, the location latitude and the hour angle respectively.

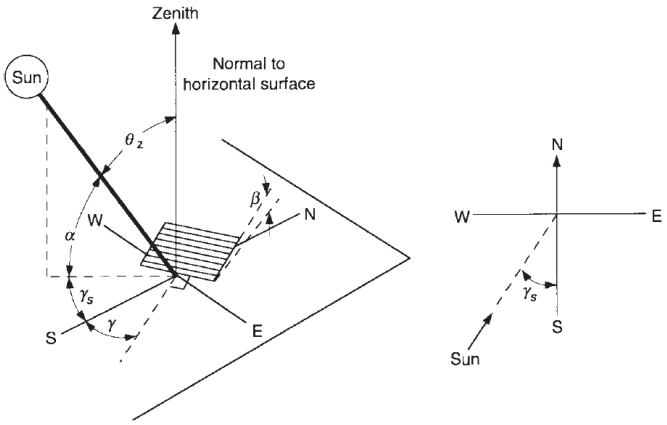

Figure A.1: Zenith angle, elevation angle and solar azimuth angle [43].

- The zenith angle is the angle between the vertical and the line to the sun, that is, the complement to the elevation angle [43]:

$$\theta_z(^\circ) = 90 - \alpha \tag{A.2}$$

- The solar azimuth angle is the angle between the horizontal projection of the sun's rays and geographic due south, shown in Figure A.1. Different expressions

are proposed, but we have chosen the expression proposed by Reda and Andreas [302] in the following equation:

$$\gamma = \arctan\left[\frac{\sin(\omega)}{\cos(\omega)\,\sin(\phi) - \tan(\delta)\,\cos(\phi)}\right] \tag{A.3}$$

For solar radiation users the azimuth angle is given in degrees as:

$$A = 180 + \gamma \tag{A.4}$$

- The hour angle has negative values before the solar noon and lies between -180 ° and 180 ° [367]:

$$\omega = \frac{15^\circ}{h}(t_s - 12) \tag{A.5}$$

where h is the hour of the day and t_s is the solar time detailed in [367].

2 The importance of the DNI resource for the proper operation of CSP plants

In the CSP field, there is a DNI threshold below which the electrical output of the plant is null [368, 369]. The choice of a certain threshold value is a more of a practical and not a theoretical choice, that can be justified by a number of constraints that the plant operation must respect, e.g., the existence of a value of circulation flow rate of the heat transfer fluid below which the circulation pump does not work any more; the constraints of operation of the turbine which does not start below a minimum value of the inlet enthalpy of the steam, etc. Therefore, each CSP plant operator can consider a value that is aligned with the specifications of the components making up the plant. After discussions with experts in the CSP field, we considered a threshold value of 300 W/m^2 below which the turbine does not operate [370].

To identify the minimum power needed to power a turbine a number of steps were followed. First March 21st, 2018 at noon is selected to identify the amount of power available at the inlet receiver for the *1S* and *HT* (the optical power impinging the receiver being the same for the *HT* and the conventional SPT plant.

$$P_{rec\ utile,\ 21March} = \frac{1000(W/m^2) \times P_{rec,\ 21March}(kW)}{DNI_{21March}(W/m^2)} \tag{A.6}$$

where, $P_{rec,\ 21March}$ is calculated using Eq. (2.6) for the *1S* approach and Eq. (2.8) for the *HT* and the conventional CSP plants (see Table A.1).

Once the normalized power impinging the receiver is identified (Eq. (A.6)) we calculated the useful thermal energy as:

$$P_{th\ utile,\ 21March} = \alpha\, P_{rec\ utile,\ 21March} - P_{loss} \tag{A.7}$$

where P_{loss} is the power loss due to convection and radiation given in Eq. (2.26).

Table A.1: The different power output computed March 21st 2018 at noon.

	1S	*HT*	SPT
$\mathrm{DNI}_{21March}$ (W/m^2)		983.779	
$P_{dir,\ 21March}$ (kW)		53	
$P_{rec,\ 21March}$ (kW)	1920	4967	
$P_{rec\ utile,\ 21March}$ (kW)	1952	4656	5048
P_{loss} (kW)		111	
$P_{th\ utile,\ 21March}$ (kW)	1743	4312	4685

3 Spectral distribution of solar radiation for the *1S* strategy

Widyolar et al. [44, 201, 239] proposed a SBS hybrid system using different cell technologies integrated into a PTC receiver. An SBS collector with aluminium gallium indium phosphide (AlInGaP) as a cell technology was used, with high reflectivity on the backside of the cells varying around 80 and 90% (Figure A.2). The availability of experimental measurements of the spectral reflectance of AlInGaP cells makes them a perfect candidate for integration at the *1S* hybrid plant, but also thanks to their good resistance to high operating temperatures demonstrated during the last couple of years [118, 317].

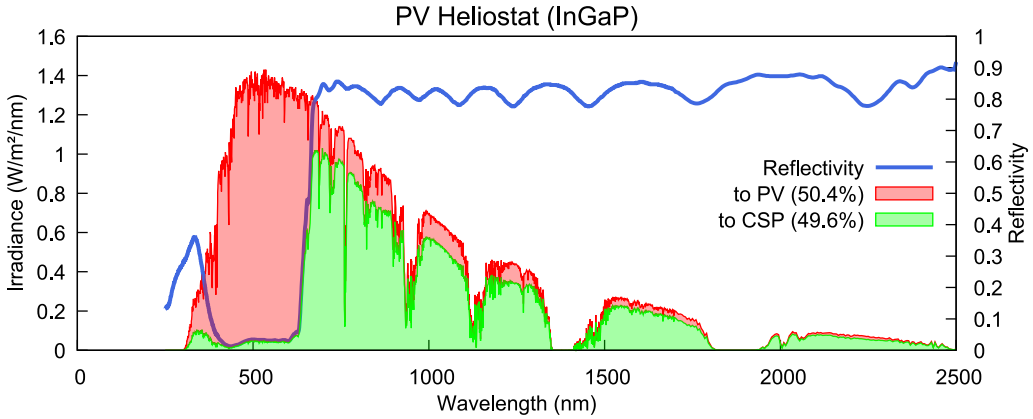

Figure A.2: Measured spectral reflectance of AlInGaP solar cell (blue: cell reflectivity [44]) and calculated fraction of solar spectrum (red: fraction of solar spectrum absorbed by PV, green: fraction sent to CSP).

Table A.2 summarizes the effective values of the Shockely-Queisser coefficients considered for AlInGaP solar cells.

Table A.2: Summary of the ζ_{SQ} values considered in this work for the two hybrid strategies investigated using AlInGaP as a cell technology.

One-sun approach	$\zeta_{SQ,1S}$	$\eta_{PV,exp}$	Reference
Optimistic scenario	0.82	22%	[102]
Realistic scenario	0.76	20.4%	[103]
Pessimistic scenario	0.7	19%	[103]
HT approach	$\zeta_{SQ,HT}$	$\eta_{PV,exp}$	Reference
Optimistic scenario	0.82	22.14%	”
Realistic scenario	0.6	16.2%	”
Pessimistic scenario	0.35	9.5%	”

4 Annual energy output of the hybrid plants and the conventional CSP plant

Table A.3 summarizes the annual energy output of the two hybrid plants and for the conventional CSP plant.

Table A.3: Variations of the annual energy output of the plants considered, for different scenarios of cell efficiency (PV) and temperatures.

			Temperature (°C)								
			300			400			500		
	Energy output (GWh)	Cell technology	**Pess**	**Real**	**Opt**	**Pess**	**Real**	**Opt**	**Pess**	**Real**	**Opt**
1S	PV	**GaAs**	2.16	2.34	2.77	2.16	2.34	2.77	2.16	2.34	2.77
		AlGaInP	1.50	1.63	1.76	1.50	1.63	1.76	1.50	1.63	1.76
	CSP	**GaAs**		0.77			0.86			0.88	
		AlGaInP		1.17			1.32			1.39	
	Heat losses	**GaAs**		0.45			0.56			0.71	
		AlGaInP		0.42			0.53			0.69	
HT	PV	**GaAs**	0.81	1.32	1.83	0.74	1.19	1.66	0.66	1.07	1.49
		AlGaInP	0.53	0.90	1.23	0.50	0.86	1.18	0.47	0.81	1.10
	CSP	**GaAs**	1.79	1.63	1.47	2.07	1.90	1.73	2.25	2.08	1.92
		AlGaInP	1.88	1.76	1.66	2.16	2.03	1.90	2.33	2.19	2.07
CSP Conv.	CSP			2.05			2.34			2.52	
HT		Heat losses		0.99			1.09			1.25	
CSP Conv.											

Appendix B

Integration of TES to the solar technologies

1 Site selection criteria

The output performances of the two-compact hybrid plants and the CR power plant are carried for 15 latitudes covering the -28 – 50 ° latitude range, which is assumed to aggregate most 'suitable' concentrating solar resource sites characterized by annual DNI resource > 1700 kWh/m^2/yr as shown in Figure B.1.

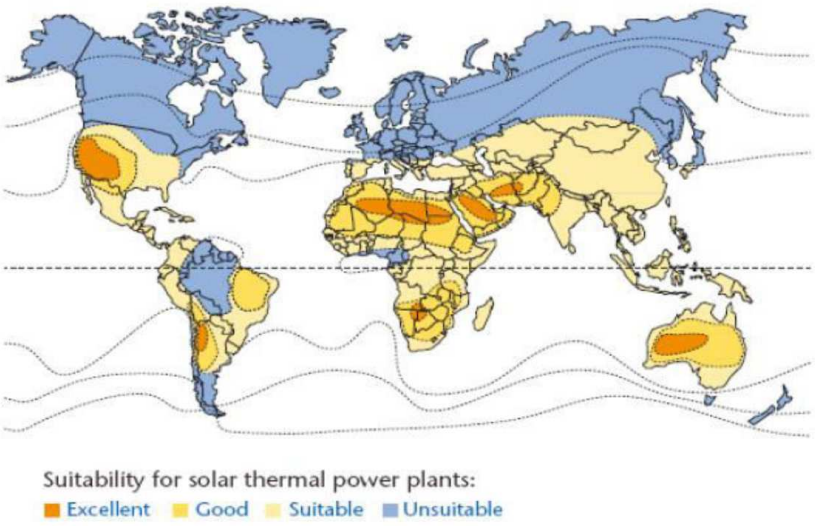

Figure B.1: Suitability map for installation of CSP plants [45].

2 Solar irradiance at the selected locations

Figures B.2, B.3 and B.4 show the hourly distribution of DNI estimated in 2018 using Solcast SDB [335]. Highly irradiated locations rarely experience high-frequency variations in the DNI resource, such as Antafogatsa, while, in Julich, strong variations are visible throughout the year, with the largest variations occurring at the beginning and end of the year.

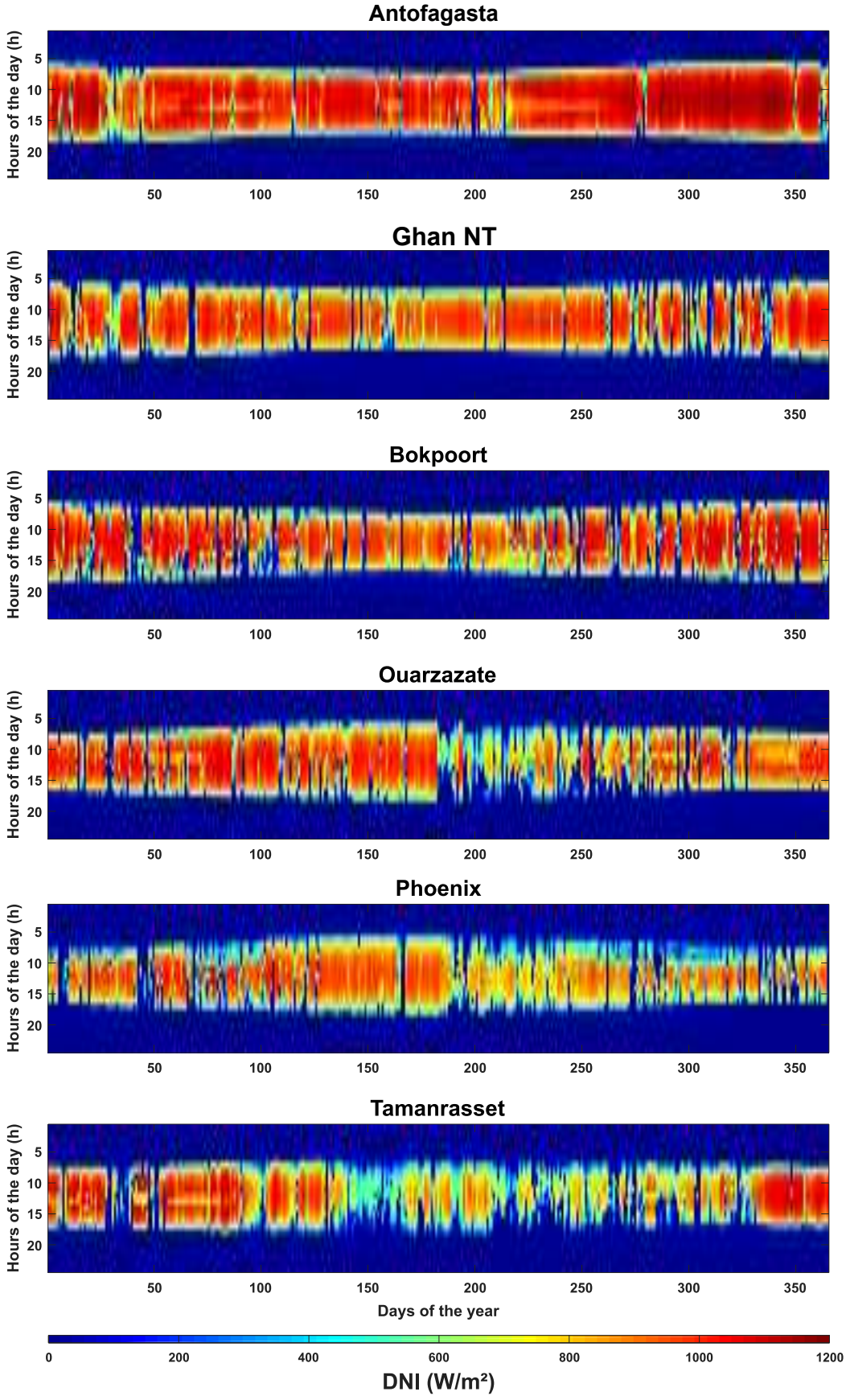

Figure B.2: Hourly estimates DNI profile from Solcast in: Antofagasta, Ghan, Bokpoort, Ouarzazate, Phoenix and Tamanrasset.

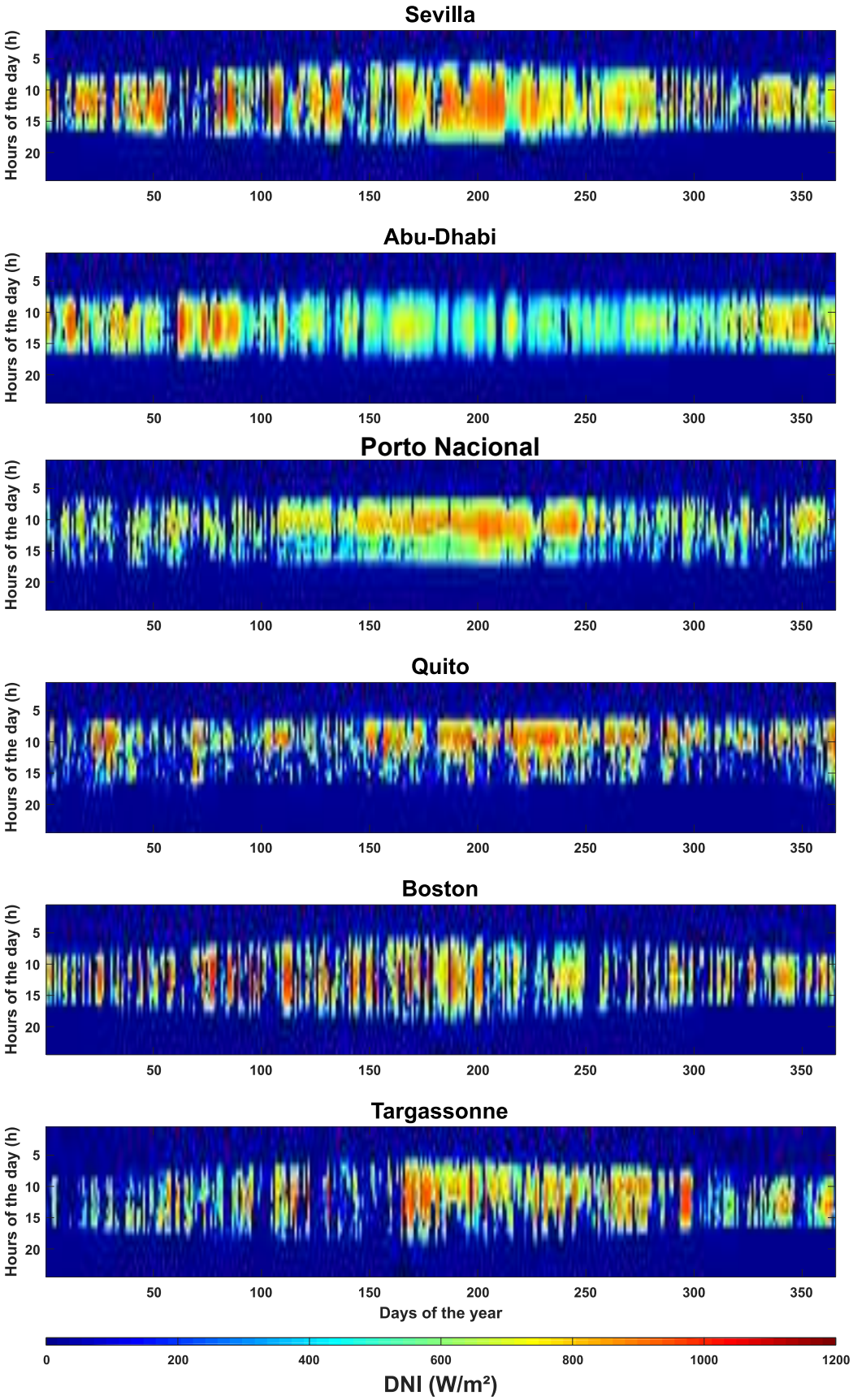

Figure B.3: Hourly estimates DNI profile from Solcast in: Sevilla, Abu-Dhabi, Porto Nacional, Quito, Boston and Targassonne.

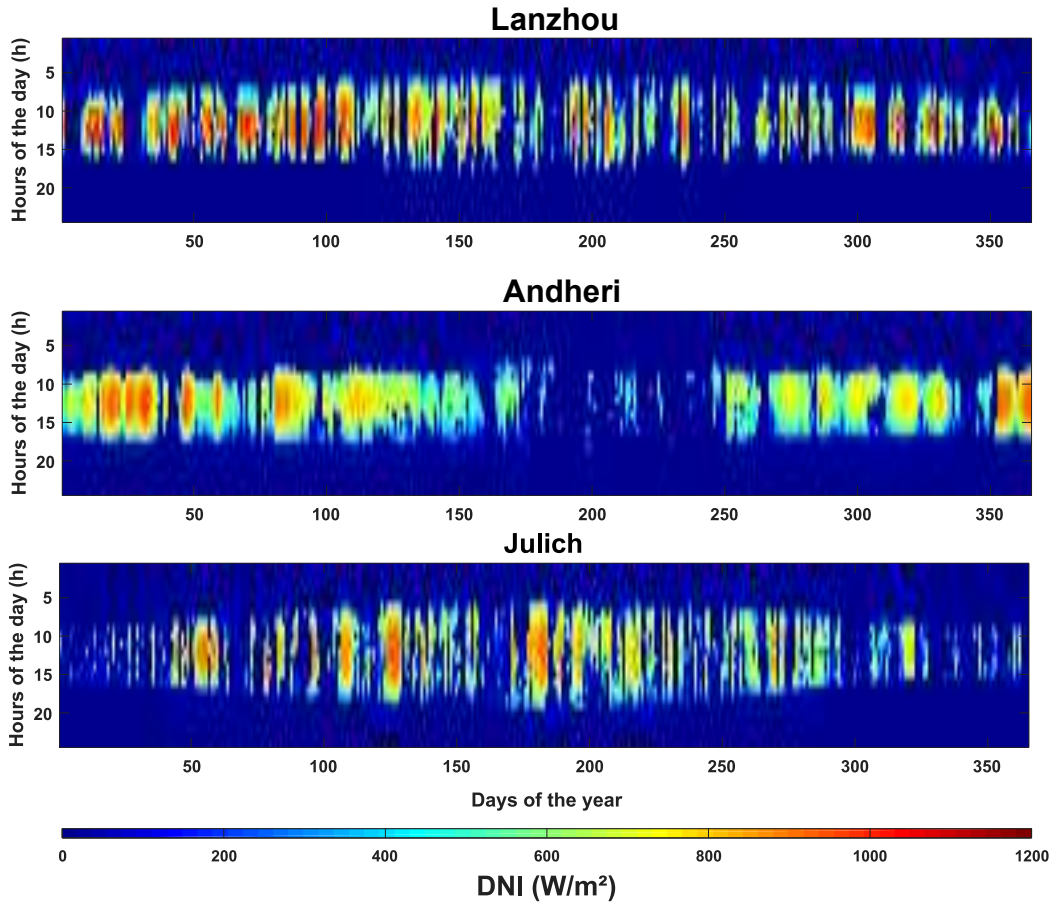

Figure B.4: Hourly estimates DNI profile from Solcast in: Lanzhou, Andheri and Jülich.

3 Flowchart of the different solar technologies

3.1 DS2 approach with the *HT* hybrid plant

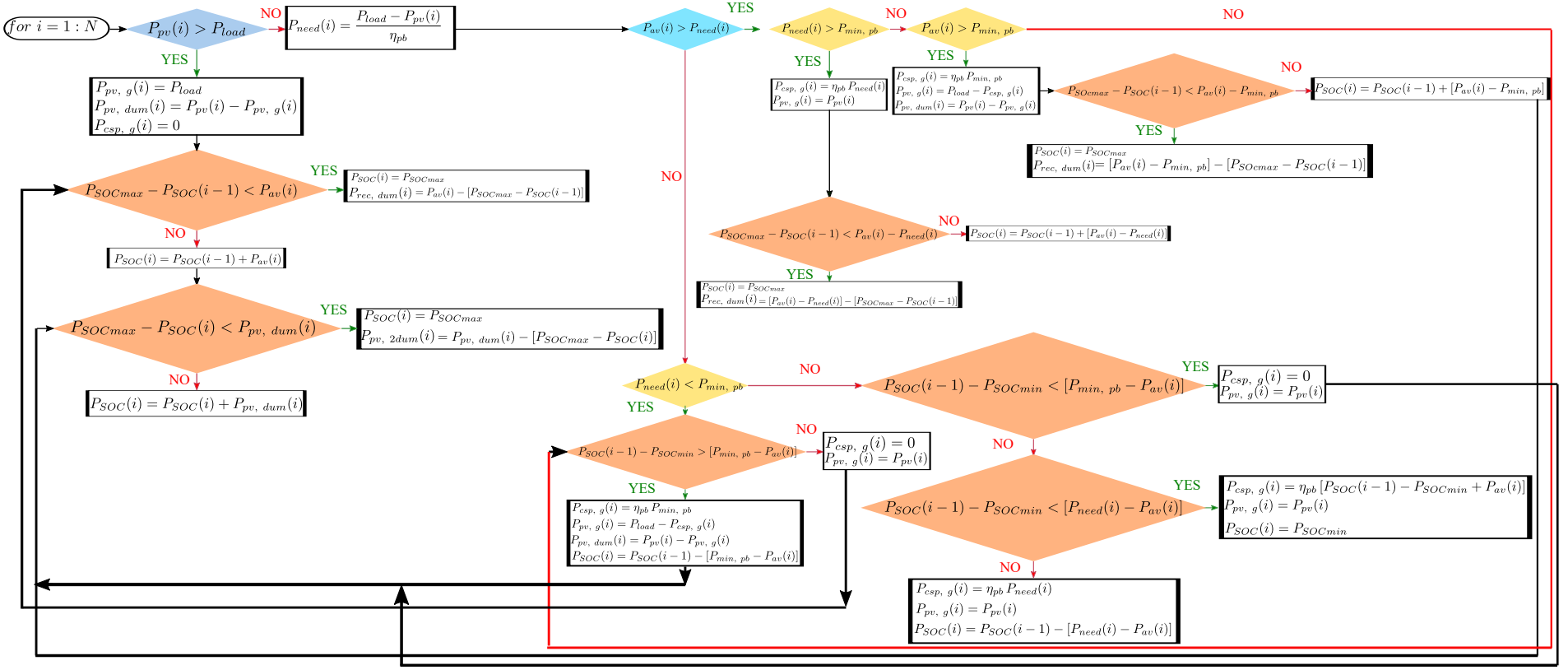

Figure B.5: Flowchart of operational strategy **DS2** of the *HT* hybrid plant. In blue the initial conditions regarding the load demand, yellow conditions related to the operation of the PB and finally orange for verifying the SOC of the TES.

3.2 Conventional CSP plant

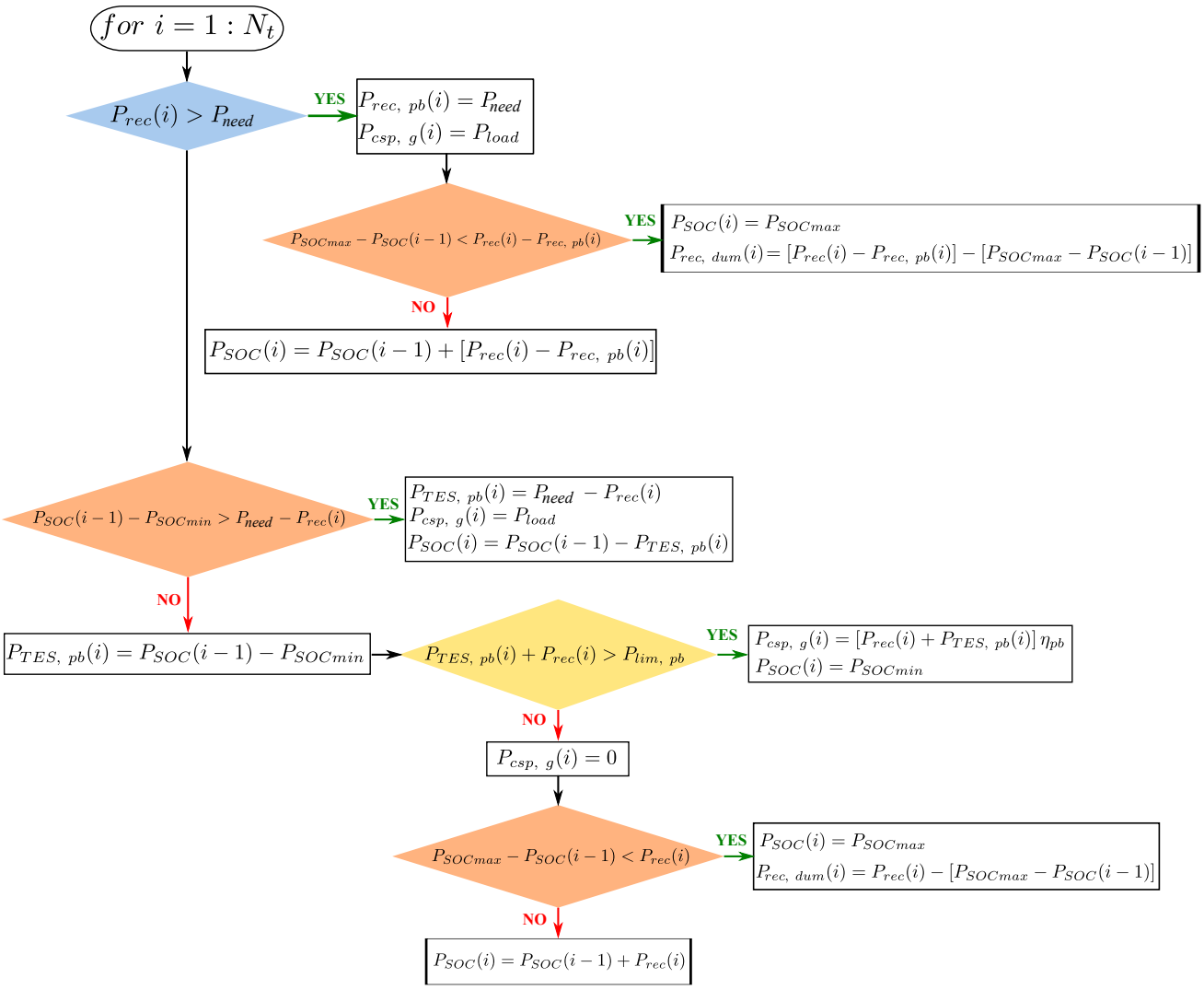

Figure B.6: Flowchart of the operational strategy of a conventional CSP plant.

3.3 Conventional PV plant with TES

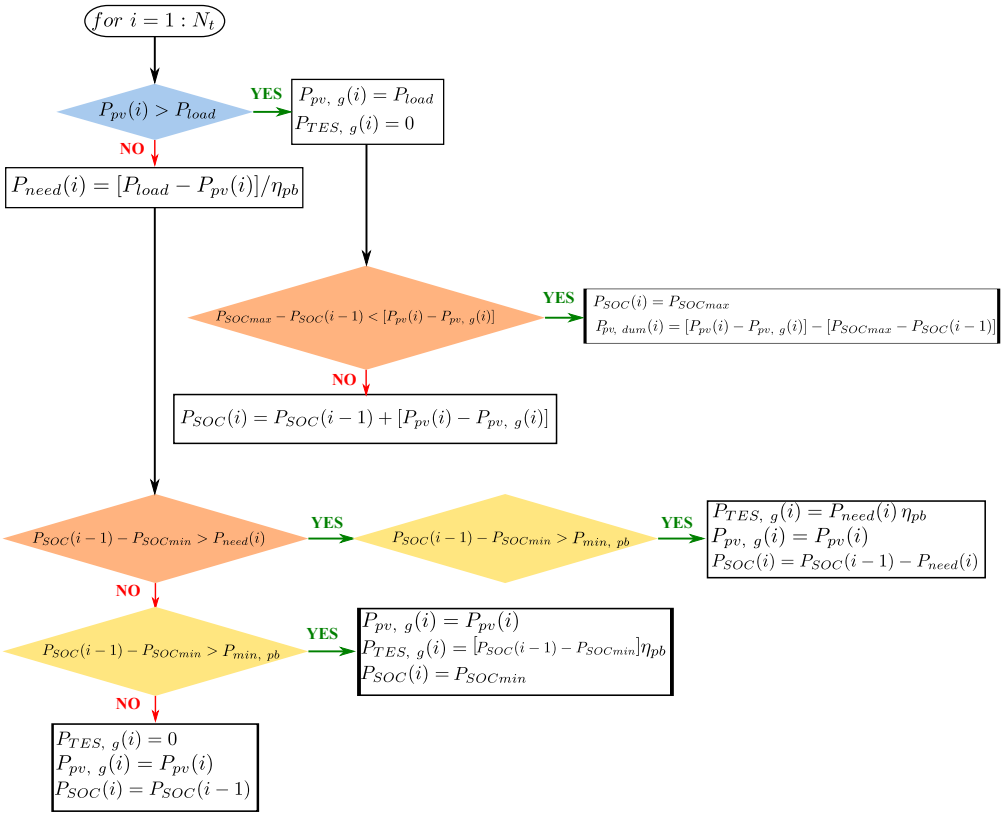

Figure B.7: Flowchart of the operating mode of a conventional PV plant with integrated TES system.

3.4 Conventional PV plant with BESS

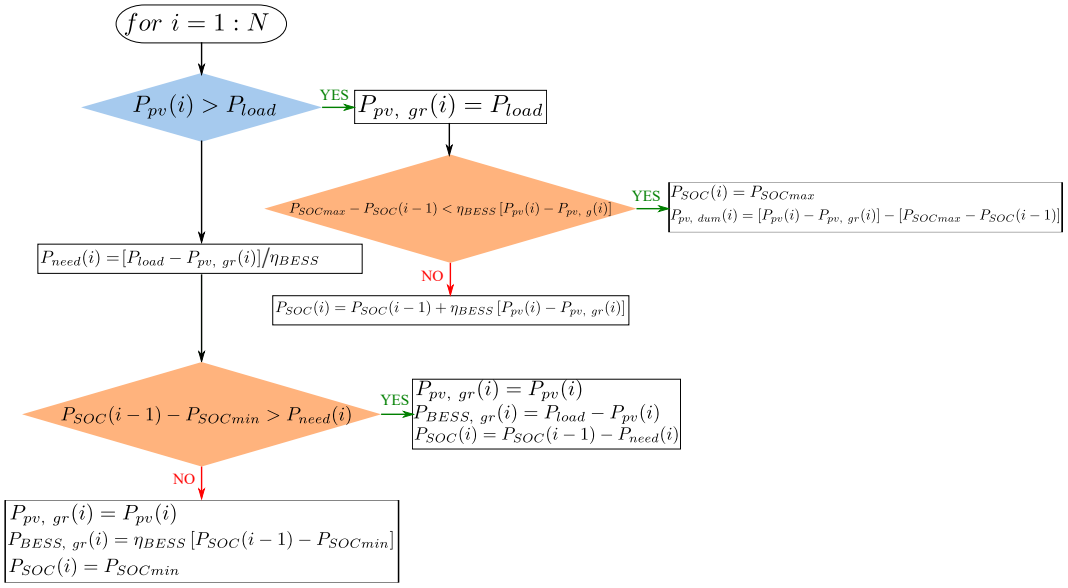

Figure B.8: Flowchart of the operating mode of a conventional PV plant with integrated BESS system.

4 Ground-measured data

The DNI measurements are made with a pyrheliometer Kipp & Zonen CH1 recorded by a Gantner eReader low voltage high precision industrial ModBus data acquisition module as shown in Figure B.9. The sun tracking is made by a 2 axis robot Kipp & Zonen SOlys 2 in open loop. In addition to periodic cleaning of the instruments, quality checks of the measurements are assured thanks to the DHI and GHI measured simultaneously with 2 Kipp & Zonen pyranometers CMP6. The checks are based on protocols from NREL's SERI QC [371, 372] with custom implementation written in Python and running on a Linux server. Live data is stored in a MariaDB database with a custom Apache+PHP internal website for easy access to the archive.

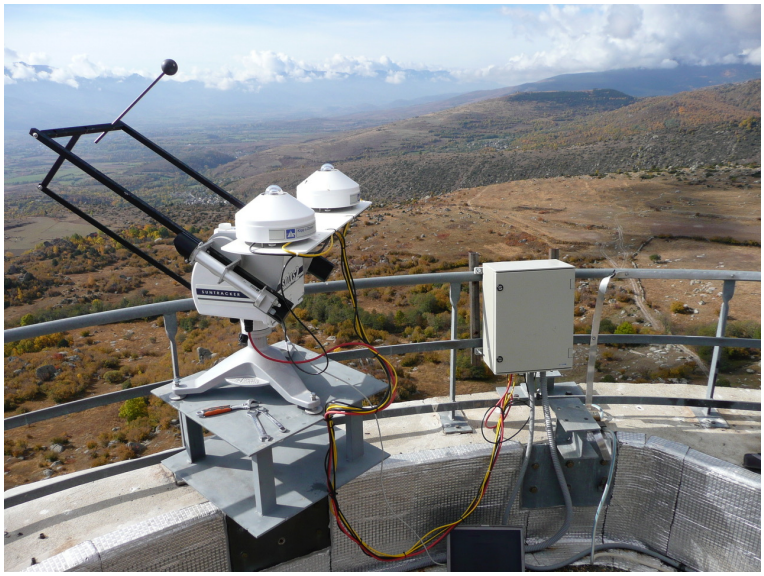

Figure B.9: Photo of meteo station with 2 Kipp & Zonen pyranometers CMP6 (GHI, DHI) and a Kipp & Zonen CH1 pyrheliometer (DNI) at THEMIS CR plant.

5 Optical model validation

The optical validation of the heliostat field was carried in chapter 2 for Targassonne. Inhere, we propose to validate the accuracy of the interpolation function used to describe the shading and blocking losses of the heliostat field at the 15^{th} locations. Table B.1 summarizes the mean relative difference of the entire heliostat field between SolarPILOT values and the interpolation function at four different days along the year. The number of data points needed for the interpolation function is irrelevant to the relative difference when comparing the locations in-between.

Table B.1: Relative difference between SolarPILOT shading losses and the interpolation function over the whole heliostat field.

	Relative difference (%)				
Days Time	**March 5th 8 a.m.**	**May 10th 10 a.m.**	**July 20th 3 p.m.**	**Nov. 15th 2 p.m.**	Mean relative difference (%)
Antofagasta	1.85	0.47	0.18	0.00	0.62
Ghan NT	0.50	0.00	2.29	0.00	0.70
Bokpoort	0.31	0.00	0.83	0.00	0.29
Ouarzazate	0.23	0.00	0.13	0.19	0.14
Phoenix	0.24	0.00	0.13	0.56	0.23
Tamanrasset	0.28	0.00	0.04	0.11	0.11
Sevilla	0.29	0.00	0.31	0.34	0.24
Abu-Dhabi	0.30	0.00	0.77	0.14	0.30
Porto Nacional	0.57	0.03	0.29	0.00	0.22
Quito	0.47	0.00	0.00	0.00	0.12
Boston	0.62	0.00	0.00	0.40	0.26
Targassonne	0.81	0.75	0.00	0.34	0.47
Lanzhou	0.18	0.00	1.48	0.30	0.49
Andheri	0.26	0.00	0.00	0.04	0.08
Jülich	0.83	0.00	0.21	1.06	0.53

For example, Ghan (AU) is the location with the highest number of data points (297 points in comparison to Tamanrasset with only 264 points as shown in Figure B.10), yet the relative of difference is the highest at 0.70%; however, it is of high relevance for a better description of shading and blocking losses of the entire heliostat field with the interpolation function. Meanwhile, the relative difference can be seen to increase with decreasing latitude as the solar path across the sky occurs at higher elevations, and the system operates further off-axis.

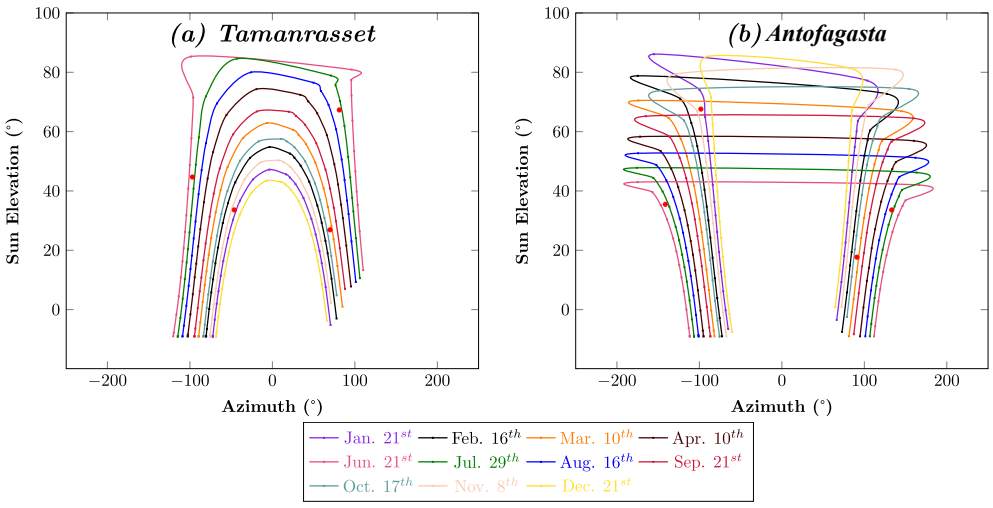

Figure B.10: Interpolation data points considering 11 days throughout the year along with the four additional points for validation of the interpolation function in: (a) Tamanrasset and (b) Antofagasta.

6 Solar databases

In Figure 3.5, it can be noticed that the regression line does not pass through the high-density distribution of data points around high DNI values; this can be explained by the fact that the function of the regression line follows the density distribution of data points at the origin (0,0). To verify the accuracy of the following observation, in Figure B.11 we plotted the probability density estimate of the solar component as a function of measured irradiance, using the two SDBs. From the distribution of the density estimate, it can be noticed that the distribution of DNI values is very large at the origin with both SDBs (see Figure B.11), thus dictating the trend of the regression line distribution.

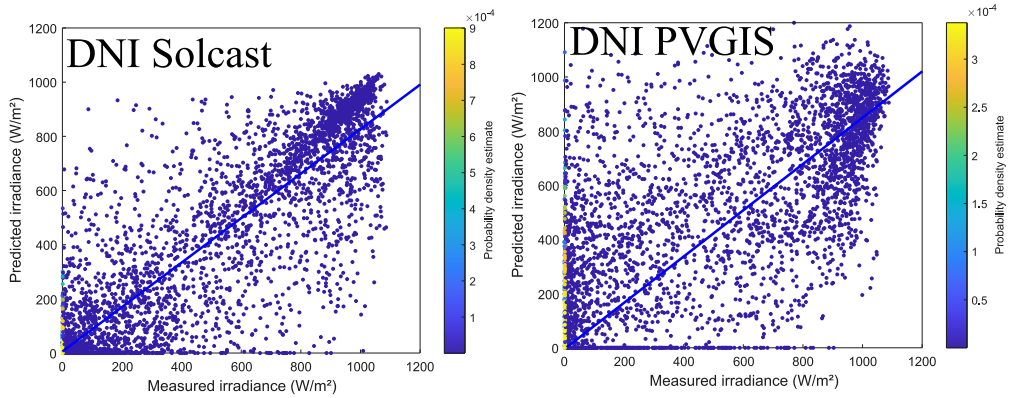

Figure B.11: Probability density estimates of the hourly estimates of DNI from Solcast and PVGIS compared to measured data at Targassonne. Yellow data points at the origin represent the highest probability density estimate of DNI values.

However, the high density of data points with very low values does not allow better visualization of the density distribution and the shape of the regression curve. For that, we consider only plotting DNI values greater than 300 W/m^2 in Figure B.12. Solcast shows a less scattered distribution of DNI data than PVGIS. More importantly, the highest probability density estimate varies around high DNI values.

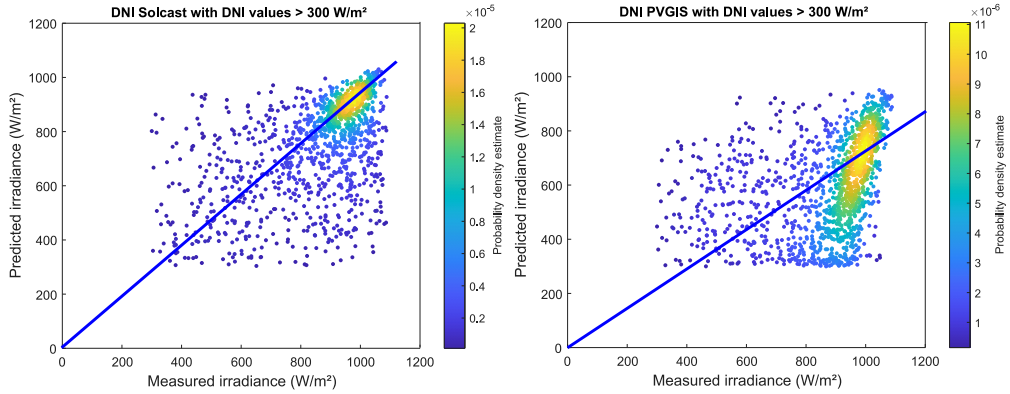

Figure B.12: Probability density estimates of the hourly estimates of DNI from Solcast and PVGIS compared to measured data at Targassonne.

Figure B.13 shows that Solcast SDB present a less scattered distribution of GHI data points than PVGIS. To maintain a representative number of data points, the filter was only applied to DNI values and not DHI and GHI.

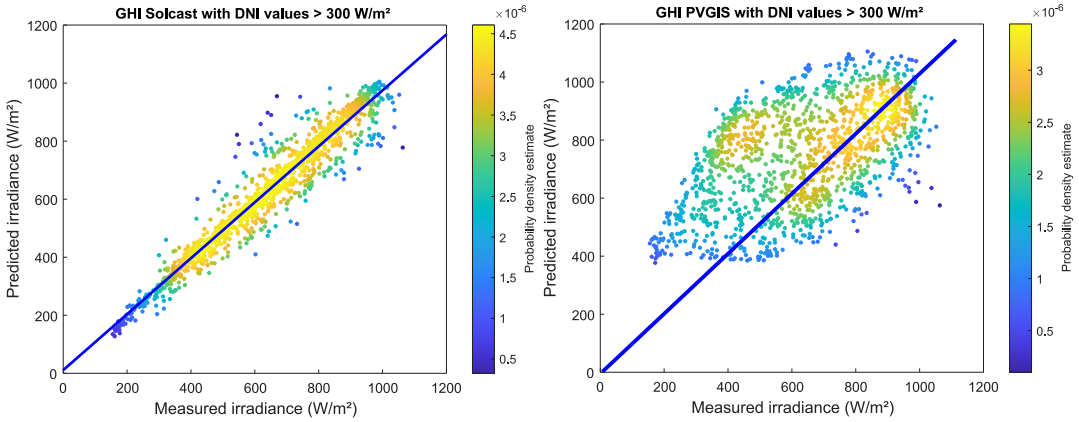

Figure B.13: Probability density estimates of the hourly estimates of GHI from Solcast and PVGIS compared to measured data at Targassonne.

PVGIS is generally used for studies focused on PV plant sizing rather than CSP plant sizing, as the main objective of this tool is to provide an accurate estimation of the PV power generation at a given location considering different PV mounting configurations. Therefore, the solar components are provided to allow the user to verify the accuracy of the power production provided.

7 Impact of time resolution

Figure B.14 shows the time variation of the DNI at Targassonne and Antofagasta over a day characterized by a highly variable solar resource (Figure B.14(a)) or a clear-sky day (Figure B.14(b)). It can be noticed that increasing the time resolution reduces the amplitude of the instantaneous variations of the DNI at both locations. Increasing the time resolution from 5 min to 60 min leads to a slight reduction of the daily resource at Targassonne which induces a slight decrease in electrical production from CSP and hybrid plants at this location.

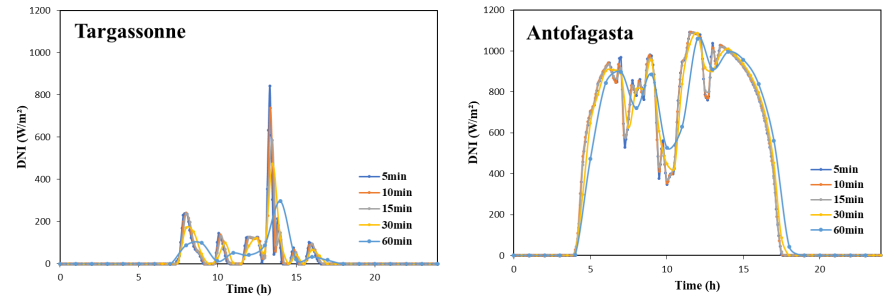

(a) **Variable solar resource day**

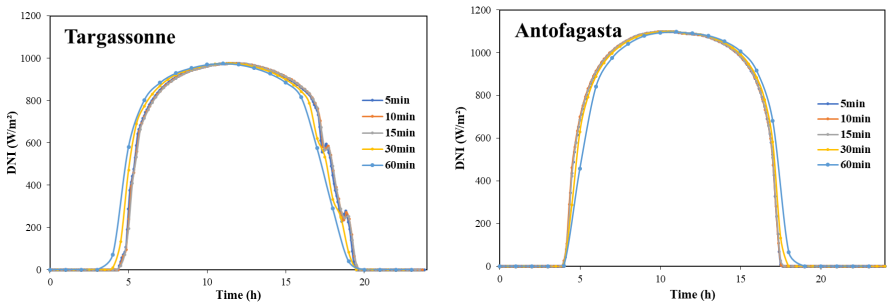

(b) **Clear-sky day**

Figure B.14: Variation of estimated DNI resource using Solcast for different time resolutions during: (a) highly variable solar resource days (January 1^{st}, 2018 at Targassonne and January 2^{nd}, 2018 at Antofagasta) and (b) clear-sky day (June 19^{th}, 2018 at Targassonne and January 1^{st}, 2018 at Antofagasta).

8 PVSyst loss diagram

There are distinctive sorts of field losses that help in analysing the various losses that are to be encountered while installing PV plants or constraints to be considered as depicted in Figure B.15.

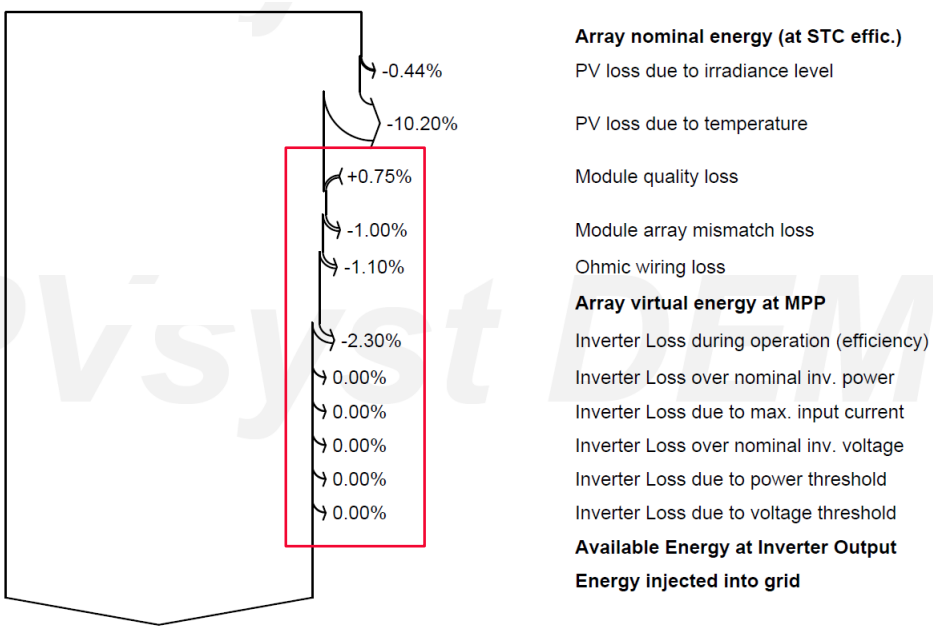

Figure B.15: Example of loss diagram simulated by PVSyst at Porto Nacional (Brazil).

9 DNI resource at different locations

Figure B.16 shows the variation of the DNI resource at three locations during six successive days. From the three locations, Ghan is the one with the least variation on the DNI resource, while Jülich remains the location with the largest variations of the DNI resource.

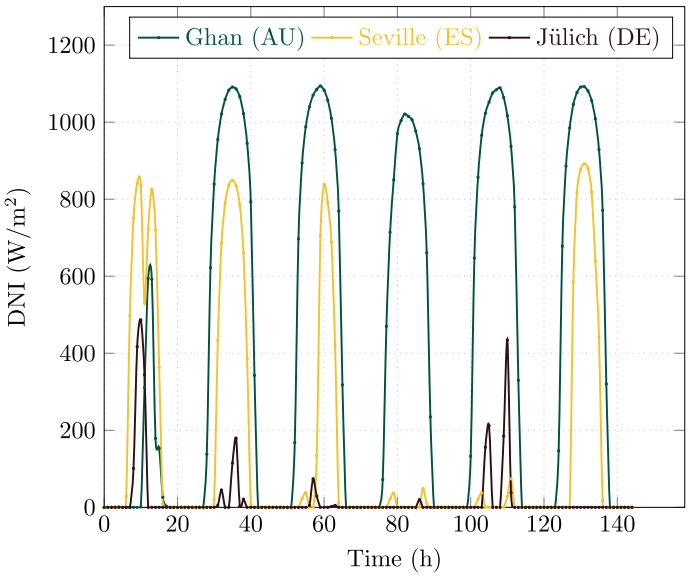

Figure B.16: DNI daily distribution at three locations during the six first days of January 2018.

10 Annual PV and CSP production

In Chapter 4, Figures 4.14 and 4.15 show the annual variation of the different performance parameters of the two hybrid plants and the two PV configurations with integrating TES system, respectively. To better understand the behaviour of the different components of the studied solar plants, Figures B.17 and B.18 show the annual PV and storage output production of the two PV configurations and the two hybrid plants located in Ouarzazate, respectively.

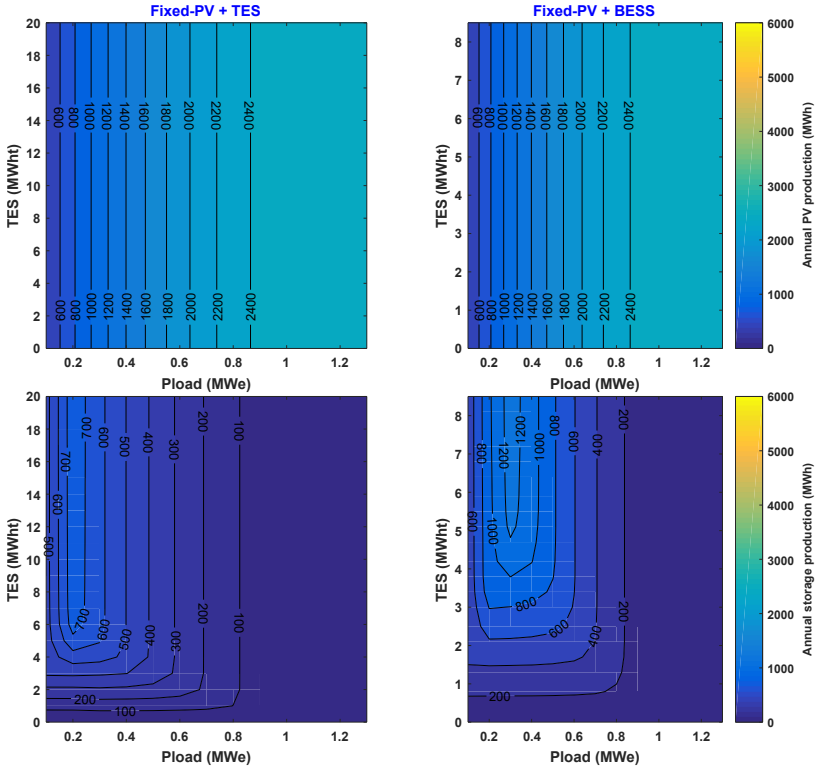

Figure B.17: Annual PV and storage contribution of the Fixed-PV + TES (left plot) and BESS system (right plot) located in Ouarzazate.

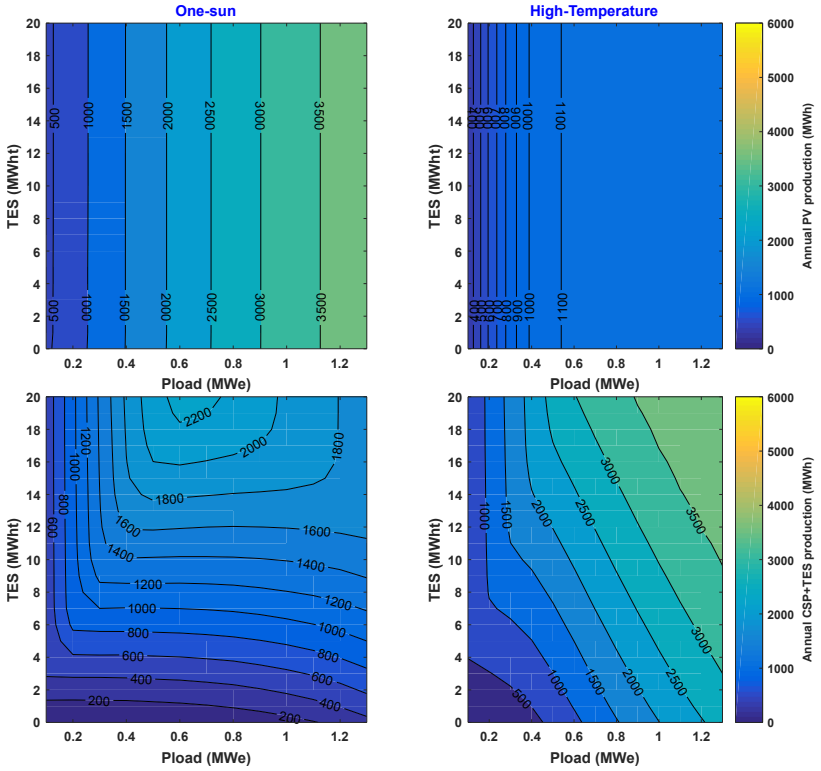

Figure B.18: Annual PV and CSP+TES contribution of the two-hybrid plants located in Ouarzazate.

11 Loss of Power Supply Probability

In the purpose of simplifying the reading of Chapter 4, the focus has been on identifying the different sets of performance parameters of the seven solar approaches at one site, namely Ouarzazate. Here, we summarize the variation of the LPSP of the seven solar plants at the 15 selected locations with increasing load demand and storage capacities.

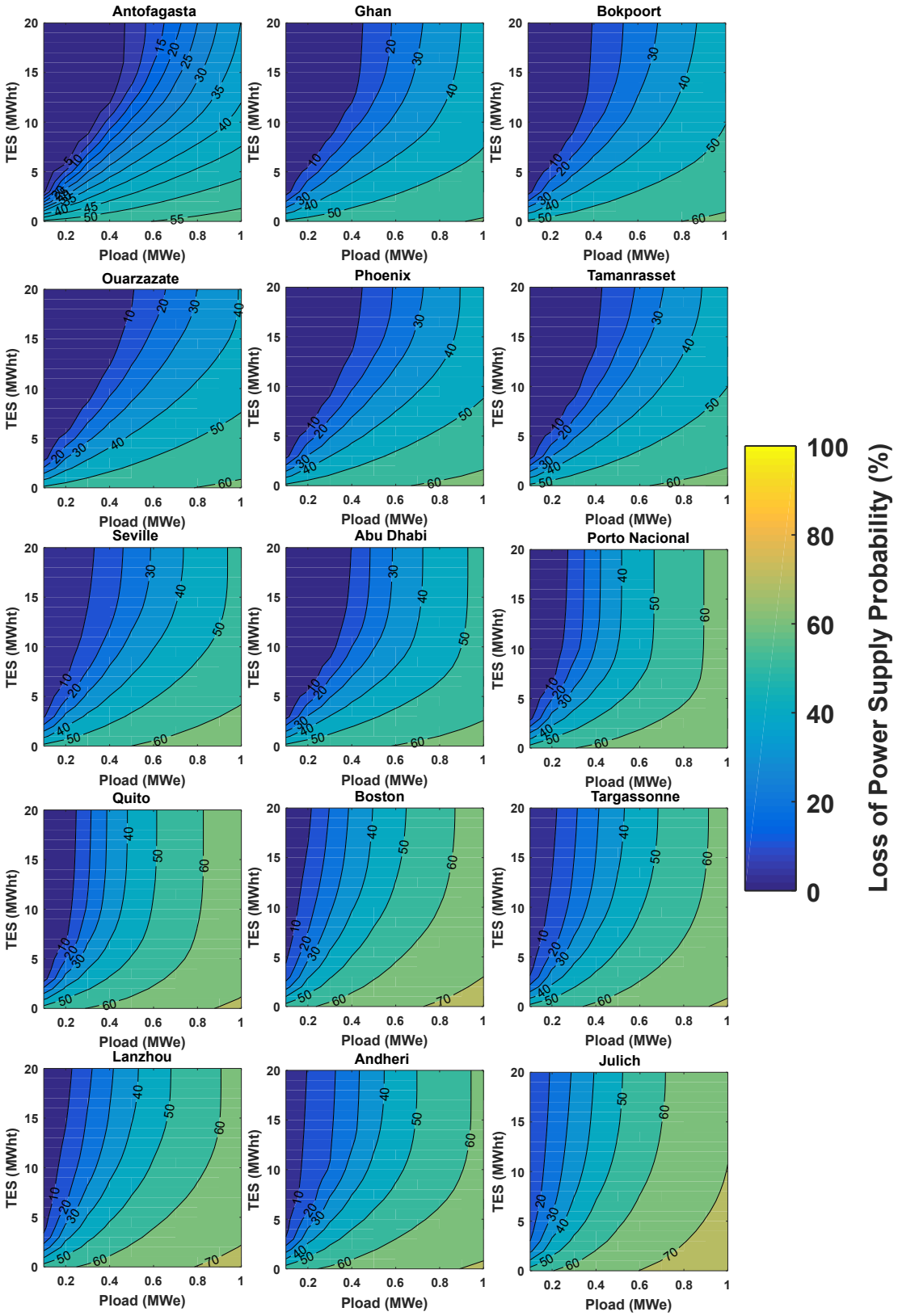

Figure B.19: Loss of power supply probability of the *1S* hybrid plant with TES capacity and P_{load} at the selected locations.

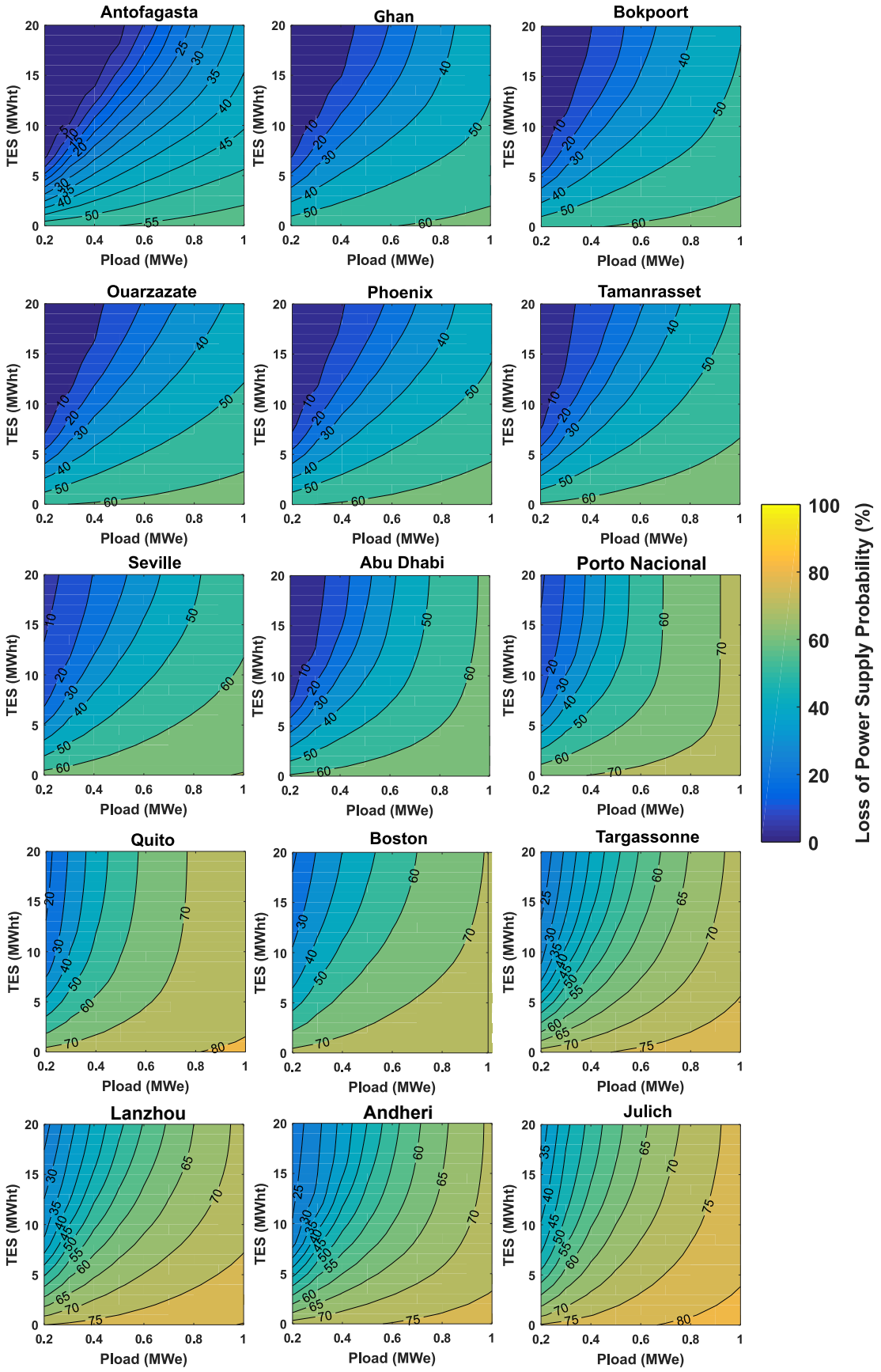

Figure B.20: Loss of power supply probability of the *HT* hybrid plant.

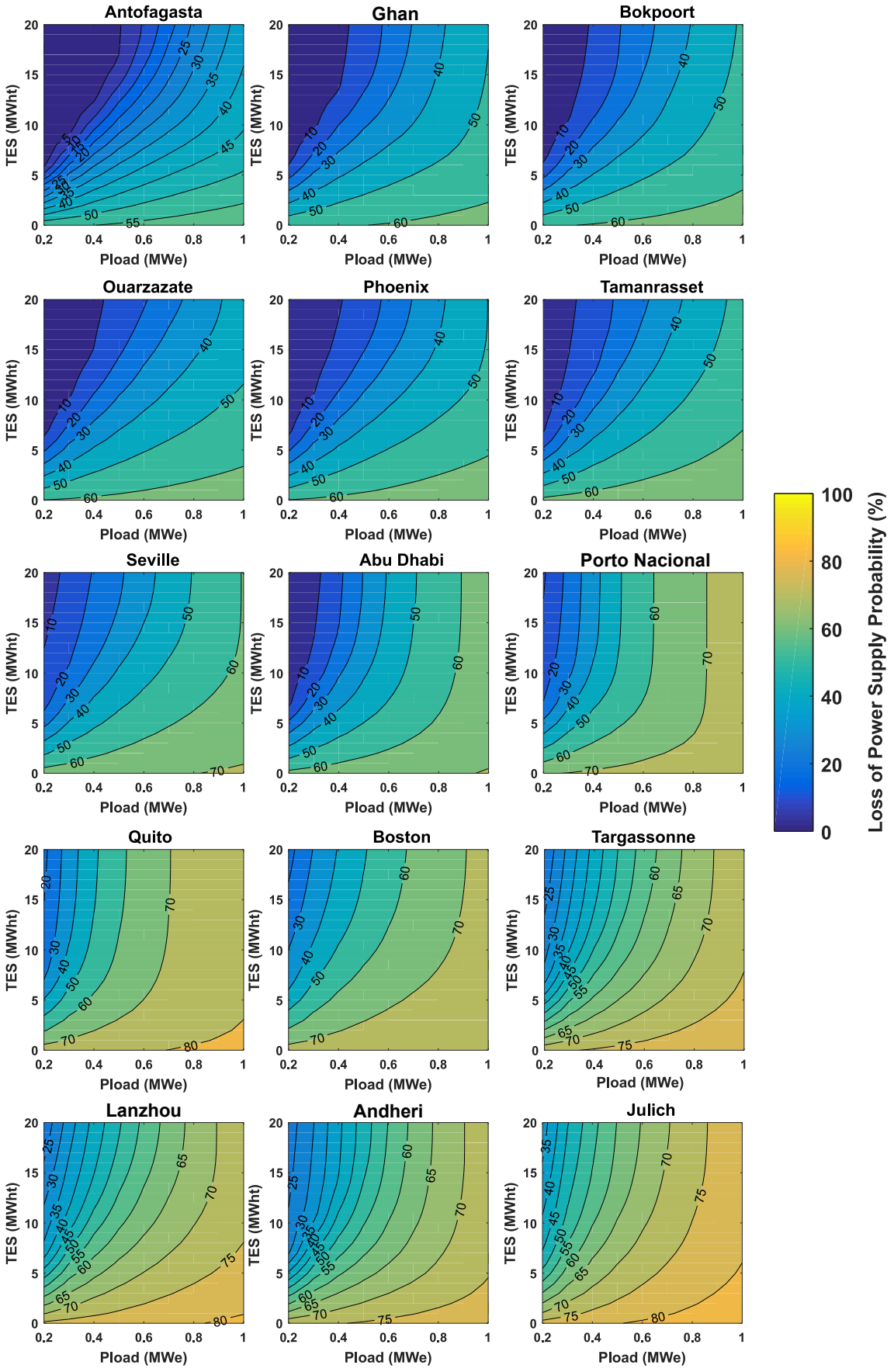

Figure B.21: Loss of power supply probability of the conventional CSP plant.

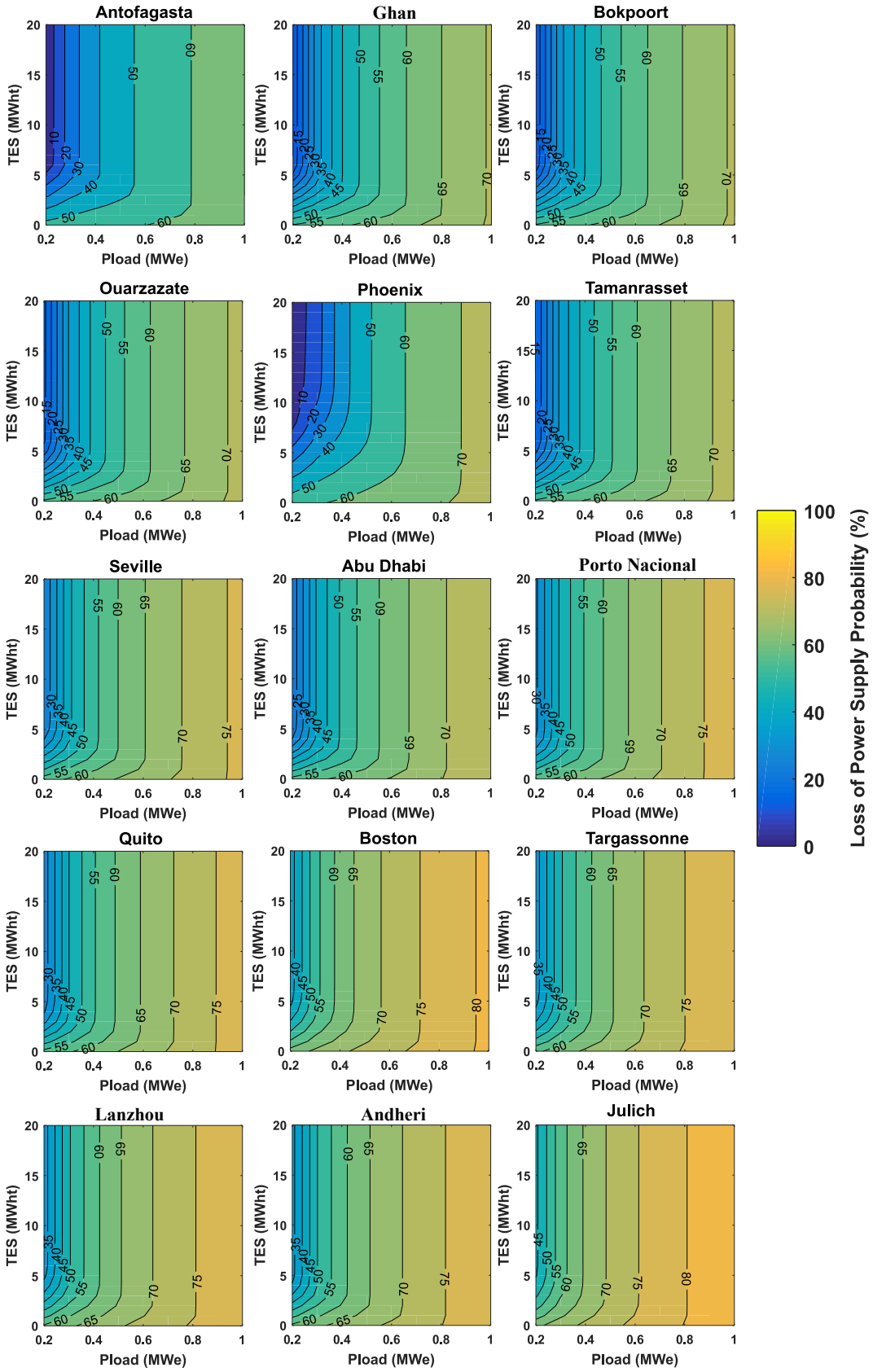

Figure B.22: Loss of power supply probability of a fixed-PV plant with integrating TES system with TES capacity and P_{load} at the selected locations.

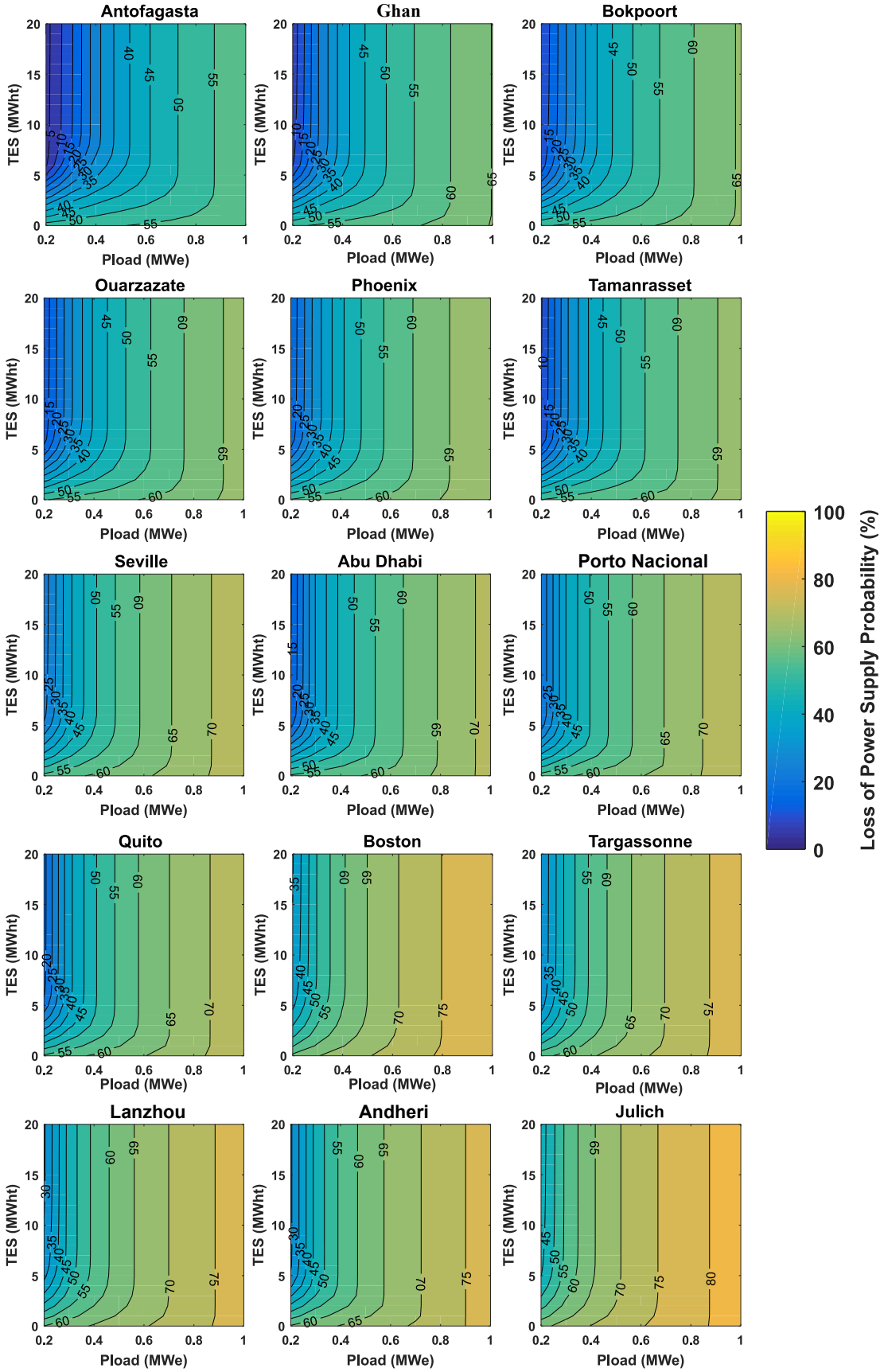

Figure B.23: Loss of power supply probability of a 1axis-PV plant with integrating TES.

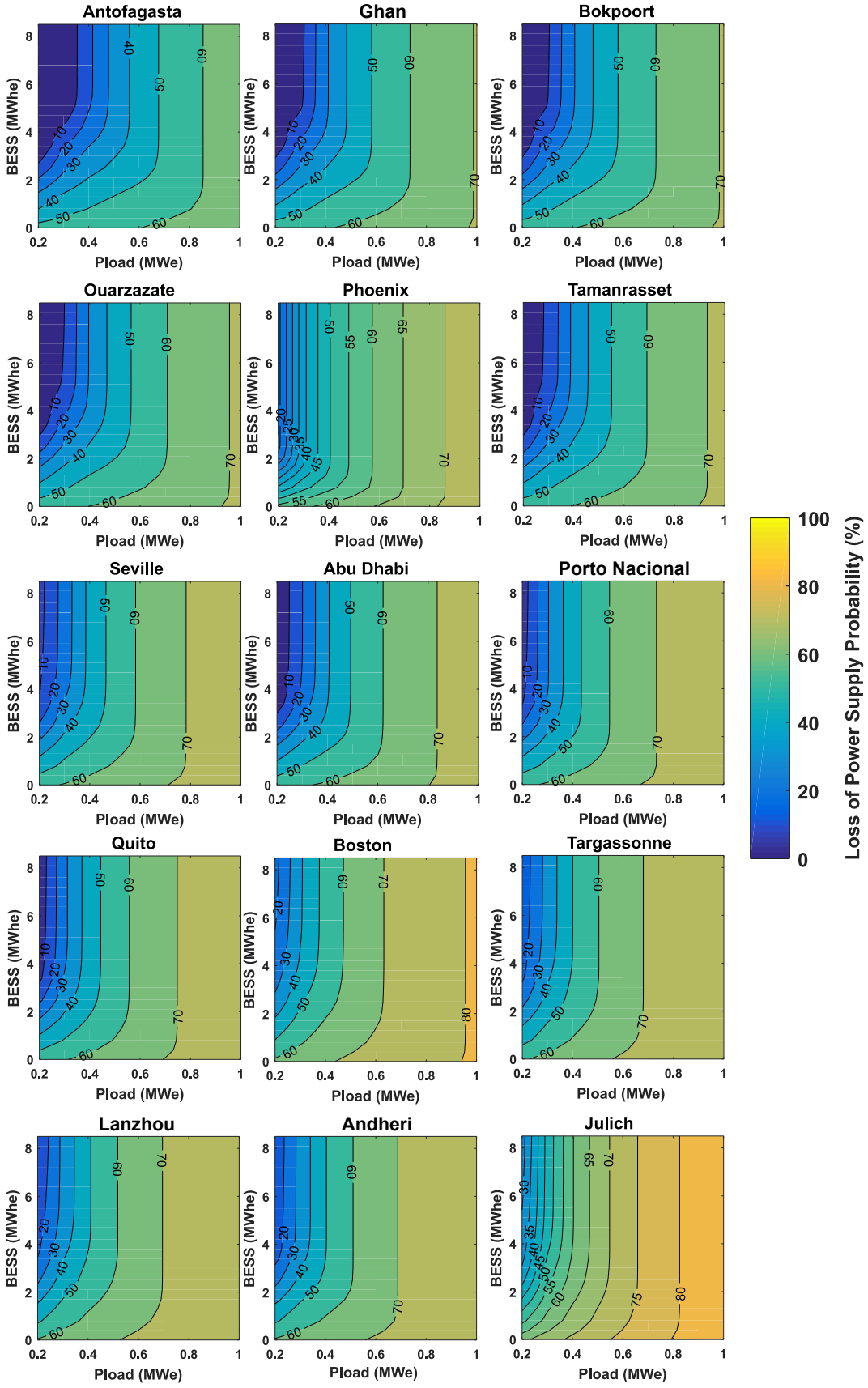

Figure B.24: Loss of power supply probability of a fixed-PV plant with integrating BESS system with BESS capacity and P_{load} at the selected locations.

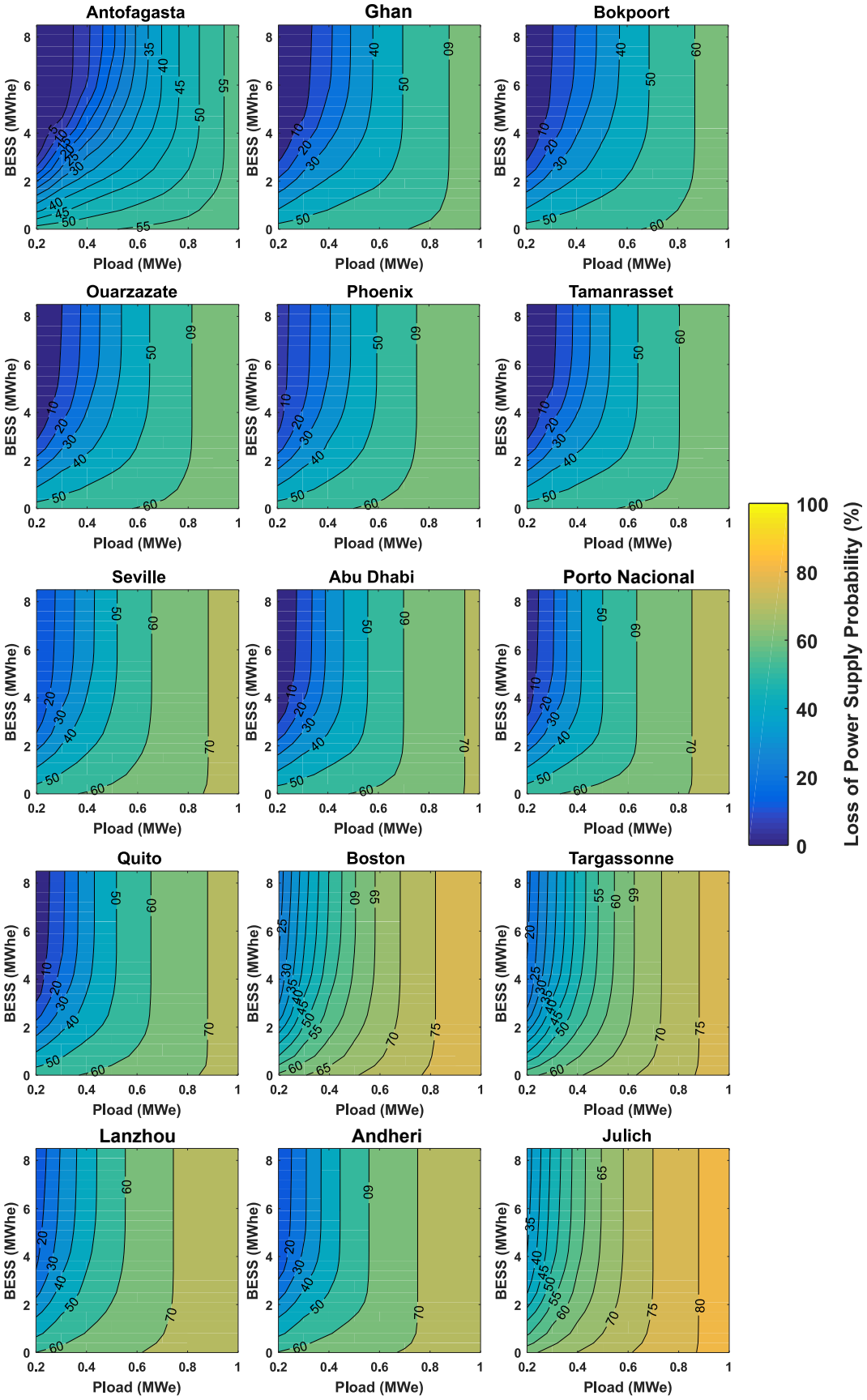

Figure B.25: Loss of power supply probability of a 1axis-PV plant with integrating BESS.

12 Variable load profiles

The identification of the recovery ratio in Chapter 3 was limited to the case study of a constant electrical demand (see Figures 3.23 and 3.25). Figures B.26 and B.27 show the variation of the recovery ratio with increasing electrical demand and storage capacity when the *HT* and *1S* plants are operated to meet a variable load demand, respectively.

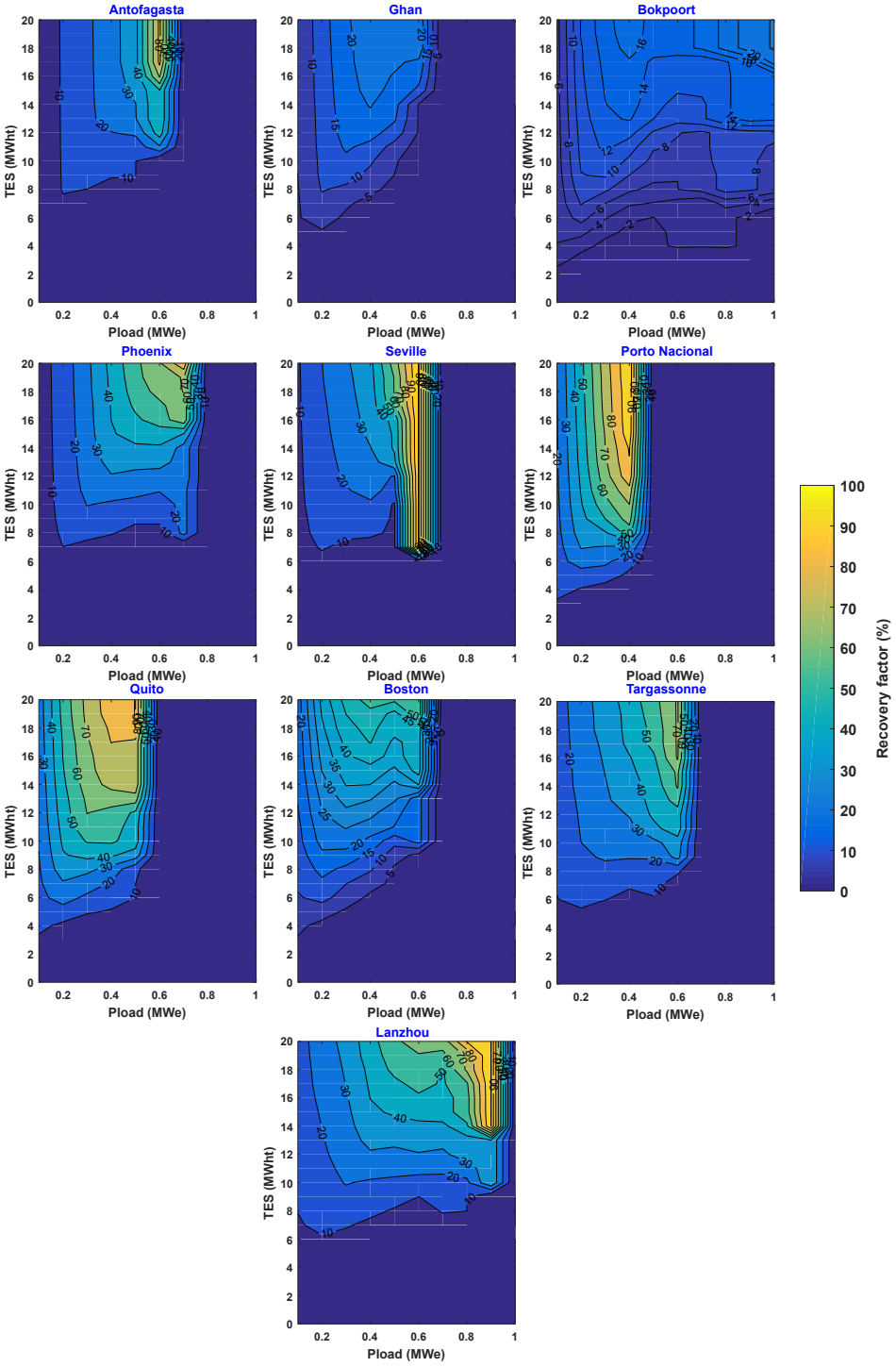

Figure B.26: Recovery ratio of the *HT* hybrid plant at the selected locations considering the **DS2** to supply a variable load demand.

Taking into account a variable load profile does not have a significant impact on the recovery ratio of the *1S* hybrid plant; due to the abundant amount of PV surplus to be recovered (Figure B.27).

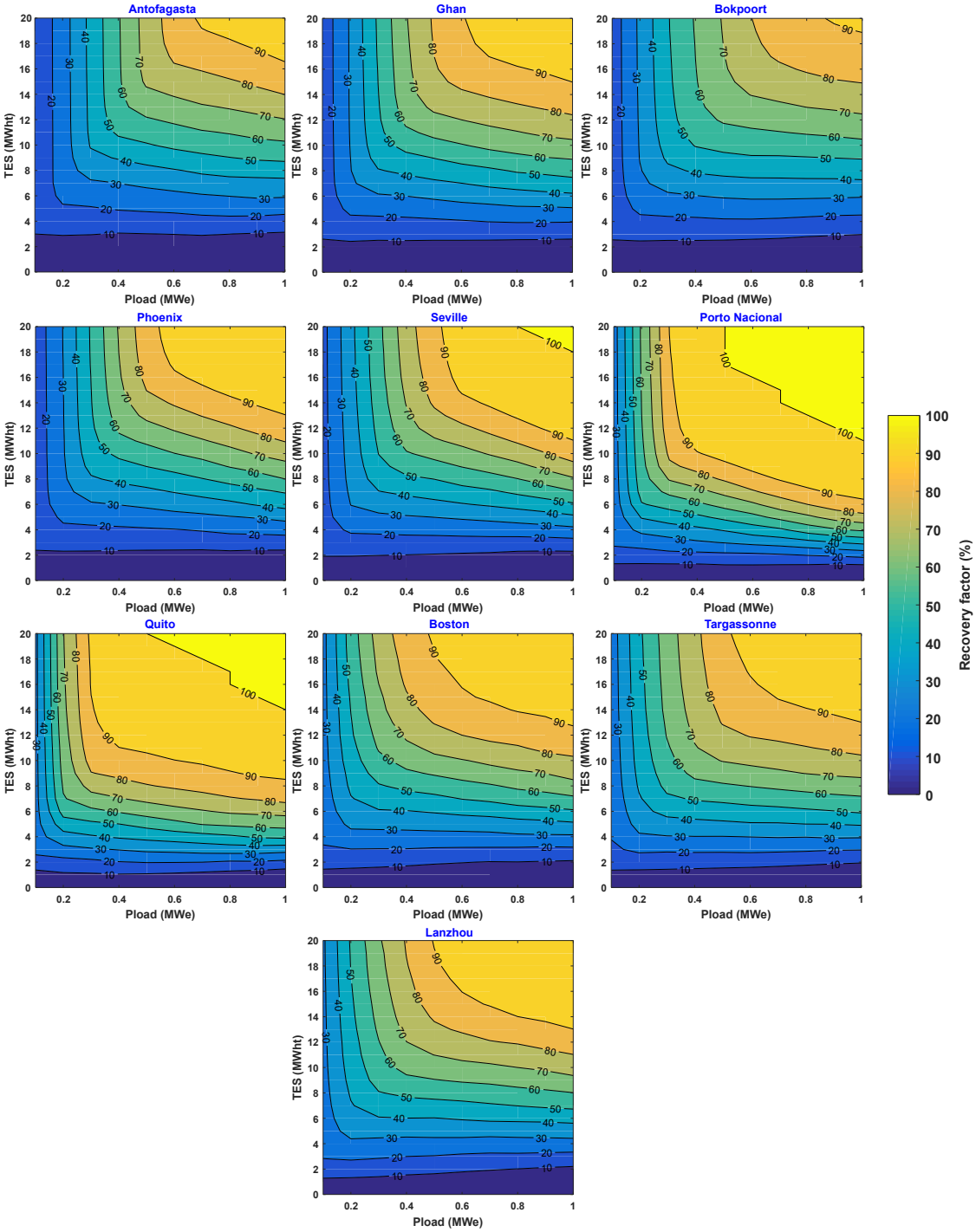

Figure B.27: Recovery ratio of the *1S* hybrid plant at the selected locations considering the **DS2** to supply a variable load demand.

Figure B.28 shows the variation in excess PV energy that is permanently rejected from the *HT* hybrid plant as a function of TES capacity. The following figure is used to further explain the trends shown in Figure 3.25 regarding the variation of the RF of the *HT* hybrid plant. It can be noticed that regardless of the location considered (either Ghan or Seville), the PV surplus first remains constant with increasing the TES capacity up to about 14-15h before decreasing slightly.

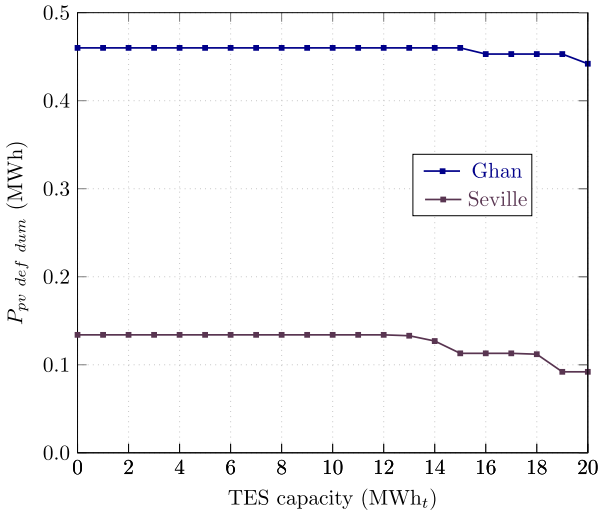

Figure B.28: The variation of excess PV definitely dumped $P_{pv,\ def\ dum}$ as a function of TES capacity at two locations of the *HT* hybrid plant to supply a baseload demand of 0.5 MWe.

Figure B.29 shows the variation of the excess thermal energy curtailed via the hybrid plants with increasing storage capacity. It can be noticed that surplus thermal energy of the *1S* hybrid plant becomes constant at very high storage capacities. On the other hand, the *HT* hybrid plant with 20h TES capacity still does not reach the constant variation range.

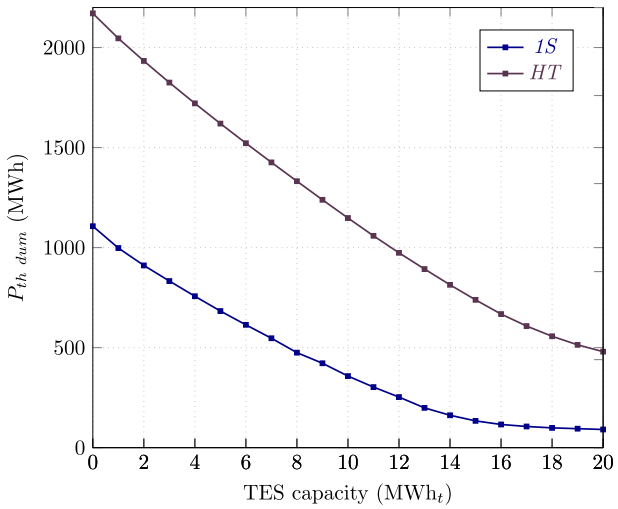

Figure B.29: The variation of excess thermal energy as a function of TES capacity for the two hybrid plants to supply a baseload demand of 0.5 MWe.

13 The annual energy output with a tracking-load profile

Figures B.30 and B.31 show the total annual energy production obtained when considering a baseload and a variable load electrical demand profile as well as the relative difference for the ten sites and the five plant configurations considered.

- Under the given demand and storage capacity conditions, replacing a constant demand profile by a tracking demand profile has a limited impact, with a difference in energy production over a year of operation not exceeding 5%, with a maximum of 4.34%, 0.60% and 2.90% noted at Bokpoort for the conventional CSP (Figure B.30(a)), Fixed-PV + BESS (Figure B.31(a)) and 1axis-PV + BESS (Figure B.31(b)), respectively . The relative difference observed in the case of the two PV configurations with integrating TES system is 2.92% and 2.73% in Seville (Figure B.30(b)) and (Figure B.30(c)), respectively.

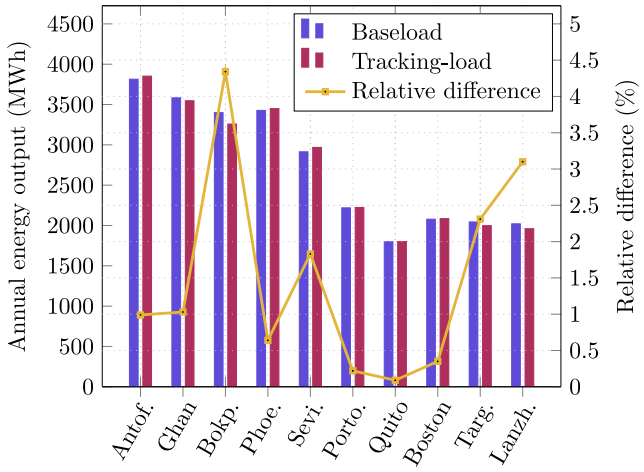

(a) **CSP**

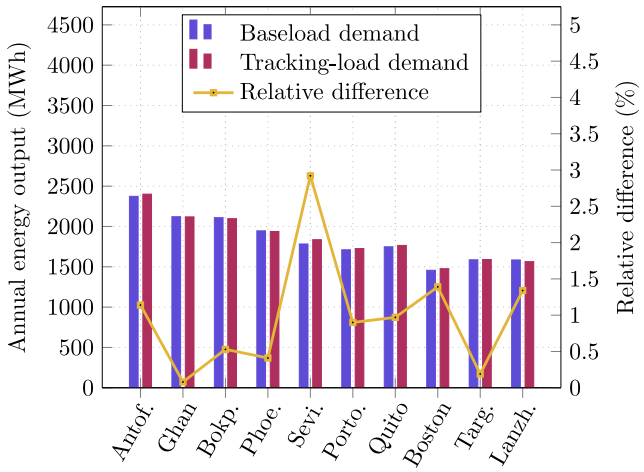

(b) **Fixed-PV +TES**

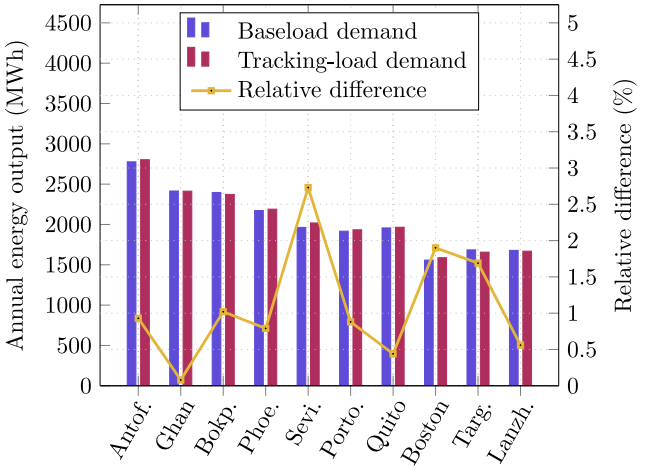

(c) **1Axis-PV + TES**

Figure B.30: Annual energy generation (left axis) in ten locations and relative difference (right axis) between a constant and a variable load profile for the: (a) conventional CSP, (b) Fixed-PV + TES and (c) 1Axis-PV + TES plants with 14 MWh_t TES capacity.

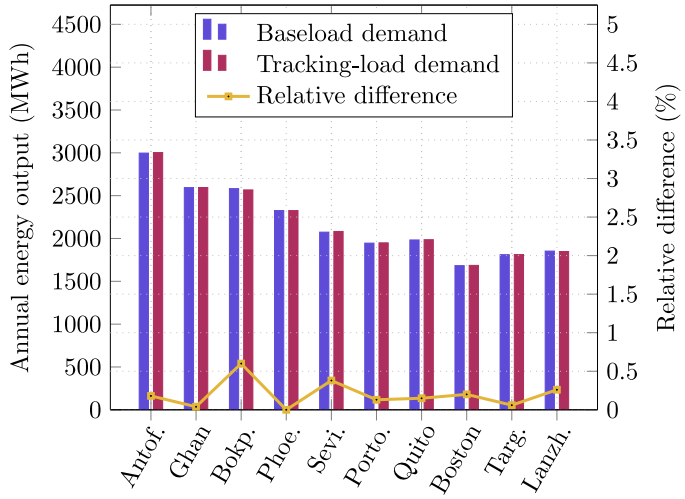

(a) **Fixed-PV + BESS**

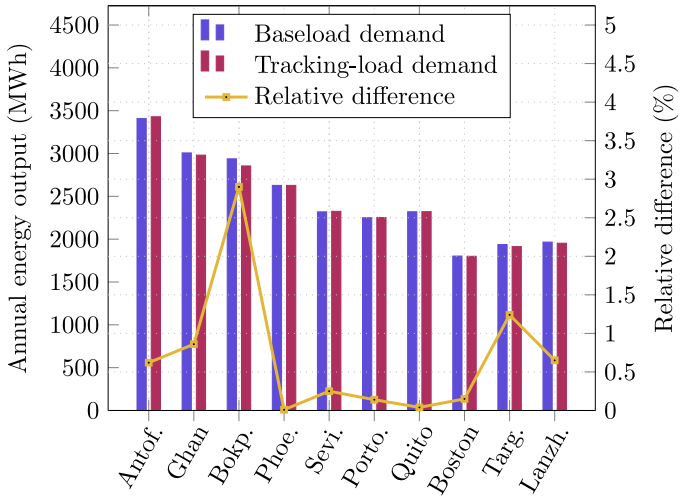

(b) **1Axis-PV + BESS**

Figure B.31: Annual energy generation (left axis) in ten locations and relative difference (right axis) between a constant and a variable load profile for the: (a) Fixed-PV + BESS and (b) 1Axis-PV + BESS plants.

Appendix C

First investigations conducted to better understand the future that awaits the development of the *HT* PV-CSP hybrid systems

Non-uniform flux density distribution over conventional solar receivers is a source of crucial problems in CR power plants, (e.g. local hot spot, thermal stress,...). Consequently, variations of the flux density distribution over the HT PV-CSP receiver formed via the interconnection of thousands of high-efficiency III-V solar cells may lead to significant reduction in the current and voltage outputs and though in the maximum power output. To assess this problem, in this appendix, we try to answer some critical questions in the process: 1) Can we maintain a high degree of flux uniformity on a HT-PV receiver without degrading the plants overall optical efficiency? 2) To what extent conventional interconnection schemes can enable the highest output performances? 3) Can we approach a good balance between uniform flux distribution, optimized interconnections, highest output power and lowest Joule heat losses with thousands of cells?

Introduction

Through a detailed literature review on non-uniform flux distribution in conventional CR plant [373–376], it was found that there is a direct link between non-uniform flux distribution and spillage losses (i.e. the percentage of solar irradiation falling beyond the boundary of the receiver effective area illustrated in Figure C.1). The heliostat field enhancement is achieved by selecting a geometrical arrangement of the solar field that minimizes optical losses and improves flux homogeneity at the receiver without changing the properties of the other components of the solar plant (i.e. tower, receiver, etc.). The improved heliostat configuration has **116** heliostats (Figure C.3(d)) compared to **201** (Figure C.2) for the original field.

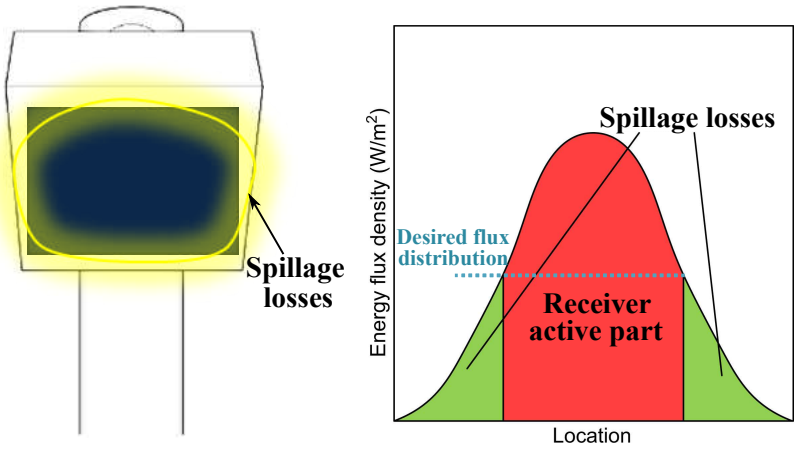

Figure C.1: An example of the flux density distribution over the receiver with a highlight of the spillage losses and the desired flux profile in optimized conditions.

Using SolarPILOT and having access to the original heliostat field layout of the THEMIS CR plant, we simulated the optical efficiency of the overall heliostat field (Figure C.2). It is worth mentioning that in Chapter 2, the study used the current layout of the heliostat field, which has only 107 heliostats fully covered with mirrors, while the other heliostat positions were either uncovered with mirrors or discarded to install a supervision room. As can be seen in Figure C.2, the lowest optical efficiencies are mainly due to heliostats located at both edges and the outer part of the field. Therefore, considering a configuration where both these heliostats are removed at the same time will improve the overall optical efficiency heliostat field, but of course will lower the overall solar power impinging the receiver.

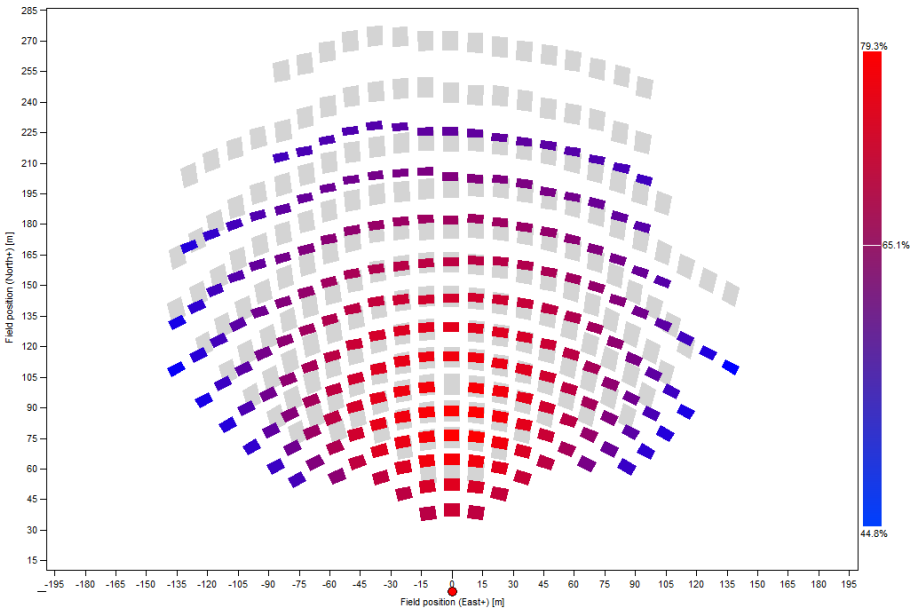

Figure C.2: Overall heliostat field efficiency obtained March 21^{st} at noon with the original heliostat field of THEMIS solar plant accounting **201** heliostats.

For this purpose, a comparison between four heliostat field arrangements to the original display was performed, as shown in Figure C.3. Regarding the original layout, it can be seen that taking off heliostats on both edges of the solar field is not very

effective because the outer heliostats will induce higher optical losses (as depicted in Figures C.3(a) and C.3(b)) as a direct consequence of the high cosine losses (Table C.1). However, the consideration of an opposite organisation (i.e. removing the outer heliostats and keeping both edges) does not guarantee any improvement of the optical losses (Figure C.3(c)) as with this configuration, heliostats on the edges will be responsible for the highest spillage losses (Table C.1). Therefore, the fourth configuration was designed to offer a good balance between cosine and spillage losses. The heliostat field of the proposed arrangement accounts for **116** heliostats similar to the **135** layout (Figure C.3(b)) without the twelfth row at the end of the field (Figure C.3(d)).

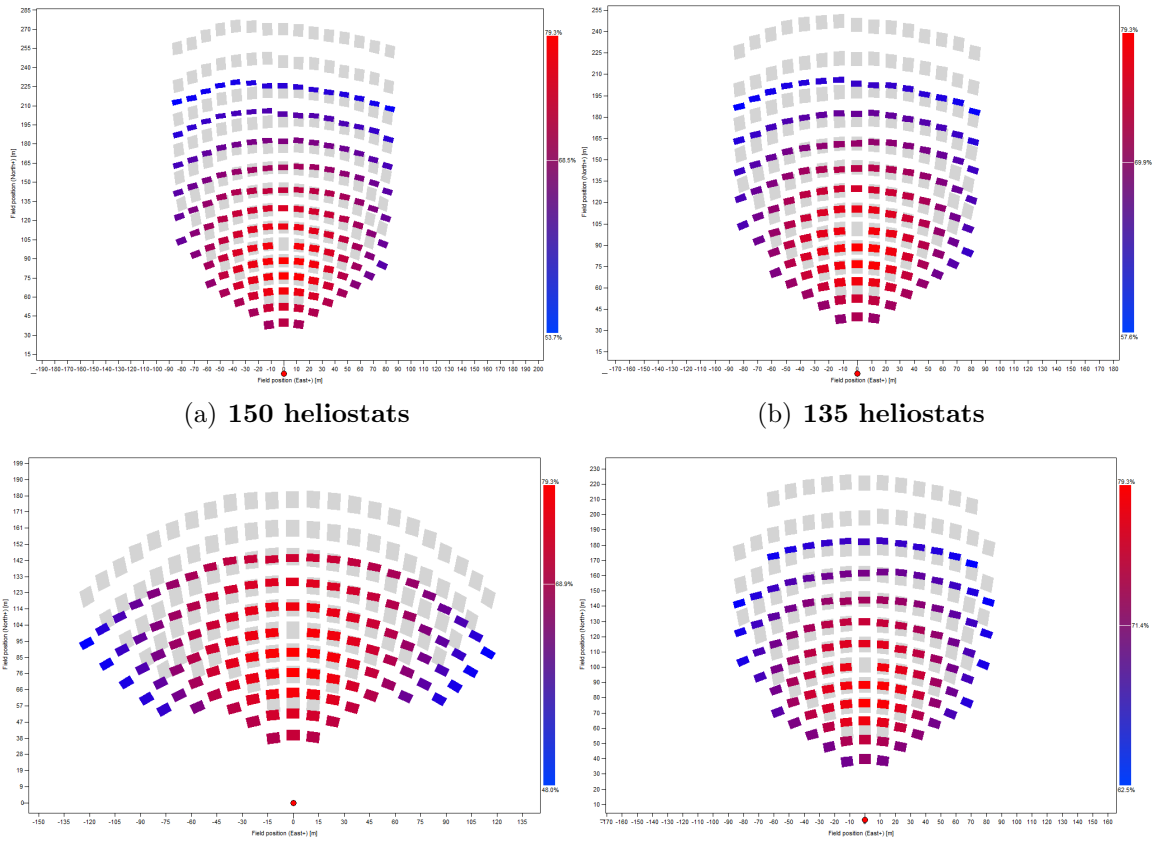

(a) **150 heliostats** (b) **135 heliostats**

(c) **118 heliostats** (d) **116 heliostats**

Figure C.3: Overall heliostat field efficiency obtained March 21st at noon with three heliostat field layouts: (a) **150**, (b) **135**, (c) **118**, and (d) **116** heliostats.

In general, the overall optical efficiency of a heliostat field decreases with increasing distance from the heliostat to the tower up to a certain distance. By placing heliostats closer to the tower, the cosine efficiency of the new layout is increased by 5.3% (Table C.1). However, by removing heliostats on the edges, the interception efficiency can be increased by $\sim$ 5% regarding the original field (Table C.1).

Table C.1: Main optical performance indicators of five heliostat layouts simulated the March 21st at noon.

Field performance	**201**	**150**	**135**	**118**	**116**
Mean field spillage efficiency (%)	79.53	83.58	83.97	81.70	84.09
Mean field cosine efficiency (%)	91.77	91.95	92.55	96.42	97.06
Mean field optical efficiency (%)	64.37	67.82	68.94	66.03	68.35

Since we have an improved heliostat field layout for the CR plant, we investigated whether works in the literature dealing with the optimization of electrical interconnection schemes for large CPV receivers operating under non-uniform illumination distributions were suitable for our case study. To date, research work on CPV receivers under non-uniform flux distribution is quite tiny [377–383] in comparison to flat PV plants. Based on the estimated or measured flux distribution (and temperature in some studies), the interconnection scheme between the cells is systematically modified and optimized to minimize the current mismatch losses in each parallel connection. This step typically involves sorting the PV cells by current intensity and building the series strings (i.e. the electrical interconnection of several cells in series is referred to as a string in the PV field) in that order. The different methods differ mainly in 1) the metric used for the sorting and 2) the flexibility along with the feasibility of the final configuration. Most of the proposed configurations were based on dividing the whole CPV receivers into a few identical and symmetrical parts according to the flux density distribution. In [379], the authors proposed a quartered rotational symmetry (QRS) connection, where a 6×6 array was divided into four symmetrical groups. Inside each group, CPV cells were connected in parallel to minimize current mismatch losses and the groups were connected in series to increase the overall voltage output. This configuration offered the best conversion efficiency and power output compared to conventional series-parallel (SP) connections. The QRS configuration was implemented by Hamza et al. [377] with a relatively larger PV array of 8×8 and demonstrated the improvement of the conversion efficiency by at most 25% in comparison to the SP connections. The QRS interconnection laid out inspiration for a suitable interconnection scheme for our case study that implies the use of a very important number of cells in the range of thousands and not only hundreds, as reported in the above-mentioned works.

1 Model description

To estimate the performance of the *HT* PV-CSP hybrid approach, one should develop an optical/electrical coupled model aiming at predicting the maximum power output at the outlet of a *HT* PV-receiver, a sketch of which is depicted in Figure C.4. The solar plant parameters, including the heliostat field layout and the CR characteristics (receiver area and operating temperature given in Table 2.1), are used as an input in the optical model to generate the flux density distribution on the receiver using SolarPILOT. The output of the optical model is fed as input to the electrical model to 1) identify the concentration level on each of the thousands of cells used to entirely cover the effective area of the receiver using cells of 1 cm^2 and 2) compute the *HT*-PV receiver electrical output using the 2D equivalent circuit model of a GaAs solar cell. Finally, several cell interconnections are considered between the thousands of cells to obtain the current-voltage (I-V) and power-voltage (P-V) characteristics at the output of the *HT*-PV receiver for two different flux density distributions. The maximum power output is obtained applying a set of equations (*vide infra*) describing the main performance parameters investigated in this study.

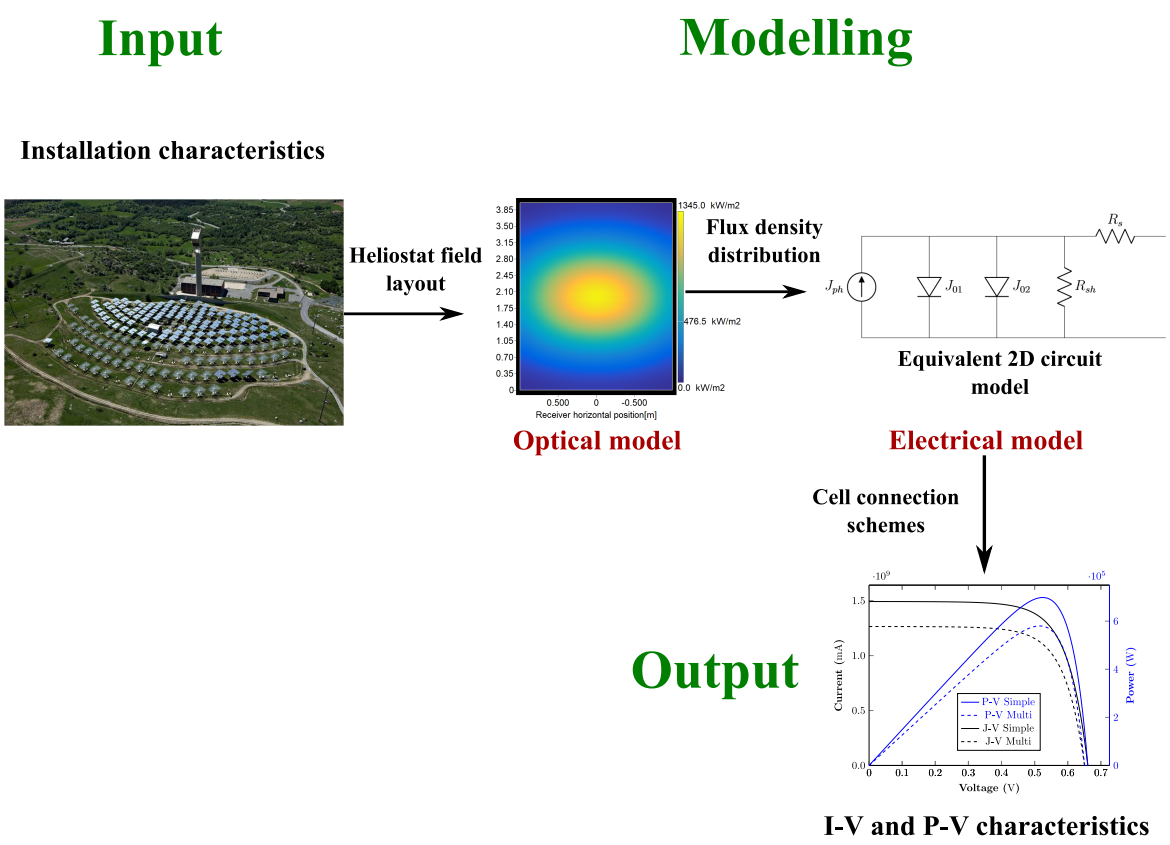

Figure C.4: Schematic diagram explaining the coupling scheme.

The aforementioned steps are used for a constant operating temperature of the HT-PV receiver and a variable flux density distribution. This assumption can be assured by varying the flow rate of the HTF following behind the cells.

1.1 Optical model

The solar flux distribution at the receiver plane has been simulated using SolarPILOT software [306], considering two aiming point strategies described hereafter.

1.1.1 Simple-aiming strategy

The *simple-aiming* strategy is a common aiming solution that consists in orientating all heliostats toward the centre of the receiver (Figure C.5(a)). This strategy leads to a large heat flux at the centre of the receiver (exceeding 1300 kW/m^2) and large flux gradients towards the edge of the receiver, as illustrated in Figure C.6(a). This strategy causes the least spillage, as all heliostats point towards the centre of the receiver as depicted in Figures C.5(a) and C.6(a).

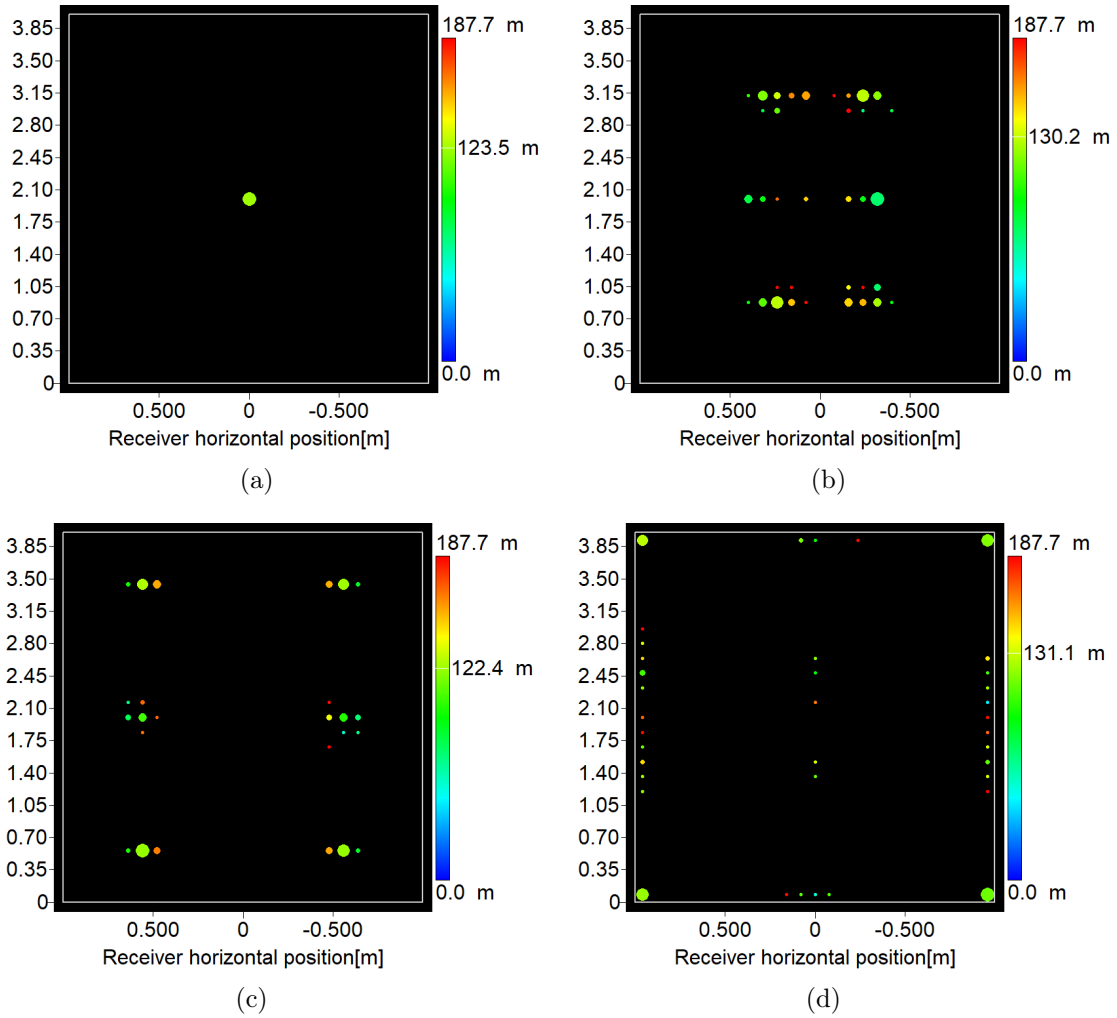

Figure C.5: Map showing the number of heliostats represented by the size of the dots aimed at (a) the centre of the receiver, (b) distributed heliostat aim points with an offset value of **1.8**, (c) a distribution with heliostat aiming at the edges of the receiver with an offset value of **1** and **0** (d). The large dot size corresponds to the number of heliostats, with greater numbers corresponding to larger dot size, and the colour of the dots indicates the mean distance of heliostats focused at a given coordinate.

1.1.2 Multi-aiming strategy

To lower the peak flux density on the receiver, distributed aiming, also known as the *multi-aiming* technique can be applied. The aiming points in this study are determined by the "Image-size Priority" option in SolarPILOT. The logic of this aiming strategy is to ensure the most homogeneous flux distribution possible (see Figure C.6) through heliostat aiming while minimising spillage by adopting geometric bounds for aim points. To do that, the most distant heliostats aim to the centre of the target. Then, aim points are progressively spread farther from the centre to fill gaps in the flux profile while remaining within a certain user-defined offset distance from the edges (Figures C.5(b), C.5(c) and C.5(d)). The offset parameter noted k is a ratio that describes the distance between the optical center of heliostat image and the receiver edge in the receiver X and Y directions and typically varies between 0 and 3 [384]. Lower offset values (e.g. $k = 0$) leads to more homogeneous flux density distributions (Figure C.6(d)) but with the highest spillage losses as most of the heliostats are aiming at the extreme edges of the receiver as illustrated in Figure C.5(d).

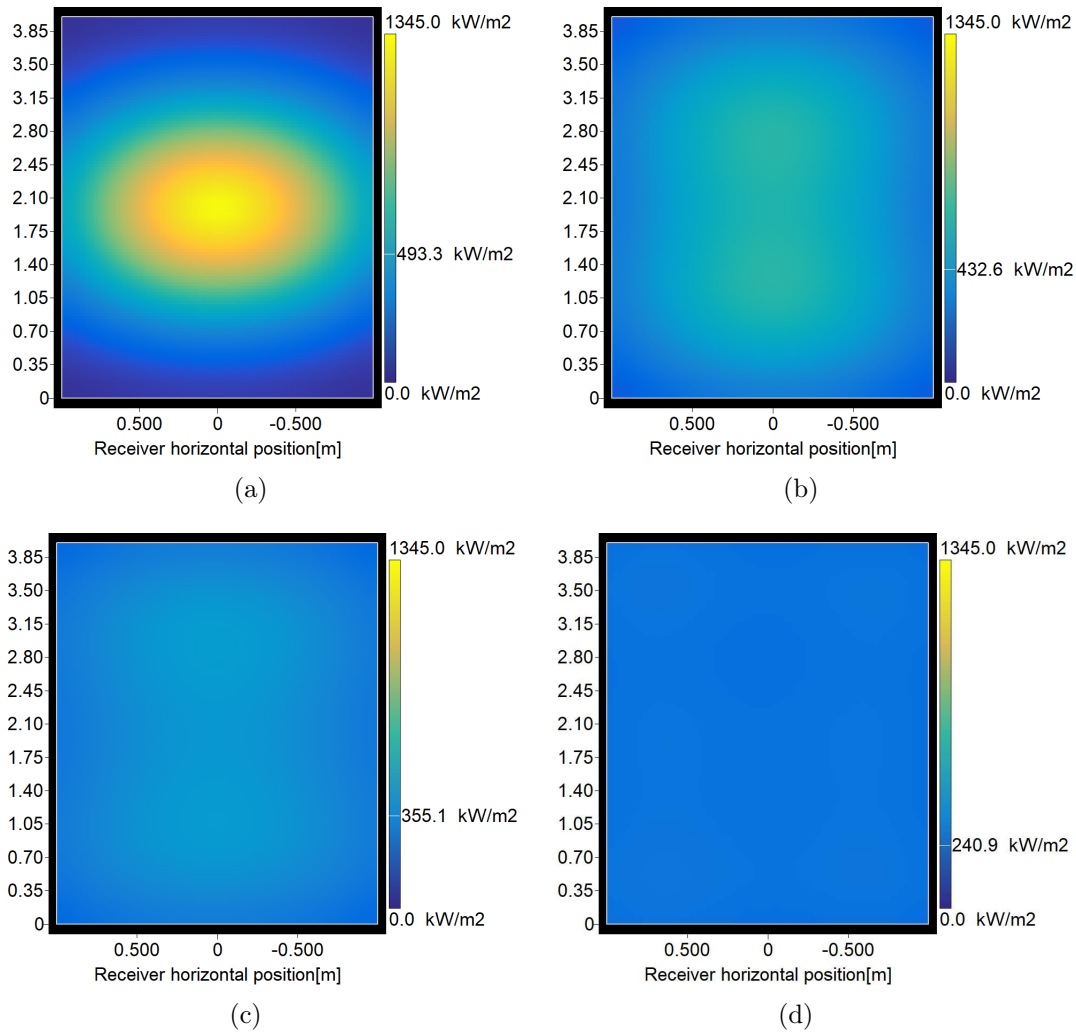

Figure C.6: Flux density distribution over the receiver with consideration of different aiming strategies: (a) *Simple*-aiming, and *multi*-aiming with an offset of **1.8** (b), **1** (c) and **0** (d).

Therefore, the choice of offset values will impact the flux distribution, the optical performance of the heliostat field and potentially the output power production of the *HT* hybrid plant. To this end, a sensitivity study was conducted to determine the offset value that provides the best balance between uniformity and the heliostat field overall optical performance. Five different flux distributions associated with five different offset values were calculated on March 21st at noon (Figure C.7), and the main optical losses of the heliostat field are summarized in Table C.2.

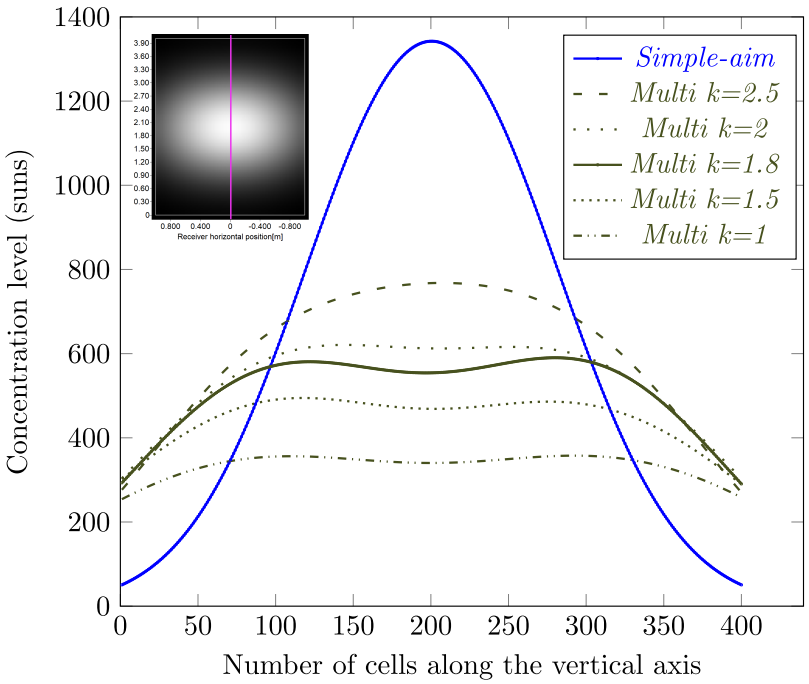

Figure C.7: Concentration level over each cell at the center using different aiming strategies.

Table C.2: Main optical parameters of the proposed heliostat field layout using the *multi*-aiming strategy on March 21st at noon with consideration of different offset values.

	Offset values "k"					
Field performance	**Simple**	**2.5**	**2**	**1.8**	**1.5**	**1**
Mean field spillage efficiency (%)	**84.09**	79.91	75.99	73.74	69.14	60.52
Mean field optical efficiency (%)	**64.93**	61.71	58.67	56.94	53.39	46.74

As can be seen in Figure C.7, decreasing the offset parameter has a significant impact on the flux distribution over the receiver. An offset value of **2** and **1.8** generates a similar distribution at the edge of the receiver with a relatively small difference of about 3%, moving toward the centre of the receiver, the difference increases up to 10%. A flatter profile is obtained with k =1, but this configuration has the lowest overall optical efficiency (expressed in chapter 2 by Eq. (2.1)) compared to the other offset values, more importantly to the *simple*-aiming strategy, with a relative decrease

of the overall efficiency of 28% (see Table C.2). Although both the **2** and **1.8** offset parameters offered similar flux distribution, we decided to conduct the study using an offset of **1.8**, as it ensures a good balance between flux homogeneity and optical performance.

1.2 Electrical model

Taking into account the non-uniform illumination distribution, the PV cells are coupled with parallel bypass diodes in opposite polarity to protect those cells from reverse-bias breakdown, as well as to avoid that PV cells with low concentration ratios become loads of other cells at high concentration ratios. The relationship between the current density and voltage of a PV cell encompassing the negative breakdown region (with the addition of J_{02}) is given by [385]:

$$J(V) = J_{ph} - J_{01}\left[\exp\left(\frac{V + J\,R_s}{n_1\,V_t}\right) - 1\right] - J_{02}\left[\exp\left(\frac{V + J\,R_s}{n_2\,V_t}\right) - 1\right] - \frac{V + J\,R_s}{R_{sh}}\left[1 + \kappa\left(1 - \frac{V + J\,R_s}{V_{br}}\right)\right]^{-m} \tag{C.1}$$

where κ is a diode coefficient ($< 1\times\ 10^{-5}$), V_{br} the junction breakdown voltage of the cell, and m is the avalanche breakdown exponent. The last term (second line) in Eq. (C.1) allows describing the negative breakdown region of the cell but it can also be used for a bypass diode in parallel to the cell, representing in this case the current in the bypass diode whereas V_{br} becomes the voltage of the diode.

In the literature, the following expressions are often used for the diode saturation current density of a solar cell [133]:

$$J_{01}(T) = C\,T^3\,\exp\left(\frac{E_g(T)}{q\,T}\right) \tag{C.2}$$

$$J_{02}(T) = D\,T^{3/2}\,\exp\left(\frac{E_g(T)}{2\,q\,T}\right) \tag{C.3}$$

where C and D are temperature dependent coefficients. These parameters were extracted from temperature-dependent J-V measurements in a wide range of temperatures varying between 25 – 400 °C, conducted by Perl et al. on III-V solar cells [116].

2 PV cells arrangements

The practical implementation of a large-scale HT PV module typically requires tens of thousands of PV cells (in our case study **80 000** cells) to be interconnected. This is particularly challenging in the light of the strong illumination gradient one may expect (Figure C.7). In this chapter, we choose to study the opposite configuration, which is a parallel-series (PS) arrangement because it is easy to construct compared

to existing solar interconnections, namely total cross tied (TCT) connection where an additional parallel connection is conducted between the strings and economical [386]. More importantly, this configuration was inspired by previous works but applied for a large-scale PV receiver [377, 379]. For that, we will start with a brief description of the series and parallel interconnections, then move on to the introduction of the proposed PS-block arrangements.

2.1 Series interconnection

Cells connected in series are linked along a single path so that the same current flow through them. The total power in such an array is lower than the sum of the individual power ratings of each cell. The main reason for that is that in a series configuration, performances are severely affected if the cells are not equally illuminated, as shown in Figure C.8.

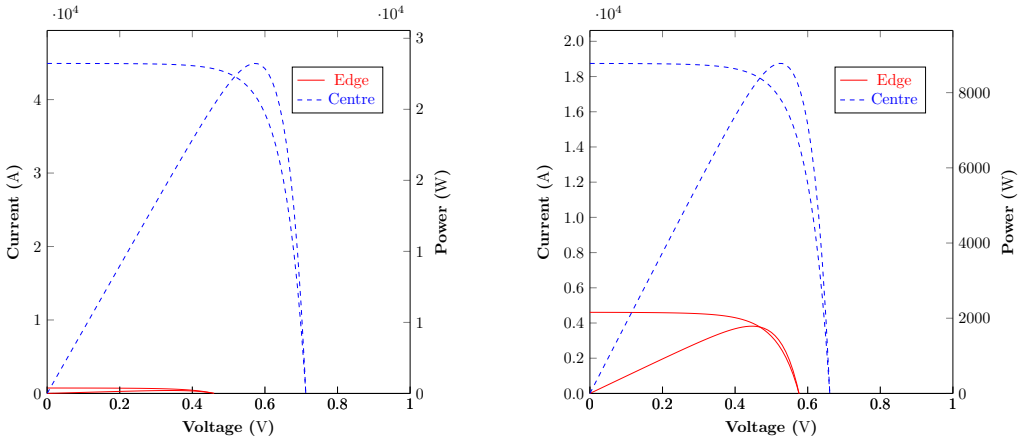

(a) *Simple-aiming* (b) *Multi-aiming*

Figure C.8: Simulated I-V and P-V curves of two cells located at the edge (red) and centre (blue) of the HT-PV receiver under two different aiming strategies: (a) *simple*, and (b) *multi*.

2.2 Parallel interconnection

Cells connected in parallel are linked to show the same voltage, conversely to the series configuration. Thus the effect of parallel wiring is that the resulting voltage in the combination stays almost the same as for a single unit (cell or panel) while the currents add up.

2.3 Block interconnection

Looking at the concentration distribution of cells in Figure C.9 it can be noticed that corner cells are subject to a very low solar concentration ratio because of the aiming point strategy. As array current will follow the lowest-performing PV cell's current

behaviour in a series-connected assembly, the cells at the corner will contribute to a higher current mismatch that causes power losses. Therefore, by adopting a parallel connection between the cells inside a block better overall performance may be achieved as current mismatch is no longer an issue and voltage mismatch has a less important impact. Besides, a parallel connection is simpler than the series case as no bypass diodes are involved. Once the blocks are accounted for using the entire cells, a series connection is applied between blocks to form a complete HT-PV receiver with an increased output voltage. As a result, bypass diodes will be placed between the blocks connected in series with the neighbouring blocks, thus, allowing for cost reductions as the number of blocks is less relevant.

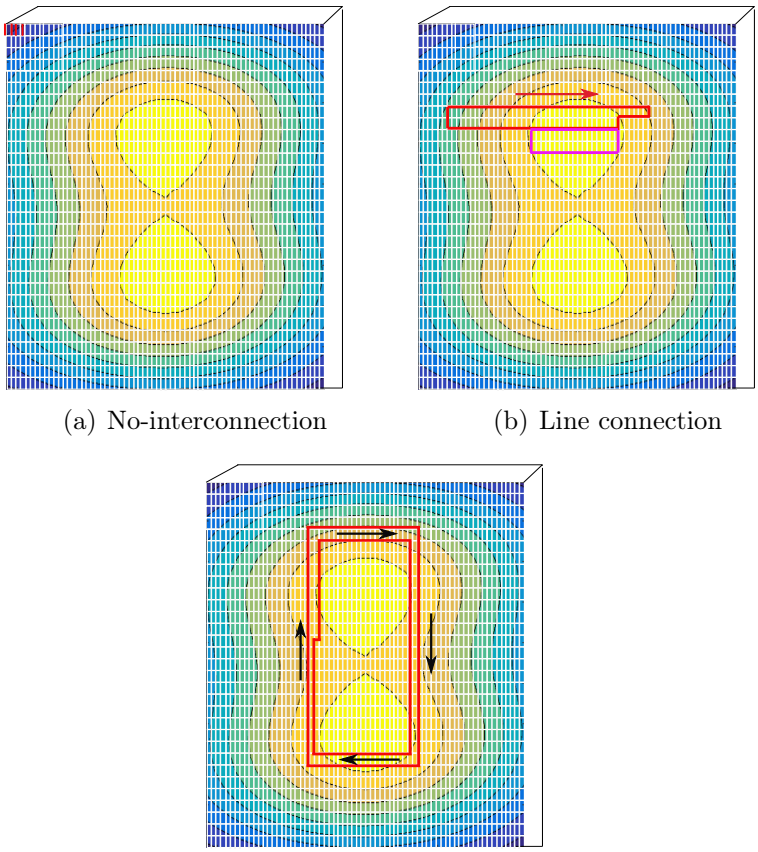

(a) No-interconnection (b) Line connection

(c) Snail-connection

Figure C.9: Different interconnection patterns studied: (a) the ideal case study where no interconnection is considered between the thousands of cells (unrealistic and unpractical cell configuration), (b) linear connection scheme between the blocs. The cells located on the same line are connected and (c) snail connection scheme.

The proposed configuration has been implemented in a Matlab R2016b script that incorporates all the steps. To demonstrate the process, a flowchart is drawn in Figure C.10.

- The process of reducing current mismatch losses starts with identifying the maximum short-circuit current density of the PV receiver, denoted $J_{sc,\ max}$ and defined in Eq. (C.4) as the sum of short-circuit current densities when no interconnection is assumed between the cells.

- Then for a given block number determine the $J_{sc,\ lim}$ that can be identified as $J_{sc,\ max}$ per the number of blocks (Eq. (C.5)).

$$J_{sc,\ max} = \sum_{ro=1}^{200} \sum_{co=1}^{400} J_{sc,\ simp/multi} \tag{C.4}$$

where $J_{sc,\ simp/multi}$ is the short circuit current density with a simple and multi aiming point strategies.

$$J_{sc,\ lim} = \frac{J_{sc,\ max}}{Nb_{bloc}} \tag{C.5}$$

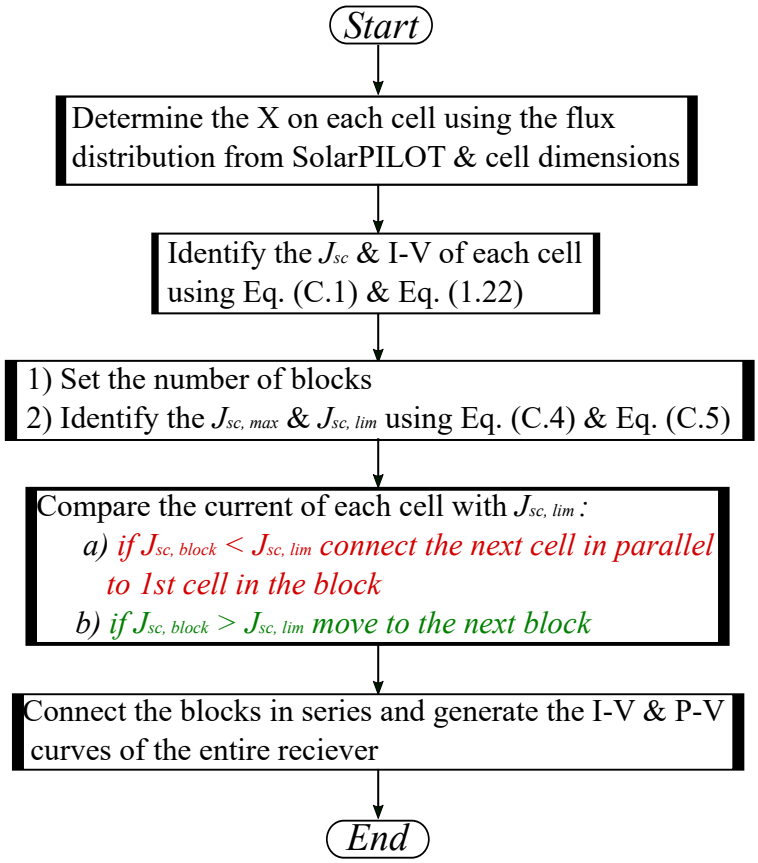

Figure C.10: A flowchart to explain the main steps for an optimized block configuration.

- For the no interconnection scheme, the power output is extracted individually from the cells. An unpractical configuration that helps identify the effectiveness of the proposed arrangement and its ability to approach a perfect case study. The next step is to choose values for the number of blocks with an output current density that should approximate the value of the $J_{sc,\ lim}$.

- Each block contains a different number of cells due to the non-uniform flux density distribution over the receiver (i.e. blocks located at the centre of the receiver will include fewer cells). For the sake of simplicity, we will describe the procedure by considering the connection of two blocks. The generalization to the general case of l series blocks is straightforward. The two blocks will contain approximately 40

000 cells connected in parallel until the target current density value is reached. For example, when considering the *simple*-point strategy, the first block will account for 40 147 cells whilst the second will account for the remaining number of cells to find the 80 000 cells used to cover the entire effective area of the PV receiver (i.e. 39 853 cells). Given the two I-V curves, we combine them by summing the output voltages to obtain the overall I-V characteristic of the entire receiver. The difference between the $J_{sc,\ lim}$ and the block output current density increases with the increasing number of blocks, e.g. 0.32% with two blocks to 10% with 10 000 blocks. Thanks to the presence of bypass diodes, the weakest of the two blocks (i.e., the one with the lowest current density output) do not constrain the current density of the strongest one; rather, when the current density gets larger than the value that can be produced by the weakest block the latter gets bypassed and only the strongest block produces power.

- At first, we only considered the connection of cells located in the same column, i.e. a block accounts for cells located in the same columns when the entire column has been connected in parallel we move to the neighbouring column until we reach the $J_{sc,\ lim}$ (Figure C.11). The second block arrangement consists of connecting cells from the inside towards the outside following the flux density contour display, this configuration also called snail interconnection (Figure C.11).

Figure C.11 better illustrates the difference between a linear and snail interconnection scheme, considering two bloc values, 10 (Figure C.11(a)) and 1000 (Figure C.11(b)) under the two illumination distributions, i.e. multi and simple aiming strategies. For the snail configuration, the closer we are to the centre of the receiver, the fewer cells are connected within a bloc to reach the target current.

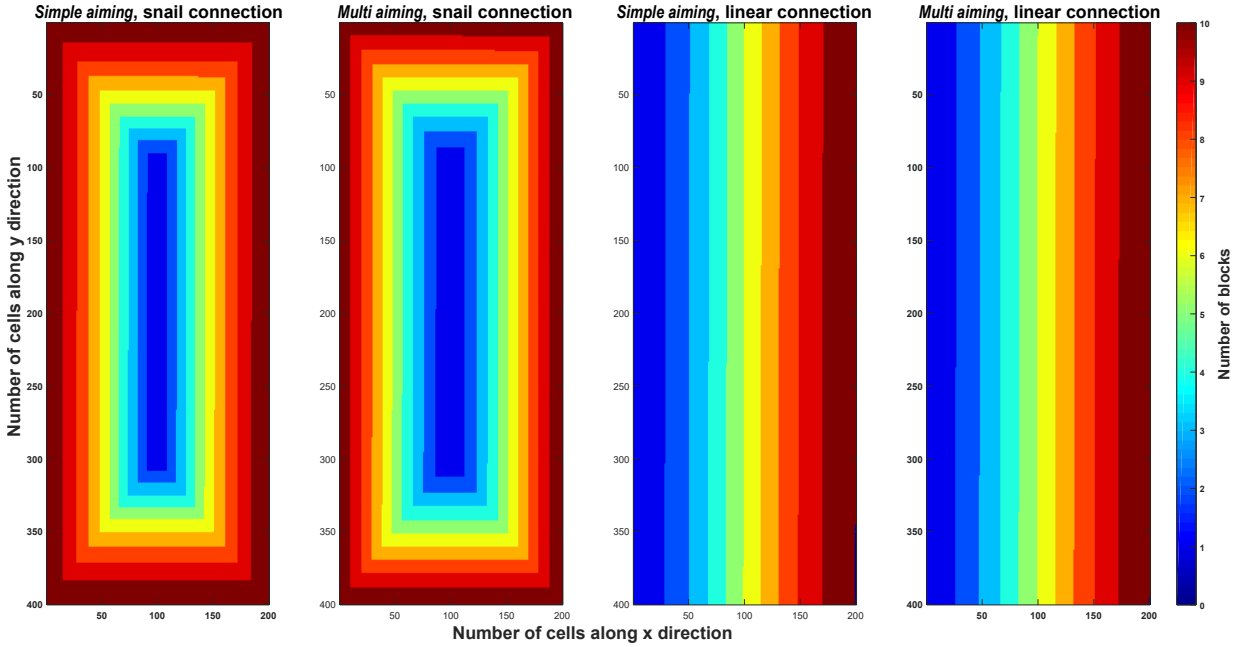

(a) **10 blocks**

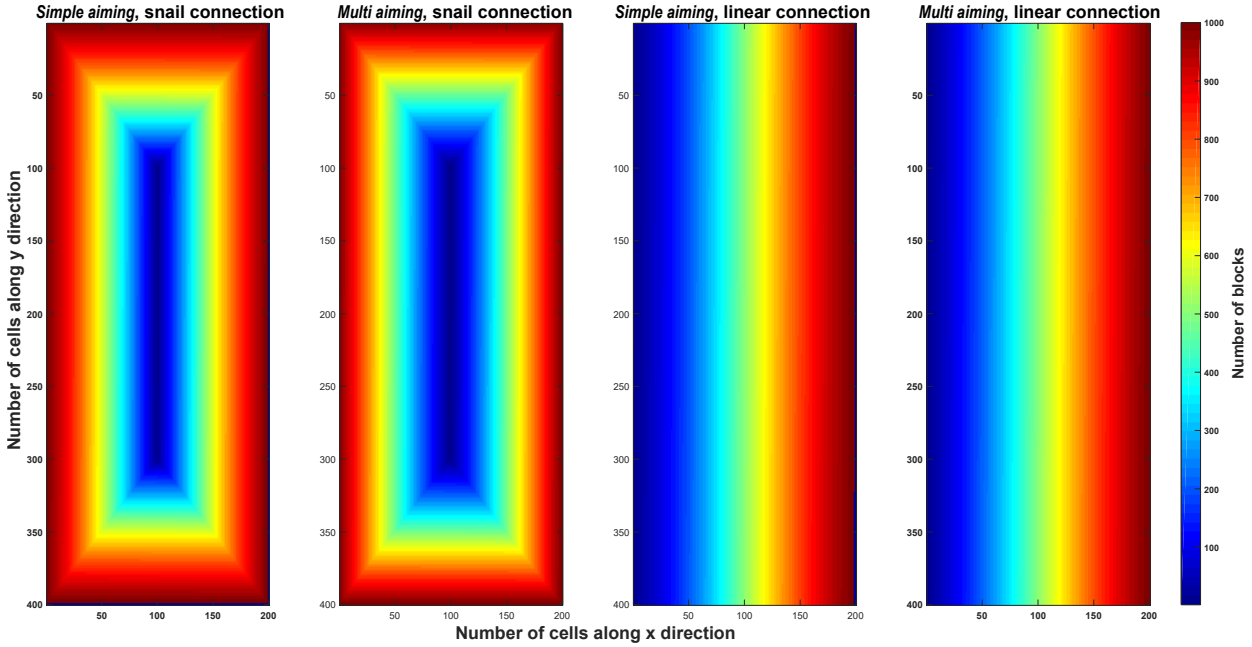

(b) **1000 blocks**

Figure C.11: Color-map representing the number of cells inside a block taking two examples: (a) 10 blocks, and (b) 1000 blocks.

Making the choice to connect cells from the inside towards the outside results in an ineffective coverage rate of the receiver area. Figure C.12 illustrates the distribution of **10 000** blocks over the PV-receiver effective area using the two bloc interconnection schemes under the *simple* aiming strategy.

- For the snail interconnection scheme, an important portion of the outer contour of the receiver, represented by the dark-blue color and highlighted with the magenta box, is not covered with cells which will result in a more important power loss in contrast to a smaller number of blocks.
- For the linear interconnection, only the right edge of the receiver does not have solar cells (magenta box in Figure C.12).

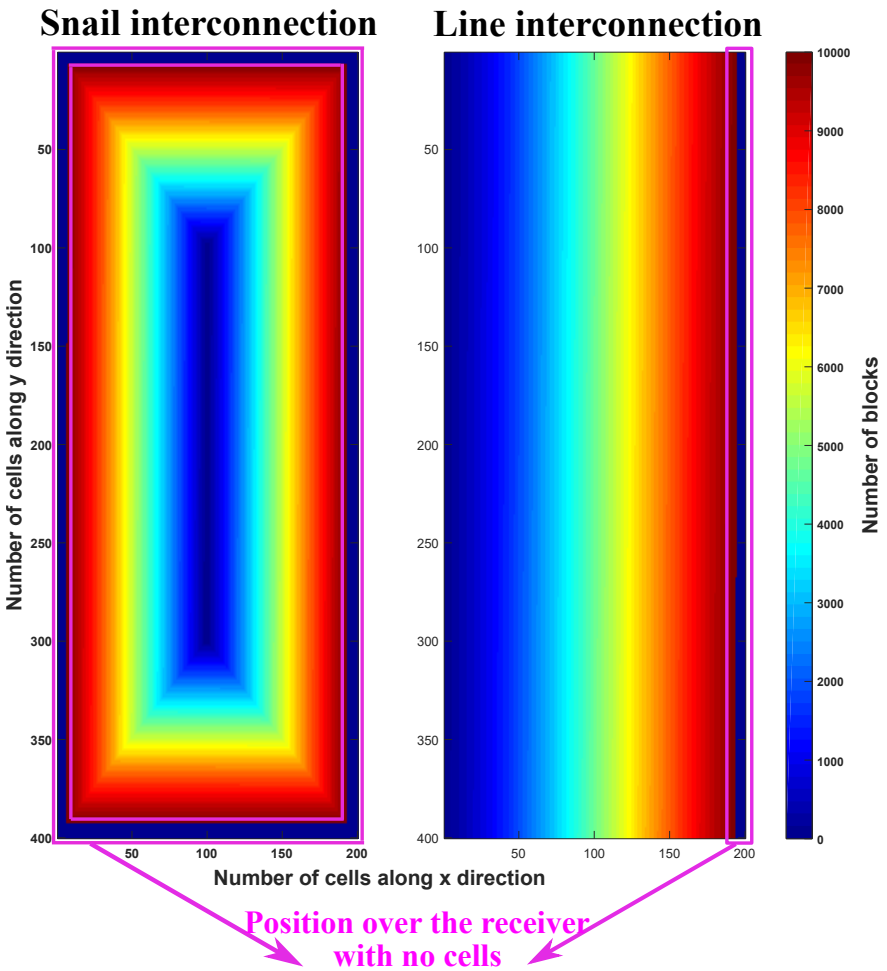

Figure C.12: Distribution of **10 000** blocks over the receiver using the two bloc interconnections with the *simple*-aiming strategy.

2.4 Future works

The results presented here do not answer the questions discussed at the beginning of this chapter: it is only a preliminary study to understand the behaviour of the *HT* hybrid plant under a particular set of operating conditions. For this reason, several perspectives are offered below, some of which are being investigated by my supervisors:

☞ A *simple*-aim point distribution may guarantee the best output performance in terms of power output, but it encapsulates a large number of problems that only make it difficult to predict the future of this hybrid technology under these conditions. The effectiveness of a system and its ability to provide power for long-duration should be more important than offering the best performance for only a short period. Therefore, a *multi*-aim point may present a more appropriate solution for this technology. The use of SolarPILOT allowed for a proper identification of the flux density distributions over a central receiver considering different aiming strategies and offset values, which was practical given the limited time we had to conduct this study. However, a detailed description using more complicated techniques to study the impact of the *multi*-aiming strategy on the flux distribution and the heliostat field operation should be conducted [387–391].

☞ It may be interesting to study different configurations with varying PV receiver sizes and compare them to the original configuration, i.e. 100% coverage rate of the receiver (Figure C.13). One of the main challenges of this study may be related to the interest in hybrid generation, so the coverage rate should be significant to justify the use of a PV receiver on the top of a solar tower; otherwise, it is only a conventional central receiver with a limited PV output.

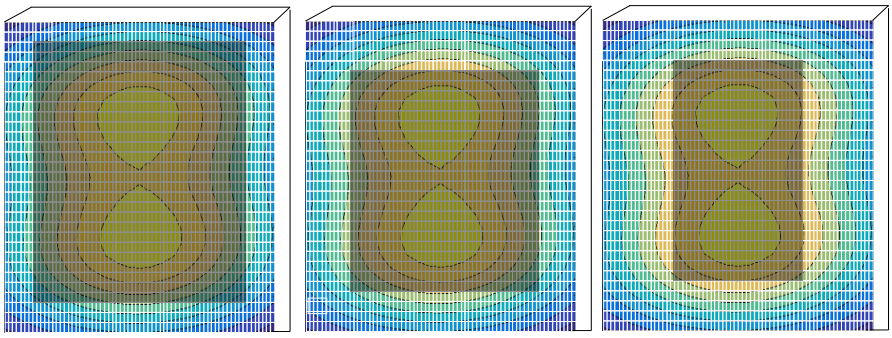

Figure C.13: Schematic distribution of the PV receiver with different coverage rate, represented by the grey bloc. The surrounding area is covered with a thermal collector.

☞ The first model developed considered a variable flux density distribution and a constant operating temperature of 400 °C. However, temperature varies significantly with varying flux density values as mentioned by Ju et al. [392]. Therefore, the evaluation of the impact of the operating temperature needs to be assessed to understand the correlation between the two parameters and their impact on the energy production in general and variations of the I-V behaviour as well as the heat transfer properties in particular.

☞ The bloc interconnection scheme proposed here consists in connecting the cells from the inside-out. It seems important to apply an opposite configuration where cells are connected from the outside-in (Figure C.14).

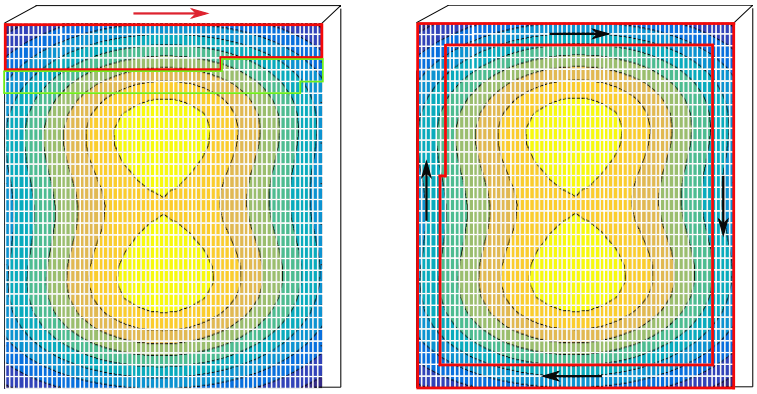

(a) Line connection (b) Snail-connection

Figure C.14: The consideration of the bloc interconnection from the outside towards the inside in two configurations: (a) linear scheme, and (b) snail scheme between the blocs.

☞ The consideration of a constant value of series resistance throughout the receiver area is not a valid assumption; in the work of Algora et al. [393], it was demonstrated that the value of series resistance is strongly correlated with the illumination level and its value appears to decrease significantly with increasing sunlight concentration. Once the detailed description of the *HT* approach is done, the results generated should be used as input parameters for the electrical model that describes the annual output performance of this technology under variable weather conditions and with an integrating storage unit. This step will allow for precise quantification of the impact on the whole plant operation and not only on the PV receiver.

Appendix D

Summary in French

Bien qu'elle présente de nombreux avantages prometteurs pour l'environnement et le développement durable, l'électricité solaire est confrontée à deux défis majeurs : l'instabilité du réseau et l'intermittence. Pour surmonter ces inconvénients, un grand nombre de technologies hybrides ont été proposées au fil des ans. Les systèmes hybrides compacts PV-CSP consistent en l'amalgame de cellules PV et de la technologie CSP dans une seule centrale, et représentent actuellement l'une des voies les plus prometteuses pour obtenir une électricité solaire efficace, répartissable et abordable. Dans ce travail, nous évaluons la production énergétique annuelle de deux approches hybrides compactes basées sur une centrale solaire existante en France : les approches haute température (HT) et 1 soleil sont évaluées et comparées d'abord à une centrale CSP conventionnelle, puis à deux configurations de centrales PV conventionnelles. Un modèle multiphysique détaillé, est développé pour analyser les caractéristiques dynamiques de sortie des centrales hybrides, sur la base de paramètres d'entrée réalistes et de données météorologiques représentatives de Targassonne, en France dans un premier temps, puis de différents sites dans le monde.

Introduction

Les énergies renouvelables devraient prendre de plus en plus d'importance dans les prochaines années, car on estime que leur coût continuera à baisser, devenant ainsi compétitif par rapport aux autres sources d'énergie. En outre, les énergies renouvelables ont la valeur ajoutée d'être des sources d'énergie propres et inépuisables, ce qui en fait d'excellentes solutions pour réduire l'impact environnemental de la production d'énergie et donc plus susceptibles d'atteindre des émissions nettes de dioxyde de carbone nulles d'ici 2050 pour donner au monde une chance de limiter l'augmentation de la température mondiale à 1,5 °C [49].

Parmi les différentes énergies renouvelables, l'énergie solaire est appelée à jouer un rôle fondamental, avec deux types d'énergie qui se complètent parfaitement : les centrales photovoltaïques et les centrales solaires à concentration. D'une part, la technologie photovoltaïque est une technologie mature, avec un développement technologique

plus important ainsi qu'un prix bas. D'autre part, la technologie de l'énergie solaire concentrée fournit des systèmes de stockage fiables et éprouvés, qui peuvent assurer en partie une production d'énergie stable, indépendamment de l'intermittence du rayonnement solaire de jour comme de nuit, facilitant ainsi son intégration dans le réseau électrique. Par conséquent, l'hybridation de ces deux technologies peut permettre à la centrale d'être entièrement gérable en donnant la priorité à l'utilisation d'une technologie moins coûteuse comme le photovoltaïque pendant les heures d'ensoleillement, tandis que la centrale à concentration stocke l'énergie produite pendant ces heures dans son système de stockage d'énergie thermique, pour l'utiliser lorsqu'il n'y a plus de rayonnement solaire. Ainsi, l'augmentation de la capacité de la centrale à produire de l'électricité en continu, 24 heures sur 24, lui permettrait de fournir de l'énergie au réseau en agissant comme une centrale de base classique.

De nombreuses approches d'hybridation ont été développées au cours des quatre dernières années, dans cette thèse nous nous intéressons à l'étude des systèmes hybrides dits « *compact* » en étudions deux configurations compact : 1) la stratégie hybride haute température (HT), qui désigne un système à couplage thermique dans lequel la chaleur dissipée par les cellules solaires est récupérée à l'aide d'un collecteur thermique collé à l'arrière des cellules PV (cette approche est également connue sous le nom de système de récupération de chaleur perdue) [63, 78] et 2) l'approche de fractionnement spectral du faisceau (SBS), qui fait appel à la famille de systèmes impliquant le fractionnement spectral du rayonnement entrant, lequel est redirigé soit vers les cellules PV, soit vers le récepteur thermique, en fonction de sa longueur d'onde [79, 394].

L'objectif de ce travail est de clarifier la position des centrales compactes par rapport aux technologies conventionnelles, en développant un modèle physique précis des principales stratégies hybrides compactes, basé sur leur intégration dans une centrale solaire réelle, et en évaluant l'énergie annuelle des centrales au lieu du rendement de conversion. Ce résumé rassemble les résultats les plus importants de cette étude. Le corps du travail et les résultats complets peuvent être trouvés dans la version anglaise.

Évaluation énergétique des systèmes compacts PV-CSP

1 Description des systèmes

1.1 L'approche 1 soleil

Les miroirs conventionnels utilisés dans le champ solaire sont remplacés par des héliostats PV comprenant un réflecteur arrière, ce qui permet aux photons sous-bande interdite d'être réfléchis sur le récepteur thermique (cf. Figure D.1).

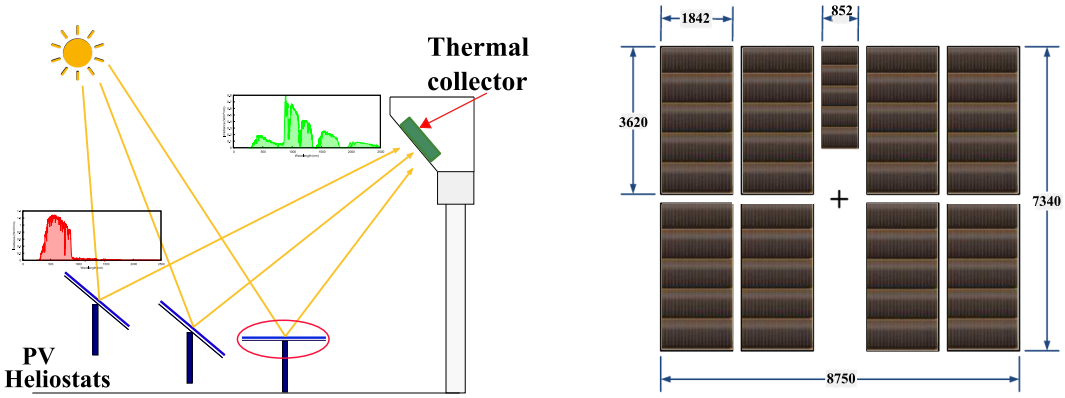

Figure D.1: Description schématique de l'approche hybride *1S* avec une vue d'un héliostat PV entièrement recouvert de cellules solaires GaAs (dimension en mm).

1.2 L'approche Haute-température

À la différence de la stratégie ***1S***, l'approche (***HT***) n'implique aucune modification du champ de l'héliostat mais utilise des cellules PV comme partie extérieure d'un récepteur intégré, qui est supposé être à une température proche mais inférieure à 400 °C, thermiquement lié à un récepteur thermique situé en dessous, comme le montre la Figure D.2.

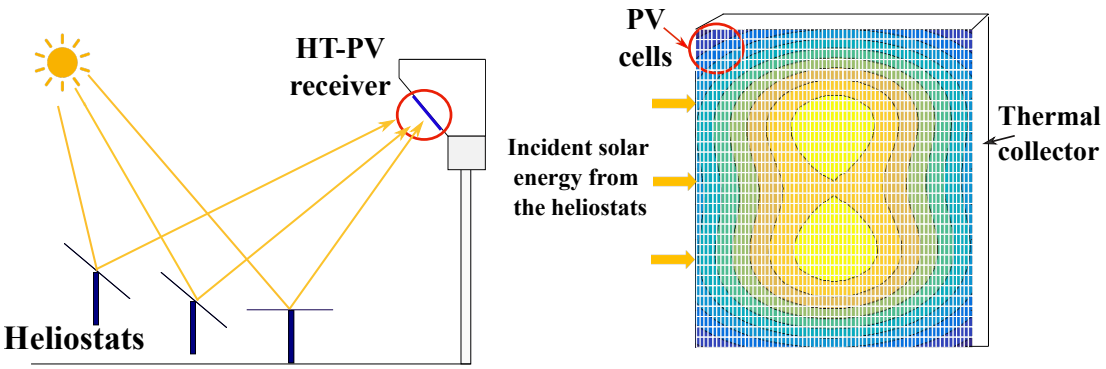

Figure D.2: Schéma de l'approche hybride *HT* avec une vue de près du récepteur PV entièrement recouvert de cellules solaires (représenté par les petits blocs séparés par des lignes blanches).

2 Description du modèle

Nous avons développé un modèle prédictif sous MATLAB R2016b fournissant la production d'énergie pour chaque stratégie sur une base annuelle afin de comparer les performances des deux centrales hybrides décrites ci-dessus avec une centrale CSP. Le schéma du modèle multiphysique est présenté dans la Figure D.3.

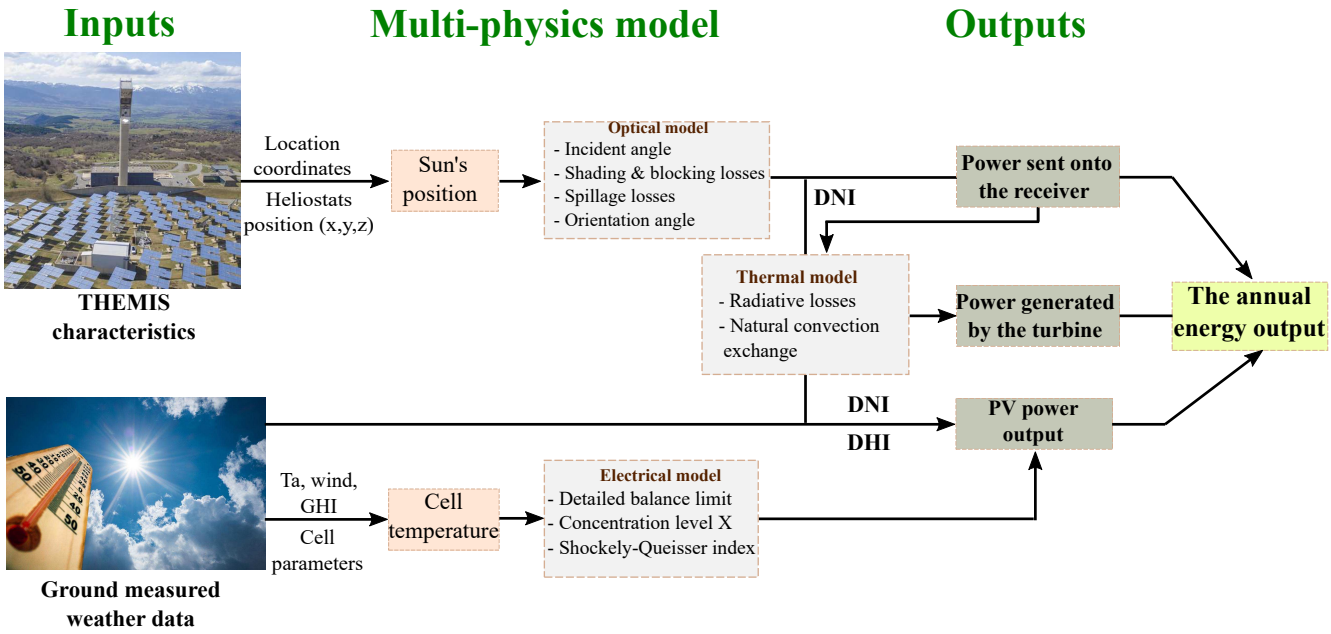

Figure D.3: Diagramme du modèle multiphysique utilisé pour évaluer la production énergétique annuelle des trois technologies solaires.

Les principales caractéristiques de THEMIS (localisation géographique et position de l'héliostat) sont introduites dans le modèle optique pour calculer la position du soleil tout au long de l'année à différentes instants ainsi que les pertes optiques du champ de l'héliostat en utilisant Eq. (D.1) [218].

$$\eta_{hel} = \rho\, \eta_{tra}\, \cos\theta\, \eta_{sh}\, \eta_{blo}\, \eta_{spil} \tag{D.1}$$

La principale perte d'énergie dans le champ de l'héliostat de THEMIS provient : de la réflectivité de l'héliostat qui prend deux valeurs différentes selon le système considéré (cf. Eq. (D.2)), les pertes par effet cosinus, et enfin les pertes par ombrage et par blocage qui ont été estimées à l'aide du logiciel SolarPILOT [306].

$$\begin{cases} \rho_{1S} = \dfrac{\int_{250}^{2500} R_{PV}(\lambda) f(\lambda) d\lambda}{\int_{250}^{2500} f(\lambda) d(\lambda)} \\ \rho_{HT} = \rho_{CSP} = \rho_{Mir} \end{cases} \tag{D.2}$$

Combiné avec le DNI, la puissance optique envoyée sur le récepteur par chaque héliostat pour les deux centrales hybrides ainsi que pour la centrale conventionnelle THEMIS

peut être calculée à l'aide des Eq. (D.3).

$$\begin{cases} P_{rec,\ 1S}(t) = \sum_{i=1}^{N_{hel}} \eta_{hel,\ 1S}(t)\, S_{hel}\, DNI(t) \\ \\ P_{rec,\ HT}(t) = P_{rec,\ CSP}(t) = \sum_{i=1}^{N_{hel}} \eta_{hel,\ Mir}(t)\, S_{hel}\, DNI(t) \end{cases} \tag{D.3}$$

Les données météorologiques mesurées au sol (rayonnement global (GHI), température ambiante et vitesse du vent) sont utilisées comme données d'entrée dans le modèle électrique afin d'obtenir la température des cellules T_c pour la stratégie *1S*, y compris le rayonnement direct (DNI) et diffure (DHI) nous permettent d'obtenir la puissance PV générée (cf. Eq. (D.4)).

$$P_{PV,\ 1S}(t) = \sum_{i=1}^{N_{hel}} \zeta_{SQ,\ 1S}\, \eta_{1S}(t)\, [P_{dir}(t) + P_{dif}(t)] \tag{D.4}$$

La puissance solaire directe frappant chaque héliostat PV individuel ainsi que la puissance solaire diffuse interceptée par chaque héliostat à un moment donné t est donnée par [314] (cf. Eq. (D.5)).

$$\begin{cases} P_{dir}(t) = S_{hel}\, cos\theta(t)\, \eta_{blo}(t)\, \eta_{sh}(t)\, DNI(t) \\ \\ P_{dif}(t) = \dfrac{[1 + cos\beta(t)]}{2} S_{hel} DHI(t) \end{cases} \tag{D.5}$$

La puissance optique délivrée au récepteur est ensuite utilisée une dernière fois pour calculer les pertes thermiques. La sortie du modèle thermique, combinée à la puissance envoyée sur le récepteur, est utilisée comme entrée pour quantifier les différentes puissances générée par la turbine de chaque centrale (cf. Eq. (D.6)).

$$\begin{cases} P_{CSP,\ 1S}(t) = \dfrac{2}{3} \eta_{Carnot}\, \eta_{th}(t)\, P_{rec,\ 1S}(t) \\ \\ P_{CSP,\ CSP}(t) = \dfrac{2}{3} \eta_{Carnot}\, \eta_{th}(t)\, P_{rec,\ CSP}(t) \\ \\ P_{CSP,\ HT}(t) = \dfrac{2}{3} \eta_{Carnot}\, [\eta_{th}(t)\, P_{rec,\ CSP}(t) - P_{PV,\ HT}(t)] \end{cases} \tag{D.6}$$

3 Résultats et discussion

Les premiers résultats obtenus permettent de tirer un certain nombre de conclusions:

☞ Si la supériorité des centrales compactes hybrides sur les centrales CSP conventionnelles restait incertaine, le modèle actuel tend à confirmer que cette famille d'approches hybrides présente systématiquement un rendement énergétique supérieur à celui de leurs homologues purement solaires thermiques (l'écart entre les centrales compactes hybrides et les centrales CSP conventionnelles ayant tendance à se creuser sensiblement avec l'augmentation de l'efficacité PV) (cf. Figure D.4(a)).

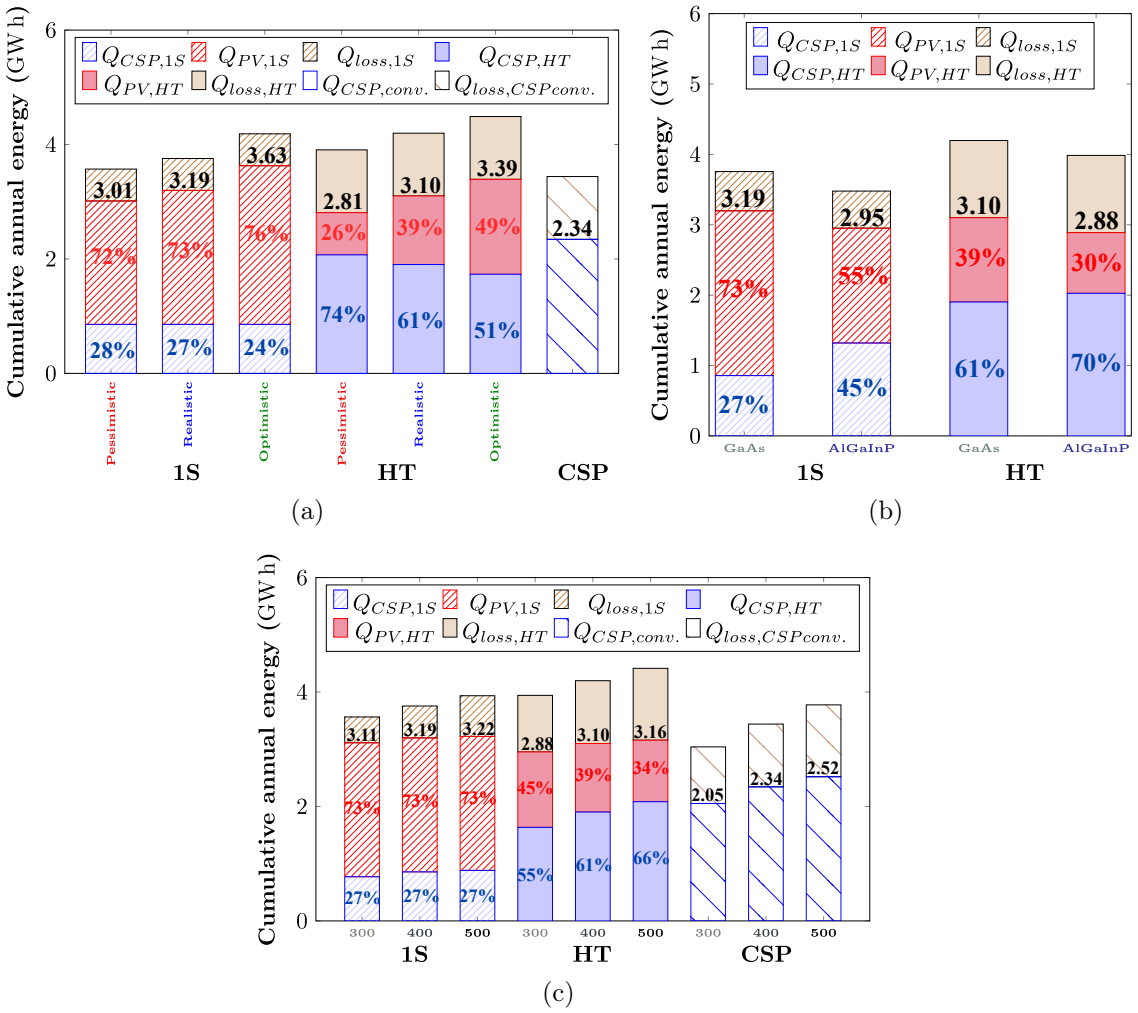

Figure D.4: La production annuelle d'énergie cumulée pour les deux approches hybrides et la centrale CSP en considérant différents : (a) scénarios, (b) technologies de cellules, (c) température du HTF.

☞ Si le choix d'un matériau à bande interdite élevée comme technologie de cellule PV dans l'approche *1S* conduit à un meilleur équilibre dans la production d'énergie de chaque convertisseur, il convient de noter que l'énergie totale fournie par le système est sensiblement plus faible par rapport aux systèmes hybrides

impliquant des cellules solaires GaAs (cf. Figure D.4(b)). Dans l'approche *HT*, l'utilisation de cellules à bande interdite élevée détériore à la fois la production d'énergie totale du système et l'équilibre entre le CSP et le PV, par rapport au cas GaAs (cf. Figure D.4(b)), ce qui suggère que la résistance à la température améliorée de ce matériau ne permet pas de contrebalancer son efficacité fondamentalement plus faible dans des conditions de soleil unique.

☞ L'avantage de la production d'énergie associée aux systèmes hybrides compacts a tendance à diminuer lorsque la température de fonctionnement du convertisseur CSP augmente (cf. Figure D.4(c)).

Installations hybrides PV-CSP compactes avec systèmes de stockage thermique en utilisant deux priorités de répartition

La Figure D.5 montre le processus de fonctionnement du système hybride PV-CSP *HT* avec un stockage thermique. Le système est basé sur une configuration de centrale à tour avec un système de stockage direct [57] (c'est-à-dire que le fluide caloporteur et le fluide de stockage sont les mêmes, dans notre étude de cas, le sel fondu a été choisi comme fluid de transfer). Lorsque le flux solaire est disponible, les cellules PV convertissent l'énergie dans la bande interdite de la cellule en électricité tandis que le sel fondu froid se réchauffe puis s'écoule vers le réservoir chaud. Finalement, le sel fondu dans le réservoir chaud échangera de la chaleur avec l'eau dans l'échangeur de chaleur pour produire de la vapeur qui alimentera la turbine pour la production d'électricité.

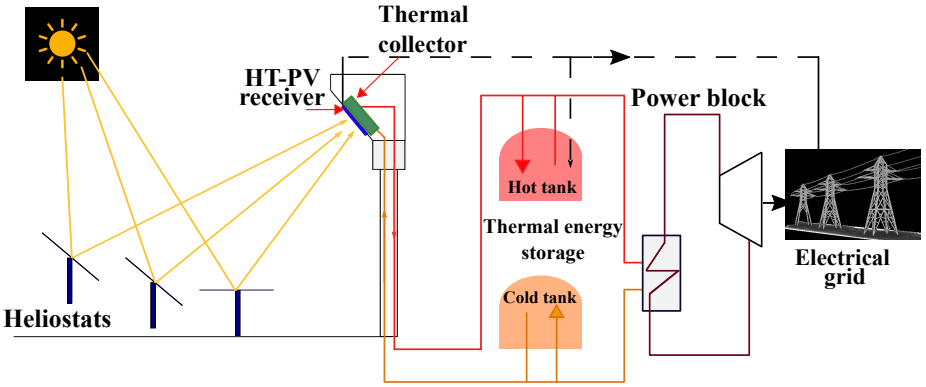

Figure D.5: Description schématique de la stratégie hybride compacte HT PV-CSP intégrée avec TES.

4 Méthodologie

L'objectif principal des technologies de stockage est de permettre une production continue pour couvrir soit 1) un profil d'électricité de base (c'est-à-dire une production

d'électricité constante indépendante de la demande d'électricité), soit 2) une électricité de suivi de la charge (la puissance électrique générée par la centrale hybride est modulée en fonction de la demande d'électricité). Pour ce faire, deux stratégies de fonctionnement ont été étudiées :

- **Stratégie 1 (S1): Priorité à la production PV**: Le premier schéma de fonctionnement des deux centrales hybrides est basé sur la fourniture d'une demande électrique donnée P_{load} (constante ou variable). Nous supposons que l'électricité PV surproduite ne peut pas être stockée (pas de stockage électrochimique, pas de possibilité de stocker l'électricité PV excédentaire sous forme de chaleur dans la cuve de stockage thermique à l'aide d'une résistance électrique). Par conséquent, l'électricité PV est prioritaire sur le réseau électrique par rapport à la production d'électricité CSP et stockage, qui fonctionne comme une sauvegarde du PV.
- **Stratégie 2 (S2): Minimiser l'énergie perdue** : Par rapport à la première stratégie de répartition, une résistance électrique est intégré aux centrales hybrides. La résistance électrique convertit l'énergie PV excédentaire (autrement rejetée) pour produire de la chaleur. La chaleur est ensuite absorbée par le fluid de transfer et stockée dans le réservoir chaude. La résistance électrique fonctionne comme une nouvelle ressource thermique pour le stockage, ce qui est bénéfique pour la flexibilité et la capacité de répartition des systèmes hybrides.

5 Résultats et discussion

La Figure D.6 illustre la production annuelle d'énergie des centrales hybrides et pour les 15 sites sélectionnés avec les deux configurations de répartition, pour une demande de base de base de 0,5 MWe avec 20 MWh_t de TES. Il s'avère que l'utilisation de l'approche **S2** avec la centrale hybride *1S* entraîne une augmentation moyenne de 17% de la production annuelle d'énergie, avec un maximum de 23% enregistré à Abu Dhabi (Figure D.6(a)), alors qu'aucune amélioration significative n'est observée dans le cas de la centrale hybride *HT* (Figure D.6(b)). Cette amélioration du rendement énergétique de l'approche 1S provient de la capacité de la stratégie **S2** à récupérer l'énergie électrique PV excédentaire sous forme de chaleur, contrairement à la stratégie **S1**.

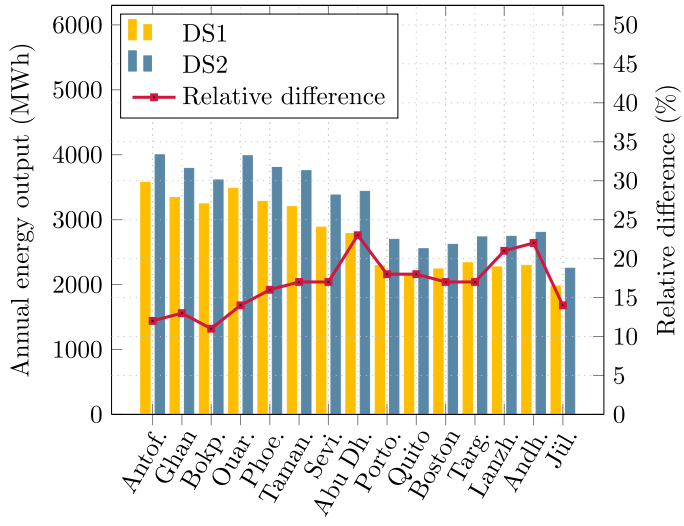

(a) *1S*

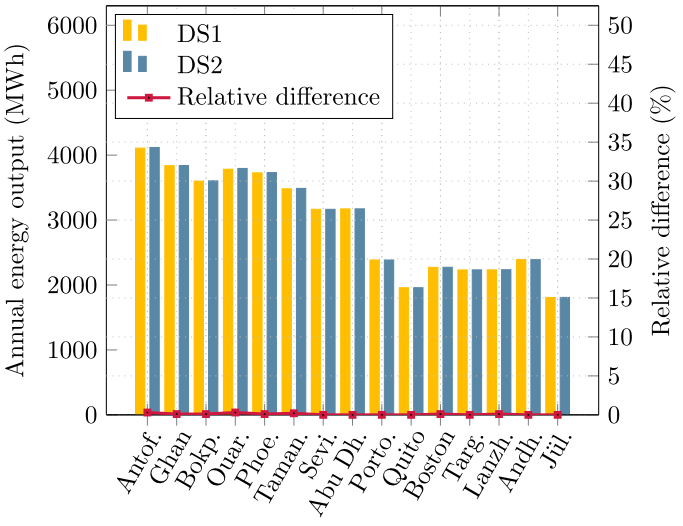

(b) *HT*

Figure D.6: Production totale annuelle (axe de gauche) et différences relatives (axe de droite) en utilisant les deux stratégies de répartition dans les emplacements sélectionnés pour les centrales hybrides : (a) centrales hybrides *1S*, et (b) *HT* pour une charge de base de 0,5 MWe avec 20 MWh_t de TES.

Pour mettre en évidence l'avantage de l'approche **S2** par rapport à l'approche **S1**, les Figures D.7 et D.8 montrent les modifications du taux de récupération (η_{recov}) en fonction de P_{load} et de la capacité de stockage pour les centrales hybrides *1S* et *HT*, respectivement. Nous observons que le ratio η_{recov} augmente avec l'augmentation de P_{load} et de la capacité de stockage, variant de manière plus significative pour la centrale hybride *1S* que pour l'approche *HT*.

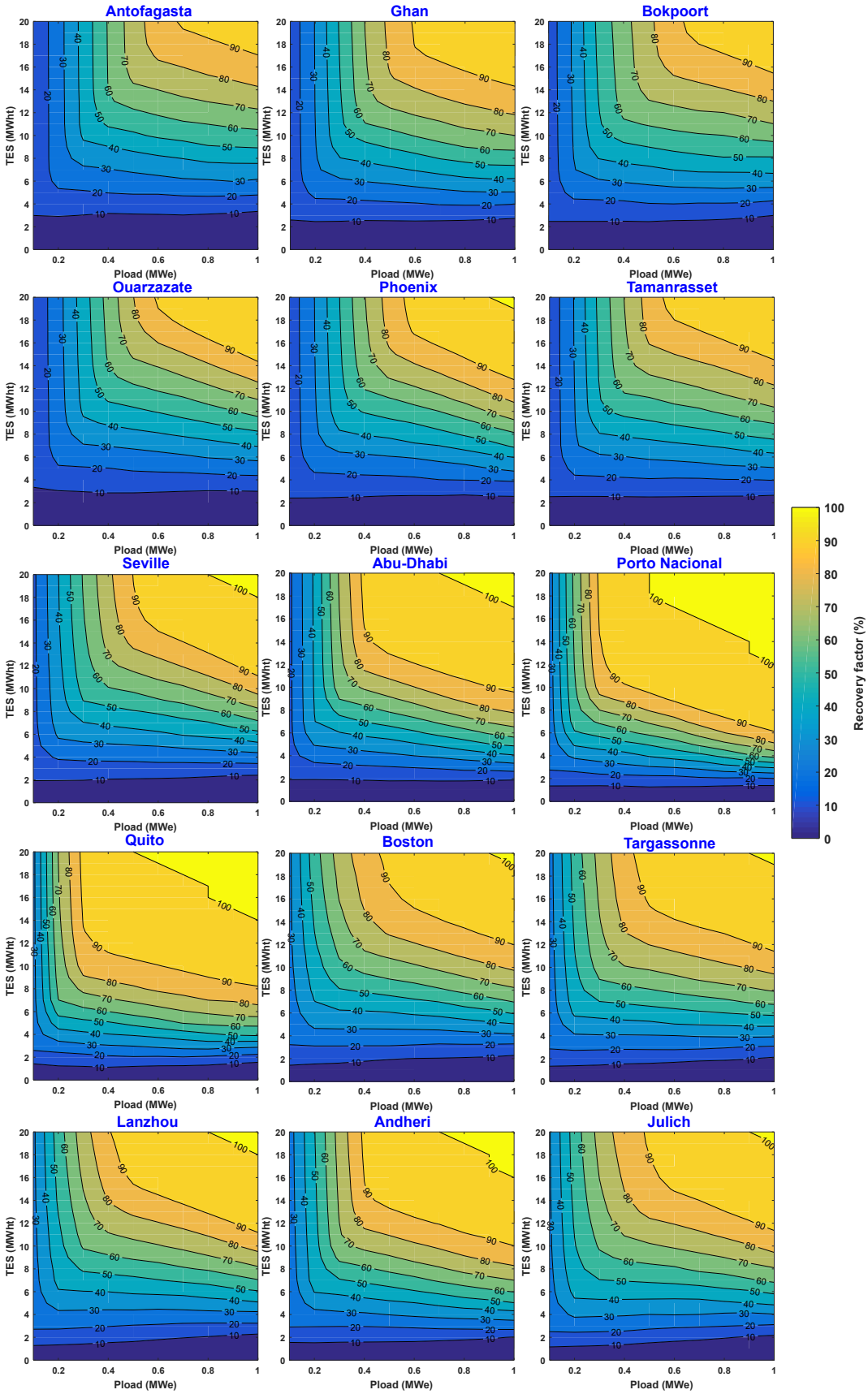

Figure D.7: Ratio de récupération de la plante hybride *1S* aux endroits sélectionnés en considérant le **S2**.

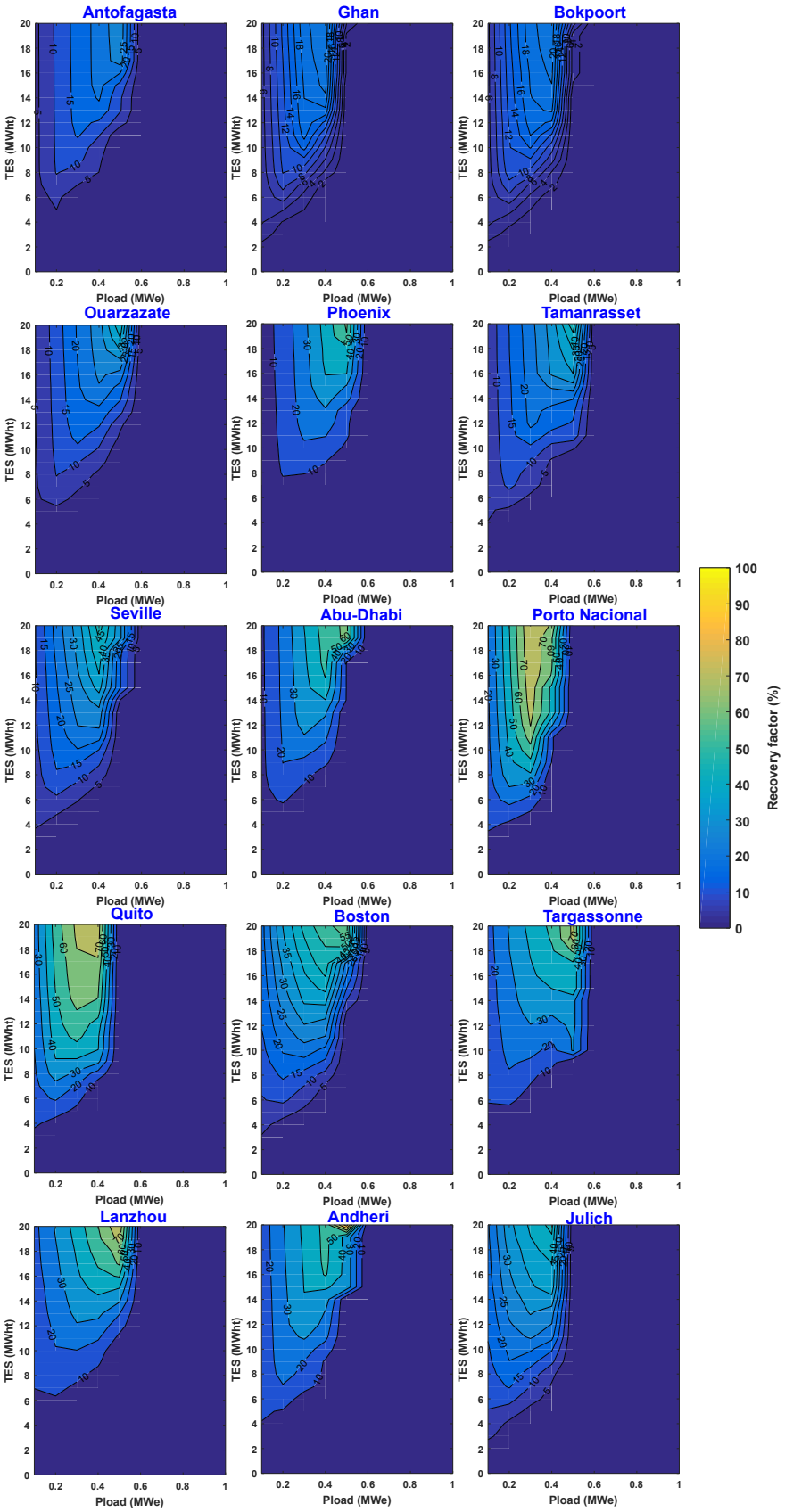

Figure D.8: Ratio de récupération de la centrale hybride *HT* aux endroits sélectionnés en considérant le **DS2**.

Technologies solaires avec stockage : quelle technologie dans quel lieu ?

Dans ce chapitre, nous proposons de répondre à la question de savoir si les centrales hybrides *compactes* peuvent ou non atteindre la meilleure performance de production avec un certain niveau de garantie d'approvisionnement, en considérant différents profils de demande (profil constant et profil variable à certains des endroits sélectionnés), et les conditions de la ressource solaire. Dans ce contexte, cinq combinaisons technologiques sont comparées : la centrale hybride *1S*, la centrale hybride *HT*, une centrale CSP-TES, une centrale PV-BESS avec batteries lithium-ion et une centrale PV-TES.

6 Méthodologie

Pour comparer les différentes technologies solaires, le même modèle multiphysique développé dans Matlab a été utilisé avec quelques modifications. L'ajout d'une partie concernant le dimensionnement de deux centrales PV conventionnelles à l'aide de l'Eq. (D.7), ainsi que l'étude des centrales PV avec stockage thermique et électrochimique.

$$P_{pv}(i) = M_{mod}\, A_{pv}\, \eta_{inver}\, f_{lpv}\, G_{inc}(i)\, \eta_{pv}(i) \tag{D.7}$$

Le modèle a besoin d'une série de paramètres techniques pour évaluer la performance de chacune des technologies solaires en plus de la production énergétique annuelle de chaque composant: le facteur de capacité, le facteur de demande et la probabilité de perte de puissance.

- **Facteur de capacité (CF):** c'est le rapport entre l'énergie électrique effectivement injectée sur le réseau et l'énergie théorique fournie par la centrale fonctionnant en continu à la puissance nominale de pointe, sur une année (cf. Eq. (D.8)) [337].

$$CF = \frac{Q_{act}}{8760\, P_{pb}} \tag{D.8}$$

- **Le facteur de demande (DF):** c'est le rapport entre l'énergie électrique produite par la centrale et l'énergie demandée par le réseau électrique (cf. Eq. (D.9)).

$$DF = \frac{Q_{act}}{8760\, P_{load}} \tag{D.9}$$

- **La probabilité de perte de puissance électrique (LPSP):** proposée pour décrire la fiabilité de l'alimentation électrique des différentes centrales, et est définie comme la fraction du temps pendant laquelle la centrale n'est pas en mesure de satisfaire la demande de la charge (cf. Eq. (D.10)).

$$LPSP = \frac{\sum_{i=1}^{8760} t_{un,\ i}\, (P_{avai} < P_{load})}{\sum_{i=1}^{8760} t_{0,\ i}} \tag{D.10}$$

7 Résultats et discussion

7.1 Impact de la ressource solaire

Le Tableau D.1 indique la production annuelle maximale d'énergie (c'est-à-dire la production maximale d'énergie qui pourrait être envoyée au réseau électrique sans aucune perte de stockage) de chaque composant des deux centrales *compactes*, ainsi que la production globale pour les cinq technologies solaires et pour les 15 sites sélectionnés.

Table D.1: La production annuelle maximale d'électricité des cinq technologies solaires sur les 15 sites sélectionnés.

Location	Maximum annual electricity generation (MWh)								
	CSP	***1S***			***HT***			**PV**$_{Fix}$	**PV**$_{1axis}$
		PV	CSP	Hybrid	PV	CSP	Hybrid		
Antofagasta	5182	4018	1769	**5787**	1164	4241	**5405**	3096	3840
Ghan	4417	3622	1473	**5095**	990	3645	**4635**	2669	3168
Bokpoort	4298	3566	1430	**4996**	965	3549	**4514**	2658	3142
Ouarzazate	4833	4017	1648	**5665**	1089	3962	**5051**	2580	2955
Phoenix	4357	3730	1463	**5192**	981	3591	**4572**	2387	2723
Tamanrasset	4128	3818	1385	**5204**	930	3404	**4334**	2518	2918
Seville	3463	3257	1139	**4396**	778	2871	**3649**	2120	2377
Abu Dhabi	3114	3355	992	**4347**	698	2610	**3308**	2260	2544
Porto Nacional	2235	2548	686	**3234**	501	1890	**2391**	1984	2303
Quito	1855	2515	574	**3089**	419	1572	**1991**	2020	2378
Boston	2393	2523	778	**3302**	539	1995	**2534**	1719	1848
Targassonne	2302	2655	740	**3395**	519	1928	**2447**	1847	1984
Lanzhou	2338	2680	768	**3448**	527	1943	**2470**	1896	2014
Andheri	2375	2756	767	**3522**	533	1983	**2516**	1870	2034
Jülich	1877	2190	593	**2783**	424	1582	**2006**	1487	1581

La production potentielle maximale d'énergie de la centrale hybride *1S* dépasse celle des quatre autres technologies solaires (Tableau D.1). Cette supériorité de l'approche *1S* s'explique par sa capacité à exploiter une plus grande fraction de la ressource solaire, grâce à sa capacité à utiliser le rayonnement diffus.
La production maximale d'électricité de la centrale hybride *HT* dépasse celle d'une centrale CSP classique de 5 % en moyenne sur les 15 sites. Cette augmentation est liée à la contribution supplémentaire du récepteur PV à la production globale de la centrale *HT*. La contribution du CSP étant inférieure à celle de la centrale CSP classique (Tableau D.1), en raison de la faible température de fonctionnement du récepteur PV (400 °C au lieu de 560 °C), il en résulte une faible efficacité de conversion du PB et donc une production CSP plus faible.
En particulier, l'amélioration annuelle de l'énergie varie différemment selon les sites sélectionnés. Par exemple, dans les sites présentant des fractions directes plus élevées, comme Antofagasta ou Ouarzazate (89% et 84%, respectivement), le gain énergétique

relatif n'est que de 4%, tandis que le gain énergétique le plus élevé (7%) est observé dans des sites comme Quito et Porto Nacional (54% et 64% respectivement. Contrairement à la centrale hybride *1S*, cela ne peut s'expliquer par la nature de la ressource solaire utilisée puisque la centrale *HT* et les centrales CSP conventionnelles utilisent uniquement la ressource DNI.

7.2 Impact d'un profil de demande électrique variable

À titre d'exemple de la performance de la combinaison de technologies, la Figure D.9 illustre la dispatchabilité des deux centrales hybrides ainsi que la centrale PV-fixe avec stockage thermique sur deux jours consécutifs, les 8^{th} et 9^{th} janvier, avec une disponibilité solaire relativement bonne, à Antofagasta. Le calcul suppose une demande de base de 0,5 MWe, 14 MWh_t de TES et 6 MWhe de BESS. Dans les Figures D.9(a), D.9(b), et D.9(c), la ligne violette représente la production PV, dont une fraction est envoyée sur le réseau électrique, le reste étant soit stocké dans le TES, soit rejetée.

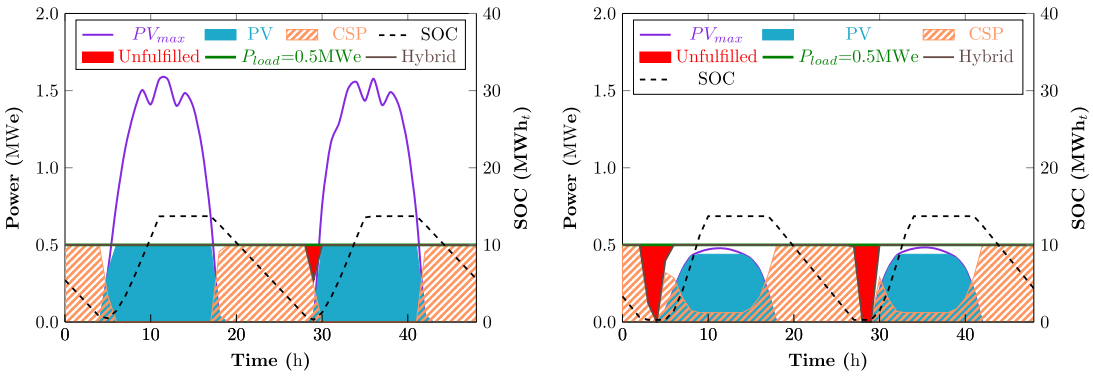

(a) *1S* (b) *HT*

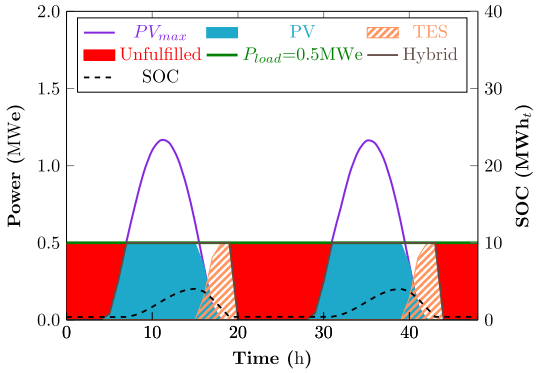

(c) **Fixed-PV + TES**

Figure D.9: Dispatchabilité des deux centrales hybrides ainsi qu'un centrale PV-fixe avec du stockage thermique en considérant une stratégie de suivi de charge pendant deux jours successifs à Antofagasta avec 14 MWh_t pour le système TES.

La Figure D.10 illustre la performance dynamique des trois mêmes centrales solaires, fonctionnant comme des centrales à suivi de charge à Antofagasta dans des conditions identiques à celles de l'étude de cas susmentionnée (Figure D.9). Des différences mineures sont notées pour la centrale hybride *1S*, où la demande a été en-

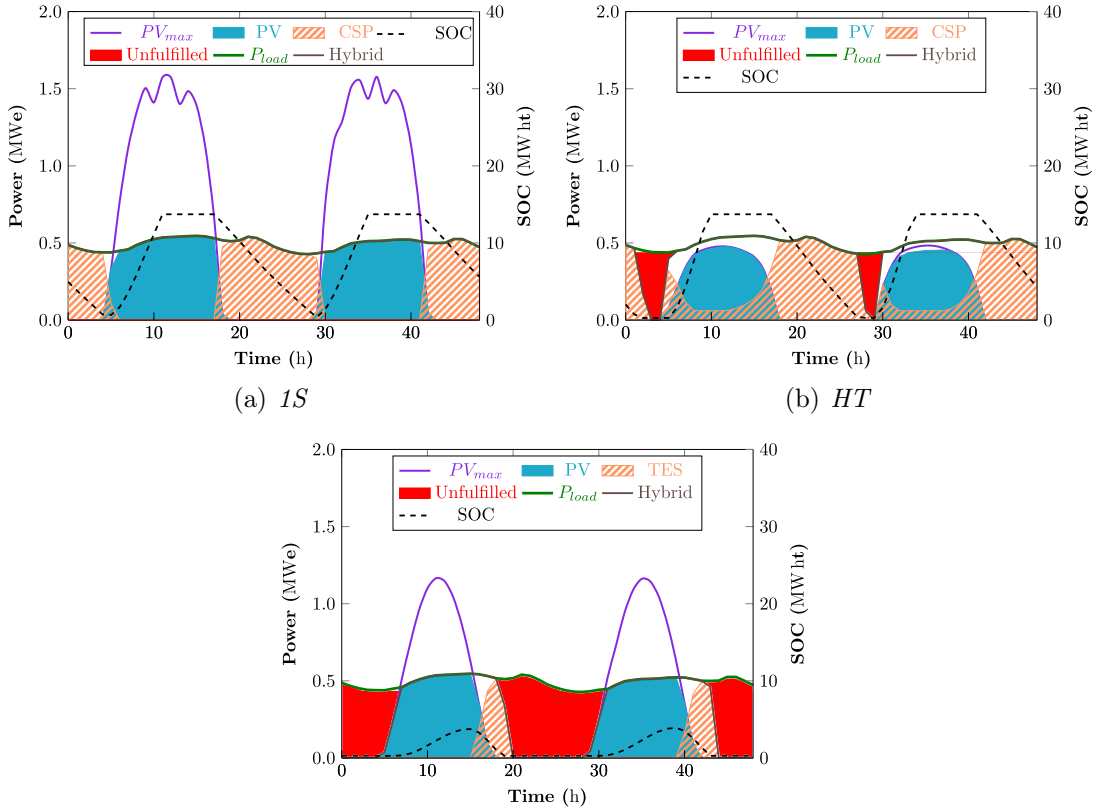

(a) *1S* (b) *HT*

(c) **Fixed-PV + TES**

Figure D.10: Dispatchabilité des trois centrales solaires en considérant une stratégie de suivi de charge pendant deux jours successifs à Antofagasta avec 14 MWh_t pour le système TES.

tièrement satisfaite puisque moins de puissance était requise tôt dans la matinée du 9^{th} janvier (0,43 MWe au lieu de 0,5 MWe) comme le montre la figure D.10(a). Pour la centrale hybride *HT*, on remarque que les SEEE se déchargent moins rapidement pendant les premières heures du matin dans le cas d'un profil de charge suiveur (figure D.10(b)), car la demande électrique est inférieure de 12 % à celle d'une demande de base. Enfin, aucune différence significative ne peut être notée pour les installations photovoltaïques classiques avec les deux systèmes de stockage utilisant une stratégie de suivi de la charge, comme le montrent la Figure D.10(c).

La Figure D.11 montre la production annuelle totale d'énergie obtenue pour les deux scénarios de demande ainsi que la différence relative pour les dix sites utilisant les deux centrales hybrides. Dans les conditions de demande et de capacité de stockage données, l'impact d'un profil de demande de suivi est limité, la variation de la production d'énergie sur une année de fonctionnement ne dépassant pas 4%, avec un maximum de 3,38% et 2,88% pour le *1S* (Figure D.11(a)) et *HT* (Figure D.11(b)), respectivement à Bokpoort. Avec un profil de charge variable, les gestionnaires de réseau sont obligés de mettre hors ligne ou de remettre en ligne rapidement la centrale pour équilibrer l'offre et la demande. Cependant, cette opération devient rapidement coûteuse car elle présente un risque d'altération de la durée de vie des turbines et peut entraîner des

pénalités financières si les opérateurs de la centrale ne peuvent pas garantir la demande seconde par seconde. Plus important encore, la prise en compte d'un profil de charge variable rend la gestion de la tension et de la fréquence plus difficile [360].

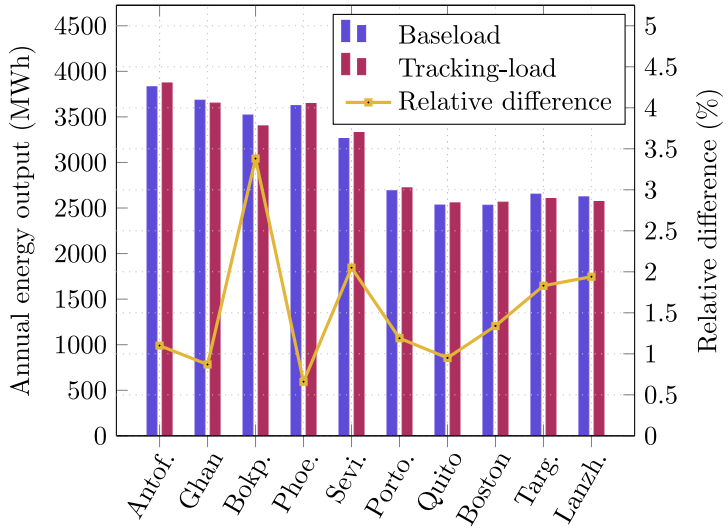

(a) *1S*

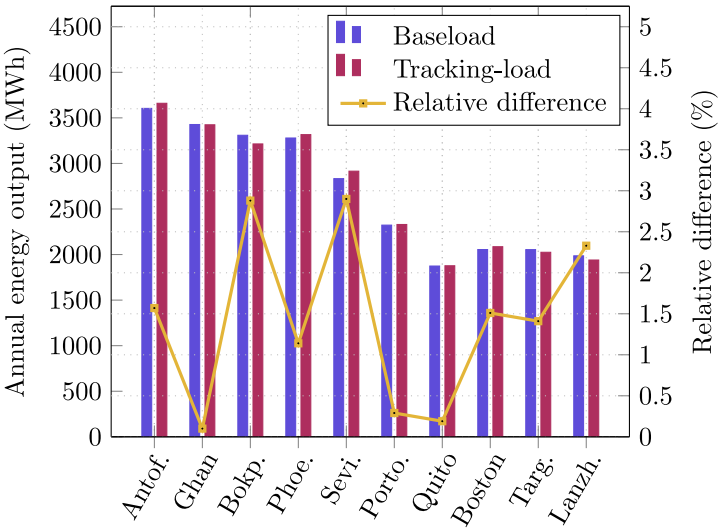

(b) *HT*

Figure D.11: Production annuelle totale (axe de gauche) et différence relative (axe de droite) en utilisant les deux stratégies de demande dans dix endroits pour les centrales hybrides : (a) *1S*, et (b) *HT* centrales hybrides avec une capacité TES de 14 MWh_t.

Conclusions

Le présent travail consiste en une étude détaillée sur la combinaison de systèmes photovoltaïques et des centrales solaire concentrée en une centrale hybride *compact*. Les objectifs de ce travail étaient de déterminer (1) si une centrale hybride *compact* PV-CSP est plus viable qu'une centrale CSP conventionnelle, (2) identifier l'impact d'une stratégie particulière de répartition du stockage sur les paramètres de performance des centrales hybrides *compactes*, et (3) comprendre où en sont aujourd'hui les centrales hybrides *compactes* par rapport aux centrales solaires conventionnelle intégrant des systèmes de stockage thermique et électrochimique.

Nous avons abordé ces objectifs en plusieurs étapes. Tout d'abord, une revue complète de la littérature a été réalisée afin de bien comprendre comment les deux types de technologies (PV et CSP) fonctionnent dans une configuration autonome et hybride, suivie d'une analyse de ce que représente l'hybridation de ces deux technologies, tant sur le plan technique que pratique, afin de pouvoir tirer parti des avantages de chacune. Deuxièmement, un nouveau modèle multiphysique a été développé. Les principales améliorations qui ont été apportées concernent les hypothèses, à savoir la description détaillée des pertes optiques du champ solaire, la variation du rendement des cellules avec la variation de la température ambiante et de la vitesse du vent, l'utilisation de données météorologiques sur site, et la description des principaux paramètres physiques. Ensuite, deux centrales hybrides *compactes* ont été évaluées, la centrale *1 soleil* et la centrale *haute température*. Dans un premier temps, l'analyse s'est limitée à l'évaluation de la production annuelle d'énergie des centrales hybrides, puis l'étude a été étendue en considérant différents paramètres de performance, à savoir le facteur de capacité de la centrale, la probabilité de perte d'alimentation électrique et la quantité d'énergie rejetée.

Les systèmes hybrides *compactes* PV-CSP peuvent effectivement surpasser la production d'une centrale solaire à tour. Néanmoins, l'écart entre les deux centrales hybrides *compactes* et la centrale à tour solaire autonome tend à se creuser considérablement avec l'augmentation du rendement PV.

L'utilisation d'une stratégie de stockage qui permet de récupérer le surplus de PV (**S2**), s'est avérée bien adaptée à la centrale hybride *1S*, car elle augmente la productivité globale de la centrale tout en maintenant une bonne réponse à la demande électrique, en particulier pour les profils de demande à faible varition le long de l'année. D'autre part, aucune différence significative n'a été notée sur la production annuelle globale de la centrale hybride *HT* avec les deux stratégies de répartition car l'excès de PV de cette centrale hybride est limité. Ce comportement différent a entraîné des valeurs de ratio de récupération différentes pour les deux centrales hybrides *compactes*.

Quel que soit l'emplacement considéré, la centrale hybride *1S* présente la production d'énergie maximale la plus élevée par rapport aux centrales CSP et PV convention-

nelles. Cependant, dans les endroits où la ressource solaire est élevée (DNI > 2500 kWh/m^2/an), la centrale hybride *1S* reste la solution la moins optimale, puisqu'elle subit les pertes d'énergie les plus importantes avec un maximum de 70% à Antofagasta, contre 44% avec la centrale à PV avec trackeur + TES.

Bibliography

[1] Hannah Ritchie and Max Roser. Co_2 and greenhouse gas emissions. *Our World in Data*, 2020.

[2] DCSP German Association for Concentrated Solar Power. Dcsp publishes study: Csp – solar power around the clock. https://deutsche-csp.de/en/, 2021. Accessed :01-08-2021.

[3] Le rayonnement solaire. https://www.nouvenergie.fr/e-formation/solaire-1/, 2019. Accessed: 04-04-2021.

[4] Égypte : ib vogt cède ses parts dans la centrale solaire "infinity 50" à benban. https://www.afrik21.africa/egypte-ib-vogt-cede-ses-parts-dans-la-centrale-solaire-%E2%80%89infinity-50%E2%80%89-a-benban/, 2020. Accessed: 05-06-2021.

[5] PHLEGON. Single-axis tracker. https://www.gp-joule.com/services/products-services/phlegonr-single-axis-tracker/. Accessed :16-09-2021.

[6] Amonix bat le record mondial en efficacité de module pv pendant le test au nrel. https://www.businesswire.com/news/home/20130426005450/fr/, 2013. Accessed: 05-06-2019.

[7] Concentrator modules. https://www.ise.fraunhofer.de/en/business-areas/photovoltaics/iii-v-and-concentrator-photovoltaics/high-concentration-systems-hcpv/concentrator-modules.html. Accessed: 12-07-2021.

[8] French bifacial standards measure up. https://www.pv-magazine.com/2020/06/11/french-bifacial-standards-measure-up/, 2020. Accessed 25-06-2021.

[9] Wenbo Gu, Tao Ma, Salman Ahmed, Yijie Zhang, and Jinqing Peng. A comprehensive review and outlook of bifacial photovoltaic (bpv) technology. *Energy Conversion and Management*, 223:113283, 2020.

[10] TRAXLE. Solar ridge concentrator tracking system traxle. http://www.solar-trackers.com/photogalery. Accessed 25-06-2021.

[11] Bruno Ehrler, Esther Alarcón-Lladó, Stefan W. Tabernig, Tom Veeken, Erik C. Garnett, and Albert Polman. Photovoltaics reaching for the shockley–queisser limit. *ACS Energy Letters*, 5(9):3029–3033, 2020.

[12] Stefan Tabernig. S-q charts. https://www.lmpv.nl/sq/, 2021. Accessed 1-07-2021.

[13] Best research-cell efficiency chart. https://www.nrel.gov/pv/cell-efficiency.html, 2021. Accessed: 17-12-2021.

[14] B Ehrhart and D Gill. Evaluation of annual efficiencies of high temperature central receiver concentrated solar power plants with thermal energy storage. *Energy Procedia*, 49:752–761, 2014.

[15] Albert Polman, Mark Knight, Erik C Garnett, Bruno Ehrler, and Wim C Sinke. Photovoltaic materials: Present efficiencies and future challenges. *Science*, 352(6283), 2016.

[16] Organic solar cell (opv) materials. https://www.tcichemicals.com/BE/fr/c/12802. Accessed: 16-07-2021.

[17] Obaidullah Mohiuddin, Madina Obaidullah, and Cumali Sabah. Improvement in dye sensitized solar cells from past to present. *Optical and Quantum Electronics*, 50(10):1–28, 2018.

[18] Andras G Pattantyus-Abraham, Illan J Kramer, Aaron R Barkhouse, Xihua Wang, Gerasimos Konstantatos, Ratan Debnath, Larissa Levina, Ines Raabe, Mohammad K Nazeeruddin, Michael Gratzel, et al. Depleted-heterojunction colloidal quantum dot solar cells. *ACS nano*, 4(6):3374–3380, 2010.

[19] Wayesh Qarony, Mohammad I Hossain, M Khalid Hossain, M Jalal Uddin, A Haque, AR Saad, and Yuen Hong Tsang. Efficient amorphous silicon solar cells: characterization, optimization, and optical loss analysis. *Results in Physics*, 7:4287–4293, 2017.

[20] Kevin L. Schulte Myles A. Steiner Andrew G. Norman Harvey L. Guthrey Matthew R. Young Tao Song John F. Geisz1, Ryan M. France1 and Thomas Moriarty. Six-junction iii–v solar cells with 47.1% conversion efficiency under 143 suns concentration. *Nature Energy*, 5:326—-335, 2020.

[21] Hugo Doeleman. Limiting and realistic efficiencies of multi-junction solar cells. *Photonic Materials Group, FOM institute AMOLF, Amsterdam*, pages 1–33, 2012.

[22] Énergie+. Caractéristiques électriques des cellules et des modules photovoltaïques. https://energieplus-lesite.be/theories/photovoltaique6/caracteristiques-electriques-des-cellules-et-des-modules-photovoltaiques/, 2010. Accessed :24-02-2022.

[23] Kaiyuan Jin. Thermofluidics of sulfur-based thermal energy storage. *University of California, Los Angeles*, 2019.

[24] Alejandro Calderón, Anabel Palacios, Camila Barreneche, Mercè Segarra, Cristina Prieto, Alfonso Rodriguez-Sanchez, and A Inés Fernández. High temperature systems using solid particles as tes and htf material: a review. *Applied Energy*, 213:100–111, 2018.

[25] DENIOS. How a lithium-ion battery works. https://www.denios.ca/expertise-advice/help-advice/safe-storage-of-lithium-ion-batteries/, 2021. Accessed :2-06-2021.

[26] S. Ekoh, I. Unsal, and A. Maheri. Optimal sizing of wind-pv-pumped hydro energy storage systems. *2016 4th International Symposium on Environmental Friendly Energies and Applications (EFEA)*, pages 1–6, 2016.

[27] Kevin Larchet. Solar pv-csp hybridisation for baseload generation: A techno-economic analysis for the chilean market. *Master of Science Thesis: KTH School of Industrial Engineering and Management*, 2015.

[28] K Wang, I Pesmazoglou, BM Franchetti, M Herrando, AM Pantaleo, and CN Markides. Thermoeconomic assessment of a spectral-splitting hybrid pvt system in dairy farms for combined heat and power. In *Proc. Int. Conf. Effic., Cost, Optim., Simul. Environ. Impact Energy Syst.*, 2019.

[29] Bennett Widyolar, Lun Jiang, Jordyn Brinkley, Sai Kiran Hota, Jonathan Ferry, Gerardo Diaz, and Roland Winston. Experimental performance of an ultra-low-cost solar photovoltaic-thermal (pvt) collector using aluminum minichannels and nonimaging optics. *Applied Energy*, 268:114894, 2020.

[30] Raygen. Next generation solar and storage. https://raygen.com/, 2020. Accessed: 05-07-2021.

[31] Lee A Weinstein, Kenneth McEnaney, Elise Strobach, Sungwoo Yang, Bikram Bhatia, Lin Zhao, Yi Huang, James Loomis, Feng Cao, Svetlana V Boriskina, et al. A hybrid electric and thermal solar receiver. *Joule*, 2(5):962–975, 2018.

[32] Daniel S Codd, Matthew D Escarra, Brian Riggs, Kazi Islam, Yaping Vera Ji, John Robertson, Christopher Spitler, Jacob Platz, Naman Gupta, and Fletcher Miller. Solar cogeneration of electricity with high-temperature process heat. *Cell Reports Physical Science*, 1(8):100135, 2020.

[33] Jeffrey M Gordon, Thomas Fasquelle, Elie Nadal, and Alexis Vossier. Providing large-scale electricity demand with photovoltaics and molten-salt storage. *Renewable and Sustainable Energy Reviews*, 135:110261, 2021.

[34] Franziska Schöniger, Richard Thonig, Gustav Resch, and Johan Lilliestam. Making the sun shine at night: comparing the cost of dispatchable concentrating solar power and photovoltaics with storage. *Energy Sources, Part B: Economics, Planning, and Policy*, 16(1):55–74, 2021.

[35] Alejandro Datas, Myrto Zeneli, Carlos del Cañizo, Ilias Malgarinos, Aristeidis Nikolopoulos, Nikolaos Nikolopoulos, Sotirios Karellas, and Antonio Martí. Molten silicon storage of concentrated solar power with integrated thermophotovoltaic energy conversion. In *AIP Conference Proceedings*, volume 2033, page 090005. AIP Publishing LLC, 2018.

[36] Alba Ramos Cabal, Alejandro Datas Medina, and Carlos del Cañizo. Solar photovoltaic power-to-heat-to-power energy storage. In *Recerca i Tecnologia en Enginyeria Gràfica i Disseny a la Universitat Politècnica de Catalunya*, pages 43–58. OmniaScience, 2020.

[37] Hamid Reza Seyf and Asegun Henry. Thermophotovoltaics: a potential pathway to high efficiency concentrated solar power. *Energy & Environmental Science*, 9(8):2654–2665, 2016.

[38] Caleb Amy, Hamid Reza Seyf, Myles A Steiner, Daniel J Friedman, and Asegun Henry. Thermal energy grid storage using multi-junction photovoltaics. *Energy & Environmental Science*, 12(1):334–343, 2019.

[39] Shimry Haviv, Natali Revivo, Nimrod Kruger, Assaf Manor, Bagrat Khachatryan, Michael Shustov, and Carmel Rotschild. Luminescent solar power—pv/thermal hybrid electricity generation for cost-effective dispatchable solar energy. *ACS Applied Materials & Interfaces*, 12(32):36040–36045, 2020.

[40] Juan Fang, Handong Wu, Taixiu Liu, Zhimei Zheng, Jing Lei, Qibin Liu, and Hongguang Jin. Thermodynamic evaluation of a concentrated photochemical–photovoltaic–thermochemical (cp-pv-t) system in the full-spectrum solar energy utilization. *Applied Energy*, 279:115778, 2020.

[41] Varun Kashyap, Siwakorn Sakunkaewkasem, Parham Jafari, Masoumeh Nazari, Bahareh Eslami, Sina Nazifi, Peyman Irajizad, Maria D Marquez, T Randall Lee, and Hadi Ghasemi. Full spectrum solar thermal energy harvesting and storage by a molecular and phase-change hybrid material. *Joule*, 3(12):3100–3111, 2019.

[42] Vidya Ganapati, T Patrick Xiao, and Eli Yablonovitch. Ultra-efficient thermophotovoltaics exploiting spectral filtering by the photovoltaic band-edge. *arXiv preprint arXiv:1611.03544*, 2016.

[43] John A Duffie and William A Beckman. *Solar engineering of thermal processes*. John Wiley & Sons, 2013.

[44] Bennett Widyolar, Lun Jiang, Mahmoud Abdelhamid, and Roland Winston. Design and modeling of a spectrum-splitting hybrid csp-cpv parabolic trough using two-stage high concentration optics and dual junction ingap/gaas solar cells. *Solar Energy*, 165:75–84, 2018.

[45] Enas R Shouman and Hesham Ezz. Forecasting transition electricity solar energy from mena to europe. *Journal of Engineering and Applied Sciences*, 11(5), 2016.

[46] Md Tasbirul Islam, Nazmul Huda, AB Abdullah, and R Saidur. A comprehensive review of state-of-the-art concentrating solar power (csp) technologies: Current status and research trends. *Renewable and Sustainable Energy Reviews*, 91:987–1018, 2018.

[47] Xinhai Xu, K Vignarooban, Ben Xu, K Hsu, and Arunachala Mada Kannan. Prospects and problems of concentrating solar power technologies for power generation in the desert regions. *Renewable and Sustainable Energy Reviews*, 53:1106–1131, 2016.

[48] Maria Simona Răboacă, Gheorghe Badea, Adrian Enache, Constantin Filote, Gabriel Răsoi, Mihai Rata, Alexandru Lavric, and Raluca-Andreea Felseghi. Concentrating solar power technologies. *Energies*, 12(6):1048, 2019.

[49] Net zero by 2050. https://www.iea.org/reports/net-zero-by-2050, 2020. Accessed: 03-06-2021.

[50] Solar Resource Maps. Gis data for 200+ countries. solargis.com/products/maps-and-gis-data/free/download/world, 2016. Accessed: 03-04-2021.

[51] Hannah Ritchie and Max Roser. Renewable energy. *Our World in Data*, 2020.

[52] Atse Louwen and Wilfried van Sark. Chapter 5 - photovoltaic solar energy. In Martin Junginger and Atse Louwen, editors, *Technological Learning in the Transition to a Low-Carbon Energy System*, pages 65–86. Academic Press, 2020.

[53] Renewables 2020 data explorer. https://www.iea.org/articles/renewables-2020-data-explorer, 2020. Accessed: 03-06-2021.

[54] ISE Fraunhofer. Stromgestehungskosten erneuerbare energien. *Fraunhofer-Institut für Solare Energiesysteme (Fhg ISE).*, 21:2014, 2013.

[55] Icaro Silvestre Freitas Gomes, Yannick Perez, and Emilia Suomalainen. Coupling small batteries and pv generation: a review. *Renewable and Sustainable Energy Reviews*, 126:109835, 2020.

[56] HL Zhang, Jan Baeyens, J Degrève, and G Cacères. Concentrated solar power plants: Review and design methodology. *Renewable and Sustainable Energy Reviews*, 22:466–481, 2013.

[57] Guruprasad Alva, Yaxue Lin, and Guiyin Fang. An overview of thermal energy storage systems. *Energy*, 144:341–378, 2018.

[58] Turgut M Gür. Review of electrical energy storage technologies, materials and systems: challenges and prospects for large-scale grid storage. *Energy & Environmental Science*, 11(10):2696–2767, 2018.

[59] Xing Luo, Jihong Wang, Mark Dooner, and Jonathan Clarke. Overview of current development in electrical energy storage technologies and the application potential in power system operation. *Applied Energy*, 137:511–536, 2015.

[60] Henok Ayele Behabtu, Maarten Messagie, Thierry Coosemans, Maitane Berecibar, Kinde Anlay Fante, Abraham Alem Kebede, and Joeri Van Mierlo. A review of energy storage technologies' application potentials in renewable energy sources grid integration. *Sustainability*, 12(24):10511, 2020.

[61] Kody M Powell, Khalid Rashid, Kevin Ellingwood, Jake Tuttle, and Brian D Iverson. Hybrid concentrated solar thermal power systems: A review. *Renewable and Sustainable Energy Reviews*, 80:215–237, 2017.

[62] K Shivarama Krishna and K Sathish Kumar. A review on hybrid renewable energy systems. *Renewable and Sustainable Energy Reviews*, 52:907–916, 2015.

[63] Xing Ju, Chao Xu, Yangqing Hu, Xue Han, Gaosheng Wei, and Xiaoze Du. A review on the development of photovoltaic/concentrated solar power (pv-csp) hybrid systems. *Solar Energy Materials and Solar Cells*, 161:305–327, 2017.

[64] Cerro dominador inaugurates its csp plant, which will provide 100% renewable energy 24/7. https://acsp.cl/en/2021/06/08/cerro-dominador-inaugurates-its-csp-plant, 2021. Accessed: 10-06-2021.

[65] HM Branz. Full-spectrum optimized conversion and utilization of sunlight (focus) program. In *Proceedings of the 20th Solar Power And Chemical Energy Systems Conference (SolarPACES 2014), Beijing, China*, 2014.

[66] Full-spectrum optimized conversion and utilization of sunlight. https://arpa-e.energy.gov/technologies/programs/focus, 2014. Accessed: 15-11-2020.

[67] Adriana Zurita, Carlos Mata-Torres, Carlos Valenzuela, Carlos Felbol, José M Cardemil, Amador M Guzmán, and Rodrigo A Escobar. Techno-economic evaluation of a hybrid csp+ pv plant integrated with thermal energy storage and a large-scale battery energy storage system for base generation. *Solar Energy*, 173:1262–1277, 2018.

[68] C Parrado, Aymeric Girard, F Simon, and E Fuentealba. 2050 lcoe (levelized cost of energy) projection for a hybrid pv (photovoltaic)-csp (concentrated solar power) plant in the atacama desert, chile. *Energy*, 94:422–430, 2016.

[69] Allan R Starke, José M Cardemil, Rodrigo A Escobar, and Sergio Colle. Assessing the performance of hybrid csp+ pv plants in northern chile. *Solar Energy*, 138:88–97, 2016.

[70] Omar Behar, Daniel Sbarbaro, and Luis Moran. Which is the most competitive solar power technology for integration into the existing copper mining plants: Photovoltaic (pv), concentrating solar power (csp), or hybrid pv-csp? *Journal of Cleaner Production*, 287:125455, 2021.

[71] Carlos Valenzuela, Carlos Mata-Torres, José M Cardemil, and Rodrigo A Escobar. Csp+ pv hybrid solar plants for power and water cogeneration in northern chile. *Solar Energy*, 157:713–726, 2017.

[72] Alae Azouzoute, Houssain Zitouni, Massaab El Ydrissi, Charaf Hajjaj, Mohammed Garoum, Abdellatif Ghennioui, et al. Developing a cleaning strategy for hybrid solar plants pv/csp: case study for semi-arid climate. *Energy*, 228:120565, 2021.

[73] Loubna Bousselamti and Mohamed Cherkaoui. Modelling and assessing the performance of hybrid pv-csp plants in morocco: A parametric study. *International Journal of Photoenergy*, 2019:1–15, 2019.

[74] Loubna Bousselamti, Wafaa Ahouar, and Mohamed Cherkaoui. Multi-objective optimization of pv-csp system in different dispatch strategies, case of study: Midelt city. *Journal of Renewable and Sustainable Energy*, 13(1):013701, 2021.

[75] Loubna Bousselamti, Wafaa Ahouar, and Mohamed Cherkaoui. Mono-objective optimization of pv-csp system using pso algorithm. In *2020 IEEE 4th International Conference on Intelligent Energy and Power Systems (IEPS)*, pages 186–189, 2020.

[76] Christoph Adrian Pan and Frank Dinter. Combination of pv and central receiver csp plants for base load power generation in south africa. *Solar Energy*, 146:379–388, 2017.

[77] Federico Dominio. Techno-economic analysis of hybrid pv-csp power plants. advantages and disadvantages of intermediate and peak load operation. Master's thesis, Universitat Politècnica de Catalunya, 2014.

[78] Xing Ju, Chao Xu, Zhirong Liao, Xiaoze Du, Gaosheng Wei, Zhifeng Wang, and Yongping Yang. A review of concentrated photovoltaic-thermal (cpvt) hybrid solar systems with waste heat recovery (whr). *Science Bulletin*, 62(20):1388–1426, 2017.

[79] Xing Ju, Chao Xu, Xue Han, Xiaoze Du, Gaosheng Wei, and Yongping Yang. A review of the concentrated photovoltaic/thermal (cpvt) hybrid solar systems based on the spectral beam splitting technology. *Applied Energy*, 187:534–563, 2017.

[80] The importance of solar energy. https://venturesolar.com/blog/the-importance-of-solar-energy/, 2017. Accessed: 01-04-2021.

[81] K Vignarooban, Xinhai Xu, A Arvay, Keng Hsu, and Arunachala Mada Kannan. Heat transfer fluids for concentrating solar power systems–a review. *Applied Energy*, 146:383–396, 2015.

[82] Parabolic trough plant noor ouarzazate i. https://www.energy.sener/projects/parabolic-trough-plant-nooro-i. Accessed: 03-05-2021.

[83] Tower of power. https://climatekids.nasa.gov/concentrating-solar/. Accessed: 03-05-2021.

[84] Reliance commissions 100 mw concentrated solar power plant in rajasthan, india. https://helioscsp.com/reliance-commissions-100-mw-concentrated-solar-power\-plant-in-rajasthan-india/, 2018. Accessed: 03-05-2021.

[85] Jason Deign. Dish stirling fights back. https://www.reutersevents.com/renewables/csp-today/technology/dish-stirling-fights-back, 2013. Accessed: 03-05-2021.

[86] Dhyia Aidroos Baharoon, Hasimah Abdul Rahman, Wan Zaidi Wan Omar, and Saeed Obaid Fadhl. Historical development of concentrating solar power technologies to generate clean electricity efficiently–a review. *Renewable and Sustainable Energy Reviews*, 41:996–1027, 2015.

[87] Miguel Diago, Nicolas Calvet, and Peter R Armstrong. Net power maximization from a faceted beam-down solar concentrator. *Solar Energy*, 204:476–488, 2020.

[88] Susan Kraemer. Beam-down demos first direct solar storage at 1/2 mwh scale. https://www.solarpaces.org/beam-down-demos-first-direct-solar-storage-at-1-2-mwh-scale/, 2021. Accessed: 12-07-2021.

[89] Alberto Sánchez-González and Jesús Gómez-Hernández. Beam-down linear fresnel reflector: Bdlfr. *Renewable Energy*, 146:802–815, 2020.

[90] Concentrating solar power (csp). https://www.iea.org/reports/concentrating-solar-power-csp, 2020. Accessed: 05-06-2021.

[91] Mark Mehos, Craig Turchi, Judith Vidal, Michael Wagner, Zhiwen Ma, Clifford Ho, William Kolb, Charles Andraka, and Alan Kruizenga. Concentrating solar power gen3 demonstration roadmap. Technical report, National Renewable Energy Lab.(NREL), Golden, CO (United States), 2017.

[92] O Achkari and A El Fadar. Latest developments on tes and csp technologies–energy and environmental issues, applications and research trends. *Applied Thermal Engineering*, 167:114806, 2020.

[93] Ahmed Bilal Awan, MN Khan, Muhammad Zubair, and Evangelos Bellos. Commercial parabolic trough csp plants: Research trends and technological advancements. *Solar Energy*, 211:1422–1458, 2020.

[94] Omar Behar, Benjamin Grange, and Gilles Flamant. Design and performance of a modular combined cycle solar power plant using the fluidized particle solar receiver technology. *Energy Conversion and Management*, 220:113108, 2020.

[95] Alhussein Albarbar and Abdullah Arar. Performance assessment and improvement of central receivers used for solar thermal plants. *Energies*, 12(16):3079, 2019.

[96] Wolf-Dieter Steinmann. Thermal energy storage systems for concentrating solar power plants. In *Concentrating solar power technology*, pages 399–440. Elsevier, 2021.

[97] J Hernández-Moro and JM Martínez-Duart. Csp electricity cost evolution and grid parities based on the iea roadmaps. *Energy Policy*, 41:184–192, 2012.

[98] Rafael Guédez, James Spelling, Björn Laumert, and Torsten Fransson. Optimization of thermal energy storage integration strategies for peak power production by concentrating solar power plants. *Energy Procedia*, 49:1642–1651, 2014.

[99] Xiaoru Zhuang, Xinhai Xu, Wenrui Liu, and Wenfu Xu. Lcoe analysis of tower concentrating solar power plants using different molten-salts for thermal energy storage in china. *Energies*, 12(7):1394, 2019.

[100] World energy outlook 2020. https://www.iea.org/reports/world-energy-outlook-2020, 2020. Accessed: 03-06-2021.

[101] Manuela Franz and Gerhard Piringer. Market development and consequences on end-of-life management of photovoltaic implementation in europe. *Energy, Sustainability and Society*, 10(1):1–21, 2020.

[102] Martin A Green, Ewan D Dunlop, Dean H Levi, Jochen Hohl-Ebinger, Masahiro Yoshita, and Anita WY Ho-Baillie. Solar cell efficiency tables (version 54). *Progress in Photovoltaics: Research and Applications*, 27(7):565–575, 2019.

[103] Champion photovoltaic module efficiency chart. https://www.nrel.gov/pv/module-efficiency.html, 2019. Accessed: 12-05-2021.

[104] Bobby. Sun tracking solar panel. https://www.upsbatterycenter.com/blog/sun-tracking-solar-panel/, 2014. Accessed: 12-07-2021.

[105] M Wiesenfarth, I Anton, and AW Bett. Challenges in the design of concentrator photovoltaic (cpv) modules to achieve highest efficiencies. *Applied Physics Reviews*, 5(4):041601, 2018.

[106] Mousaab Benhammane, Gilles Notton, Grégoire Pichenot, Philippe Voarino, and David Ouvrard. Overview of electrical power models for concentrated photovoltaic systems and development of a new operational model with easily accessible inputs. *Renewable and Sustainable Energy Reviews*, 135:110221, 2021.

[107] Wenbo Gu, Senji Li, Xing Liu, Zhenwu Chen, Xiaochun Zhang, and Tao Ma. Experimental investigation of the bifacial photovoltaic module under real conditions. *Renewable Energy*, 173:1111–1122, 2021.

[108] Monika Agrawal, Avinash Kumar, and Amartya Chowdhury. A detailed simulation-based study on the effect of mirror integration on pv module (s) with analysis of different wind flow scheme. *Solar Energy*, 222:129–144, 2021.

[109] Sishaj P Simon, Kevin Ark Kumar, Kinattingal Sundareswaran, P Srinivasa Rao Nayak, Narayana Prasad Padhy, et al. Impact and economic assessment on solar pv mirroring system–a feasibility report. *Energy Conversion and Management*, 203:112222, 2020.

[110] Roberto Baccoli, Amit Kumar, Andrea Frattolillo, Costantino Mastino, Emilio Ghiani, and Gianluca Gatto. Enhancing energy production in a pv collector–reflector system supervised by an optimization model: Experimental analysis and validation. *Energy Conversion and Management*, 229:113774, 2021.

[111] Prashant Malik and Shyam Singh Chandel. Performance enhancement of multi-crystalline silicon photovoltaic modules using mirror reflectors under western himalayan climatic conditions. *Renewable Energy*, 154:966–975, 2020.

[112] DTP Wijesuriya, KDSH Wickramathilaka, LS Wijesinghe, DM Vithana, and HY Ranjit Perera. Reduction of solar pv payback period using optimally placed reflectors. *Energy Procedia*, 134:480–489, 2017.

[113] William Shockley and Hans J Queisser. Detailed balance limit of efficiency of p-n junction solar cells. *Journal of Applied Physics*, 32(3):510–519, 1961.

[114] Anco S Blazev. *Solar Technologies for the 21st Century*. CRC Press, 2021.

[115] Martin Green, Ewan Dunlop, Jochen Hohl-Ebinger, Masahiro Yoshita, Nikos Kopidakis, and Xiaojing Hao. Solar cell efficiency tables (version 57). *Progress in Photovoltaics: Research and Applications*, 29(1):3–15, 2021.

[116] Emmett E Perl, John Simon, John F Geisz, Minjoo Larry Lee, Daniel J Friedman, and Myles A Steiner. Measurements and modeling of iii-v solar cells at high temperatures up to 400 °C. *IEEE Journal of Photovoltaics*, 6(5):1345–1352, 2016.

[117] Rodolphe Vaillon, Stéphanie Parola, Chrysovalantou Lamnatou, and Daniel Chemisana. Solar cells operating under thermal stress. *Cell Reports Physical Science*, page 100267, 2020.

[118] Emmett E Perl, John Simon, Daniel J Friedman, Nikhil Jain, Paul Sharps, Claiborne McPheeters, Yukun Sun, Minjoo L Lee, and Myles A Steiner. (al) gainp/gaas tandem solar cells for power conversion at elevated temperature and high concentration. *IEEE Journal of Photovoltaics*, 8(2):640–645, 2018.

[119] Nikhil Jain, Kevin L Schulte, John F Geisz, Daniel J Friedman, Ryan M France, Emmett E Perl, Andrew G Norman, Harvey L Guthrey, and Myles A Steiner. High-efficiency inverted metamorphic 1.7/1.1 ev gainasp/gainas dual-junction solar cells. *Applied Physics Letters*, 112(5):053905, 2018.

[120] Yiqing Dai and Yu Bai. Performance improvement for building integrated photovoltaics in practice: A review. *Energies*, 14(1):178, 2021.

[121] Ashwith Kumar Chilvery, Ashok K Batra, Bin Yang, Kai Xiao, Padmaja Guggilla, Mohan D Aggarwal, Raja Surabhi, Ravi B Lal, James R Currie, and Benjamin G Penn. Perovskites: transforming photovoltaics, a mini-review. *Journal of Photonics for Energy*, 5(1):057402, 2015.

[122] Taesoo D Lee and Abasifreke U Ebong. A review of thin film solar cell technologies and challenges. *Renewable and Sustainable Energy Reviews*, 70:1286–1297, 2017.

[123] Jing Zhang, Wei Zhang, Hui-Ming Cheng, and S Ravi P Silva. Critical review of recent progress of flexible perovskite solar cells. *Materials Today*, 39:66–88, 2020.

[124] Lin Xie, Wei Song, Jinfeng Ge, Bencan Tang, Xiaoli Zhang, Tao Wu, and Ziyi Ge. Recent progress of organic photovoltaics for indoor energy harvesting. *Nano Energy*, page 105770, 2021.

[125] Mohd Sukor Su'ait, Mohd Yusri Abd Rahman, and Azizan Ahmad. Review on polymer electrolyte in dye-sensitized solar cells (dsscs). *Solar Energy*, 115:452–470, 2015.

[126] Khushboo Sharma, Vinay Sharma, and SS Sharma. Dye-sensitized solar cells: fundamentals and current status. *Nanoscale Research Letters*, 13(1):1–46, 2018.

[127] Dongxiao Wang, Wangen Zhao, Yi Zhang, and Shengzhong Frank Liu. Path towards high-efficient kesterite solar cells. *Journal of Energy Chemistry*, 27(4):1040–1053, 2018.

[128] Long Hu, Qian Zhao, Shujuan Huang, Jianghui Zheng, Xinwei Guan, Robert Patterson, Jiyun Kim, Lei Shi, Chun-Ho Lin, Qi Lei, et al. Flexible and efficient perovskite quantum dot solar cells via hybrid interfacial architecture. *Nature Communications*, 12(1):1–9, 2021.

[129] William E McMahon, Daniel J Friedman, and John F Geisz. Multijunction solar cell design revisited: disruption of current matching by atmospheric absorption bands. *Progress in Photovoltaics: Research and Applications*, 25(10):850–860, 2017.

[130] Masafumi Yamaguchi, Frank Dimroth, John F Geisz, and Nicholas J Ekins-Daukes. Multi-junction solar cells paving the way for super high-efficiency. *Journal of Applied Physics*, 129(24):240901, 2021.

[131] J Li, A Aierken, Y Liu, Y Zhuang, X Yang, JH Mo, RK Fan, QY Chen, SY Zhang, YM Huang, et al. A brief review of high efficiency iii-v solar cells for space application. *Frontiers in Physics*, 2021.

[132] Mohammad I Hossain, Wayesh Qarony, Sainan Ma, Longhui Zeng, Dietmar Knipp, and Yuen Hong Tsang. Perovskite/silicon tandem solar cells: from detailed balance limit calculations to photon management. *Nano-micro Letters*, 11(1):1–24, 2019.

[133] Martin A Green. Solar cells: operating principles, technology, and system applications. *Englewood Cliffs*, 1982.

[134] Priyanka Singh and Nuggehalli M Ravindra. Temperature dependence of solar cell performance—an analysis. *Solar Energy Materials and Solar Cells*, 101:36–45, 2012.

[135] Ben G Streetman and Sanjay Banerjee. *Solid state electronic devices*, volume 5. Englewood Cliffs, NJ, USA: Prentice-Hall, 2000.

[136] John CC Fan. Theoretical temperature dependence of solar cell parameters. *Solar Cells*, 17(2-3):309–315, 1986.

[137] Vincenzo Franzitta, Aldo Orioli, and Alessandra Di Gangi. Assessment of the usability and accuracy of the simplified one-diode models for photovoltaic modules. *Energies*, 9(12):1019, 2016.

[138] Avi Braun, Eugene A Katz, and Jeffrey M Gordon. Basic aspects of the temperature coefficients of concentrator solar cell performance parameters. *Progress in Photovoltaics: Research and Applications*, 21(5):1087–1094, 2013.

[139] Martin A Green. General temperature dependence of solar cell performance and implications for device modelling. *Progress in Photovoltaics: Research and Applications*, 11(5):333–340, 2003.

[140] Olivier Dupré. *Physics of the thermal behavior of photovoltaic devices*. PhD thesis, Lyon, INSA, 2015.

[141] Seama Koohi-Fayegh and Marc A Rosen. A review of energy storage types, applications and recent developments. *Journal of Energy Storage*, 27:101047, 2020.

[142] AG Olabi, C Onumaegbu, Tabbi Wilberforce, Mohamad Ramadan, Mohammad Ali Abdelkareem, and Abdul Hai Al-Alami. Critical review of energy storage systems. *Energy*, page 118987, 2020.

[143] Furquan Nadeem, SM Suhail Hussain, Prashant Kumar Tiwari, Arup Kumar Goswami, and Taha Selim Ustun. Comparative review of energy storage systems, their roles, and impacts on future power systems. *IEEE Access*, 7:4555–4585, 2018.

[144] Alfonso J Carrillo, José González-Aguilar, Manuel Romero, and Juan M Coronado. Solar energy on demand: A review on high temperature thermochemical heat storage systems and materials. *Chemical Reviews*, 119(7):4777–4816, 2019.

[145] Ioan Sarbu and Calin Sebarchievici. A comprehensive review of thermal energy storage. *Sustainability*, 10(1):191, 2018.

[146] HP Garg, SC Mullick, and AK Bhargava. Sensible heat storage. In *Solar Thermal Energy Storage*, pages 82–153. Springer, 1985.

[147] Frank Dinter and Lucas Möller. A review of andasol 3 and perspective for parabolic trough csp plants in south africa. In *AIP Conference Proceedings*, volume 1734, page 100005. AIP Publishing LLC, 2016.

[148] Nicolas Calvet, Alexander H Slocum, Antoni Gil, Benjamin Grange, Radia Lahlou, Tyler T Hamer, Miguel Diago, Melanie Tetreault-Friend, Daniel S Codd, David L Trumper, et al. Dispatchable solar power using molten salt directly irradiated from above. *Solar Energy*, 220:217–229, 2021.

[149] Mario Petrollese, Giorgio Cau, and Daniele Cocco. The ottana solar facility: dispatchable power from small-scale csp plants based on orc systems. *Renewable Energy*, 147:2932–2943, 2020.

[150] Wenjin Ding, Alexander Bonk, Joachim Gussone, and Thomas Bauer. Electrochemical measurement of corrosive impurities in molten chlorides for thermal energy storage. *Journal of Energy Storage*, 15:408–414, 2018.

[151] Wenjin Ding and Thomas Bauer. Progress in research and development of molten chloride salt technology for next generation concentrated solar power plants. *Engineering*, 7(3):334–347, 2021.

[152] Rebecca I Dunn, Patrick J Hearps, and Matthew N Wright. Molten-salt power towers: newly commercial concentrating solar storage. *Proceedings of the IEEE*, 100(2):504–515, 2011.

[153] Gilles Flamant, Daniel Gauthier, Hadrien Benoit, Jean-Louis Sans, Roger Garcia, Benjamin Boissière, Renaud Ansart, and Mehrdji Hemati. Dense suspension of solid particles as a new heat transfer fluid for concentrated solar thermal plants: On-sun proof of concept. *Chemical Engineering Science*, 102:567–576, 2013.

[154] Zhiwen Ma, Patrick Davenport, and Ruichong Zhang. Design analysis of a particle-based thermal energy storage system for concentrating solar power or grid energy storage. *Journal of Energy Storage*, 29:101382, 2020.

[155] Claudio Tregambi, Maurizio Troiano, Fabio Montagnaro, Roberto Solimene, and Piero Salatino. Fluidized beds for concentrated solar thermal technologies—a review. *Frontiers in Energy Research*, 9:13, 2021.

[156] Mario Cascetta, Mario Petrollese, Joseph Oyekale, and Giorgio Cau. Thermocline vs. two-tank direct thermal storage system for concentrating solar power plants: A comparative techno-economic assessment. *International Journal of Energy Research*, 2021.

[157] Khadija El Alami, Mohamed Asbik, and Hassan Agalit. Identification of natural rocks as storage materials in thermal energy storage (tes) system of concentrated solar power (csp) plants–a review. *Solar Energy Materials and Solar Cells*, 217:110599, 2020.

[158] K Jin, A Barde, K Nithyanandam, and RE Wirz. Sulfur heat transfer behavior in vertically-oriented isochoric thermal energy storage systems. *Applied Energy*, 240:870–881, 2019.

[159] Amey Barde, Kaiyuan Jin, Mitchell Shinn, Karthik Nithyanandam, and Richard E Wirz. Demonstration of a low cost, high temperature elemental sulfur thermal battery. *Applied Thermal Engineering*, 137:259–267, 2018.

[160] K Schwaiger, M Haider, M Hämmerle, D Wünsch, M Obermaier, M Beck, A Niederer, S Bachinger, D Radler, C Mahr, et al. sandtes–an active thermal energy storage system based on the fluidization of powders. *Energy Procedia*, 49:983–992, 2014.

[161] Peter Steiner, Karl Schwaiger, Heimo Walter, and Markus Haider. Active fluidized bed technology used for thermal energy storage. In *Energy Sustainability*, volume 50220, page V001T05A001. American Society of Mechanical Engineers, 2016.

[162] Jessica Giro-Paloma, Mònica Martínez, Luisa F Cabeza, and A Inés Fernández. Types, methods, techniques, and applications for microencapsulated phase change materials (mpcm): a review. *Renewable and Sustainable Energy Reviews*, 53:1059–1075, 2016.

[163] Hassan Nazir, Mariah Batool, Francisco J Bolivar Osorio, Marllory Isaza-Ruiz, Xinhai Xu, K Vignarooban, Patrick Phelan, Arunachala M Kannan, et al. Recent developments in phase change materials for energy storage applications: A review. *International Journal of Heat and Mass Transfer*, 129:491–523, 2019.

[164] Raja Elarem, Talal Alqahtani, Sofiene Mellouli, Faouzi Askri, Abhilash Edacherian, Tirth Vineet, Irfan Anjum Badruddin, and Jemni Abdelmajid. A comprehensive review of heat transfer intensification methods for latent heat storage units. *Energy Storage*, 3(1), 2021.

[165] Joseph Stekli, Levi Irwin, and Ranga Pitchumani. Technical challenges and opportunities for concentrating solar power with thermal energy storage. *Journal of Thermal Science and Engineering Applications*, 5(2), 2013.

[166] Hannah Ritchie. The price of batteries has declined by 97% in the last three decades. https://ourworldindata.org/battery-price-decline. Accessed 30-06-2021.

[167] Hojong Kim, Dane A Boysen, Jocelyn M Newhouse, Brian L Spatocco, Brice Chung, Paul J Burke, David J Bradwell, Kai Jiang, Alina A Tomaszowska, Kangli

Wang, et al. Liquid metal batteries: past, present, and future. *Chemical reviews*, 113(3):2075–2099, 2013.

[168] Ambri Incorporated. The ambri technology. https://ambri.com/technology/, 2021. Accessed: 23-07-2021.

[169] Nancy W. Stauffer. A battery of molten metals: Low-cost, long-lasting storage for the grid. https://energy.mit.edu/news/a-battery-of-molten-metals/, 2015. Accessed: 23-07-2021.

[170] Kenneth Karlsson, Stefan Petrovic, and Diana Abad Hernando. Global outlook on energy technology development. *DTU International Energy Report 2018*, 21, 2018.

[171] Mustafa E Amiryar and Keith R Pullen. A review of flywheel energy storage system technologies and their applications. *Applied Sciences*, 7(3):286, 2017.

[172] Ujwal Kishor Zore, Sripadh Guptha Yedire, Narasimha Pandi, Sivakumar Manickam, and Shirish H Sonawane. A review on recent advances in hydrogen energy, fuel cell, biofuel and fuel refining via ultrasound process intensification. *Ultrasonics Sonochemistry*, page 105536, 2021.

[173] Guoping Hu, Chao Chen, Hiep Thuan Lu, Yue Wu, Congmin Liu, Lefu Tao, Yuhan Men, Guangli He, and Kevin Gang Li. A review of technical advances, barriers, and solutions in the power to hydrogen (p2h) roadmap. *Engineering*, 2020.

[174] JJ Brey. Use of hydrogen as a seasonal energy storage system to manage renewable power deployment in spain by 2030. *International Journal of Hydrogen Energy*, 46(33):17447–17457, 2021.

[175] US Department of ENERGY. Biomass conversion: From feedstocks to final products. https://www.energy.gov/sites/prod/files/2016/07/f33/conversion_factsheet.pdf, 2016.

[176] Riccardo Battisti. Molten salt storage 33 times cheaper than lithium-ion batteries. https://helioscsp.com/molten-salt-storage-33-times-cheaper-than-lithium-ion-batteries/, 2018. Accessed: 20-07-2021.

[177] David Feldman, Vignesh Ramasamy, Ran Fu, Ashwin Ramdas, Jal Desai, and Robert Margolis. Us solar photovoltaic system and energy storage cost benchmark: Q1 2020. Technical report, National Renewable Energy Lab.(NREL), Golden, CO (United States), 2021.

[178] Haisheng Chen, Thang Ngoc Cong, Wei Yang, Chunqing Tan, Yongliang Li, and Yulong Ding. Progress in electrical energy storage system: A critical review. *Progress in Natural Science*, 19(3):291–312, 2009.

[179] Fenil Desai, Jenne Sunku Prasad, P Muthukumar, and Muhammad Mustafizur Rahman. Thermochemical energy storage system for cooling and process heating applications: A review. *Energy Conversion and Management*, 229:113617, 2021.

[180] AR Dehghani-Sanij, E Tharumalingam, MB Dusseault, and R Fraser. Study of energy storage systems and environmental challenges of batteries. *Renewable and Sustainable Energy Reviews*, 104:192–208, 2019.

[181] Bashria AA Yousef, Ahmed A Hachicha, Ivette María Rodríguez Pérez, Mohammad Ali Abdelkareem, and Abrar Inyaat. Perspective on integration of concentrated solar power plants. *International Journal of Low-Carbon Technologies*, pages 1–28, 2021.

[182] Howard M Branz, William Regan, Kacy J Gerst, J Brian Borak, and Elizabeth A Santori. Hybrid solar converters for maximum exergy and inexpensive dispatchable electricity. *Energy & Environmental Science*, 8(11):3083–3091, 2015.

[183] Adam Green, C Diep, R Dunn, and J Dent. High capacity factor csp-pv hybrid systems. *Energy Procedia*, 69:2049–2059, 2015.

[184] Jozef Paska, Piotr Biczel, and Mariusz Kłos. Hybrid power systems–an effective way of utilising primary energy sources. *Renewable Energy*, 34(11):2414–2421, 2009.

[185] Santanu Pramanik and RV Ravikrishna. A review of concentrated solar power hybrid technologies. *Applied Thermal Engineering*, 127:602–637, 2017.

[186] Khalid Rashid, Seyed Mostafa Safdarnejad, Kevin Ellingwood, and Kody M Powell. Techno-economic evaluation of different hybridization schemes for a solar thermal/gas power plant. *Energy*, 181:91–106, 2019.

[187] Joseph Oyekale, Florian Heberle, Mario Petrollese, Dieter Brüggemann, and Giorgio Cau. Biomass retrofit for existing solar organic rankine cycle power plants: Conceptual hybridization strategy and techno-economic assessment. *Energy Conversion and Management*, 196:831–845, 2019.

[188] Jingze Yang, Zhen Yang, and Yuanyuan Duan. Load matching and techno-economic analysis of csp plant with s–co2 brayton cycle in csp-pv-wind hybrid system. *Energy*, 223:120016, 2021.

[189] Kewen Li, Changwei Liu, Shanshan Jiang, and Youguang Chen. Review on hybrid geothermal and solar power systems. *Journal of Cleaner Production*, 250:119481, 2020.

[190] Mohammed Chennaif, Hassan Zahboune, Mohammed Elhafyani, and Smail Zouggar. Electric system cascade extended analysis for optimal sizing of an autonomous hybrid csp/pv/wind system with battery energy storage system and thermal energy storage. *Energy*, 227:120444, 2021.

[191] Werner J Platzer. Combined solar thermal and photovoltaic power plants–an approach to 24h solar electricity? In *AIP Conference Proceedings*, volume 1734, page 070026. AIP Publishing LLC, 2016.

[192] JA Aguilar-Jiménez, N Velázquez, A Acuña, R Cota, E González, L González, R López, and S Islas. Techno-economic analysis of a hybrid pv-csp system with thermal energy storage applied to isolated microgrids. *Solar Energy*, 174:55–65, 2018.

[193] Lukas Haack and Martin Schlecht. Water saving potential of csp-pv hybrid plants. In *AIP Conference Proceedings*, volume 2126, page 220003. AIP Publishing LLC, 2019.

[194] Rhetta Wingert, Hannah O'Hern, Matthew Orosz, Parameswar Harikumar, Kenneth Roberts, and Todd Otanicar. Spectral beam splitting retrofit for hybrid pv/t using existing parabolic trough power plants for enhanced power output. *Solar Energy*, 202:1–9, 2020.

[195] J Yu Zhengshan, Kathryn C Fisher, Brian M Wheelwright, Roger P Angel, and Zachary C Holman. Pvmirror: a new concept for tandem solar cells and hybrid solar converters. *IEEE Journal of Photovoltaics*, 5(6):1791–1799, 2015.

[196] Zhengshan J Yu, Kathryn C Fisher, Xiaodong Meng, Justin J Hyatt, Roger P Angel, and Zachary C Holman. Gaas/silicon pvmirror tandem photovoltaic mini-module with 29.6% efficiency with respect to the outdoor global irradiance. *Progress in Photovoltaics: Research and Applications*, 27(5):469–475, 2019.

[197] Adriana Zurita, Carlos Mata-Torres, José M Cardemil, and Rodrigo A Escobar. Assessment of time resolution impact on the modeling of a hybrid csp-pv plant: A case of study in chile. *Solar Energy*, 202:553–570, 2020.

[198] Kai Wang, Antonio M Pantaleo, María Herrando, Michele Faccia, Ioannis Pesmazoglou, Benjamin M Franchetti, and Christos N Markides. Spectral-splitting hybrid pv-thermal (pvt) systems for combined heat and power provision to dairy farms. *Renewable Energy*, 159:1047–1065, 2020.

[199] Todd P Otanicar, Rhetta Wingert, Matthew Orosz, and Clay McPheeters. Concentrating photovoltaic retrofit for existing parabolic trough solar collectors: Design, experiments, and levelized cost of electricity. *Applied Energy*, 265:114751, 2020.

[200] Wanjun Qu, Xueli Xing, Yali Cao, Taixiu Liu, Hui Hong, and Hongguang Jin. A concentrating solar power system integrated photovoltaic and mid-temperature solar thermochemical processes. *Applied Energy*, 262:114421, 2020.

[201] Bennett Widyolar, Lun Jiang, Jonathan Ferry, Roland Winston, Alexander Kirk, Mark Osowski, David Cygan, and Hamid Abbasi. Theoretical and experimental performance of a two-stage (50x) hybrid spectrum splitting solar collector tested to 600°C. *Applied Energy*, 239:514–525, 2019.

[202] Xing Ju, Mostafa M Abd El-Samie, Chao Xu, Hangyu Yu, Xinyu Pan, and Yongping Yang. A fully coupled numerical simulation of a hybrid concentrated photovoltaic/thermal system that employs a therminol vp-1 based nanofluid as a spectral beam filter. *Applied Energy*, 264:114701, 2020.

[203] Xue Han, Guankun Zhao, Chao Xu, Xing Ju, Xiaoze Du, and Yongping Yang. Parametric analysis of a hybrid solar concentrating photovoltaic/concentrating solar power (cpv/csp) system. *Applied Energy*, 189:520–533, 2017.

[204] Xue Han, Chao Xu, XinYu Pan, Xing Ju, and XiaoZe Du. Dynamic analysis of a concentrating photovoltaic/concentrating solar power (cpv/csp) hybrid system. *Science China Technological Sciences*, 62(11):1987–1998, 2019.

[205] P Richter, T Trimborn, and L Aldenhoff. Predictive storage strategy for optimal design of hybrid csp-pv plants with immersion heater. *Solar Energy*, 218:237–250, 2021.

[206] Rongrong Zhai, Ying Chen, Hongtao Liu, Hao Wu, and Yongping Yang. Optimal design method of a hybrid csp-pv plant based on genetic algorithm considering the operation strategy. *International Journal of Photoenergy*, 2018, 2018.

[207] Catalina Hernández Moris, Maria Teresa Cerda Guevara, Alois Salmon, and Álvaro Gálvez Lorca. Comparison between concentrated solar power and gas-based generation in terms of economic and flexibility-related aspects in chile. *Energies*, 14(4):1063, 2021.

[208] R Bravo and D Friedrich. Two-stage optimisation of hybrid solar power plants. *Solar Energy*, 164:187–199, 2018.

[209] Fei Li, Canbing Li, Kai Sun, Jiamei Zhang, and Hua Li. Capacity configuration of hybrid csp/pv plant for economical application of solar energy. *Chinese Journal of Electrical Engineering*, 6(2):19–29, 2020.

[210] SolarPaces 2020. Morocco pioneers pv with thermal storage at 800 mw midelt csp project. https://www.solarpaces.org/morocco-pioneers-pv-to-thermal-storage-at-800-mw-midelt-csp-project/, 2020. Accessed 25-07-2020.

[211] Andreas Rosenstiel, Nathalie Monnerie, Jürgen Dersch, Martin Roeb, Robert Pitz-Paal, and Christian Sattler. Electrochemical hydrogen production powered by pv/csp hybrid power plants: A modelling approach for cost optimal system design. *Energies*, 14(12):3437, 2021.

[212] Ahmed Khouya. Hydrogen production costs of a polymer electrolyte membrane electrolysis powered by a renewable hybrid system. *International Journal of Hydrogen Energy*, 46(27):14005–14023, 2021.

[213] Carlos Mata-Torresa, Adriana Zuritaa, Jose M Cardemilb, and Rodrigo A Escobara. Thermoeconomic analysis of a csp+ pv+ med plant in chile: Assessing the impact of the pv plant integration. In *Proceedings of ecos 2019-the 32nd international conference on efficiency, cost, optimization, simulation and environmental impact of energy systems, wroclaw, Poland, June 23-28*, 2019.

[214] Carlos Mata-Torres, Patricia Palenzuela, Adriana Zurita, José M Cardemil, Diego-César Alarcón-Padilla, and Rodrigo A Escobar. Annual thermoeconomic analysis of a concentrating solar power+ photovoltaic+ multi-effect distillation plant in northern chile. *Energy Conversion and Management*, 213:112852, 2020.

[215] Daniele Cocco, Luca Migliari, and Mario Petrollese. A hybrid csp–cpv system for improving the dispatchability of solar power plants. *Energy Conversion and Management*, 114:312–323, 2016.

[216] Sara Ghaem Sigarchian, Matthew S Orosz, Harry F Hemond, and Anders Malmquist. Optimum design of a hybrid pv–csp–lpg microgrid with particle swarm optimization technique. *Applied Thermal Engineering*, 109:1031–1036, 2016.

[217] Rongrong Zhai, Hongtao Liu, Ying Chen, Hao Wu, and Yongping Yang. The daily and annual technical-economic analysis of the thermal storage pv-csp system in two dispatch strategies. *Energy Conversion and Management*, 154:56–67, 2017.

[218] Hongtao Liu, Rongrong Zhai, Jiaxin Fu, Yulong Wang, and Yongping Yang. Optimization study of thermal-storage pv-csp integrated system based on ga-pso algorithm. *Solar Energy*, 184:391–409, 2019.

[219] Alberto Giaconia and Roberto Grena. A model of integration between pv and thermal csp technologies. *Solar Energy*, 224:149–159, 2021.

[220] José A López-Álvarez, Miguel Larrañeta, Elena Pérez-Aparicio, Manuel A Silva-Pérez, and Isidoro Lillo-Bravo. An approach to the operation modes and strategies for integrated hybrid parabolic trough and photovoltaic solar systems. *Sustainability*, 13(8):4402, 2021.

[221] Jianqing Lin, Xing Ju, Chao Xu, Yu Yang, and Xiaoze Du. High temperature stability and optical properties investigation of a novel ito-therminol 66 nanofluid for spectral splitting pv/t systems. *Optical Materials*, 109:110373, 2020.

[222] Todd Otanicar, John Dale, Matthew Orosz, Nick Brekke, Drew DeJarnette, Ebrima Tunkara, Kenneth Roberts, and Parameswar Harikumar. Experimental evaluation of a prototype hybrid cpv/t system utilizing a nanoparticle fluid absorber at elevated temperatures. *Applied Energy*, 228:1531–1539, 2018.

[223] Jun Ni, Jun Li, Wei An, and Tong Zhu. Performance analysis of nanofluid-based spectral splitting pv/t system in combined heating and power application. *Applied Thermal Engineering*, 129:1160–1170, 2018.

[224] A Vossier, J Zeitouny, EA Katz, A Dollet, G Flamant, and JM Gordon. Performance bounds and perspective for hybrid solar photovoltaic/thermal electricity-generation strategies. *Sustainable Energy & Fuels*, 2(9):2060–2067, 2018.

[225] Joya Zeitouny, Noémie Lalau, Jeffrey M Gordon, Eugene A Katz, Gilles Flamant, Alain Dollet, and Alexis Vossier. Assessing high-temperature photovoltaic performance for solar hybrid power plants. *Solar Energy Materials and Solar Cells*, 182:61–67, 2018.

[226] Chr Lamnatou, Rodolphe Vaillon, S Parola, and D Chemisana. Photovoltaic/thermal systems based on concentrating and non-concentrating technologies: Working fluids at low, medium and high temperatures. *Renewable and Sustainable Energy Reviews*, 137:110625, 2021.

[227] Hussein M Maghrabie, Khaled Elsaid, Enas Taha Sayed, Mohammad Ali Abdelkareem, Tabbi Wilberforce, and AG Olabi. Building-integrated photovoltaic/thermal (bipvt) systems: Applications and challenges. *Sustainable Energy Technologies and Assessments*, 45:101151, 2021.

[228] Yuanlong Cui, Jie Zhu, Stamatis Zoras, and Jizhe Zhang. Comprehensive review of the recent advances in pv/t system with loop-pipe configuration and nanofluid. *Renewable and Sustainable Energy Reviews*, 135:110254, 2021.

[229] John Lasich, Ian Thomas, Wolfgang Hertaeg, David Shirley, Neil Faragher, Neil Erenstrom, Sam Carter, Brian Cox, and Xinyi Zuo. A 200kw central receiver cpv system. In *AIP Conference Proceedings*, volume 1679, page 030004. AIP Publishing LLC, 2015.

[230] Steve Horne and John Lasich. Concentrating photovoltaic systems and applications. In *Concentrating solar power technology*, pages 357–397. Elsevier, 2021.

[231] John Lasich, Richard Payne, Wolfgang Hertaeg, David Shirley, Ian Thomas, Sam Carter, Will Mosley, and Zoran Lasich. Central receiver photovoltaics-a new generation of solar power. In *AIP Conference Proceedings*, volume 2012, page 020007. AIP Publishing LLC, 2018.

[232] Mark Keevers. 40% efficient sunlight to electricity conversion. *Progress in Photovoltaics: Research and Applications*, 23(6):685–691, 2015.

[233] Mohammad Mohsen Sarafraz, Marjan Goodarzi, Iskander Tlili, Tawfeeq Abdullah Alkanhal, and Maziar Arjomandi. Thermodynamic potential of a high-concentration hybrid photovoltaic/thermal plant for co-production of steam and electricity. *Journal of Thermal Analysis and Calorimetry*, 143(2):1389–1398, 2021.

[234] Myles A Steiner, Emmett E Perl, John Simon, Daniel J Friedman, Nikhil Jain, Paul Sharps, Claiborne McPheeters, and Minjoo Larry Lee. Algainp/gaas tandem solar cells for power conversion at 400 c and high concentration. In *AIP Conference Proceedings*, volume 1881, page 040007. AIP Publishing LLC, 2017.

[235] Ahmad Mojiri, Robert Taylor, Elizabeth Thomsen, and Gary Rosengarten. Spectral beam splitting for efficient conversion of solar energy—a review. *Renewable and Sustainable Energy Reviews*, 28:654–663, 2013.

[236] Wanjun Qu, Hui Hong, and Hongguang Jin. A spectral splitting solar concentrator for cascading solar energy utilization by integrating photovoltaics and solar thermal fuel. *Applied Energy*, 248:162–173, 2019.

[237] Huaxu Liang, Fuqiang Wang, Luwei Yang, Ziming Cheng, Yong Shuai, and Heping Tan. Progress in full spectrum solar energy utilization by spectral beam splitting hybrid pv/t system. *Renewable and Sustainable Energy Reviews*, 141:110785, 2021.

[238] Gan Huang, Sara Riera Curt, Kai Wang, and Christos N Markides. Challenges and opportunities for nanomaterials in spectral splitting for high-performance hybrid solar photovoltaic-thermal applications: A review. *Nano Materials Science*, 2(3):183–203, 2020.

[239] Bennett Widyolar, Lun Jiang, and Roland Winston. Spectral beam splitting in hybrid pv/t parabolic trough systems for power generation. *Applied Energy*, 209:236–250, 2018.

[240] Gang Wang, Yubo Yao, Jianqing Lin, Zeshao Chen, and Peng Hu. Design and thermodynamic analysis of a novel solar cpv and thermal combined system utilizing spectral beam splitter. *Renewable Energy*, 155:1091–1102, 2020.

[241] Xinyue Han, Dengshuai Xue, Jun Zheng, Sami M Alelyani, and Xiaobin Chen. Spectral characterization of spectrally selective liquid absorption filters and exploring their effects on concentrator solar cells. *Renewable Energy*, 131:938–945, 2019.

[242] Gaoming Zhang, Jinjia Wei, Huling Xie, Zexin Wang, Yonghao Xi, and Muhammad Khalid. Performance investigation on a novel spectral splitting concentrating photovoltaic/thermal system based on direct absorption collection. *Solar Energy*, 163:552–563, 2018.

[243] Gan Huang, Kai Wang, Sara Riera Curt, Benjamin Franchetti, Ioannis Pesmazoglou, and Christos N Markides. On the performance of concentrating fluid-based spectral-splitting hybrid pv-thermal (pv-t) solar collectors. *Renewable Energy*, 2021.

[244] Yusuf Bicer, André Felipe Vitorio Sprotte, and Ibrahim Dincer. Concentrated solar light splitting using cold mirrors for photovoltaics and photonic hydrogen production applications. *Applied Energy*, 197:169–182, 2017.

[245] Sanli Tang, Hui Hong, Hongguang Jin, and Yimin Xuan. A cascading solar hybrid system for co-producing electricity and solar syngas with nanofluid spectrum selector. *Applied Energy*, 248:231–240, 2019.

[246] Gan Huang, Kai Wang, and Christos N Markides. Efficiency limits of concentrating spectral-splitting hybrid photovoltaic-thermal (pv-t) solar collectors and systems. *Light: Science & Applications*, 10(1):1–14, 2021.

[247] Amal Herez, Hicham El Hage, Thierry Lemenand, Mohamad Ramadan, and Mahmoud Khaled. Parabolic trough photovoltaic/thermal hybrid system: Thermal modeling and parametric analysis. *Renewable Energy*, 165:224–236, 2021.

[248] Sheng Wang, Junxiang Shi, Hsiu-Hung Chen, Steven R Schafer, Moiz Munir, Greg Stecker, Wei Pan, Jong-Jan Lee, and Chung-Lung Chen. Cooling design and evaluation for photovoltaic cells within constrained space in a cpv/csp hybrid solar system. *Applied Thermal Engineering*, 110:369–381, 2017.

[249] Nipun Goel, Hannah O'Hern, Matthew Orosz, and Todd Otanicar. Annual simulation of photovoltaic retrofits within existing parabolic trough concentrating solar powerplants. *Solar Energy*, 211:600–612, 2020.

[250] Pvmirror – a high-efficiency solar module. https://repository.arizona.edu/handle/10150/603589, 2016. Accessed 22-07-2019.

[251] Ju Huang, Xinyue Han, Xiaobo Zhao, and Chunfeng Meng. Facile preparation of core-shell ag@ sio_2 nanoparticles and their application in spectrally splitting pv/t systems. *Energy*, 215:119111, 2021.

[252] Xinyue Han, Xiaobin Chen, Yao Sun, and Jian Qu. Performance improvement of a pv/t system utilizing ag/coso4-propylene glycol nanofluid optical filter. *Energy*, 192:116611, 2020.

[253] Kate Fisher, Zhengshan Yu, Rob Striling, and Zachary Holman. Pvmirrors: Hybrid pv/csp collectors that enable lower lcoes. In *AIP Conference Proceedings*, volume 1850, page 020004. AIP Publishing LLC, 2017.

[254] J Yu Zhengshan, Kathryn C Fisher, and Zachary C Holman. Modeling of gaas/silicon pvmirror tandem system: A case study. In *2016 IEEE 43rd Photovoltaic Specialists Conference (PVSC)*, pages 0200–0203. IEEE, 2016.

[255] Zachary Holman and Zhengshan Jason Yu. High-efficiency solar power with integrated storage. *Solar & Alternative Energy SPIE Newsroom*, 2015.

[256] Xiaodong Meng, Kathryn C Fisher, Lennon O Reinhart, Wyatt S Taylor, Michael Stuckelberger, Zachary C Holman, and Mariana I Bertoni. Optical characterization of curved silicon pv modules with dichroic polymeric films. *Solar Energy Materials and Solar Cells*, 201:110072, 2019.

[257] Luis Miguel Lozano Pimentel. Diseño y estimación de la producción de una central híbrida cst-pv. *Thesis master*, 2020.

[258] Sushil Kumar, Robin Thakur, Arvind Singhy, RK Tripathi, and Muneesh Sethi. A review of heat removal mechanism in concentrated pvt systems using beam splitter. *Materials Today: Proceedings*, 50:952–961, 2021.

[259] Nick Brekke, John Dale, Drew DeJarnette, Parameswar Hari, Matthew Orosz, Kenneth Roberts, Ebrima Tunkara, and Todd Otanicar. Detailed performance model of a hybrid photovoltaic/thermal system utilizing selective spectral nanofluid absorption. *Renewable Energy*, 123:683–693, 2018.

[260] Kiyarash Rahbar, Alireza Riasi, Hamed Khatam Bolouri Sangjoeei, and Nima Razmjoo. Heat recovery of nano-fluid based concentrating photovoltaic thermal (cpv/t) collector with organic rankine cycle. *Energy Conversion and Management*, 179:373–396, 2019.

[261] Tao Zhu, Qiang Li, Yimin Xuan, Dong Liu, and Hui Hong. Performance investigation of a hybrid photovoltaics and mid-temperature methanol thermochemistry system. *Applied Energy*, 256:113908, 2019.

[262] Gang Wang, Fasi Wang, Fan Shen, Zeshao Chen, and Peng Hu. Novel design and thermodynamic analysis of a solar concentration pv and thermal combined system based on compact linear fresnel reflector. *Energy*, 180:133–148, 2019.

[263] Xinyue Han, Xiaobin Chen, Qian Wang, Sami M Alelyani, and Jian Qu. Investigation of coso4-based ag nanofluids as spectral beam splitters for hybrid pv/t applications. *Solar Energy*, 177:387–394, 2019.

[264] Huaxu Liang, Han Han, Fuqiang Wang, Ziming Cheng, Bo Lin, Yuzhai Pan, and Jianyu Tan. Experimental investigation on spectral splitting of photovoltaic/thermal hybrid system with two-axis sun tracking based on sio2/tio2 interference thin film. *Energy Conversion and Management*, 188:230–240, 2019.

[265] Gang Wang, Yubo Yao, Zeshao Chen, and Peng Hu. Thermodynamic and optical analyses of a hybrid solar cpv/t system with high solar concentrating uniformity based on spectral beam splitting technology. *Energy*, 166:256–266, 2019.

[266] Space solar cells: Solar cells optimized for all space missions and are fully space qualified. https://solaerotech.com/space-solar-cells-cics/, 2018. Accessed :30-07-2021.

[267] Liang Huaxu, Wang Fuqiang, Zhang Dong, Cheng Ziming, Zhang Chuanxin, Lin Bo, and Xu Huijin. Experimental investigation of cost-effective zno nanofluid based spectral splitting cpv/t system. *Energy*, 194:116913, 2020.

[268] Wei An, Jinrui Wu, Tong Zhu, and Qunzhi Zhu. Experimental investigation of a concentrating pv/t collector with cu9s5 nanofluid spectral splitting filter. *Applied energy*, 184:197–206, 2016.

[269] Xinyue Han, Xiaobo Zhao, and Xiaobin Chen. Design and analysis of a concentrating pv/t system with nanofluid based spectral beam splitter and heat pipe cooling. *Renewable Energy*, 162:55–70, 2020.

[270] Gang Wang, Botong Wang, Yubo Yao, Jianqing Lin, Zeshao Chen, and Peng Hu. Parametric study on thermodynamic performance of a novel pv panel and thermal hybrid solar system. *Applied Thermal Engineering*, 180:115807, 2020.

[271] James Walshe, Pauraic Mc Carron, Sarah McCormack, John Doran, and George Amarandei. Organic luminescent down-shifting liquid beam splitters for hybrid photovoltaic-thermal (pvt) applications. *Solar Energy Materials and Solar Cells*, 219:110818, 2021.

[272] Gang Wang, Botong Wang, Xipeng Yuan, Jianqing Lin, and Zeshao Chen. Novel design and analysis of a solar pvt system using lfr concentrator and nano-fluids optical filter. *Case Studies in Thermal Engineering*, 27:101328, 2021.

[273] Nicholas JY Liew, Zhengshan Jason Yu, Zachary Holman, and Hyun-Jin Lee. Application of spectral beam splitting using wavelength-selective filters for photovoltaic/concentrated solar power hybrid plants. *Applied Thermal Engineering*, page 117823, 2021.

[274] Ayad K Khlief, Syed Ihtsham Ul Haq Gilani, Hussain H Al-Kayiem, and Sanan T Mohammad. Concentrated solar tower hybrid evacuated tube–photovoltaic/thermal receiver with a non-imaging optic reflector: A case study. *Journal of Cleaner Production*, 298:126683, 2021.

[275] J Hernández-Moro and Jose Manuel Martinez-Duart. Analytical model for solar pv and csp electricity costs: Present lcoe values and their future evolution. *Renewable and Sustainable Energy Reviews*, 20:119–132, 2013.

[276] Rosalinda H van Leest, Peter Mulder, Natasha Gruginskie, Simone CW van Laar, Gerard J Bauhuis, Hyenseok Cheun, Heonmin Lee, Wonki Yoon, Remco van der Heijden, Ed Bongers, et al. Temperature-induced degradation of thin-film iii–v solar cells for space applications. *IEEE Journal of Photovoltaics*, 7(2):702–708, 2017.

[277] A Datas, DL Chubb, and A Veeraragavan. Steady state analysis of a storage integrated solar thermophotovoltaic (sistpv) system. *Solar Energy*, 96:33–45, 2013.

[278] Alejandro Datas, Alba Ramos, Antonio Martí, Carlos del Cañizo, and Antonio Luque. Ultra high temperature latent heat energy storage and thermophotovoltaic energy conversion. *Energy*, 107:542–549, 2016.

[279] NATHALIE. Amadeus project. https://amadeus-project.eu/. Accessed 25-03-2021.

[280] Jianmeng Jiao, Bettina Grorud, Caroline Sindland, Jafar Safarian, Kai Tang, Kathrine Sellevoll, and Merete Tangstad. The use of eutectic fe-si-b alloy as a phase change material in thermal energy storage systems. *Materials*, 12(14):2312, 2019.

[281] Yang Wang, Haizhou Liu, and Jia Zhu. Solar thermophotovoltaics: Progress, challenges, and opportunities. *APL Materials*, 7(8):080906, 2019.

[282] M Zeneli, A Bellucci, G Sabbatella, DM Trucchi, A Nikolopoulos, N Nikolopoulos, S Karellas, and E Kakaras. Performance evaluation and optimization of the cooling system of a hybrid thermionic-photovoltaic converter. *Energy Conversion and Management*, 210:112717, 2020.

[283] Dounia Ziyati, Alain Dollet, Gilles Flamant, Yann Volut, Emmanuel Guillot, and Alexis Vossier. A multiphysics model of large-scale compact pv–csp hybrid plants. *Applied Energy*, 288:116644, 2021.

[284] Alexis Vossier, Alberto Riverola, Daniel Chemisana, Alain Dollet, and Christian A Gueymard. Is conversion efficiency still relevant to qualify advanced multi-junction solar cells? *Progress in Photovoltaics: Research and Applications*, 25(3):242–254, 2017.

[285] A Amri, Michel Izygon, and B Tedjiza. Central receiver plant evaluation:(2) themis collector subsystem evaluation. Technical report, Sandia National Lab.(SNL-CA), Livermore, CA (United States), 1988.

[286] B Grange and G Flamant. Aiming strategy on a prototype-scale solar receiver: Coupling of tabu search, ray-tracing and thermal models., 2021.

[287] AF Baker and AC Skinrood. Characteristics of current solar central receiver projects. Technical report, Sandia National Labs., Livermore, CA (USA), 1987.

[288] Alain Ferriere, Mikael Volut, Antoine Perez, and Yann Volut. In-situ measurement of concentrated solar flux and distribution at the aperture of a central solar receiver. In *AIP Conference Proceedings*, volume 1734, page 130007. AIP Publishing LLC, 2016.

[289] MR Rodríguez-Sánchez, C Leray, A Toutant, A Ferriere, and G Olalde. Development of a new method to estimate the incident solar flux on central receivers from deteriorated heliostats. *Renewable Energy*, 130:182–190, 2019.

[290] Jesús García, Rodrigo Barraza, Yen Chean Soo Too, Ricardo Vásquez Padilla, David Acosta, Danilo Estay, and Patricio Valdivia. Aiming clusters of heliostats over solar receivers for distributing heat flux using one variable per group. *Renewable Energy*, 160:584–596, 2020.

[291] Robert Flesch, Cathy Frantz, Daniel Maldonado Quinto, and Peter Schwarzbözl. Towards an optimal aiming for molten salt power towers. *Solar Energy*, 155:1273–1281, 2017.

[292] Seonghyeok Yang, Kyungeun Lee, and Ikjin Lee. Pattern-free heliostat field layout optimization using physics-based gradient. *Solar Energy*, 206:722–731, 2020.

[293] Wen-Qi Wang, Yu Qiu, Ming-Jia Li, Ya-Ling He, and Ze-Dong Cheng. Coupled optical and thermal performance of a fin-like molten salt receiver for the next-generation solar power tower. *Applied Energy*, 272:115079, 2020.

[294] Maimoon Atif and Fahad A Al-Sulaiman. Optimization of heliostat field layout in solar central receiver systems on annual basis using differential evolution algorithm. *Energy Conversion and Management*, 95:1–9, 2015.

[295] JG Barberena, A Mutuberria Larrayoz, Marcelino Sánchez, and Ana Bernardos. State-of-the-art of heliostat field layout algorithms and their comparison. *Energy Procedia*, 93:31–38, 2016.

[296] Francisco J Collado and Jesús Guallar. A review of optimized design layouts for solar power tower plants with campo code. *Renewable and Sustainable Energy Reviews*, 20:142–154, 2013.

[297] Caitou He, Xiaoyue Duan, Yuhong Zhao, and Jieqing Feng. An analytical flux density distribution model with a closed-form expression for a flat heliostat. *Applied Energy*, 251:113310, 2019.

[298] Yves Jannot. Transferts thermiques. *Ecole des mines Nancy*, page 161, 2012.

[299] Martin A Green, Ewan D Dunlop, Jochen Hohl-Ebinger, Masahiro Yoshita, Nikos Kopidakis, and Xiaojing Hao. Solar cell efficiency tables (version 56). *Progress in Photovoltaics: Research and Applications*, 28(7):629–638, 2020.

[300] S. Moreno-Tejera, L. Ramírez-Santigosa, and M.A. Silva-Pérez. A proposed methodology for quick assessment of timestamp and quality control results of solar radiation data. *Renewable Energy*, 78:531–537, 2015.

[301] J Meeus. Astronomical algorithms.(2dedition.) willmann-bell. *Richmond, VA*, 1998.

[302] Ibrahim Reda and Afshin Andreas. Solar position algorithm for solar radiation applications. *Solar Energy*, 76(5):577–589, 2004.

[303] Standard solar spectra. https://www.pveducation.org/pvcdrom/appendices/standard-solar-spectra. Accessed: 03-04-2021.

[304] The World Bank. Source: Global solar atlas 2.0, solar resource data: Solargis. https://solargis.com/maps-and-gis-data/download/france, 2019. Accessed 5-07-2021.

[305] Xiudong Wei, Zhenwu Lu, Weixing Yu, Hongxin Zhang, and Zhifeng Wang. Tracking and ray tracing equations for the target-aligned heliostat for solar tower power plants. *Renewable Energy*, 36(10):2687–2693, 2011.

[306] Michael J Wagner and Tim Wendelin. Solarpilot: A power tower solar field layout and characterization tool. *Solar Energy*, 171:185–196, 2018.

[307] Kan-Hua Lee, Kenji Araki, Li Wang, Nobuaki Kojima, Yoshio Ohshita, and Masafumi Yamaguchi. Assessing material qualities and efficiency limits of iii–v on silicon solar cells using external radiative efficiency. *Progress in Photovoltaics: Research and Applications*, 24(10):1310–1318, 2016.

[308] Joya Zeitouny, Alain Dollet, and Alexis Vossier. Combining sunlight concentration and angular confinement: Studying the effects of series resistance and external radiative efficiency. In *AIP Conference Proceedings*, volume 1766, page 080008. AIP Publishing LLC, 2016.

[309] I Vurgaftman, J áR Meyer, and L áR Ram-Mohan. Band parameters for iii–v compound semiconductors and their alloys. *Journal of Applied Physics*, 89(11):5815–5875, 2001.

[310] DL Evans. Simplified method for predicting photovoltaic array output. *Solar energy*, 27(6):555–560, 1981.

[311] T. J. Silverman, M. G. Deceglie, B. Marion, S. Cowley, B. Kayes, and S. Kurtz. Outdoor performance of a thin-film gallium-arsenide photovoltaic module. In *2013 IEEE 39th Photovoltaic Specialists Conference (PVSC)*, pages 0103–0108, 2013.

[312] Matthew Muller, Bill Marion, and Jose Rodriguez. Evaluating the iec 61215 ed. 3 nmot procedure against the existing noct procedure with pv modules in a side-by-side configuration. In *2012 38th IEEE Photovoltaic Specialists Conference*, pages 000697–000702. IEEE, 2012.

[313] Alexis Vossier, Federico Gualdi, Alain Dollet, Richard Ares, and Vincent Aimez. Approaching the Shockley-Queisser limit: General assessment of the main limiting mechanisms in photovoltaic cells. *Journal of Applied Physics*, 117(1):epub, January 2015.

[314] Sarah Paul Ayeng'o, Hendrik Axelsen, David Haberschusz, and Dirk Uwe Sauer. A model for direct-coupled pv systems with batteries depending on solar radiation, temperature and number of serial connected pv cells. *Solar Energy*, 183:120–131, 2019.

[315] Daniel Murray. *Small-scale solar central receiver system design and analysis*. PhD thesis, Faculty at California Polytechnic State University San Luis Obispo, 2012.

[316] Sven Rühle. Tabulated values of the shockley–queisser limit for single junction solar cells. *Solar Energy*, 130:139–147, 2016.

[317] EE Perl, D Kuciauskas, J Simon, DJ Friedman, and MA Steiner. Identification of the limiting factors for high-temperature gaas, gainp, and algainp solar cells from device and carrier lifetime analysis. *Journal of Applied Physics*, 122(23):233102, 2017.

[318] Gilles Notton, Christian Cristofari, Michel Mattei, and Philippe Poggi. Modelling of a double-glass photovoltaic module using finite differences. *Applied Thermal Engineering*, 25(17-18):2854–2877, 2005.

[319] Association internationale pour l'évaluation du rendement scolaire. *Technology roadmap solar thermal electricity*. OECD Publishing, 2015.

[320] Asegun Henry and Ravi Prasher. The prospect of high temperature solid state energy conversion to reduce the cost of concentrated solar power. *Energy & Environmental Science*, 7(6):1819–1828, 2014.

[321] Marc T Dunham and Brian D Iverson. High-efficiency thermodynamic power cycles for concentrated solar power systems. *Renewable and Sustainable Energy Reviews*, 30:758–770, 2014.

[322] Clifford K Ho and Brian D Iverson. Review of high-temperature central receiver designs for concentrating solar power. *Renewable and Sustainable Energy Reviews*, 29:835–846, 2014.

[323] Lori Aniti. California's curtailments of solar electricity generation continue to increase. https://www.eia.gov/todayinenergy/detail.php?id=49276, 2021. Accessed :25-08-2021.

[324] Adriana Zurita, Carlos Mata-Torres, José M Cardemil, Rafael Guédez, and Rodrigo A Escobar. Multi-objective optimal design of solar power plants with storage systems according to dispatch strategy. *Energy*, page 121627, 2021.

[325] Mario Petrollese and Daniele Cocco. Optimal design of a hybrid csp-pv plant for achieving the full dispatchability of solar energy power plants. *Solar Energy*, 137:477–489, 2016.

[326] Rafael Osuna, Rafael Olavarrıa, Rafael Morillo, Marcelino Sánchez, Felipe Cantero, Valerio Fernández-Quero, Pedro Robles, T López, Antonio Esteban, Francisco Céron, et al. Ps10, construction of a 11mw solar thermal tower plant in seville, spain. In *Proc. SolarPACES conference, Seville, Spain*, 2006.

[327] Olivier Farges, Jean-Jacques Bézian, and Mouna El Hafi. Global optimization of solar power tower systems using a monte carlo algorithm: Application to a redesign of the ps10 solar thermal power plant. *Renewable Energy*, 119:345–353, 2018.

[328] Manajit Sengupta, Aron Habte, Stefan Wilbert, Christian Gueymard, and Jan Remund. Best practices handbook for the collection and use of solar resource

data for solar energy applications. Technical report, National Renewable Energy Lab.(NREL), Golden, CO (United States), 2021.

[329] Christian A Gueymard and Dazhi Yang. Worldwide validation of cams and merra-2 reanalysis aerosol optical depth products using 15 years of aeronet observations. *Atmospheric Environment*, 225:117216, 2020.

[330] Germán Salazar, Christian Gueymard, Janis Bezerra Galdino, Olga de Castro Vilela, and Naum Fraidenraich. Solar irradiance time series derived from high-quality measurements, satellite-based models, and reanalyses at a near-equatorial site in brazil. *Renewable and Sustainable Energy Reviews*, 117:109478, 2020.

[331] BE Psiloglou, HD Kambezidis, DG Kaskaoutis, D Karagiannis, and JM Polo. Comparison between mrm simulations, cams and pvgis databases with measured solar radiation components at the methoni station, greece. *Renewable Energy*, 146:1372–1391, 2020.

[332] The European Commission's science and knowledge service. Photovoltaic geographical information system. https://re.jrc.ec.europa.eu/pvg_tools/fr/#MR, 24/03/2021. Accessed :31-08-2021.

[333] Jamie M Bright. Solcast: Validation of a satellite-derived solar irradiance dataset. *Solar Energy*, 189:435–449, 2019.

[334] Diane Palmer and Richard Blanchard. Evaluation of high-resolution satellite-derived solar radiation data for pv performance simulation in east africa. 2021.

[335] Solcast. Inputs and algorithms: How we estimate and use satellite, aerosol and weather sources to make our data. https://solcast.com/historical-and-tmy/inputs-and-algorithms/, 2021. Accessed :01-06-2021.

[336] HD Kambezidis, BE Psiloglou, D Karagiannis, UC Dumka, and DG Kaskaoutis. Recent improvements of the meteorological radiation model for solar irradiance estimates under all-sky conditions. *Renewable Energy*, 93:142–158, 2016.

[337] Allan R Starke, José M Cardemil, Rodrigo Escobar, and Sergio Colle. Multi-objective optimization of hybrid csp+ pv system using genetic algorithm. *Energy*, 147:490–503, 2018.

[338] QCELLS. Q.peak duo ml-g9 375-395 enduring high performance. https://q-cells.picturepark.com/v/VgpYpvtY/, 2021. Accessed :01-30-2021.

[339] Mark Z Jacobson and Vijaysinh Jadhav. World estimates of pv optimal tilt angles and ratios of sunlight incident upon tilted and tracked pv panels relative to horizontal panels. *Solar Energy*, 169:55–66, 2018.

[340] Monica Chinchilla, David Santos-Martín, Miguel Carpintero-Rentería, and Scott Lemon. Worldwide annual optimum tilt angle model for solar collectors and photovoltaic systems in the absence of site meteorological data. *Applied Energy*, 281:116056, 2021.

[341] Hassan Z Al Garni, Anjali Awasthi, and David Wright. Optimal orientation angles for maximizing energy yield for solar pv in saudi arabia. *Renewable Energy*, 133:538–550, 2019.

[342] Ibrahem S Altarawneh, Saleh I Rawadieh, Muafag S Tarawneh, Sultan M Alrowwad, and Firas Rimawi. Optimal tilt angle trajectory for maximizing solar energy potential in ma'an area in jordan. *Journal of Renewable and Sustainable Energy*, 8(3):033701, 2016.

[343] Colienne Demain, Michel Journée, and Cédric Bertrand. Evaluation of different models to estimate the global solar radiation on inclined surfaces. *Renewable Energy*, 50:710–721, 2013.

[344] B Liu and R Jordan. Daily insolation on surfaces tilted towards equator. *ASHRAE J.;(United States)*, 10, 1961.

[345] Amin Lahnaoui, Peter Stenzel, and Jochen Linssen. Tilt angle and orientation impact on the techno-economic performance of photovoltaic battery systems. *Energy Procedia*, 105:4312–4320, 2017.

[346] Linus Idoko, Olimpo Anaya-Lara, and Alasdair McDonald. Enhancing pv modules efficiency and power output using multi-concept cooling technique. *Energy Reports*, 4:357–369, 2018.

[347] AEMO. Aggregated price and demand data. https://www.aemo.com.au/energy-systems/electricity/national-electricity-market-nem/data-nem/aggregated-data, 2020. Accessed :24-06-2021.

[348] RTE. eco2mix - electricity consumption in france. https://www.rte-france.com/en/eco2mix/electricity-consumption-france#, 2021. Accessed :01-11-2020.

[349] Real time demand and generation. Red eléctrica. https://www.ree.es/en/activities/realtime-demand-and-generation, 2021. Accessed :01-10-2020.

[350] U.S. Energy Information Administration. Hourly electric grid monitor. https://www.eia.gov/electricity/gridmonitor/dashboard/custom/pending, 2018. Accessed :07-10-2021.

[351] Zeyu Ding, Hongjuan Hou, Gang Yu, Eric Hu, Liqiang Duan, and Jin Zhao. Performance analysis of a wind-solar hybrid power generation system. *Energy Conversion and Management*, 181:223–234, 2019.

[352] Elvis Tshiani Ilunga. *Short-term hourly load forecasting in South Africa using neutral networks*. PhD thesis, 2018.

[353] Coordinador Eléctrico Nacional. Demanda programada del sistema. https://www.coordinador.cl/operacion/graficos/operacion-programada/demanda-programada/, 2021. Accessed :01-11-2020.

[354] Agora energiewende. Power generation and consumption. https://www.agora-energiewende.de/en/service/recent-electricity-data/chart/power_generation/01.01.2018/31.12.2018/today/, 2021. Accessed :01-11-2020.

[355] HX Yang, Lin Lu, and J Burnett. Weather data and probability analysis of hybrid photovoltaic–wind power generation systems in hong kong. *Renewable Energy*, 28(11):1813–1824, 2003.

[356] Ravi Kumar, CS Rajoria, Amit Sharma, and Sathans Suhag. Design and simulation of standalone solar pv system using pvsyst software: A case study. *Materials Today: Proceedings*, 46:5322–5328, 2021.

[357] André Mermoud, Adrien Villoz, Bruno Wittmer, Hizir Apaydin, and SA PVsyst. Economic optimization of pv systems with storage. In *Paper presented at the 37th European Photovoltaic Solar Energy Conference*, 2020.

[358] Mohammad Baqir and Harpreet Kaur Channi. Analysis and design of solar pv system using pvsyst software. *Materials Today: Proceedings*, 48:1332–1338, 2022.

[359] PVSyst. Array and system losses. https://www.pvsyst.com/help/array_losses.htm, 2021. Accessed :24-02-2022.

[360] Thomas Veyrenc, Vincent Rious, Olivier Houvenagel, Thibault Prevost, Guillaume Denis, Mathilde Francon, Julien Peret, Marc Le-Du, Frederic Bienvenu, Julien Callec, et al. Conditions and requirements for the technical feasibility of a power system with a high share of renewables in france towards 2050. 2021.

[361] Joshua M Christian, Jesus D Ortega, and Clifford K Ho. Novel tubular receiver panel configurations for increased efficiency of high-temperature solar receivers. In *Energy Sustainability*, volume 56840, page V001T05A014. American Society of Mechanical Engineers, 2015.

[362] Mohanad Salih Mahdi and Ahmed Fakhrey Khudheyer. Central receivers design in concentrated solar thermal power plants: A review. In *IOP Conference Series: Materials Science and Engineering*, volume 1094, page 012018. IOP Publishing, 2021.

[363] Zhiwen Ma, Greg Glatzmaier, and Mark Mehos. Fluidized bed technology for concentrating solar power with thermal energy storage. *Journal of Solar Energy Engineering*, 136(3), 2014.

[364] NREL Transforming Energy. Concentrating solar power projects by technology. https://solarpaces.nrel.gov/by-technology, 2021. Accessed :02-02-2022.

[365] Janine Freeman. Recent and planned improvements to the system advisor model (sam). Technical report, National Renewable Energy Lab.(NREL), Golden, CO (United States), 2022.

[366] Luis Merino. *Modélisation du rayonnement solaire pour la simulation thermique en milieu urbain*. PhD thesis, University of Compiègne, 2013.

[367] Svetlana Afanasyeva, Dmitrii Bogdanov, and Christian Breyer. Relevance of pv with single-axis tracking for energy scenarios. *Solar Energy*, 173:173–191, 2018.

[368] International Energy Agency. *Technology roadmap solar thermal electricity*. OECD Publishing, 2015.

[369] C Philibert. Luz solar power stations: success in california and worldwide prospects, 1991. Accessed: 10-07-2021.

[370] Charles E Andraka, Ellen Stechel, Peter Becker, and Brian Messick. White paper on dish stirling technology: Path toward commercial deployment. Technical report, Sandia National Lab.(SNL-NM), Albuquerque, NM (United States); Stirling ..., 2016.

[371] S Moreno-Tejera, L Ramírez-Santigosa, and MA Silva-Pérez. A proposed methodology for quick assessment of timestamp and quality control results of solar radiation data. *Renewable Energy*, 78:531–537, 2015.

[372] S Younes, R Claywell, and T Muneer. Quality control of solar radiation data: Present status and proposed new approaches. *Energy*, 30(9):1533–1549, 2005.

[373] Ya-Ling He, Kun Wang, Yu Qiu, Bao-Cun Du, Qi Liang, and Shen Du. Review of the solar flux distribution in concentrated solar power: non-uniform features, challenges, and solutions. *Applied Thermal Engineering*, 149:448–474, 2019.

[374] Marco Astolfi, Marco Binotti, Simone Mazzola, Luca Zanellato, and Giampaolo Manzolini. Heliostat aiming point optimization for external tower receiver. *Solar Energy*, 157:1114–1129, 2017.

[375] Alberto Sánchez-González, María Reyes Rodríguez-Sánchez, and Domingo Santana. Aiming factor to flatten the flux distribution on cylindrical receivers. *Energy*, 153:113–125, 2018.

[376] Kun Wang, Ya-Ling He, Xiao-Dai Xue, and Bao-Cun Du. Multi-objective optimization of the aiming strategy for the solar power tower with a cavity receiver by using the non-dominated sorting genetic algorithm. *Applied Energy*, 205:399–416, 2017.

[377] Marwa Hamza and Habib Sammouda. Modeling and optimizing of non-imaging disc concentrator (nidc) photovoltaic system performance under non-uniform illumination. *Optik*, 203:163906, 2020.

[378] S Lokeswaran, Tapas K Mallick, and KS Reddy. Design and analysis of dense array cpv receiver for square parabolic dish system with cpc array as secondary concentrator. *Solar Energy*, 199:782–795, 2020.

[379] Xinyu Pan, Xing Ju, Chao Xu, Xiaoze Du, and Yongping Yang. A novel rotational symmetry (rs) connection approach for dense-array concentrator photovoltaic (da-cpv) modules. *Energy Conversion and Management*, 181:359–371, 2019.

[380] Tiong-Keat Yew, Kok-Keong Chong, and Boon-Han Lim. Performance study of crossed compound parabolic concentrator as secondary optics in non-imaging dish concentrator for the application of dense-array concentrator photovoltaic system. *Solar Energy*, 120:296–309, 2015.

[381] Chee-Woon Wong, Kok-Keong Chong, and Ming-Hui Tan. Performance optimization of dense-array concentrator photovoltaic system considering effects of circumsolar radiation and slope error. *Optics Express*, 23(15):A841–A857, 2015.

[382] Fei-Lu Siaw, Kok-Keong Chong, and Chee-Woon Wong. A comprehensive study of dense-array concentrator photovoltaic system using non-imaging planar concentrator. *Renewable Energy*, 62:542–555, 2014.

[383] Fei-Lu Siaw and Kok-Keong Chong. A systematic method of interconnection optimization for dense-array concentrator photovoltaic system. *The Scientific World Journal*, 2013:1–11, 2013.

[384] Alberto Sánchez-González, María Reyes Rodríguez-Sánchez, and Domingo Santana. Aiming strategy model based on allowable flux densities for molten salt central receivers. *Solar Energy*, 157:1130–1144, 2017.

[385] Assaf Ben Or and Joseph Appelbaum. Performance analysis of concentrator photovoltaic dense-arrays under non-uniform irradiance. *Solar Energy Materials and Solar Cells*, 117:110–119, 2013.

[386] Suneel Raju Pendem and Suresh Mikkili. Modeling, simulation, and performance analysis of pv array configurations (series, series-parallel, bridge-linked, and honey-comb) to harvest maximum power under various partial shading conditions. *International Journal of Green Energy*, 15(13):795–812, 2018.

[387] N Speetzen and P Richter. Dynamic aiming strategy for central receiver systems. *Renewable Energy*, 180:55–67, 2021.

[388] Zhichen Zeng, Dong Ni, and Gang Xiao. Real-time heliostat field aiming strategy optimization based on reinforcement learning. *Applied Energy*, 307:118224, 2022.

[389] Ruidi Zhu, Dong Ni, Tianfeng Yang, Jiamin Yang, Jinli Chen, and Gang Xiao. Heliostat field aiming strategy optimization with post-installation calibration. *Applied Thermal Engineering*, 202:117720, 2022.

[390] Elisa Ghirardi, Giovanni Brumana, Giuseppe Franchini, and Antonio Perdichizzi. Heliostat layout optimization for load-following solar tower plants. *Renewable Energy*, 168:393–405, 2021.

[391] Laurin Oberkirsch, Daniel Maldonado Quinto, Peter Schwarzbözl, and Bernhard Hoffschmidt. Gpu-based aim point optimization for solar tower power plants. *Solar Energy*, 220:1089–1098, 2021.

[392] Xing Ju, Xinyu Pan, Zheyang Zhang, Chao Xu, and Gaosheng Wei. Thermal and electrical performance of the dense-array concentrating photovoltaic (da-cpv) system under non-uniform illumination. *Applied Energy*, 250:904–915, 2019.

[393] Carlos Algora and Vicente Díaz. Influence of series resistance on guidelines for manufacture of concentrator p-on-n gaas solar cells. *Progress in Photovoltaics: Research and Applications*, 8(2):211–225, 2000.

[394] Capsun Technologies. Bluesolar: The first pv technology with integrated thermal energy storage. https://www.capsun-technologies.com/, 2021. Accessed :02-02-2022.

Abstract

Solar energy represents a promising solution to meet future energy demands in an era of depleting fossil fuel sources. However, solar energy faces two main challenges: grid instability and intermittency. To overcome these drawbacks, a large number of combinations of solar technologies have been studied over the years. In this thesis, we propose to focus on the hybridization of PV and CSP technologies into one compact system. Therefore, the objective of this thesis is to go beyond general descriptions and assumptions to study the annual energy production of two compact hybrid systems, one-sun and high-temperature plants. To answer these questions, a detailed electrical, thermal, and optical model is developed to analyze the dynamic output characteristics of the hybrid plants, based on realistic input parameters of a large-scale solar tower plant in Targassonne, France. We demonstrate the superiority of the two compact hybrid plants over stand-alone technologies. The addition of a thermal energy storage system in the compact plants has the advantage of making the energy production independent of the solar resource, which allows for better control of the plant and longer production time. We also investigate the extent to which weather conditions and demand profiles are likely to affect the capacity of compact PV-CSP hybrid systems.

Keywords: *Photovoltaic system, Concentrating Solar Power plants, Compact hybridization, numerical modeling.*

L'énergie solaire représente une solution prometteuse pour répondre aux besoins énergétiques futurs à une époque où les sources de combustibles fossiles s'épuisent. Cependant, l'énergie solaire est confrontée à deux principaux défis : l'instabilité du réseau et l'intermittence. Pour surmonter ces inconvénients, un grand nombre de combinaisons entre les technologies solaires ont été étudiées au fil des années. Dans cette thèse, nous proposons de nous concentrer sur l'hybridation des technologies PV et CSP en un seul système compact. L'objectif de cette thèse est donc d'aller au-delà des descriptions et des hypothèses générales pour étudier la production énergétique annuelle de deux systèmes hybrides compacts, les centrales à un soleil et à haute température. Pour répondre à ces questions, un modèle électrique, thermique et optique détaillé est développé pour analyser les caractéristiques dynamiques de sortie des centrales hybrides, sur la base de paramètres d'entrée réalistes d'une centrale solaire à tour à grande échelle à Targassonne, en France. Nous démontrons la supériorité des deux centrales hybrides compactes par rapport aux technologies autonomes. L'ajout d'un système de stockage d'énergie thermique dans les centrales compactes a l'avantage de rendre la production d'énergie indépendante de la ressource solaire, ce qui permet de mieux contrôler la centrale et d'allonger le temps de production. Nous étudions également dans quelle mesure les conditions météorologiques et les profils de demande sont susceptibles d'affecter la capacité des systèmes hybrides compacts PV-CSP.

Keywords: *Système Photovoltaique, Solar à concentration, hybridation compact, modélisation numérique.*